POLITECNICO DI TORINO



Master's Degree in Materials Engineering

Master's Degree Thesis

3D Printing and Functionalization of Composite Constructs with Natural Biomolecules

Supervisor

Prof. Silvia Spriano

Co-supervisors

Prof. Marco Sangermano

Prof. Elia Marin

Prof. Xu Huaizhong

Ph.D Canditate Anna Rossanese

Candidate

Lorenzo Trenta

ACADEMIC YEAR 2025-2026

Table of Contents

Abstract 5
1 Introduction 6
2 State of the Art and Current Limitations of biomaterials for wound healing 7
2.1 Historical Evolution and Fundamental Principles of Electrospinning 7
2.2 The Electrospinning Process and Its Advantages 8
2.3 Extraordinary Diversity of Use Cases of Electrospinning 8
2.4 Polycaprolactone as a Premier Scaffold Material 10
2.5 Current Limitations and Engineering Challenges of Electrospinning 11
2.6 Fundamental Mechanisms and Equipment Architecture of Electrospinning 11
2.7 The Role of Solvents in PCL Electrospinning 13
3 Scaffold Functionalization with Natural Biomolecules 18
3.1 Drug Release Kinetics and Challenges 21
3.2 Mechanical Limitations of Single-Layer Functionalized Scaffolds 22
4 Materials and Methods 23
4.1 Materials 24
4.1.1 Polymer and Solvents 24
4.1.2 Bioactive Agents 24
4.1.3 In Vitro Biological Assay Reagents 24
4.1.4 Drug Release Assay Reagents 24
4.2 Custom Electrospinning Apparatus 24
4.3 Polymer Solution Preparation and Optimization 25
4.4 Electrospinning Process Parameters 26
4.5 Bilayer Scaffold Fabrication and Sample Preparation 26
4.6 Morphological Characterization 28
4.6.1 Laser-Optical Microscopy and Image Analysis 28
4.6.2 Field Emission Scanning Electron Microscopy (FESEM) 29
4.6.3 Fluorescence Confocal Laser Scanning Microscopy 30
4.7 Chemical and Structural Characterization 30
4.7.1 Fourier Transform Infrared Spectroscopy (FTIR) 30
4.7.2 Raman Spectroscopy 32
4.8 Thermal Analysis 34
4.8.1 Differential Scanning Calorimetry (DSC) 34

4.9 Colloidal and Surface Characterization....35
4.9.1 Dynamic Light Scattering (DLS) and Particle Size....35
4.9.2 Zeta Potential and Electrophoretic Light Scattering (ELS)....36
4.9.3 Water Contact Angle (WCA)....38
4.10 Mechanical Characterization....39
4.11 In Vitro Biological Assay....41
4.11.1 Rationale for Indirect Cytocompatibility Testing....41
4.11.2 Scaffold Sterilization and Preconditioning....42
4.11.3 Eluate Preparation....42
4.11.4 Cell Culture....42
4.11.5 Exposure to Eluates....43
4.11.6 Cell Viability Assessment and Imaging....44
4.11.7 Experimental Controls....45
4.11.8 Data Handling....45
4.12 Drug Release Kinetics....45
4.12.1 Rationale for the In Vitro Release Testing Design....45
4.12.2 Sample Preparation and Release Medium....46
4.12.3 Sampling Protocol....46
4.12.4 Quantitative Analysis by UV-Vis Spectrophotometry....46
5 Results....47
5.1 Morphological Characterisation....47
5.1.1 Laser-Optical Microscopy....47
5.1.2 FESEM....51
5.1.3 Fluorescence Confocal Laser Scanning Microscopy....53
5.2 Chemical and Structural Characterization....56
5.2.1 FTIR....56
5.2.2 Raman Spectroscopy....57
5.3 Thermal Analysis (DSC)....59
5.4 Colloidal and Surface Characterization....60
5.4.1 Zeta Potential of Released Species (ELS)....60
5.4.2 Surface Zeta Potential....61
5.4.3 DLS Particle Size....63
5.4.4 Water Contact Angle (WCA)....64

5.5 Mechanical Characterization (Tensile Test) 65
5.5.1 Young's Modulus 67
5.5.2 Elongation at Break 68
5.5.3 Maximum Stress (Ultimate Tensile Strength) 69
5.6 In Vitro Biological Assay 70
5.6.1 Cell Viability 71
5.6.2 Cell Proliferation (Total Cell Count) 73
5.7 Drug Release Kinetics (UV-Vis) 75
5.7.1 β-Carotene Release 75
5.7.2 Curcumin Release 76
5.7.3 Mix Release 77
5.7.4 PCL Control Background 78
5.7.5 Estimated Released Concentration and Calibration-Related Limitations 79
6 Discussion 82
6.1 Process Robustness and Fibre Morphology 82
6.2 Molecular-Level Integration of the Bioactive Agents 83
6.3 Thermal Behaviour and Crystallinity 85
6.4 Surface Properties and their Biological Relevance 86
6.5 Mechanical Performance and the Bilayer Strategy 87
6.6 Biocompatibility 89
6.7 Release Kinetic and Clinical Implications 90
7 Conclusions 92
8 References 94
9 Appendix 99
9.1 Morphological Characterisation 99
9.1.1 Laser-Optical Microscopy 99
9.1.2 FESEM 109
9.2 Chemical and Structural Characterisation 116
9.2.1 Raman Spectroscopy 116
9.3 In Vitro Biological Assay 118
10 Acknowledgements 126

Abstract

The management of complex and chronic wounds remains a critical challenge in modern medicine, driving the need for advanced wound-dressing materials. An ideal wound dressing must not only protect the damaged tissue from external pathogens but also actively participate in the healing process by providing an optimal and highly dynamic environment. Physiologically, variations in pH depend on tissue state, ranging from a slightly acidic environment in healthy intact skin (pH 5.5) to neutral in acute wounds (pH 7.4) or acidic in the case of infections (pH 4-5), up to highly alkaline conditions (pH 9.0) in chronic lesions. Consequently, modern tissue engineering focuses on developing three-dimensional scaffolds that mimic the native extracellular matrix (ECM) while adapting to these diverse physiological conditions.

Among the various techniques available for scaffold fabrication, electrospinning has emerged as a highly versatile method capable of generating nanofibrous and microfibrous structures with high surface-area-to-volume ratios and interconnected pores closely resembling the natural ECM.

Polycaprolactone (PCL), a synthetic aliphatic polyester, is widely regarded as an excellent candidate for electrospinning due to its well-documented biocompatibility, biodegradability and suitable mechanical strength.

The successful electrospinning of PCL relies heavily on the optimization of solution and process parameters, with the choice of solvent being a primary determining factor for fibre morphology and stability. While pure chloroform exhibits excellent solubility for PCL, its poor electrical conductivity and low dielectric constant typically hinder the formation of stable and uniform fibres. To overcome these limitations and stabilize the electrospinning jet, a binary solvent system consisting of chloroform and ethanol (7:3 ratio) can be employed. The addition of ethanol significantly increases the electrical conductivity of the solution, reduces the evaporation rate and yields uniform, bead-free functionalized fibres.

Despite its favourable structural properties, pristine PCL lacks inherent biological cues, making it highly hydrophobic and limiting spontaneous cell adhesion and interaction. To functionalize the polymeric matrix and actively support the healing cascade, the incorporation of natural bioactive molecules has gained significant attention.

Plant-derived compounds are increasingly preferred over synthetic drugs due to their lower toxicity, broad-spectrum bioactivity, and cost-effectiveness. Curcumin, a natural polyphenol renowned for its potent anti-inflammatory, antioxidant and antimicrobial properties, has shown high efficacy when loaded into electrospun nanofibers, enhancing cell proliferation and accelerating wound closure. However, its application is often hindered by poor aqueous solubility, rapid degradation in alkaline environments and burst release profiles.

This is complemented by β-carotene, a natural antioxidant and precursor to vitamin A, known for its cell-stimulating properties, its ability to mitigate oxidative stress at the wound site and its capability to act as an osteoinductive agent. While curcumin tends to exhibit a rapid release

profile suggesting indirect or systemic activity, β-carotene typically provides a slower release, acting primarily via direct contact with the tissue.

Exploring a spinning approach with a 50:50 mixture of these two biomolecules represents a novel strategy to investigate the feasibility of achieving a dual-release profile within a single composite structure.

To address current limitations in mechanical performance while maximizing therapeutic efficacy, the primary objective of this study is a PCL-based bilayer patch functionalized with a high concentration of natural biomolecules for wound dressing applications. This work introduces a novel bilayer architecture designed to decouple the structural and therapeutic scaffold functions. The construct consists of a first layer of pure PCL acting as a robust structural base, followed by a second layer of functionalized PCL (containing curcumin, β-carotene or a mix 50:50). By employing this bilayer design, it is possible to significantly increase the concentration of the bioactive agents (up to 5% by mass relative to the PCL, which was kept at 20% w/v in the solvent) without sacrificing the overall tensile properties of the patch.

To ensure broad clinical relevance, the release profiles of these highly loaded bilayer constructs were evaluated across multiple pH levels (5.5, 7.4 and 9.0), providing a comprehensive understanding of the patch's behaviour in different wound environments.

1 Introduction

The aim of this thesis is to develop and characterise a PCL-based bilayer electrospun patch, functionalized with high concentrations of curcumin, β-carotene or their combination, and to evaluate how the bilayer architecture affects the mechanical performance and pH-dependent release kinetics of the incorporated biomolecules (*Figure 1*).

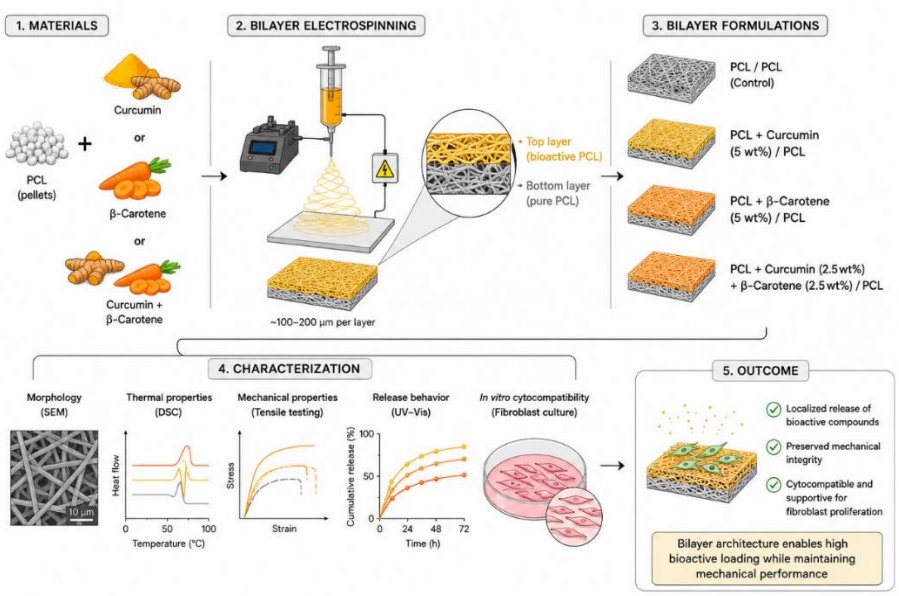


Figure 1 - Schematic overview of the experimental workflow

This thesis is structured into six additional chapters. Chapter 2 provides a comprehensive overview of the state of the art regarding electrospinning and PCL scaffolds. Chapter 3 addresses the functionalization of these scaffolds with natural biomolecules, covering their release kinetics and the resulting mechanical trade-offs. Chapter 4 details the materials, the solvent optimization strategy and the electrospinning parameters used to fabricate the bilayer scaffolds, alongside the morphological, physicochemical, surface, mechanical and biological assays employed for characterization. The objective experimental results of these investigations, focusing on fibre uniformity, mechanical integrity and specific release kinetics, are presented in Chapter 5. Chapter 6 provides a critical discussion of the results, evaluating how the bilayer architecture mitigates the plasticizing effect of active agents and interpreting the clinical implications of the observed release profiles. Finally, Chapter 7 summarizes the key findings and outlines future perspectives for the clinical translation of these composite wound dressing constructs.

2 State of the Art and Current Limitations of biomaterials for wound healing

Chronic and complex wounds are characterized by a highly heterogeneous physiological microenvironment, and pH represents one of the most clinically relevant parameters to monitor. Healthy intact skin typically presents a slightly acidic surface with a pH of around 5.5, which shifts towards neutrality (pH 7.4) in acute wounds, becomes more acidic (pH 4-5) in the presence of infection and can reach highly alkaline values (up to pH 9.0) in chronic, non-healing lesions. This pH variability directly influences enzymatic activity, bacterial proliferation and the healing cascade, making it a key design parameter for advanced wound-dressing materials capable of adapting to – or actively modulating – the local environment.[1]

2.1 Historical Evolution and Fundamental Principles of Electrospinning

The continuous evolution of materials science and regenerative medicine relies heavily on the development of advanced structures capable of mimicking native biological systems and performing highly specialized functions. While traditional manufacturing technologies have been utilized to create synthetic and biological scaffolds, they frequently encounter major drawbacks, including severe particle agglomeration, uneven particle size distribution and a lack of precise control over the microarchitecture. To overcome these manufacturing limitations, the electrospinning technique has garnered immense interest, rapidly progressing from a niche experimental observation to a cornerstone fabrication method widely recognized for its ability to generate nanofibrous structures with tunable properties (*Figure 2*).[2], [3], [4]

Historically, the fundamental principles of electrohydrodynamics date back to 1747 with the earliest observations of electrospraying by Abbé Nollet. Further investigations by Rayleigh in 1897 and Zeleny in 1914 provided the foundational understanding of fluid disintegration under electrical forces. The concept was first patented for artificial thread production by Cooley and Morton in the early 1900s, and later refined by Anton Formhals in 1934, who is widely considered the father of the modern electrospinning technique. However, the technology remained largely obscured until the 1960s, when Geoffrey Taylor mathematically defined the

conical shape of the electrified droplet, now known as the "Taylor cone". The true modern era of electrospinning began in the 1990s, driven by researchers like Reneker and Rutledge, who utilized advanced scanning electron microscopy (SEM) to observe and characterize the sub-micron and nanoscale fibres produced. Today, electrospinning is recognized as a scalable, cost-effective and highly versatile method capable of producing continuous fibres with immense length-to-diameter ratios. [5], [6]

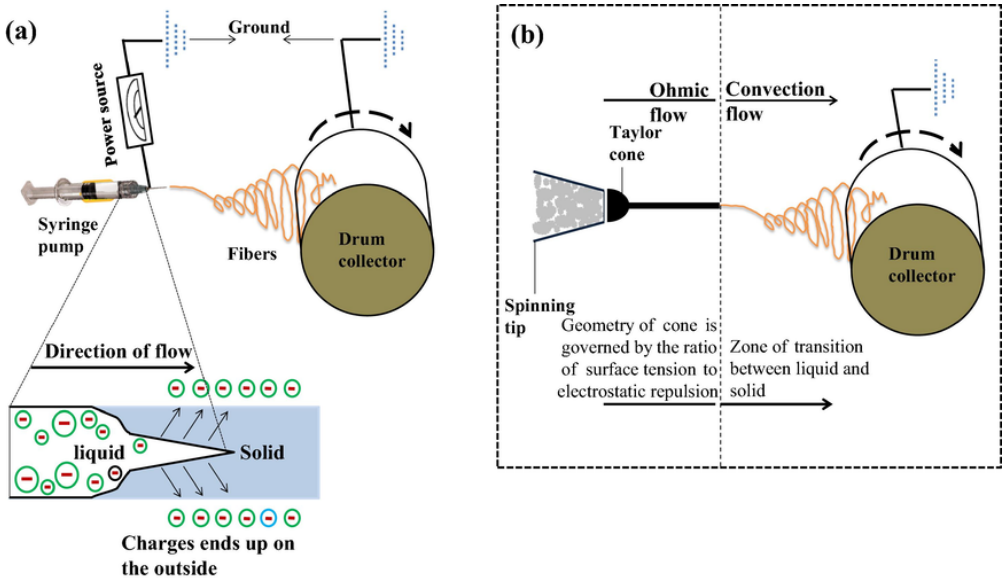


Figure 2 - Schematic depicting electrospinning setup and phenomenon of electrospinning [3]

2.2 The Electrospinning Process and Its Advantages

The core mechanism of this technology relies on the application of a high voltage electric field to draw a polymer solution, or a polymer melt from a syringe tip. As the solvent evaporates or the melt solidifies during the jet's flight, ultrafine fibres are deposited onto a collector. Compared to other conventional manufacturing technologies, electrospinning is relatively simple, inexpensive and easily implemented. The entire fabrication process is performed in a single basic step, and it successfully overcomes major traditional drawbacks associated with particle distribution. Furthermore, the amount of toxic fumes emitted into the environment during the process is minimal and can be effectively contained.[5], [6], [7]

The resulting electrospun matrices are characterized by extremely high surface-area-to-volume ratios and interconnected porous architectures that closely mimic the natural ECM of human tissues. This structural biomimicry makes electrospinning exceptionally valuable across a vast array of disciplines.[2], [8]

2.3 Extraordinary Diversity of Use Cases of Electrospinning

Currently, nearly two-thirds of all electrospinning applications are focused on the biomedical and healthcare sectors, specifically targeting tissue engineering, wound dressing and advanced drug delivery systems. By precisely controlling the electrospinning parameters, the topography of the nanofibrous scaffolds can be modified to best suit the implantation site, allowing for the

formation of diverse shapes including patches, mats, tubes, individual fibres and multilayer arrays.[2], [4], [9]

- Biomedical and Tissue Engineering: Electrospinning is predominantly utilized in the biomedical sector because the resulting nanofibrous networks closely resemble the hierarchical structure of the natural ECM. Scaffolds have been extensively developed for both soft and hard tissue regeneration, including skin, blood vessels, nerves, bones, cartilage and tendons/ligaments. For example, aligned electrospun fibres can mimic the anisotropic architecture of tendons and nerves to guide cellular migration and axonal extension, while highly porous 3D configurations are employed to stimulate osteogenesis in bine defects.[2], [8]
- Drug Delivery Systems: Electrospun mats act as a highly efficient nano-cargo carriers, capable of localized, targeted delivery of pharmaceuticals ranging from hydrophilic and hydrophobic drugs to proteins, RNA and DNA. By altering the polymers composition or using advanced spinneret designs, researchers can tailor release kinetics to achieve sustained drug delivery or controlled burst releases, minimizing systemic toxicity and enhancing bioavailability.[3], [10]
- Wound Dressing and Healing: The high oxygen permeability, tunable porosity and exudate absorption capabilities of electrospun meshes make them ideal physical barriers against microorganisms. When loaded with antibacterial agents, silver nanoparticles or herbal extracts (such as curcumin or baicalin), these fibrous dressings actively inhibit bacterial colonization while promoting re-epithelialization and tissue granulation.[2], [11], [12]

Beyond regenerative medicine, the flexibility of electrospinning extends to numerous other advanced use cases.

- Enzyme Immobilization: In biotechnology, electrospun nanofibers are utilized as inert, non-soluble carriers for enzymes. The immense surface area enhances the catalytic activity and structural stability of immobilized enzymes (such as lipases or α-chymotrypsin), preventing their denaturation and improving bioprocessing efficiency.[3]
- Environmental Engineering and Filtration: The interconnected porosity and small pore size of electrospun membranes provide excellent filtration capabilities. They are actively used as affinity membranes to remove highly toxic heavy metals (e.g., Chromium(VI), Lead, Copper) from contaminated water. Additionally, they serve as highly efficient membranes for water desalination via membrane distillation and capacitive deionization.[3]
- Defence and Protective Clothing: Electrospun fabrics are incorporated into military protective clothing to neutralize biological and chemical warfare agents. The nanofiber layers offer extreme resistance to aerosol particle penetration while maintaining low impedance to moisture vapor diffusion, ensuring breathability.[3]
- Energy, Electronics, Sensors and Nanoreactors: Intrinsically conductive polymers and piezoelectric materials (like polyvinylidene fluoride, PVDF) are electrospun to create flexible electronics, supercapacitors and energy-harvesting nanogenerators.

Furthermore, the high surface area allows for maximum interaction with target analytes, resulting in highly sensitive optical, chemical and biological nanosensors capable of detecting specific molecules or physical changes. Additionally, the technology is highly promising for the production of nanoreactors; the large surface area allows for efficient catalyst distribution, significantly improving chemical reactions for fuel cells and advanced energy storage systems.[3], [6]

2.4 Polycaprolactone as a Premier Scaffold Material

Among the vast selection of applicable materials (which ranges from natural polymers like collagen and gelatine to synthetic ones), PCL has emerged as a favoured candidate for scaffold fabrication.

Chemically, PCL is a semi-crystalline, linear aliphatic polyester, synthesised via ring-opening polymerization of the seven-membered ε-caprolactone monomer, a process first investigated in the 1930s. Its repeating unit combines five non-polar methylene groups with a single, relatively polar ester group (*Figure 3*), a structural balance that governs much of its favourable processing and biological behaviour.[13]

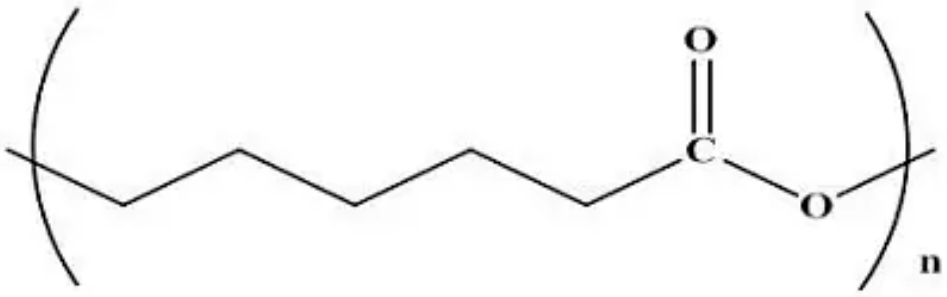


Figure 3 - Chemical structure of poly(ε-caprolactone)(PCL)

From a thermal standpoint, PCL exhibits a low melting temperature (approximately 59-64°C) and a glass transition temperature well below room temperature (around -60°C), meaning it remains in a rubbery, highly flexible state under physiological conditions. This low melting point simplifies melt-based processing, while its superior rheological and viscoelastic properties, compared to many other aliphatic polyesters, make PCL solutions particularly well-suited to electrospinning without the need for carrier polymers or extensive additives.[13], [14], [15]

PCL offers an excellent strength-to-weight ratio, ease of processing and highly desirable biochemical traits including non-toxicity, biodegradability, biocompatibility and excellent chemical and thermal stability. Its degradation proceeds via hydrolytic cleavage of the backbone ester bonds, a process considerably slower than that of other common resorbable polyester such as poly-lactic acid (PLA) or poly-glycolic acid (PGA), which typically lasts two to four years in vivo. Critically, unlike PLA and PGA, PCL degradation does not generate a pronounced acidic microenvironment, reducing the risk of local inflammatory or foreign-body responses and making it particularly attractive for long-term implantable devices and sustained drug-delivery systems.[13], [14]

These favourable properties, combined with FDA approval, relatively low production costs and a long clinical track record (including its use in slowly resorbing suture materials), have made PCL one of the most widely utilized synthetic polymers for constructing three-dimensional scaffolds that safely interface with human tissue, spanning applications from bone and cartilage regeneration to vascular grafts and, as explored in this work, skin and wound-healing constructs.[12], [13], [14]

2.5 Current Limitations and Engineering Challenges of Electrospinning

Despite this immense versatility, the successful fabrication of reproducible and mechanically robust electrospun materials requires navigating a complex matrix of operational parameters, fluid dynamics and equipment architectures, which remain a significant engineering challenge. Achieving consistent, high-quality PCL nanofibers is entirely dependent on the careful optimization of the electrospinning parameters, with the choice of the solvent being one of the most critical factors. The selected solvent directly impacts the viscosity, conductivity, dielectric properties and evaporation rate of the solution, which fundamentally dictate the morphology, mechanical performance and clinical applicability of the resulting scaffold (*Figure 4*).[6], [9], [16]

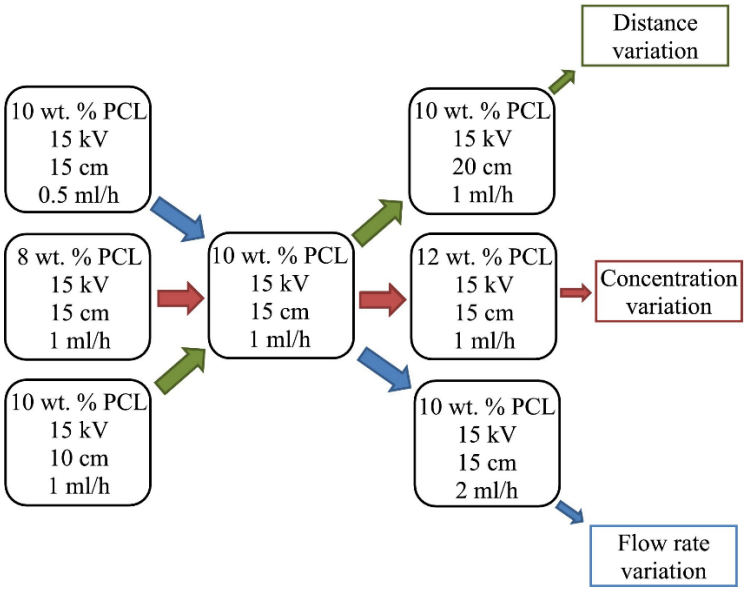


Figure 4 - Schematic representation of the electrospinning process for nanofiber fabrication [9]

2.6 Fundamental Mechanisms and Equipment Architecture of Electrospinning

The fundamental principle of electrospinning is governed by electrohydrodynamics, where an external electric filed is utilized to overcome the intrinsic surface tension of a polymeric fluid. In a typical operation, the polymer solution is subjected to a high voltage direct current (DC) power supply, which continuously injects electrical charges into the liquid. As the charge accumulates at the droplet suspended at the capillarity tip, electrostatic repulsive forces (specifically Coulombic forces) build up against the opposing viscoelastic and surface tension

forces the polymer solution. When the applied electric field surpasses a critical voltage threshold (Eq. (1)), these Coulombic forces dominate, causing the spherical droplet to distort into a conical shape known as the Taylor cone (*Figure 5)*.[5], [6], [12]

Taylor equation

$$V_c^2 = \frac{4H^2}{L^2}\left[ln\left(\frac{2L}{R}\right) - 1.5\right](0.117\pi\gamma R) \quad (1)$$

Where V_c is the critical voltage, H is the needle-to-collector distance, L Is the needle length, R is the needle radius and γ is the surface tension of the solution

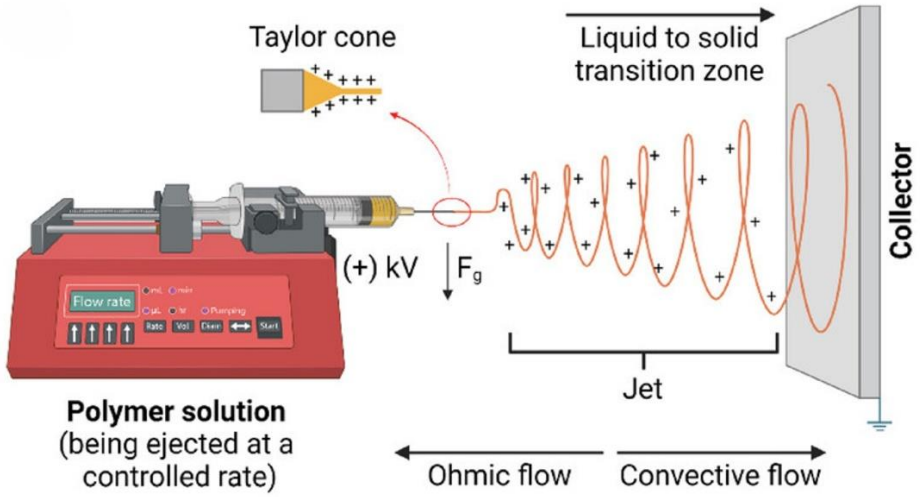


Figure 5 - Schematic representation of the monoaxial electrospinning process [6]

From the apex of this cone, a charged polymer jet is forcefully ejected toward a grounded or oppositely charged target cathode. During its flight across the designated working distance, the jet is subjected to continuous elongation driven by the electric field. Crucially, the jet undergoes a phenomenon known as "bending instability" or whipping motion. During this chaotic, rapid whipping phase, the electrical forces stretch and thin the polymer jet by massive ratios. Simultaneously, the solvent within the jet rapidly evaporates (or, in case of a polymer melt, the material solidifies) leading to a phase transition from liquid to solid. This delicate balance between electrostatic stretching and solvent evaporation reduces the jet's diameter significantly, culminating in the deposition of solid, ultrafine continuous threads with diameters typically in the range of several hundred nanometres, generating a web-like non-woven fibrous mat.[5], [12], [17]

The physical architecture required to execute and control these electrohydrodynamic phenomena relies on precise, interconnected arrangements of engineering components. To meet specific research requirements and provide superior architectural flexibility, laboratory scale fabrication often utilizes custom-built, modular apparatuses assembled by integrating essential, independent components. For the scaffolds fabricated in this study, the core fluid-delivery apparatus involves an automated infusion system, utilizing a medical-grade plastic syringe (e.g., 10 mL capacity) securely mounted onto a programmable syringe pump. This pump guarantees a strictly controlled and constant flow rate of the solution delivered to the emitting tip. The emitter itself is generally a blunt stainless-steel needle (such as 23G or 25G) connected directly

to the isolated high-voltage DC power supply, which is capable of generating potentials up to 30 kV.[6], [12], [14]

The collection unit, which acts as the grounded cathode, is positioned at a fixed working distance, typically ranging from 5 to 20 cm from the needle tip. This distance is a critical parameter, as it provides the necessary time and space for the jet to stretch and the solvent to fully evaporate before deposition. Collectors can vary in their geometric design, encompassing stationary flat plates or rotating stainless-steel cylindrical drums (operating at specific rotation speeds, such as 300 rpm) depending on whether random or aligned fibre deposition is required. The use of a custom-assembled electrospinner provides the crucial spatial and electrical adaptability needed to finely tune the nozzle-to-collector distance and voltage distribution.[12], [17]

Regardless of the specific geometry, the versatile metallic collector surface is conventionally wrapped in a fresh, perfectly smooth layer of aluminium foil. The incorporation of aluminium foil serves several pivotal functions in the process. Primarily, its highly conductive nature facilitates the rapid dissipation of residual electrical charges from the newly deposited fibres. This charge dissipation effectively minimizes the electrostatic repulsion between accumulating fibre layers, which directly promotes the formation of fibres with smaller, more consistent diameters. Furthermore, the conformal and smooth application of the foil is critical for maintaining the structural and physical integrity of the delicate nanofiber mat. A smooth substrate ensures that the final scaffold can be safely and non-destructively peeled away once the electrospinning cycle is complete. Finally, to ensure process reproducibility and mitigate the risk of structural defects (such as excessive fibre fusion or droplet formation), the entire equipment is housed within a controlled environmental chamber where ambient parameters, such as room temperature (e.g., 18-28°C) and relative humidity, are strictly monitored and regulated.[12], [14], [15]

2.7 The Role of Solvents in PCL Electrospinning

The selection of an appropriate solvent system is a critical step in the production of smooth, uniform and bead-free electrospun nanofibers. The solvent directly influences the fundamental properties of the polymeric solution, including its viscosity, electrical conductivity, dielectric constant and surface tension. Consequently, the evaporation rate and volatility of the chosen solvent fundamentally dictate the final morphology of the scaffold.[4], [18], [19]

Solvent volatility primarily affects the resulting fibre diameter, while the surface tension dictates the formation of defects like bubbles or beads along the strand. If the surface tension is too high relative to the applied voltage and centrifugal or electrostatic drawing forces, the jet will destabilize, leading to a highly polydisperse “bead-on-string” morphology. Furthermore, the vapor pressure of the solvent plays a role in the formation of surface nanopores. Fast evaporating solvents, such as acetone (*Figure 6 – a*), dichloromethane (DCM) (*Figure 6 – b*) or tetrahydrofuran (THF) (*Figure 6 – c*), promote rapid fibre solidification. However, excessive volatility can lead to surface irregularities or unintended pore formation because the components lack sufficient time to distribute evenly. Specifically, highly volatile solvents rapidly evaporate, causing localized cooling on the fibre surface; this cooling condenses

atmospheric water vapor into droplets (a phenomenon known as phase separation or “breath figures”) which leave behind nanometre-sized pores once the water evaporates. Conversely, slower evaporating solvents – such as toluene (*Figure 6 – d*) or dimethylformamide, DMF (*Figure 6 – e*) – allow for gradual solvent release and shape retention, yielding a smoother and more homogeneous fibre structure, although they can reduce the degree of unidirectional alignment due to prolonged whipping instabilities.[3], [4], [19]

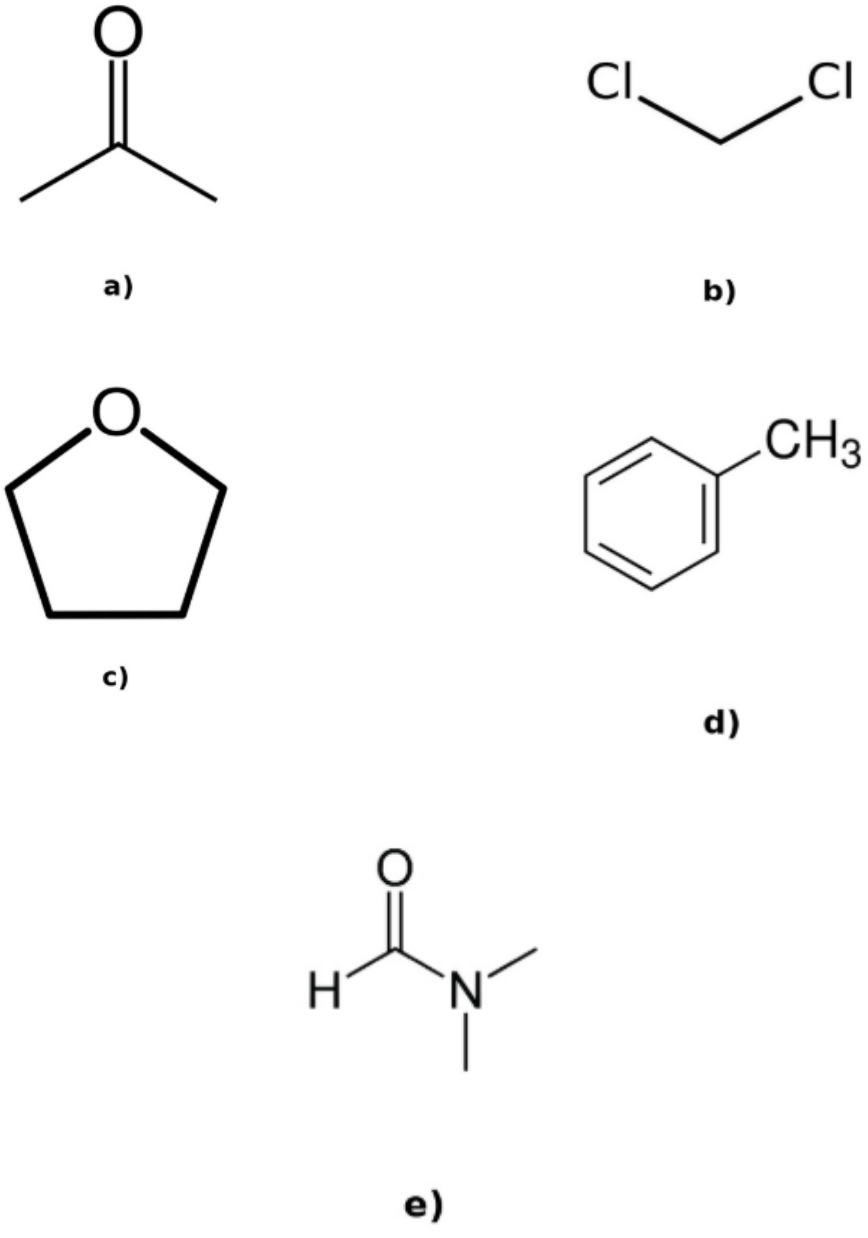


Figure 6 - Chemical structure of different solvents. a) acetone, b) DCM, c) THF, d) toluene, e) DMF

The electrical properties of the solvent are equally paramount. Solvents with higher electrical conductivity and higher dielectric constants (permittivity) enhance the electrostatic repulsion within the jet. This increased charge density promotes greater stretching and thinning of the polymer jet during its flight, successfully reducing the final fibre diameter into the nanoscale.

However, if the conductivity is too high, it can lead to severe jet instability, electrical discharges and an inability to spin continuous fibres.[5], [18]

Chloroform (CF, *Figure 7*) is one of the most frequently utilized solvent for PCL electrospinning due to its excellent solubility, which promotes the highly efficient packing of the polymer chains. Scaffolds produced with CF exhibit a homogeneous, granule-free morphology with fibres arranged in orderly layers. The rapid evaporation rate of CF minimizes residual solvent in the core of the as-spun fibres and is highly beneficial for the formation of bead-free structures. Furthermore, its relatively lower viscosity prevents the common issue of polymer agglomeration during the spinning process. From a mechanical standpoint, PCL nanofibers spun from CF yield the strongest structures. Testing has shown that these fibres can reach an elastic modulus of up to 9.86 MPa and a yield strength of 1.11 MPa. These values closely match the mechanical properties of human biological tissues, corresponding up to 98.6% with the elastic modulus of liver and kidney walls (*Table 2.1*).[4], [18], [19], [20]

Tissue	Elastic Modulus (E)
Skin	60-850 kPa (bulk); 35 kPa (dermis), 2 kPa (hypodermis)
Spinal Cord	1.23 MPa
Cornea	0.2 MPa
Liver	≈ 6 kPa*
Kidney	≈ 12 – 24 kPa*

Table 2.1- Elastic modulus of representative human tissues, adapted from Guimarães et al.[20]

***Converted from shear modulus (G) via E ≈ 3G, assuming near-incompressible soft tissue (Poisson's ratio ν ≈ 0.5).**

Despite these advantages, the use of pure CF presents significant limitations. CF is recognized as toxic and harmful to human health, necessitating operation within fume hoods and posing environmental concerns. From a technical standpoint, CF possesses poor electrical conductivity and a very low dielectric constant (approximately 4.8 at 20°C). These poor electrical properties severely restrict the electrostatic stretching of the polymeric jet during the electrospinning process, meaning that CF solutions often yield thicker microfibers rather than true nanoscale fibres. [4], [18]

In response to the toxicity of halogenated solvents, recent research has shifted towards "green" alternative solvents such as pure acetone or acetic acid (*Figure 8*). However, studies have demonstrated that these environmentally friendly solvents are rarely suitable for direct electrospinning without compromising the material's structure. For example, when PCL is dissolved in acetic acid, the deposition often results in many elongated droplets and beads, indicating suboptimal electrical fields or poor solution stability. The high viscosity of acetic acid specifically causes the PCL polymer to clump and clog at the tip of the needle, a frequent and disruptive issue in electrospinning. This clogging leads to a highly unstable spinning process, ultimately resulting in irregularly shaped fibre strands, clustered polymer aggregations and a severe reduction in the mechanical strength of the scaffold. With acetic acid, the elastic modulus drops to around 2.75-2.92 MPa, yielding mechanical properties corresponding only to softer tissues like arteries, veins or the spinal cord. Pure acetone similarly yields weaker

scaffolds with an elastic modulus comparable to human cornea, lacking the robust load-bearing capacity of CF-spun fibres. Furthermore, PCL dissolved in acetic acid-formic acid mixtures creates extremely dense 3D meshes with the lowest pore-to-areas and porosities, severely hindering cellular infiltration and viability in 3D in vitro cultures.[4], [7]

To navigate the drawbacks of single solvents systems, the implementation of binary and ternary solvents mixtures has proven highly effective. The strategic combination of solvents with different evaporation rates, vapor pressures and dielectric properties allows for precise control over the morphological properties of the resulting scaffold. For example, combining CF with other solvents like methanol (MeOH, *Figure 9 – a*), ethanol (EtOH, *Figure 9 – b*), acetone or DCM alters the solution properties significantly. Mixtures of CF and DCM (e.g., at a 7:3 volume ratio) have been shown to produce highly porous structures with thick fibres (up to 5.97µm in diameter) and distinct surface roughness; this specific topography drastically improves cell attachment, intercellular communication and overall cell viability for lung adenocarcinoma cells compared to acetic acid solutions.[18], [19], [21]

To specifically optimize the electrical profile of CF without relying entirely on highly toxic co-solvents, adding EtOH dramatically improves the solution parameters. While CF has a dielectric constant of 4.8, EtOH possesses a much higher dielectric constant of 24.5 (at 25°C). This addition enables a larger electrostatic field, leading to a much more stable Taylor cone and improved jet formation. Furthermore, EtOH has a lower vapor pressure (7.83 kPa) compared to CF (25.90 kPa); thus, adding EtOH increases the overall viscosity and reduces the overly rapid evaporation of pure CF, enhancing electrospinnability. Because EtOH is a non-solvent for PCL and has low intrinsic conductivity, researchers have further refined this approach by introducing trace amount of formic acid to the CF/EtOH mixture. Formic acid, acts as a powerful conductivity enhancer, boasting a high dielectric constant of 58 (at 20°C). Additionally, the higher boiling points of EtOH (78.37°C) and formic acid (100.80°C) compared to CF (61.20°C) prolong the evaporation of the jet. This extended evaporation window provides the polymer chains with sufficient time to organize and align, resulting in higher crystallinity in the final PCL fibres (un po to 61.33%). Creating an optimized ternary solvent systems (e.g., CF/EtOH/formic acid (*Figure 10*) at a 9:1:0.1 volumetric ratio) perfectly leverages the solubility of CF, the dielectric boost of EtOH and the conductivity enhancement of formic acid to produce highly uniform, bead-free and continuous PCL nanofibers suitable for advanced biomedical applications (*Figure 11, 12, 13*).[4], [9], [18]

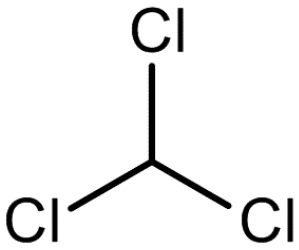


Figure 7 - Chemical structure of CF

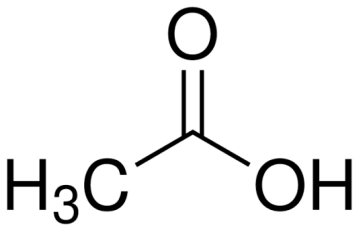


Figure 8 - Chemical structure of acetic acid

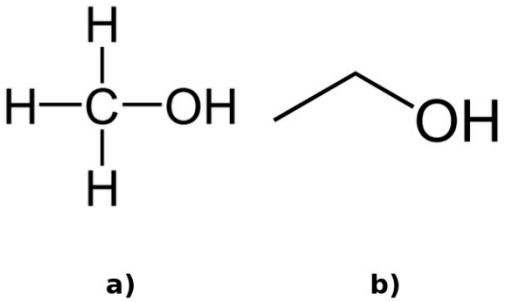


Figure 9 - Chemical structure of a) methanol and b) ethanol

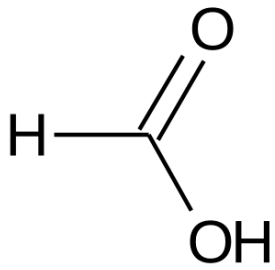


Figure 10 - Chemical structure of formic acid

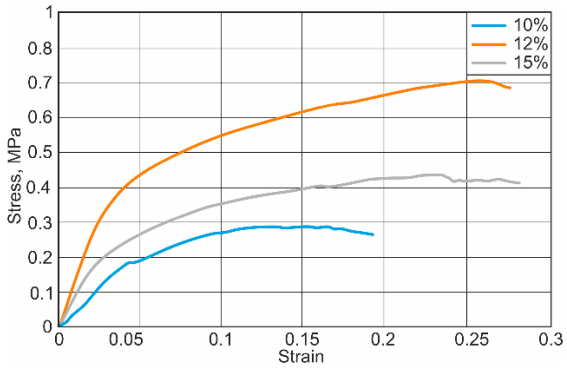


Figure 11 - Stress-strain curve for PCL scaffolds electrospun with chloroform as the solvent [4]

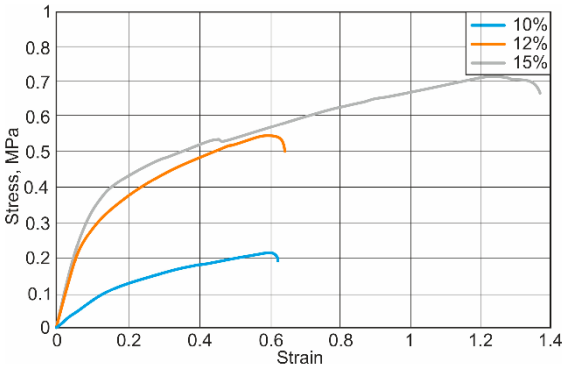


Figure 12 - Stress-strain curve for PCL scaffolds electrospun with acetone as the solvent [4]

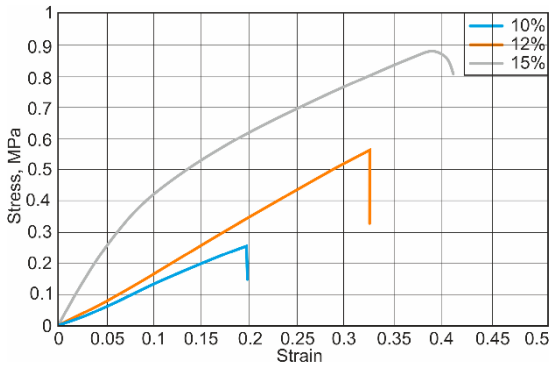


Figure 13 - Stress-strain curve for PCL scaffolds electrospun with acetic acid as the solvent [4]

3 Scaffold Functionalization with Natural Biomolecules

While pristine PCL provides an excellent, mechanically robust structural framework, its highly hydrophobic nature significantly restricts its biological integration. Hydrophobic surfaces hinder favourable or bioactive protein adsorption, although they often promote high total protein adsorption through hydrophobic interaction, which is a critical prerequisite for integrin-mediated cell adhesion, focal adhesion maturation and subsequent cell spreading. To overcome this barrier and actively stimulate tissue regeneration, the direct incorporation of bioactive natural molecules into the electrospun fibres has become a major point in current biomedical research.[12], [15]

Curcumin (*Figure 14*), a natural polyphenolic compound extracted from *Curcuma longa* (turmeric), is widely integrated into PCL scaffolds to exploit its potent antioxidant, anti-inflammatory, antimicrobial and anticarcinogenic properties. The electrospinning process itself can induce a structural transformation of curcumin. While it naturally resides in an energetically stable enol form in the solid phase or keto form in acid/polar media, the electrospinning process forces a transition that allows the central hydrogen atom of the enol form to act as a hydrogen donor, interacting directly with the weak hydrogen bond acceptors of the PCL matrix's carbonyl groups. This chemical interaction significantly alters the scaffold's properties: curcumin acts as a plasticizer, disrupting crystal formation, reducing the overall crystallinity of PCL and decreasing its ultimate tensile stress while simultaneously increasing elongation at break and toughness. Furthermore, curcumin integration introduces a distinct micro-roughness to the fibre surface and increases hydrophilicity. This drastically improves the biocompatibility of the scaffold, resulting in superior cell adhesion and proliferation, as observed with human BJ-1 fibroblasts. Clinically, curcumin-loaded PCL nanofibers have demonstrated exceptional efficacy in treating full-thickness and diabetic wounds by accelerating wound closure, enhancing collagen synthesis and re-epithelialization, and modulating the inflammatory response through the downregulation of pro-inflammatory cytokines like IL-6 and TNF-α and the quenching of reactive oxygen species (ROS, *Figure 15*).[2], [8], [15], [22]

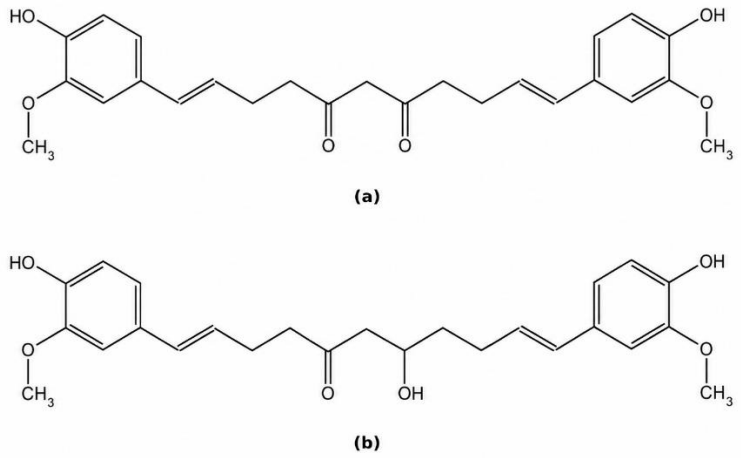


Figure 14 - Chemical structure of curcumin a) keto form, b) enol form

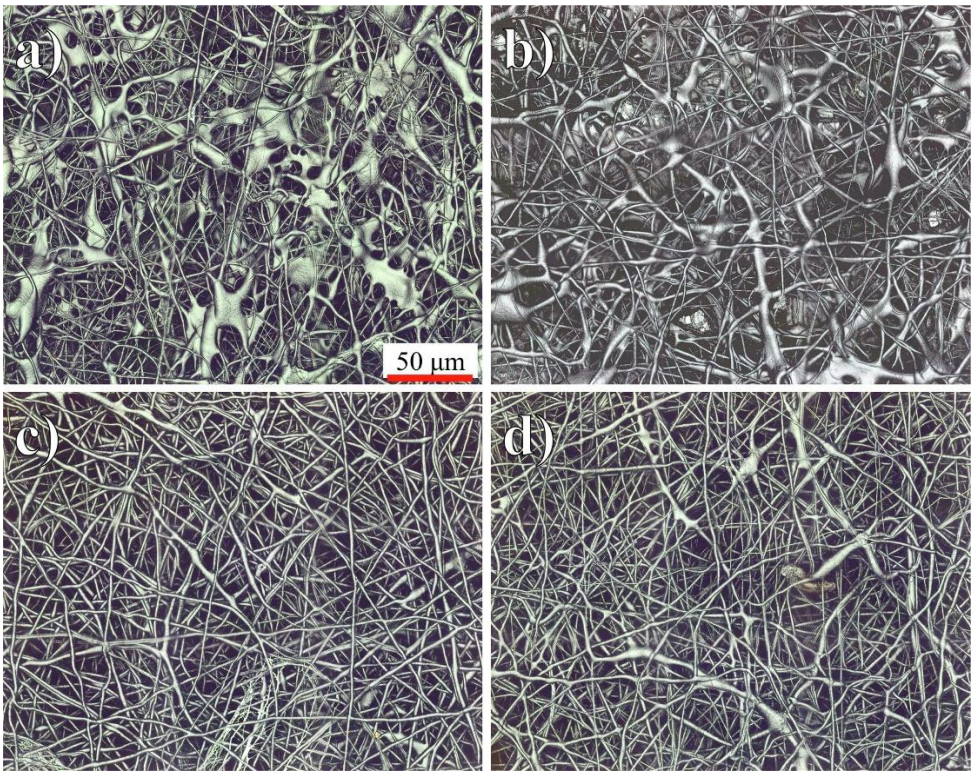


Figure 15 - Low-magnification confocal micrographs of PCL scaffolds at increasing curcumin concentration, showing the effect on fibre deposition quality. a) Pure PCL, b) 1.2% Curcumin, c) 2.4% Curcumin, d) 3.6% Curcumin [8]

Another highly effective natural biomolecule is β-carotene (*Figure 16*), a carotenoid pigment and natural precursor to vitamin A, known for its outstanding ROS-scavenging, anti-inflammatory and cell-stimulating capabilities. When incorporated into PCL electrospinning solutions, β-carotene typically remains in a particulate form within the polymeric matrix rather than forming strong covalent bonds, yet it still imparts a significant plasticizing effect. This incorporation lowers the crystallinity index and elastic modulus of the PCL fibres while increasing their ultimate strain. Dermatologically, β-carotene-loaded PCL scaffolds are investigated as a novel, long-term treatment for skin disease such as eczema, benefiting from the sustained, slow release of the active compound over hundreds of hours. Beyond soft tissue, β-carotene acts as a potent natural osteogen. PCL/β-carotene scaffolds actively promote the proliferation of mesenchymal stem cells (MSCs) and KUSA-A1 cells, successfully inducing their differentiation into osteoblasts without the need for any external osteogenic differential agents (e.g., dexamethasone). This osteoinductive effect is confirmed by the upregulation of specific bone markers, including RUNX2, SOX9, osteocalcin and osteonectin, alongside enhanced matrix mineralization and calcium deposition. Additionally, scaffolds loaded with higher concentrations of β-carotene exhibit a marginal bacteriostatic effect against *Escherichia*

coli, demonstrating its potential to reduce bacterial colonization in wound sites (*Figure 17*). [3], [6], [7], [14]

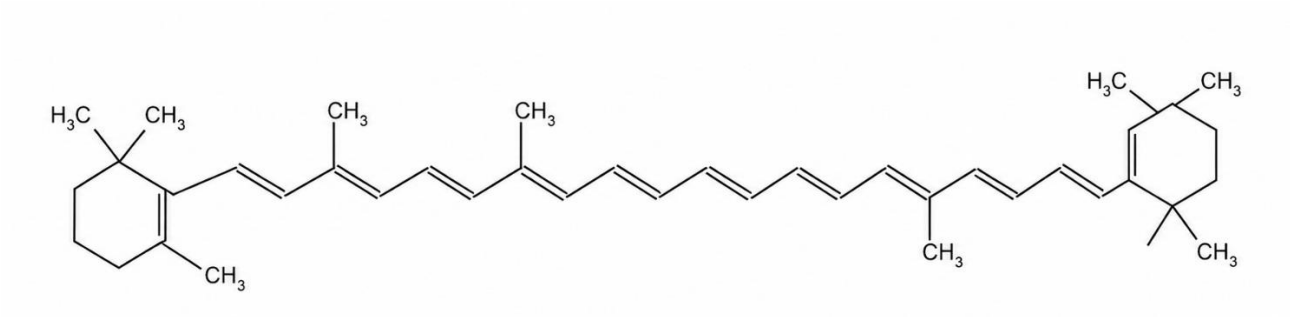


Figure 16 - Chemical structure of β-carotene

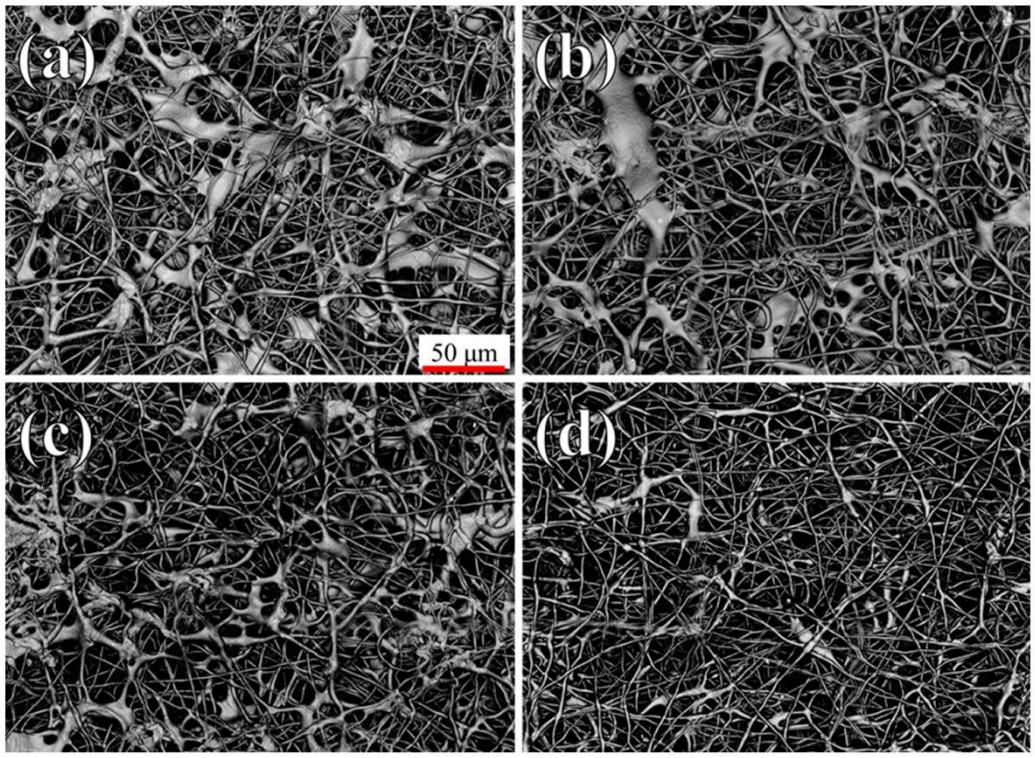


Figure 17 - Low-magnification confocal micrographs of PCL scaffolds with increasing β-carotene concentration. a) Pure PCL, b) 1.2% β-carotene, c) 2.4% β-carotene, d) 3.6% β-carotene [7]

Similarly, baicalin (*Figure 18*), a flavonoid extracted from the Chinese herb *Scutellaria baicalensis*, has been successfully utilized as a multitherapeutic, antibacterial component in PCL-based nanofibrous wound dressings. The incorporation of baicalin introduces abundant hydroxyl groups that significantly shift the PCL surface from a hydrophobic to a hydrophilic state. This transition strongly decreases the water contact angle, fostering the release of the active compound and providing broad-spectrum antibacterial activity, particularly against Gram-positive bacteria such as *Staphylococcus aureus*, while maintaining excellent cytocompatibility with skeletal myoblast cells.[5]

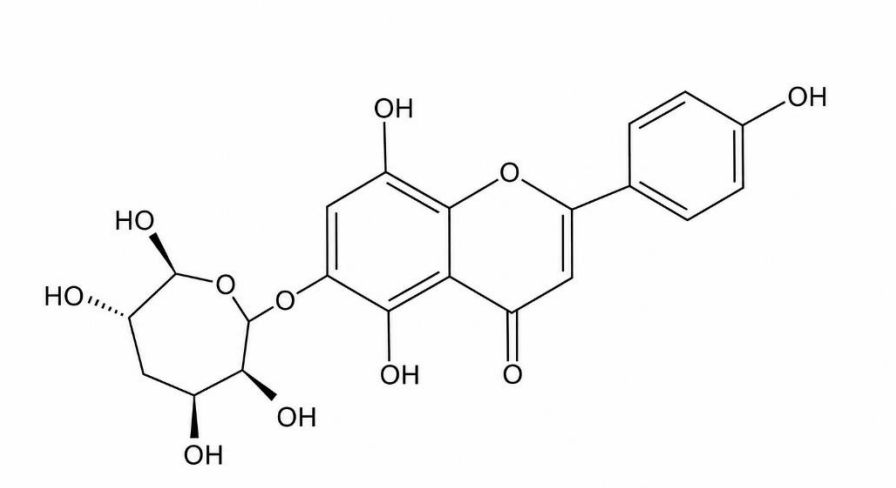


Figure 18 - Chemical structure of baicalin

3.1 Drug Release Kinetics and Challenges

Despite these profound biological advantages, governing the release kinetics of these natural molecules presents a distinct engineering challenge. Hydrophilic drugs and molecules tend to exhibit a lower affinity for the hydrophobic PCL matrix and a higher affinity for the evaporating solvents. During the rapid evaporation of the solvent mixture in the electrospinning flight, the active molecules are pulled toward the surface of the nanofibers. This phenomenon typically results in a biphasic release profile characterized by an undesirable initial "burst release" (where a large percentage of the drug is discharged within the first few hours), followed by a much slower, Fickian diffusion-driven release dictated by PCL's exceptionally slow degradation rate and limited water penetration.[2], [17]

To quantitatively characterize and predict this behaviour, drug release data are typically fitted to established mathematical models. The Higuchi model describes drug transport as a purely Fickian diffusion process from a homogenous matrix (Eq. (2)), whereas the Korsmeyer-Peppas model is more broadly applicable to polymeric systems and introduces a release exponent (n) that identifies the underlying transport mechanism (Eq. (3)): values of $n \leq 0.45$ indicate Fickian diffusion, $0.45 < n < 0.89$ indicates anomalous (non-Fickian) transport driven by a combination of diffusion and polymer chain relaxation, and $n \geq 0.89$ indicates Case-II transport, governed primarily by polymer erosion or relaxation rather than diffusion. Fitting experimental release data to these models therefore allows the dominant release mechanism to be identified and compared across different scaffold formulations. [23]

Higuchi equation

$$Q_t = k_H \cdot t^{1/2} \quad (2)$$

Where Q_t is the cumulative amount of drug released at time t, and k_t is the Higuchi release constant, which depends on the physicochemical properties of the drug delivery system

Korsmeyer-Peppas equation

$$\frac{M_t}{M_\infty} = k \cdot t^n \quad (3)$$

Where $\frac{M_t}{M_\infty}$ is the fraction of drug released at time t, k is the kinetic constant characteristic of the polymer-drug system and n is the release exponent that describes the drug release mechanism

Beyond the general mechanism described above, curcumin and β-carotene present distinct, molecule-specific release challenges. Curcumin's poor aqueous solubility and rapid degradation under the alkaline or light-exposed conditions further exacerbate its burst release tendency, often resulting in a substantial fraction of the loaded drug being inactivated before reaching the target tissue. β-Carotene, being considerably more hydrophobic and prone to oxidative degradation, is retained more effectively within the PCL matrix, resulting in the comparatively slower, contact-mediated release profile discussed previously; however, this same hydrophobicity can limit its overall bioavailability once released. [7], [8], [10], [24]

3.2 Mechanical Limitations of Single-Layer Functionalized Scaffolds

While the biological benefits of functionalized PCL with natural biomolecules are well documented, the current state of the art faces a significant hurdle regarding the structural integrity of these composite materials. The direct incorporation of bioactive powders into a single-layer PCL matrix often leads to a severe degradation of its mechanical properties, creating a bottleneck for clinical translation.[7], [8], [14], [15]

Molecules such as β-carotene fail to form strong covalent bonds with the PCL matrix. Because of differing polarities, β-carotene being highly hydrophobic and PCL being semi-crystalline, and the rapid solvent evaporation during electrospinning, the β-carotene remains largely in a particulate form, instead of blending homogeneously to reinforce the matrix without establishing cohesive chemical bonds. Consequently, β-carotene acts as a plasticizer. This plasticizing effect disrupts the crystalline formation of the polymer, increasing the amorphous fraction, which melts in a wider temperature range with lower enthalpy. In macroscopic terms, while this plasticization increases the scaffold's ultimate strain (elongation) and flexibility, it causes a drastic reduction in both the ultimate tensile stress and the elastic (Young's) modulus as the concentration of the additive increases.[7], [14]

A similar, concentration-dependent mechanical deterioration is observed with curcumin. At lower concentrations (up to 1.2% or 2.4%), curcumin can transform from a di-keto state into a reactive keto-enol form during electrospinning, enabling it to form non-covalent hydrogen bonds with the carbonyl groups of the PCL matrix. This interaction can momentarily retain or marginally increase the ultimate strength and toughness of the fibres. However, raising the concentration to 3.6% or beyond (often necessary to maximize therapeutic and antimicrobial efficacy) overwhelms these structural benefits. At higher loadings, the excess additive fails to fully convert to the bonding enol-form, leaving residual keto-curcumin which is far less likely to bond with the PCL. This lack of integration leads to a sharp, progressive drop in mechanical strength, with the Young's modulus failing to less than half of that of a pristine PCL scaffold.

The excessive plasticizing effect destabilizes the structure, weakening the chemical bonds between PCL molecules and accelerating the scaffold's structural dissolution. [7], [8], [15]

This structural weakening critically limits the clinical application of highly loaded, single-layer patches, as they lose the necessary load-bearing capacity, ultimate strength and stiffness required to withstand physiological stress and mimic native tissues. To circumvent this inherent limitation, the development of a multi-layer architecture allows for a highly loaded, bioactive outer layer designed for immediate tissue interaction, supported by a pristine or minimally loaded inner polymeric layer that preserves the robust mechanical strength, elastic modulus and load-bearing capacity of the original PCL. This hierarchical approach effectively bypasses the mechanical degradation caused by excessive plasticization, enabling the scaffold to simultaneously satisfy the conflicting demands of high biological activity and robust biomechanical performance.[7], [8], [12], [14], [15]

4 Materials and Methods

This chapter details the materials, experimental procedures and analytical techniques employed to fabricate and characterize the novel PCL-based bilayer patches for wound dressing. The primary goal of the experimental design was to successfully decouple the structural and therapeutic functions of the scaffold, mitigating the mechanical degradation typically caused by high concentrations of bioactive molecules.

To achieve this, all fabricated patches share a common bilayer architecture: a structural base layer of pristine PCL, overlaid with a functionalized PCL layer. The samples were divided into distinct experimental groups based on the bioactive agents incorporated into the second layer:

- PCL Control (CTRL): A bilayer sample consisting exclusively of pristine PCL, used as the baseline for all structural and biological comparisons.
- PCL-Curcumin (PCL-Cur): A bilayer sample where the active layer is loaded with curcumin.
- PCL-β-Carotene (PCL-Beta): A bilayer sample where the active layer is loaded with β-carotene.
- PCL-Mix (PCL-Mix): A bilayer sample featuring a 50:50 combination of both curcumin and β-carotene in the active layer.

All functionalized samples were loaded with a high concentration of bioactive agents (up to 5% w/w relative to the PCL content) to evaluate the maximum therapeutic efficacy and the mitigating effect of the bilayer design on the plasticizing behaviour of the molecules.

Following the fabrication process, the scaffolds were subjected to a comprehensive characterization protocol. The remainder of this chapter is divided into four main sections according to the nature of the analyses performed: Morphological Characterization (to assess fibre structure and bilayer integrity), Physicochemical and Thermal Characterization (to evaluate molecular interactions and thermal properties), Mechanical Characterization (to test the load bearing capacity), and finally, *In Vitro* Release and Biological Characterization (to evaluate therapeutic delivery at varying pH levels and cellular compatibility).

4.1 Materials

4.1.1 Polymer and Solvents

- Polycaprolactone (PCL): CAPA 6800, supplied by Perstorp Holding AB, Sweden [25]
- Chloroform (CF): ≥ 99.0% (GC), purchased from Nacalai Tesque (Kyoto, Japan) [26]
- Ethanol (EtOH): ≥ 99.5vol% (ρ), purchased from Nacalai Tesque (Kyoto, Japan) [27]

4.1.2 Bioactive Agents

- Curcumin: 100% purity, purchased from Nacalai Tesque (Kyoto, Japan) [28]
- β-Carotene: 100% purity, purchased from Nacalai Tesque (Kyoto, Japan) [29]

4.1.3 In Vitro Biological Assay Reagents

- **Cell line**: Human dermal fibroblasts, obtained from Cell Applications inc. (San Diego, CA, USA) [30]
- **Culture Media and Supplements**: Dulbecco's Modified Eagle Medium (DMEM) and Penicillin/Streptomycin mixed solution (stabilized), all purchased from Nacalai Tesque (Kyoto, Japan) [31]
- Fetal Bovine Serum provided by Corning (New York, USA) [32]
- **Staining and Fixation**: Hoechst 33342 fluorescent nuclear stain, purchased from Thermo Fisher Scientific (Waltham, MA, USA) [33]
- Paraformaldehyde (PFA) purchased from Nacalai Tesque (Kyoto, Japan) [34]
- Tris-Buffered Saline with Tween-20 (TBST), was made by purchasing the singular components, Tris(hydroxymethyl)aminomethane, Sodium Chloride and Tween-20 (Polyoxyethylene Sorbitan Monolaurate) all provided by Nacalai Tesque (Kyoto, Japan) [35], [36], [37]
- **Buffer Solutions**: Phosphate-Buffered Saline (PBS), was made by purchasing the singular components, Disodium Hydrogen Phosphate Dodecahydrate, Potassium Dihydrogen Phosphate, Sodium Chloride and Potassium Chloride all provided by Nacalai Tesque (Kyoto, Japan) [36], [38], [39], [40]

4.1.4 Drug Release Assay Reagents

- Surfactant: Sodium Dodecyl Sulphate (SDS), purchased from Sigma-Aldrich (St. Louis, MO, USA) [41]
- pH Titration Reagents: Hydrochloric Acid (HCl, 1 M) and Sodium hydroxide (NaOH, 1 M), provided by Nacalai Tesque (Kyoto, Japan) [42], [43]

4.2 Custom Electrospinning Apparatus

The bilayer scaffolds were fabricated using a custom-assembled electrospinning apparatus (*Figure 19*). The core of the system features a programmable syringe pump utilizing 1 mL syringes, coupled with a decoupled motorized 3-axis system to ensure precise spatial control over the deposition path. Specifically, the dispensing nozzle translates along the Y and Z axes, while the collector plate operates along the X-axis. To achieve the desired scaffold architecture, the motorized system was programmed to follow a continuous 5x5 mm square movement pattern. The dispensing mechanism and collector are enclosed within a metal-

reinforced, transparent PVC chamber, equipped with internal illumination to allow continuous visual monitoring of the electrospinning jet. The required electrical field was generated using a high-voltage dual power supply connected via alligator clips to both the dispersing nozzle (anode) and the collector plate (cathode). Additionally, the chamber was fitted with an internal thermometer to accurately monitor environmental conditions during the process.



Figure 19 - Custom-assembled electrospinning apparatus, comprising the enclosed spinning chamber and the dual high-voltage power supply units

4.3 Polymer Solution Preparation and Optimization

Prior to solution formulation, PCL pellets were dehydrated in an oven at 40°C for a minimum of 24 hours to eliminate residual moisture, thereby minimizing humidity-related instabilities during the electrospinning process. Initial electrospinning trials using pure CF resulted in excessive rapid solvent evaporation, which destabilized the jet and caused the polymer to drip rather than forming continuous fibres. Through a systematic trial-and-error optimization process, validated via laser-optical microscopy, a binary solvent system comprising of CF and EtOH at a 7:3 volumetric ratio was established as the optimal formulation. Furthermore, various PCL concentrations (4 g, 3 g and 2 g per 10 mL of solvent) were evaluated. A concentration of 2 g per 10 mL (20% m/v) was selected for the final protocol, as it yielded the most stable Taylor cone and superior fibre morphology.

Once the PCL was fully solubilized under magnetic stirring, the functionalizing agents (curcumin, β-carotene or a 50:50 mixture of both) were incorporated into the solution at a concentration of 5% by weight (wt.) relative to the PCL mass. To verify the state of dispersion of the bioactive agents, a laser beam was passed through the mixtures to quantitatively assess whether the bioactive agent was present as a molecular solution or as a dispersed phase. The appearance of a visible light path (Tyndall effect) indicates light scattering by dispersed particles, whereas its absence is consistent with complete solubilization of the compound. [44]

These observations revealed that, at the 5% wt. concentration, β-carotene formed a uniform suspension (evidence by visible light diffraction), whereas curcumin achieved complete dissolution (indicated by the absence of light diffraction). Driven by the complete solubility of curcumin at 5% wt., an attempt was made to increase its concentration to 10% wt. to maximize the bioactive loading. However, at this elevated concentration, curcumin exceeded its solubility limit in the solvent system, leading to an unstable mixture that severely compromised the spinnability of the solution. Consequently, the 10% wt. formulation was discarded, and the 5% wt. concentration was maintained as the standard for all functionalized scaffolds.

4.4 Electrospinning Process Parameters

Similarly to the solution formulation, the optimal electrospinning process parameters were established through a rigorous trial-and-error approach. To ensure consistent and defect-free fibre deposition, the final parameters were strictly maintained as follows:

- Collector Substrate: Preliminary deposition tests for parameter optimization were conducted on aluminium foil. However, for the fabrication of the final samples, parchment paper (non-stick baking paper) was utilized as the collection substrate to facilitate the safe detachment of the delicate electrospun scaffolds without inducing mechanical damage.
- Nozzle: 25G needle.
- Flow Rate: 50 μL/min.
- Tip-to-Collector Distance: 15 cm (measured precisely from the tip of the nozzle to the collection surface).
- Applied Voltage: A total potential difference of 15 kV, achieved by applying +12 kV to the nozzle and -3 kV to the collector.
- Environmental Conditions: The internal chamber temperature was consistently monitored, ranging between 24°C and 28°C, with relative humidity fluctuating between 25% and 40%.

Despite the natural ambient variations in temperature and humidity, the selected parameter set ensured highly reproducible and excellent fibre quality across all fabrication batches.

4.5 Bilayer Scaffold Fabrication and Sample Preparation

The bilayer architecture of the scaffolds was achieved by sequentially electrospinning two distinct polymer solutions onto the same parchment paper substrate. Initially, 1 mL of the pure PCL solution was electrospun to form the structural base layer. Immediately following the completion of the first deposition, another layer of PCL (control specimen) or the

functionalized PCL solution (containing either curcumin, β-carotene or their mixture) was electrospun directly on top of the base layer, ensuring optimal adhesion and interface integration between the two strata.

Following the electrospinning process, the as-spun scaffolds were immediately subjected to preliminary morphological validation using the laser-optical microscope. Images at 20X magnification were captured to verify the macroscopic surface morphology and layer uniformity, while high-magnification images at 150X were acquired to supply the data required for the ImageJ fibre diameter analysis.

Once the macroscopic quality of the electrospun mats was verified, the scaffolds were cut into specific geometries depending on the required characterization techniques. For all subsequent analyses (with the sole exception of mechanical testing) circular specimens were obtained using a 0.5-inch (approximately 12.7 mm) craft punch (*Figure 20*). The parchment paper backing was carefully peeled off from the electrospun discs prior to storage. Conversely, to meet the specific dimensional requirements of the mechanical tensile test, rectangular specimens measuring 20 x 5 mm were precisely cut from the bulk mats using a laser cutter.

To preserve the stability of the bioactive agents and prevent degradation prior to testing, a rigorous storage protocol was implemented. The circular samples were housed in custom-designed, 3D-printed multi-well containers (featuring 10 individual samples slots) fabricated from matte black PET-G (*Figure 21*), which effectively shielded the functionalized scaffolds from light exposure. These containers were subsequently vacuum-sealed (*Figure 22*) to prevent oxygen-induced oxidative degradation and stored in a dark drawer until further use.

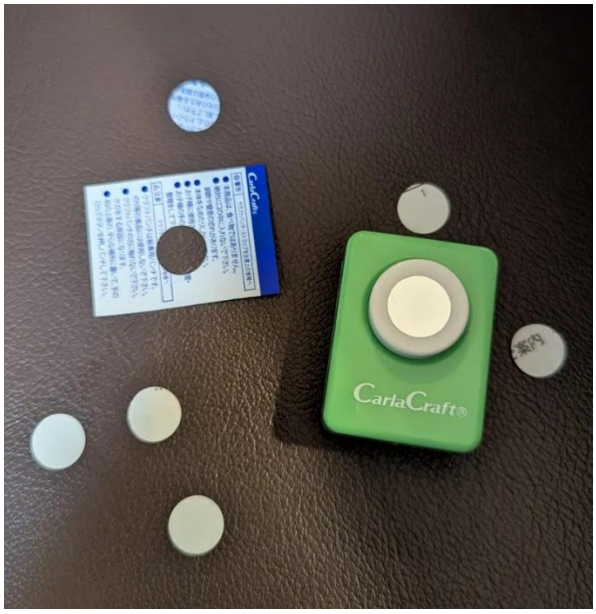


Figure 20 - 0.5-inch craft punch used to cut circular specimens



Figure 21 - 3D-printed multi-well storage container with β-carotene samples



Figure 22 - vacuum-sealed sample bag

4.6 Morphological Characterization

4.6.1 Laser-Optical Microscopy and Image Analysis

Laser-optical microscopy is an advanced profiling technique that utilizes focused laser light to scan sample surfaces and generate high-contrast 3D microstructural topography. This method is particularly advantageous for polymeric scaffolds as it allows for non-destructive, high-resolution observation of surface features without requiring invasive sample preparation or conductive coatings.[45]

The microscopic surface topography and microstructural morphology of the electrospun bilayer scaffolds were evaluated using a laser-optical microscope (VK-X200 series, Keyence, Osaka, Japan, *Figure 23*) at a high magnification of 150X. This technique allowed for a non-destructive observation of the surface features, evaluating the homogeneous deposition of the layers. To quantitively assess the morphological consistency of the scaffolds, the acquired optical images were processed using ImageJ software (National Institutes of Health, Bethesda, MD, USA). For each sample group, the diameter of individual fibres was measured across multiple randomly selected regions. Specifically, to ensure statistical robustness and accurately capture

morphological variations, three independent measurements were taken along the length of each selected fibre, evaluating a minimum of 34 randomly chosen fibres per image. These aggregated measurements were then utilized to calculate the mean fibre diameter (µm) and the standard deviation, allowing for a precise evaluation of the overall diameter distribution, fibre uniformity and the specific impact of the varying bioactive inclusions on the electrospinning jet stability.



Figure 23 - laser-optical microscope (VK-X200 series)

4.6.2 Field Emission Scanning Electron Microscopy (FESEM)

Field emission scanning electron microscopy (FESEM) is an advanced microscopy technique used to capture the microstructure of materials, delivering high-resolution topographical evidence with an almost unlimited depth of field. Unlike conventional SEM, FESEM uses a field emission gun that provides narrower probing beams, resulting in improved spatial resolution and minimized sample charging and thermal damage on delicate polymeric specimens. [46]

To perform a high-resolution investigation of the microscopic architecture, a FESEM (SUPRATM 40, Zeiss, Germany) was employed. Specific attention was dedicated to observing the cross-sections and the fracture surfaces of the bilayer scaffold following the mechanical tensile tests. This approach was crucial to meticulously examine the mechanical behaviour of the construct under stress, identifying any potential delamination events between the pure PCL structural base and the bioactive-loaded layer, as well as evaluating the specific failure mechanisms of the composite fibres. Prior to the FESEM observation, the fractured samples were sputter-coated with a thin layer of platinum (7 nm, Q150T plus, Quorum) to impart adequate electrical conductivity and prevent charge accumulation under the electron beam. The images were acquired at an accelerating voltage of 5 kV.

4.6.3 Fluorescence Confocal Laser Scanning Microscopy

Fluorescence microscopy involves illuminating specimens with specific wavelengths of light to excite and observe fluorescent substances, offering extremely high sensitivity and specificity. Confocal microscopy improves upon this by effectively separating the excitation light and the emitted light through a spatial pinhole, eliminating out-of-focus emissions so that only the signal from the exact focal plane reaches the detector. [47]

Fluorescence confocal microscopy (LSM 900, ZEISS, Oberkochen, Germany, *Figure 24*) was incorporated into the morphological and biological characterization protocol. For the morphological analysis, the technique was employed to evaluate the distribution of the functionalizing agents across the sample surface by exploiting its fluorescent properties. For the biological evaluation, confocal microscopy was used to visualize fluorescently stained cell nuclei and quantify cell proliferation. Details of the cell staining and imaging protocol are described in *Chapter 4.11.6*.



Figure 24 - LSM 900 confocal laser scanning microscope (Zeiss)

4.7 Chemical and Structural Characterization

4.7.1 Fourier Transform Infrared Spectroscopy (FTIR)

Among the analytical techniques available for probing molecular structure, Fourier Transform Infrared Spectroscopy (FTIR) is rooted in the interaction of infrared radiation with matter, offering a non-destructive route to the conformation and chemical environment of a material. Absorption occurs only when the frequency of the incoming radiation matches the vibrational frequency of a molecular bond, producing a net change in dipole moment during the

vibration. Rather than scanning wavelengths sequentially, as in traditional dispersive instruments, modern FTIR spectrometers use an interferometer (typically a Michelson interferometer) to split a polychromatic light beam and collect an interferogram containing all infrared frequencies at once; a Fourier transformation is then applied to convert this raw interferogram into the familiar absorbance or transmittance spectrum as a function of wavenumber (cm^{-1}). This approach offers a better signal-to-noise ratio, faster acquisition and higher optical throughput than dispersive instruments, and is correspondingly well suited to both qualitative identification and quantitative analysis of polymers, organic compounds and composite systems. [48]

Building upon these fundamental principles, when applied to the analysis of electrospun scaffolds, FTIR (particularly when utilized in Attenuated Total Reflectance, ATR, mode) becomes a vital analytical tool to confirm the successful incorporation of active biomolecules within polymeric matrices and to verify their chemical stability post-electrospinning. In the context of PCL scaffolds, FTIR is highly effective in identifying the characteristics functional groups of the polymer. A pristine PCL spectrum typically exhibits a strong, sharp absorption band around 1720 cm^{-1}, corresponding to the carbonyl (C=O) stretching vibrations, alongside distinct peaks around 2949 cm^{-1} and 2865 cm^{-1}, which are attributed to the asymmetric and symmetric aliphatic (C-H) stretching of the hydrocarbon backbone, respectively. Furthermore, the C-O-C stretching vibrations generally appear in the region between 1160 cm^{-1} and 1240 cm^{-1}. [49], [50]

When evaluating the functionalized layer of the bilayer scaffold, FTIR becomes an essential tool to investigate the intermolecular interactions between the synthetic matrix and the natural active agents. For composite nanofibers loaded with curcumin, the technique can detect the interaction between the active molecule and the polymer chains. During the electrospinning process, curcumin often undergoes a structural transformation, shifting from a stable di-keto state into a reactive keto-enol form. In this configuration, the central hydrogen atom of the enol form acts as a strong hydrogen bond donor, directly interacting with the weak hydrogen bond acceptors provided by the PCL's carbonyl groups. [6], [8]

This specific non-covalent interaction can be observed in the FTIR spectra as a slight shift, broadening or variation in the intensity of the PCL carbonyl peak, as well as the appearance of curcumin's characteristic phenolic O-H stretching broad band in the 3500 – 3200 cm^{-1} region and mixed C=C / C=O vibrations around 1620 cm^{-1}. Consequently, spectral shifts in these specific absorption bands not only confirm the presence of the active principle but also demonstrate its chemical integration without undergoing thermal or voltage-induced degradation. [49]

Similarly, for β-carotene functionalization, FTIR assists in evaluating the chemical state of the biomolecule within the matrix. Given that β-carotene is highly hydrophobic and lacks highly polar functional groups capable of strong hydrogen bonding, it typically remains in a particulate form within the PCL matrix due to differing polarities and the rapid solvent evaporation during electrospinning. Therefore, FTIR spectra of β-carotene loaded scaffolds are crucial to confirm the absence of unintended covalent bonding (ensuring the polymer backbone is not chemically

altered) and to verify that the molecule's structural integrity remains intact despite the high electrical fields applied during fabrication. [7], [14]

To experimentally investigate the chemical composition of the fabricated scaffolds and confirm the successful incorporation of the bioactive agents, FTIR spectra were acquired in ATR mode (Nicolet iS50 FT, Thermo Scientific, USA). Each electrospun sample was mounted flat against the ATR crystal, ensuring uniform contact pressure across the fibre mat surface. Spectra were collected over a wavelength range of 4000 – 500 cm^{-1}, averaging 12 scans per acquisition at a spectral resolution of 4 cm^{-1}.

4.7.2 Raman Spectroscopy

A complementary vibrational technique, Raman spectroscopy relies instead on the inelastic scattering of monochromatic light, typically from a laser source, to probe low-frequency molecular vibrational and rotational states. Most incident photons undergo elastic Rayleigh scattering, retaining their original energy and frequency; only a small fraction — roughly one in ten million — instead undergoes an inelastic collision with the sample molecules. In this process, energy is exchanged between the photon and the molecule's vibrational modes, so that the scattered light emerges with a shifted frequency, either lower (Stokes scattering) or higher (anti-Stokes scattering) than the incident beam. This frequency difference, the Raman shift, corresponds directly to the vibrational energy levels of the molecular bonds present, generating a unique chemical fingerprint. [51]

Crucially, the selection rules governing Raman scattering differ fundamentally from those of infrared absorption. While FTIR requires a net change in the molecular dipole moment, a vibration is only Raman active if it induces a change in the polarizability (the deformability of the electron cloud) of the molecule during the vibration. [51]

Because of these distinct physical mechanisms, while FTIR provides comprehensive and highly detailed data regarding polar functional groups and hydrogen bonding dynamics, Raman Spectroscopy serves as an optimal and deeply complementary technique to further validate the structural conformation, degree of crystallinity and molecular distribution of the active principles within the electrospun fibres. Unlike FTIR, which relies on changes in the dipole moment during molecular vibrations, Raman scattering is intrinsically sensitive to changes in electron cloud polarizability. This makes it exceptionally powerful for analysing non-polar, highly symmetric and conjugated carbon bonds that generally yield weak, masked or entirely inactive signals in FTIR spectra. [52]

This complementary capability is particularly critical for the analysis of β-carotene. The molecular structure of β-carotene features a long, heavily conjugated polyene chain (a C=C backbone) that exhibits an intense and highly characteristic resonance Raman effect when excited by appropriate laser wavelengths. The Raman spectrum of β-carotene is unequivocally identifiable by three major distinctive peaks; the ν_1 strong band around 1515 cm^{-1} corresponding to the in-phase C=C double bond stretching, the ν_2 band around 1155 cm^{-1} related to the C-C single bond stretching and the ν_3 band at approximately 1005 cm^{-1} attributed to the in-plane rocking motions of the methyl groups attached to the polyene chain.

Identifying these sharp peaks within the functionalized PCL layer irrefutably confirms the survival and structural stability of the β-carotene molecules following the high-voltage electrospinning flight. [53]

Raman spectra were acquired using a Horiba Jobin-Yvon T64000 triple monochromator Raman Spectrometer, equipped with an Andor iDus DU420 CCD detector (*Figure 25*), using a 488 nm laser excitation line (*Figure 26*), an 1800 grooves/mm grating, a 50x objective and an entrance slit of 1000 μm, operating in multi-window acquisition mode, with four spectral windows stitched together to cover the full spectral range. For the Control and PCL-β-carotene groups, spectra were collected using a laser power of 30 mW, with an exposure time of 60s and 1 accumulation per window. For the PCL-Curcumin and PCL-Mix groups, a reduced power of 10 mW and 30 mW respectively was combined with shorter exposure times (5s and 1s) and 4 accumulation per window, to minimise laser-induced photodegradation of the curcumin-loaded samples.



Figure 25 - Horiba Jobin-Yvon T64000 detection system



Figure 26 - Coherent Saphire laser source

4.8 Thermal Analysis

4.8.1 Differential Scanning Calorimetry (DSC)

To investigate the physical transformations and phase transitions of the fabricated scaffolds as a function of temperature and time, Differential Scanning Calorimetry (DSC) was the thermo-analytical technique of choice. The method operates by continuously measuring the difference in heat flow required to raise the temperature of a sample and an inert reference pan, with both subjected to identical, precisely controlled temperature programs. When the sample undergoes a physical transformation — melting, crystallization or a glass transition — it requires either more or less heat flow than the reference to maintain the same temperature, and this differential heat flow is recorded as a quantitative measure of the underlying endothermic (e.g. melting) or exothermic (e.g. cold crystallization) process. This makes DSC a standard method for determining thermal parameters in polymers, including the glass transition temperature (T_g), melting temperature (T_m), crystallization temperature (T_c) and the enthalpies associated with these transitions (ΔH). [54]

In the context of the present study, DSC is a crucial analytical tool to evaluate the thermal properties and the degree of crystallinity of the electrospun PCL scaffolds. PCL is a semi-crystalline aliphatic polyester characterized by a distinct and highly advantageous thermal profile. [13]

Under standard conditions, pristine PCL exhibits a very low T_g ranging from -60°C to -65°C, ensuring that the polymer remains in a flexible, rubbery state at both room temperature and physiological temperatures. Furthermore, PCL possesses a relatively low T_m, typically manifesting as an endothermic peak between 59°C and 64°C, which greatly facilitates its thermal processing and extrusion. [13]

Beyond identifying these transition temperatures, the integration of the melting peak (enthalpy of fusion, ΔH_m) allows for the quantitative determination of the polymer's fractional crystallinity (X_c). the degree of crystallinity is calculated using the crystallinity equation (Eq. 4).

Fractional Crystallinity $$X_c(\%) = (\Delta H_m / \Delta H_m^0) \times 100 \quad (4)$$

Where ΔH_m is measured melting enthalpy of the electrospun sample, and $\Delta H^0{}_m$ represents the theoretical melting enthalpy of a 100% crystalline PCL sample (widely accepted in literature as 139 J/g). [13]

Thermal properties were investigated by DSC using a Mettler Toledo DSC-1 instrument, under a continuous nitrogen purge flow of 40 mL/min to prevent oxidative degradation during heating. Samples were sealed in crimped aluminium pans, pierced with a needle to allow pressure equalisation, with an empty pan of the same type used as a reference; sample weights were 9.2 mg, 11.5 mg, 12.9 mg and 8.9 mg for the Control, PCL-Curcumin, PCL-β-carotene and PCL-Mix groups, respectively. Each specimen was first heated from ambient temperature to 120°C at a constant rate of 10°C/min and held isothermally for 2 minutes; this first heating scan was used to assess the as-processed thermal behaviour of the electrospun samples, reflecting the combined effect of the electrospinning process and the incorporated bioactive agents on the polymer matrix. Samples were subsequently cooled to -80°C at constant rate of -10°C/min and held isothermally, to record crystallization behaviour under controlled conditions and erase previous thermal history. A second heating scan was then performed from -80°C to 120°C at a constant rate of 10°C/min, followed by a final isothermal step of 2 minutes, to evaluate the intrinsic melting behaviour of the functionalized polymer independent of processing related effect. Melting enthalpy (ΔH_m) was determined by integrating the area under the melting endotherm using the trapezoidal rule, while fractional crystallinity (X_c) was subsequently calculated according to the equation (4). Both parameters were evaluated on the first and second heating scans, allowing a comparison between the as-processed thermal response and the thermal history-independent behaviour, in order to isolate the effect of the functionalizing agents on the polymer matrix from that of the electrospinning process itself.

4.9 Colloidal and Surface Characterization

4.9.1 Dynamic Light Scattering (DLS) and Particle Size

Particle size and its distribution in liquid suspension can be determined via Dynamic Light Scattering (DLS), also known as Photon Correlation Spectroscopy (PCS), a non-invasive technique applicable to particles, emulsions and molecular aggregates alike. A colloidal suspension is illuminated with a monochromatic laser beam, and the resulting time-dependent fluctuations in the intensity of the scattered light are measured; these fluctuations arise from the continuous, random thermal motion of the particles, known as Brownian motion. [55]

The temporal fluctuations in the scattered light intensity are processed through an autocorrelation function, from which the translational diffusion coefficient (D) is obtained. This coefficient is inversely proportional to the particle size and is utilized to calculate the hydrodynamic diameter (D_H) using the fundamental Stokes-Einstein equation (Eq. 5).

Stokes-Einstein equation

$$D_H = \frac{k_B T}{3\pi\eta D} \quad (5)$$

Where k_B is the Boltzmann constant, T is the absolute temperature and η is the dynamic viscosity of the dispersant medium. [55]

In the context of evaluating the functionalized bilayer wound dressings, DLS is employed to thoroughly characterize the behaviour of the active agents (curcumin and β-carotene) once they are released from the PCL matrix into the fluid medium. Determining the hydrodynamic diameter of the released species is valuable for assessing their aggregation state. Curcumin is expected to remain largely dissolved or to form relatively small molecular aggregates in the ethanol-based release medium. Conversely, owing to its highly hydrophobic nature and limited aqueous compatibility, β-carotene may exhibit a stronger tendency to aggregate after release, resulting in larger apparent hydrodynamic diameters. [7], [14]

Therefore, DLS provides valuable information on the colloidal behaviour of the released compounds, allowing the assessment of their aggregation state and dispersion stability within the release medium.

Release solutions were obtained by immersing the electrospun samples in EtOH for approximately two hours. The pH of the release solutions was then manually adjusted to eight target values, ranging from approximately pH 2.8 to 9.6, using HCl and NaOH under monitoring with an electronic pH meter, and the ionic strength was adjusted by dilution with 0.1 M KCl. DLS measurements were performed on the resulting solutions using a Litesizer 500 (Anton Paar, Graz, Austria), using the instrument's default measurement settings. Measurements were carried out at a target temperature of 20°C, with an equilibration time of 30 s, using disposable cuvettes and an automatic scattering angle selection; data were analysed using the general analysis model with the ISO 22412 cumulant fit. Each sample/pH point was measured in triplicate.

4.9.2 Zeta Potential and Electrophoretic Light Scattering (ELS)

While DLS evaluates particle dimensions, analysing the surface charge is equally critical to predict colloidal stability and biological interactions. Zeta potential (ζ) represents the electrical potential at the slipping plane (the boundary between the stern layer and the diffuse layer) of a particle suspended in a liquid. It is a fundamental indicator of the magnitude of electrostatic repulsion or attraction between particles. [56]

- Colloidal Zeta Potential (Release Solutions):

To measure the zeta potential of the molecules released from the scaffolds, Electrophoretic Light Scattering (ELS) is employed. When an electric field is applied across the sample solution, charged particles migrate towards the electrode of opposite charge at a velocity proportional to their zeta potential. This electrophoretic mobility is measured by analysing the Doppler shift of the scattered laser light and is subsequently converted into zeta potential values using the Henry equation (often incorporating the Smoluchowski approximation for aqueous media). [56]

For this study, zeta potential measurements were performed on the same release solutions described above, using the Litesizer 500 (Anton Paar, Graz, Austria) with the instrument's default measurement settings. Measurements were carried out at a target temperature of 25°C, with an equilibration time of 30 s, using an Omega-type measurement cell, an automatically adjusted voltage of up to 200 V, and the Smoluchowski approximation (Henry factor = 1.5). Each sample/pH point was measured in triplicate.

- Surface Zeta Potential of the Solid Scaffolds

Beyond analysing the released particles in the fluid medium, determining the surface charge of the macroscopic solid patch is of paramount importance, as the surface chemistry directly dictates initial protein adsorption and subsequent cell adhesion. To evaluate the macroscopic surface zeta potential of the bulk electrospun constructs, an electrokinetic analyser (SurPASS Anton Paar GmbH, Austria) equipped with an adjustable gap cell was utilized. Unlike standard ELS, which measures the mobility of suspended particles, this specialized electrokinetic setup determines the solid surface charge by measuring the streaming potential. This potential is generated when an aqueous electrolyte solution is hydrodynamically forced to flow through narrow gap between two identical flat sample surfaces under a precise, applied pressure gradient. [57]

By applying this technique specifically to the top functionalized layer of the bilayer patches, it is possible to quantify how the high-concentration loading (5% w/w) of biomolecules modifies the intrinsic surface charge of the pristine PCL base. Pristine PCL generally exhibits a slightly negative surface charge due to its ester groups. [12]

The integration of curcumin, which alters the surface topography and introduces phenolic hydroxyl groups via its keto-enol structural transition and the inclusion of non-polar β-carotene aggregates, are expected to induce measurable shifts in the surface zeta potential. [7], [8], [15]

The surface zeta potential of the solid scaffolds was determined using an electrokinetic analyser (SurPASS, Anton Paar GmbH, Austria, *Figure 27*) equipped with an adjustable gap cell. For each experimental group (Control, PCL-Curcumin, PCL-β-carotene and PCL-Mix), samples were cut in half to fit the sample holder, and measurements were performed on the top functionalized layer of the bilayer patches. A 0.001 M KCl solution was used as the supporting electrolyte, while 0.05 M HCl and 0.05 M NaOH were employed for acidic and basic titrations, respectively, via the instrument's automatic titration unit. For each pH point, the acidic and basic titrations were performed on two distinct sample halves, with the instrument automatically acquiring 10–15 individual measurements per point; mean and standard deviation values were subsequently calculated and plotted.

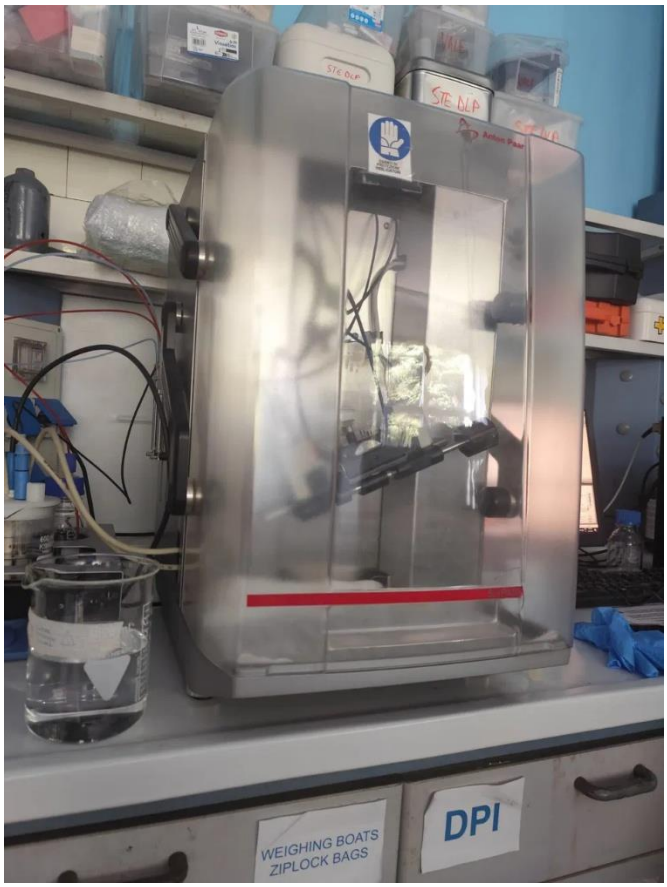


Figure 27 - SurPASS electrokinetic analyser (Anton Paar)

4.9.3 Water Contact Angle (WCA)

Water contact angle (WCA) measurement is among the most widely used techniques to characterize the wettability of a solid surface, offering a direct and non-destructive insight into its hydrophilic or hydrophobic characteristic. When a liquid droplet is deposited on a solid substrate, the equilibrium shape it assumes is governed by the balance of the interfacial tensions acting at the three-phase (solid-liquid-vapour) contact line (*Figure 28*), as formalised by Young's equation (Eq. 6). By convention, a WCA below 90° denotes a hydrophilic surface, capable of promoting rapid liquid spreading and favourable exudate absorption, whereas a WCA above 90° indicates a hydrophobic surface that resists wetting. [58]

Young's equation

$$\gamma_{sv} = \gamma_{sl} + \gamma_{lv} \cdot \cos(\theta) \tag{6}$$

Where γ_{sv}, γ_{sl} and γ_{lv} are the solid-vapour, solid-liquid and liquid-vapour interfacial tensions, respectively, and θ is the equilibrium contact angle

In the context of biomaterials, surface wettability represents a first-order determinant of the biological response elicited by a scaffold, as it directly governs protein adsorption and, consequently, subsequent cell adhesion and proliferation; moderately wettable surfaces are generally regarded as the most favourable for supporting cellular attachment. [58]

Given the intrinsically hydrophobic nature of pristine PCL, WCA analysis was employed as a complementary tool to the surface zeta potential measurements (*Chapter 4.9.2*), to assess how

the incorporation of curcumin, β-carotene or their mixture modifies the wetting behaviour of the functionalized layer of the bilayer scaffolds.

Water contact angle measurements were performed using a Phoenix 300 goniometer (Kromtek Co., Selangor, Malaysia) at room temperature. For each experimental group (Control, PCL-Curcumin, PCL-β-carotene and PCL-Mix), 5 µL droplets of deionised water were deposited onto the surface of the functionalized layer, and the resulting droplet profile was captured and analysed using ImageJ software. To ensure statistical representatives, measurements were acquired at five different locations across the surface of each sample group (n=5) and the results were averaged.

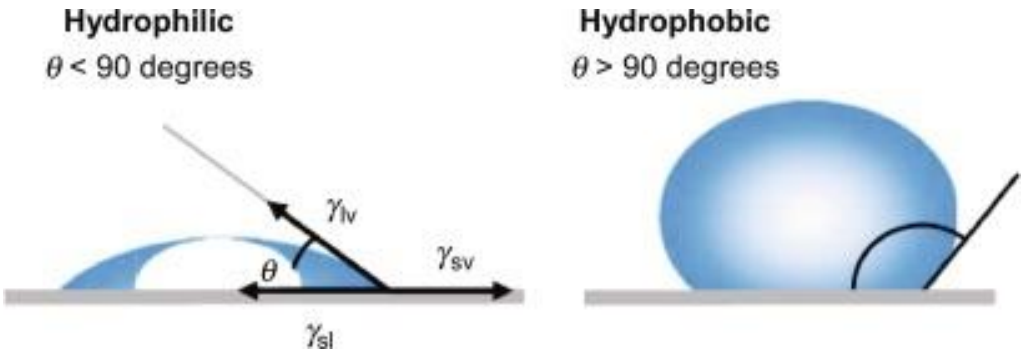


Figure 28 – Schematic representation of a water droplet on a hydrophilic (θ < 90°) versus a hydrophobic (θ > 90°) surface, illustrating the interfacial tensions (γ_{lv}, γ_{sv}, γ_{sl}) and the equilibrium contact angle (θ) as defined by Young's equation. [58]

4.10 Mechanical Characterization

Beyond fibre morphology and molecular interactions, the mechanical performance of a wound dressing scaffold is a critical determinant of its clinical viability, governing both practical handling during application and the scaffold's ability to support and protect the wound bed throughout the healing process. As discussed in *Chapter 3*, the incorporation of natural biomolecules such as curcumin and β-carotene, while therapeutically advantageous, introduces a significant risk of mechanical degradation through a plasticizing effect that compromises tensile strength and stiffness as biomolecule loading increases. A thorough mechanical characterization is therefore essential not only to quantify this structural trade-off but also to verify whether the proposed bilayer architecture successfully preserves adequate load-bearing capacity despite the high biomolecule concentration of the functionalized layer. Furthermore, benchmarking the measured elastic modulus against the physiological stiffness range of the target tissue (see *Table 2.1*) provides a direct indication of the scaffold's biomechanical compatibility with native skin and its potential for effective clinical translation. [7], [8], [12], [14]

The tensile mechanical properties of the electrospun bilayer scaffolds were evaluated using a tensile tester (STA-1150, Orientec Co., LTD., Tokyo, Japan, *Figure 29*). Rectangular specimens (20 x 5 mm) were mounted on a paper support frame with a rectangular window (10 x 5 mm) cut in the centre, marked with a reference scale to facilitate handling. Double-sided adhesive tape was applied to the upper and lower edges of the window, and the specimen was centred

and fixed in place, leaving a 5 mm free length on each side; sandpaper was placed over the taped regions to increase friction and prevent slippage during testing (*Figure 30*). The frame edges – avoiding contact with the specimen itself – were held with tweezers and secured between the pneumatic clamps of the testing machine; once alignment was confirmed, both sides of the frame were cut with scissors immediately prior to testing, releasing the specimen from its support while preserving the fixed gauge length of 10 mm. Uniaxial tensile tests were performed at a constant crosshead speed of 10 mm/min. Tensile strength was defined as the maximum stress recorded during the test, while the tensile modulus was calculated within the elastic deformation range, specifically between 5% and 10% strain. Testing was recorded via digital camera for post-hoc verification. Given the low mass of the rectangular specimens, which fell below the reliable detection threshold of the available analytical balance, the areal mass density was instead determined from the circular specimens (obtained via the 0.5-inch craft punch, as described previously) and used to estimate the mass of each rectangular specimen by proportional scaling based on specimen area. Specimens exhibiting evidence of grip slippage or premature failure at the clamping interface were excluded from the statistical analysis.



Figure 29 - STA-1150 tensile tester (Orientec) with specimen mounted between the pneumatic clamps

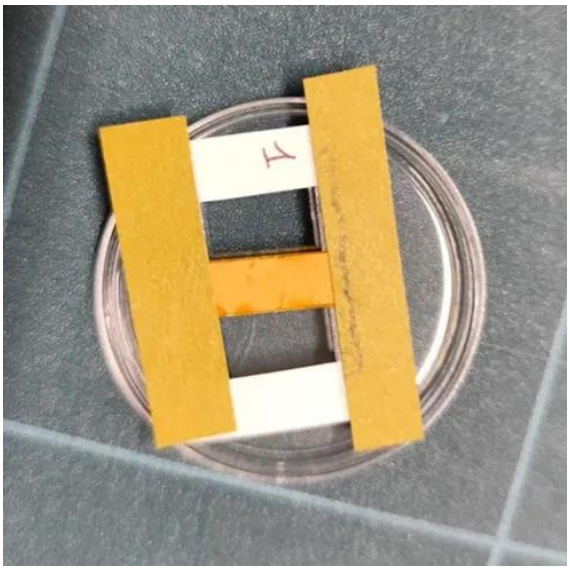


Figure 30 - Rectangular specimen mounted on the paper support frame prior to tensile testing

For each experimental group (pure PCL control, curcumin-loaded, β-carotene-loaded and 50:50 mixture-loaded bilayer scaffolds), six specimens were tested (n = 6). Prior to testing, the thickness of each specimen was measured using an electronic calliper to determine the cross-sectional area used for stress calculation. Given the low mass of rectangular specimens, which fell below the reliable detection threshold of the available analytical balance, the areal mass density was instead determined from the circular specimens (obtained via the 0.5-inch craft punch, as described previously) and used to estimate the mass of each rectangular specimen by proportional scaling based on specimen area. Specimens exhibiting evidence of grip slippage or premature failure at the clamping interface were excluded from the statistical analysis. From the resulting stress-strain curves, the ultimate tensile strength (UTS), elongation at break and Young's modulus (calculated from the slope of the initial linear region of the curve) were extracted for each specimen and averaged (mean ± standard deviation) across each group.

4.11 In Vitro Biological Assay

4.11.1 Rationale for Indirect Cytocompatibility Testing

The biocompatibility of a wound dressing scaffold is a fundamental prerequisite for its clinical translation, and its assessment is formally addressed by the ISO 10993-5 standard for the in vitro evaluation of medical devices. The standard defines three principal testing categories – extract (indirect) tests, direct contact tests and indirect contact (diffusion) tests – with the choice depending on the nature of the material and its intended clinical application. In the extract-based approach, cells are exposed not to the material itself but to a fluid extract obtained by incubating the material under controlled conditions, thereby assessing exclusively the biological effect of any substances released into the surrounding medium. This method offers the advantage of isolating the response attributable to the released bioactive compounds and any soluble degradation products from confounding physical variables (such as surface topography, fibre alignment or roughness) that would instead influence the outcome of a direct-contact assay. Given that the primary therapeutic mechanism of the functionalized scaffolds developed in this work relies on the controlled release of curcumin and β-carotene into the

wound environment, an extract-based (indirect) cytotoxicity assay was adopted to evaluate human fibroblast response to the scaffold-conditioned medium, offering higher reproducibility and more rapid turnaround compared to direct-contact seeding. [59]

4.11.2 Scaffold Sterilization and Preconditioning

Prior to biological testing, all scaffolds were sterilized by immersion in 70% EtOH for 30 minutes, followed by three washing steps in sterile PBS to remove residual EtOH. Samples were subsequently pre-incubated in complete DMED (supplemented with 10% FBS) for 1 hour at 37°C to improve surface wettability and minimize non-specific effects arising from the intrinsic hydrophobicity of PCL.

4.11.3 Eluate Preparation

Each scaffold was immersed in 3 ml of complete DMEM (10% FBS, 1% penicillin/streptomycin, *Figure 31*) and incubated at 37°C in a humified atmosphere with 5% CO_2, maintaining a constant mass-to-volume ratio across samples. Eluates were collected at three time points (24 hours, 72 hours and 7 days), filtered through a 0.22 µm membrane to ensure sterility and used immediately for cell exposure at full concentration (100%, undiluted). After each collection, the conditioning medium was replaced with fresh medium to allow evaluation of cumulative release over time.

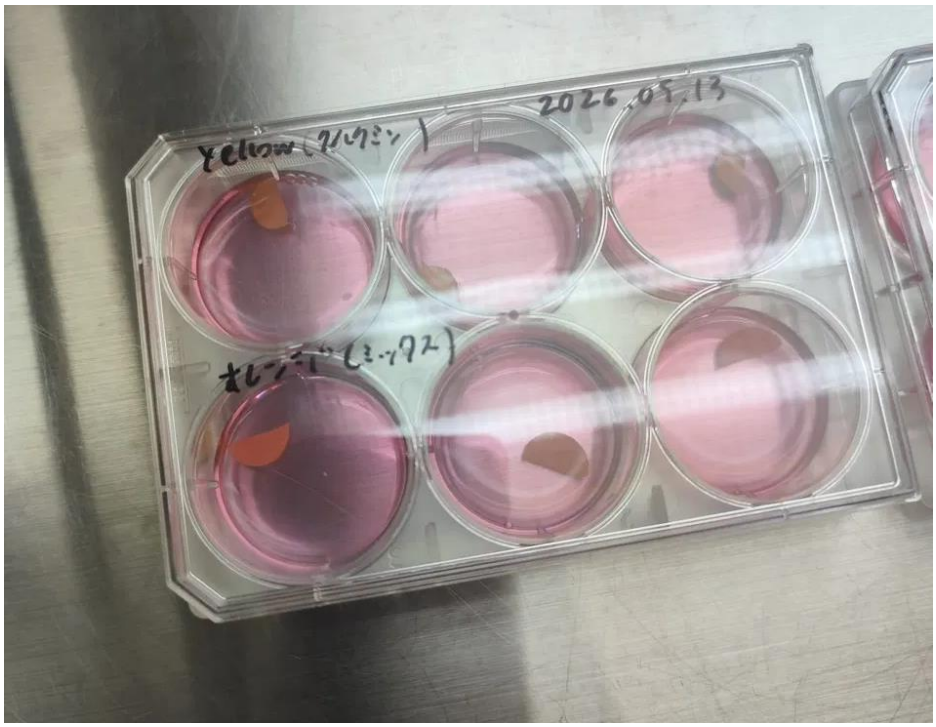


Figure 31 - Scaffold immersed in DMEM during eluate collection

4.11.4 Cell Culture

Human dermal fibroblasts were seeded in 24-well plates at a density of approximately 2-3 x 10^4 cells per well in complete DMEM and cultured at 37°C in a 5% CO_2 atmosphere. Cells were allowed to adhere and stabilize for 24 hours prior to eluate exposure (*Figure 32*).

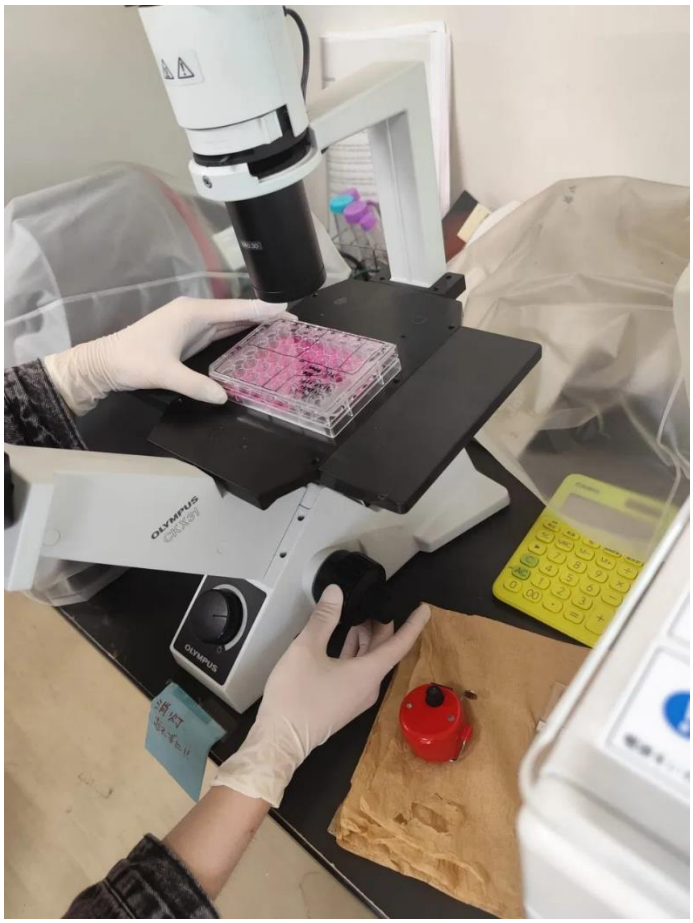


Figure 32 - Inverted light microscope (Olympus CKX31) used to monitor cell culture

4.11.5 Exposure to Eluates

Following the 24-hour adhesion period, the standard culture medium was replaced with the scaffold-conditioned eluate corresponding to each release time point (24h, 27h. 7 days), used undiluted (*Figure 33*). Cells were incubated with the eluates for 24 hours under standard culture conditions.

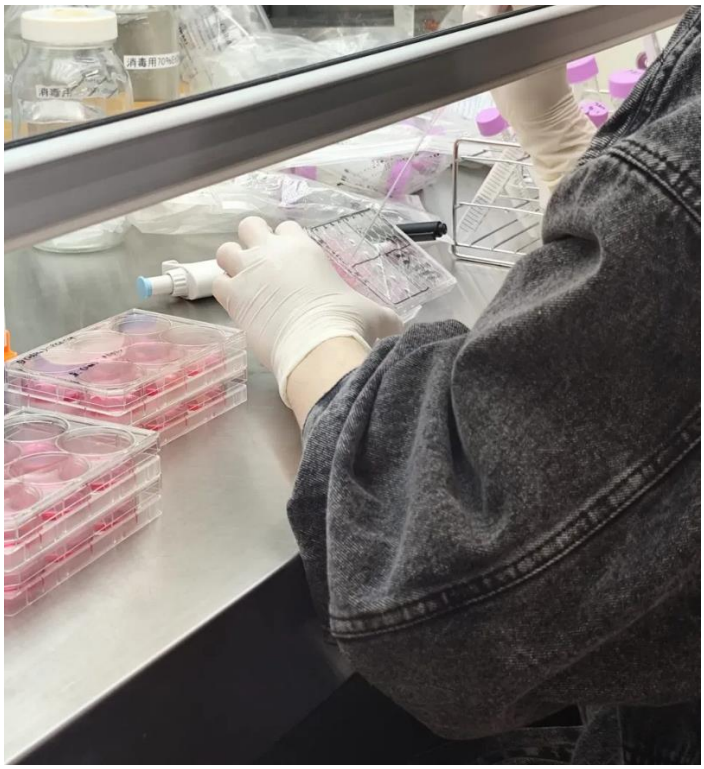


Figure 33 - Transfer of scaffold-conditioned eluate to cell culture wells under a biosafety cabinet

4.11.6 Cell Viability Assessment and Imaging

Following the 24-hour exposure period, the eluate was aspirated from each well and the remaining conditioning medium was transferred to storage tubes and kept at 4°C. Cells were fixed by adding 300 µL of 4% paraformaldehyde (PFA) per well for 30 minutes. The fixative was then removed, and cells were washed with 200 µL of Tris-Buffered Saline with Tween-20 (TBST) for 5 minutes; the non-ionic detergent (Tween-20) partially permeabilizes the cell membrane, facilitating access of the nuclear stain to the DNA. Following the removal of the washing buffer, a Hoechst 33342 staining solution (prepared at 1:1000 dilution in TBST) was added at 200 µL per well and incubated for 10 minutes to label cell nuclei. Cells were then washed again with TBST for 5 minutes. Samples were maintained in 200 µL of PBS (1X) prior to imaging: an antifade mounting medium (Fluoro-KEEPER) was considered to minimize photobleaching during acquisition but was omitted as unnecessary for immediate confocal imaging.

For each well, three images were acquired by fluorescence microscopy. Cell counting was performed manually and blinded – the operator was not aware of the specific experimental condition of each well during counting – to minimize observer bias. Cells were classified as viable or non-viable based on nuclear morphology, with condensed or fragmented nuclei identified as non-viable; to avoid double-counting, cells were sequentially marked in groups of 20 during the counting process. Cell viability was expressed as the percentage of viable cells relative to the total cell count (viable + non-viable) for each field and results were averaged across the three wells prepared for each experimental condition and time point.

4.11.7 Experimental Controls

Appropriate controls were included to ensure reliable interpretation of the results: a negative control consisting of cells cultured in fresh, non-conditioned medium; a material control represented by eluates obtained from unloaded (pure PCL) scaffolds, to isolate any effect attributable to the polymer itself.

4.11.8 Data Handling

One well from the pure PCL control group at the 7-day time point showed evidence of accidental contamination and was excluded from the statistical analysis as a methodological outlier.

4.12 Drug Release Kinetics

4.12.1 Rationale for the In Vitro Release Testing Design

Assessing the in vitro release kinetics of the incorporated bioactive agents is essential to predict the therapeutic behaviour of the scaffold once applied to a wound. Phosphate-buffered saline (PBS) was selected as the release medium owing to its ionic strength and osmolarity, which closely approximate those of physiological fluids, making it the standard reference medium for release and dissolution studies of biomedical devices. As discussed in *Chapter 3*, curcumin and β-carotene are both highly hydrophobic molecules; consequently, their aqueous solubility in an unmodified PBS medium would fall far short of the "sink condition" required for a release profile to meaningfully reflect physiological absorption – that is, a medium volume and solubilizing capacity sufficient to keep the dissolved drug concentration well below saturation, so that the release process remains driven by diffusion from the matrix rather than being artificially limited by the medium itself. To this end, the release medium was supplemented with the anionic surfactant sodium dodecyl sulphate (SDS), a widely adopted approach for improving the aqueous solubility of poorly water-soluble compounds in dissolution testing without altering the intrinsic release mechanism from the polymer matrix. [60]

The release medium was further buffered at three pH values (5.5, 7.4 and 9.0), selected to replicate the distinct clinical scenarios discussed in *Chapter 2* – namely, the mildly acidic environment of healthy or re-epithelializing skin, the near-neutral environment of an open acute wound in contact with systemic fluids and the alkaline environment characteristic of chronic or infected wounds. Incubation was carried out at 32 °C rather than at core body temperature (37°C), reflecting evidence that the external wound bed surface – as opposed to the internal, vascularized tissue – typically registers temperatures in the 30-33°C range, particularly following dressing changes. [1], [61]

Quantification of the released compounds was performed by UV-Vis spectrophotometry, a rapid and non-destructive analytical technique well-suited to monitoring cumulative release kinetics over time from small sample volumes and widely applied for this purpose in the drug-delivery literature. Both curcumin and β-carotene possess extended conjugated chromophore systems – the β-diketone/enol tautomeric structure in curcumin and the long polyene backbone in β-

carotene – which give rise to their characteristic strong absorption in the visible range, around 420 nm, allowing, direct spectrophotometric quantification without the need for derivatization. [7], [8], [10], [24]

4.12.2 Sample Preparation and Release Medium

Four scaffold formulations were tested: pure PCL (blank control), PCL functionalized with 5% curcumin, PCL functionalized with 5% β-carotene and PCL functionalized with a 2.5%/2.5% curcumin/β-carotene mixture, all fabricated with the same bilayer architecture (a structural pure-PCL layer combined with the functionalized layer) described in the previous sections. Each release medium consisted of PBS adjusted to the target pH (5.5, 7.4 or 9.0) using NaOH/HCl, supplemented with 0.1% (w/v) SDS. Samples were fully submerged in 10 mL of medium to maintain sink conditions and incubated in sealed tubes (screwcap) at 32°C (*Figure 34*).



Figure 34 - Example of a curcumin sample in the release medium

4.12.3 Sampling Protocol

Aliquots were collected at three time points – 24 hours (Day 1), 72 hours (Day 3) and 168 hours (Day 7) – with the released solution transferred to a cuvette for immediate spectrophotometric analysis.

4.12.4 Quantitative Analysis by UV-Vis Spectrophotometry

Released curcumin and β-carotene were quantified by UV-Vis spectrophotometry against calibration curves constructed for each compound at each pH value, using three known concentrations spanning in the expected release range. Absorbance values at the characteristic

peak wavelength of approximately 420 nm were used as the quantification reference. To isolate the signal attributable exclusively to the bioactive agents, the spectrum of the unloaded PCL control (at pH 5.5) was subtracted as background from all measurements.

5 Results

5.1 Morphological Characterisation

5.1.1 Laser-Optical Microscopy

Surface morphology and fibre diameter of all bilayer scaffold formulations were assessed by laser-optical microscopy at 10X and 150X magnification. *Figure 35* and *Tables 5.1* to *5.4* report the mean fibre diameter (± standard deviation) measured for each electrospun deposition of every experimental group, obtained from a minimum of 34 randomly selected fibres per image, as described in *Chapter 4.6.1.*

At 10X magnification (*Figure 36*), the Control group (*Figure 36 a*) exhibited a dense, homogeneous nanofiber network free of macroscopic irregularities. The Curcumin-loaded samples (*Figure 36 c*) showed a uniform yellowish coloration distributed across the entire mesh, with a fibre morphology comparable to the Control. In contrast, the β-Carotene-loaded samples (*Figure 36 b*) displayed visible reddish spots and aggregates distributed across the fibre surface. The Mix samples (*Figure 36 d*) showed the characteristic yellowish colouration of curcumin together with the same reddish aggregates observed in the β-Carotene group.

At 150X magnification (*Figure 37*), the Control group (*Figure 37 a*) produced fibres with an overall mean diameter of approximately 0.96 µm, with the six depositions ranging from 0.617 to 1.236 µm. One deposition of the β-Carotene group (*Figure 37 b,* Beta 1) exhibited a substantially larger mean diameter (4.213 ± 0.953 µm) compared to the remaining six depositions of the same group (0.518 – 0.953 µm). The Curcumin group (*Figure 37 c*) showed mean diameters ranging from 0.692 to 1.782 µm across its eight depositions. The Mix group (*Figure 37 d*) showed one deposition (Mix 1) with a mean diameter of 3.543 ± 0.518 µm, while the remaining six depositions ranged from 0.666 to 1.292 µm.

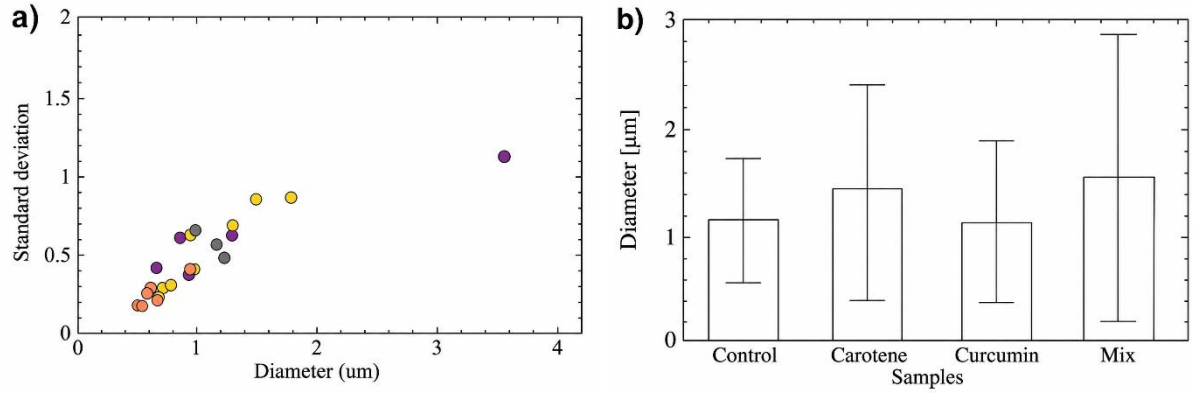


Figure 35 – a) Standard deviation of fibre diameter as a function of mean diameter for each individual deposition of the Control (grey), β-Carotene (orange), Curcumin (yellow) and Mix (purple) groups; b) Mean fibre diameter (± SD) of the four groups, pooled across all depositions.

Representative examples of macroscopic deposition defects, observed at 10X magnification, are shown in *Figure 38*. In the Control group the defects consisted primarily of localized mechanical irregularities within the nanofiber mesh, appearing as fold-like or tear-like discontinuities in the deposition pattern. In the β-Carotene group, the defects were structural in nature, consisting of discrete reddish aggregates around which the surrounding fibres appeared radially entangled.

Sample	Deposition	Mean diameter [µm]
Pure PCL	Control 1	1,236 ± 0,201
	Control 2	0,990 ± 0,136
	Control 3	1,172 ± 0,150
	Control 4	0,617 ± 0,076
	Control 5	0,731 ± 0,100
	Control 6	1,017 ± 0,110

Table 5.1 – Mean fibre diameter of the pure PCL samples measured by laser-optical microscopy (150X) for each deposition

Sample	Deposition	Mean diameter [µm]
5% Beta - Carotene Layer	Beta 1	4,213 ± 0,953
	Beta 2	0,953 ± 0,160
	Beta 3	0,518 ± 0,057
	Beta 4	0,556 ± 0,091
	Beta 5	0,679 ± 0,078
	Beta 6	0,633 ± 0,065
	Beta 7	0,597 ± 0,075

Table 5.2 – Mean fibre diameter of the PCL-β-carotene samples measured by laser-optical microscopy (150X) for each deposition

Sample	Deposition	Mean diameter [µm]
5% Curcumin Layer	Curcumin 1	1,782 ± 0,467
	Curcumin 2	1,303 ± 0,245
	Curcumin 3	1,493 ± 0,379
	Curcumin 4	0,952 ± 0,131
	Curcumin 5	0,986 ± 0,125
	Curcumin 6	0,725 ± 0,105
	Curcumin 7	0,692 ± 0,091
	Curcumin 8	0,793 ± 0,083

Table 5.3 – Mean fibre diameter of the PCL-Curcumin samples measured by laser-optical microscopy (150X) for each deposition

Sample	Deposition	Mean diameter [µm]
Mix 2,5% + 2,5% Layer (Curcumin + Beta-Carotene)	Mix 1	3,543 ± 0,518
	Mix 2	1,292 ± 0,182
	Mix 3	0,862 ± 0,144
	Mix 4	0,666 ± 0,081
	Mix 5	0,942 ± 0,124
	Mix 6	0,950 ± 0,138
	Mix 7	0,682 ± 0,073

Table 5.4 – Mean fibre diameter of the PCL-Mix samples measured by laser-optical microscopy (150X) for each deposition

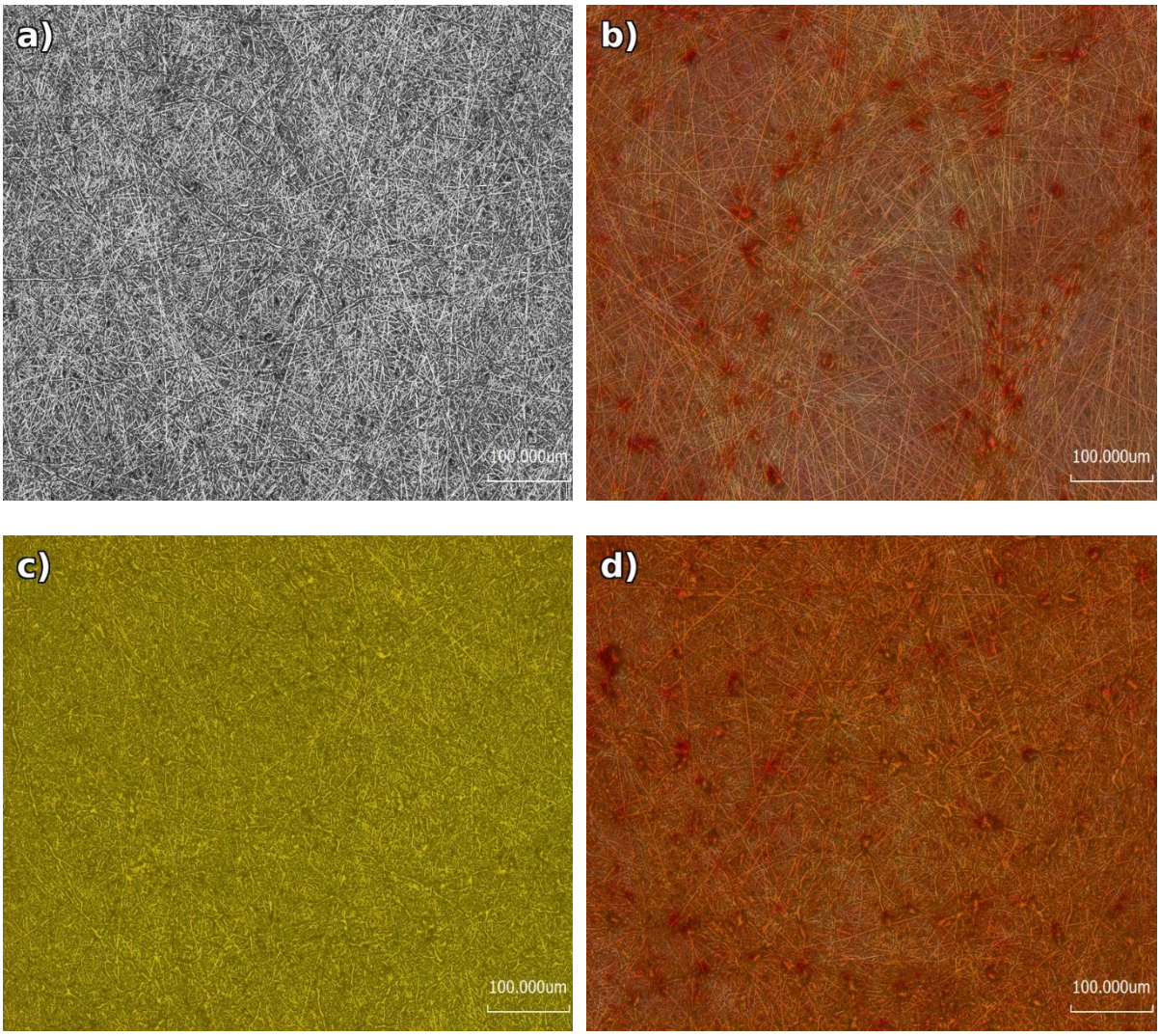


Figure 36 – Laser-optical image (10X) - a) PCL control, b) β-carotene sample, c) curcumin sample, d) mix sample

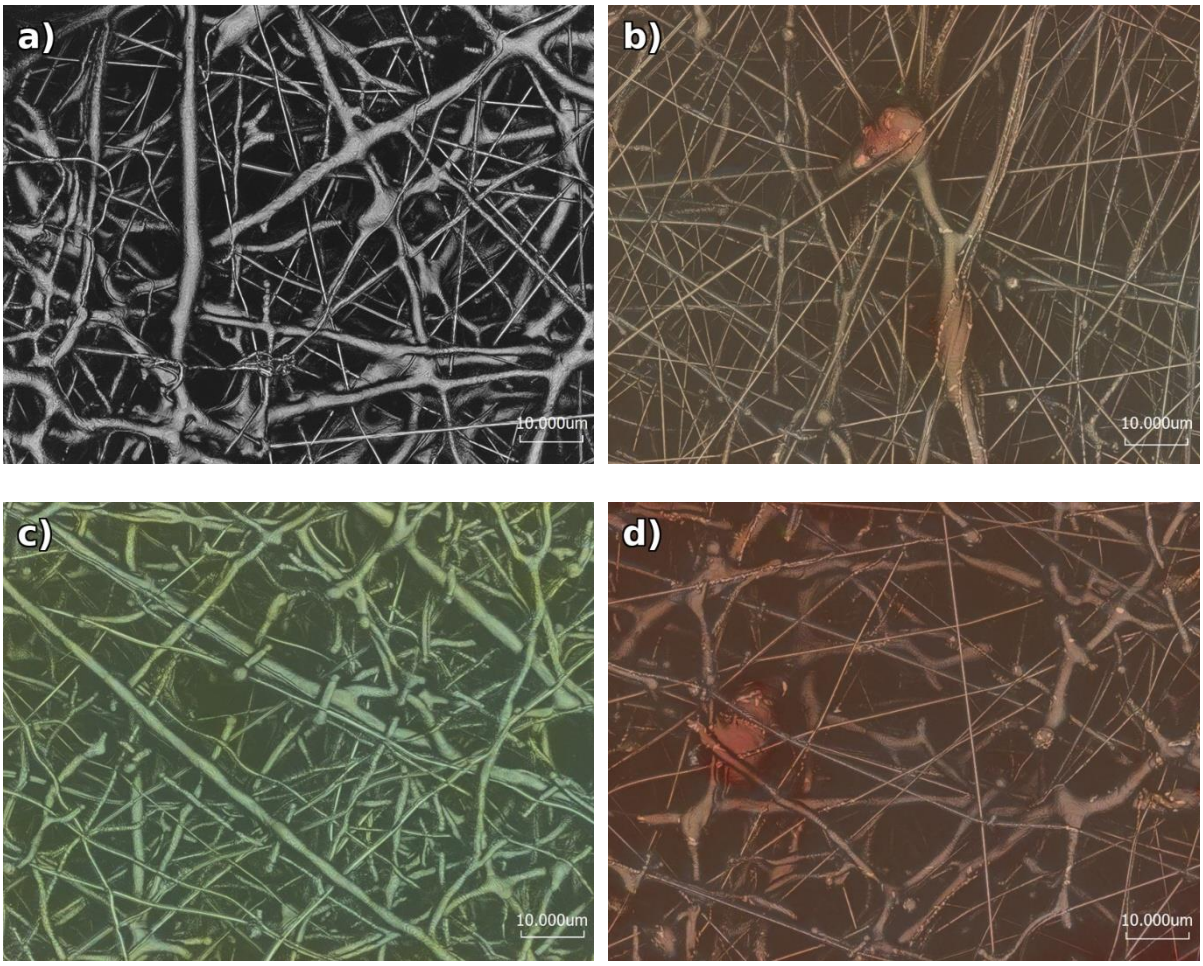


Figure 37 – Laser-optical image (150X) - a) PCL control, b) β-carotene sample, c) curcumin sample, d) mix sample

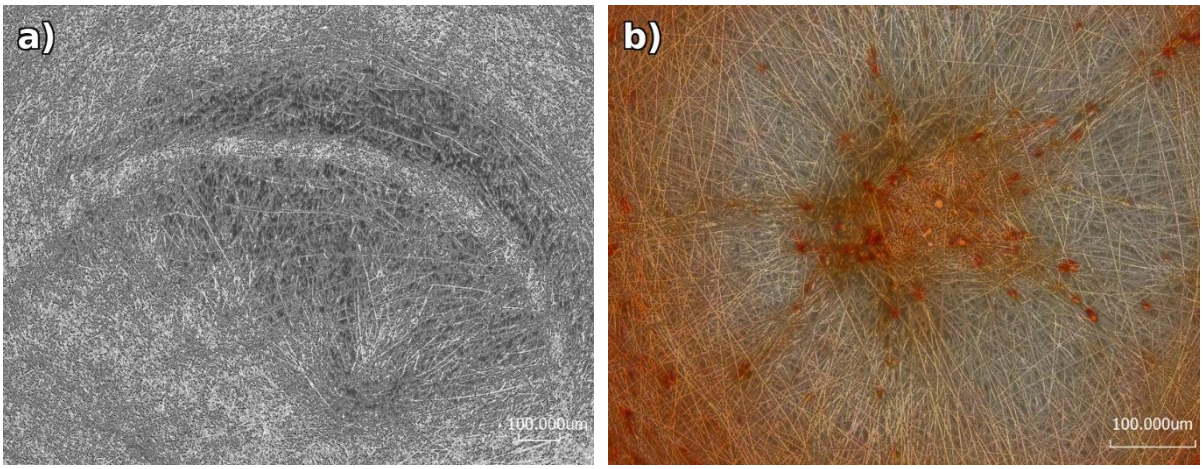


Figure 38 – Examples of deposition defects observed by laser-optical microscopy (10X). a) Control, b) β-Carotene

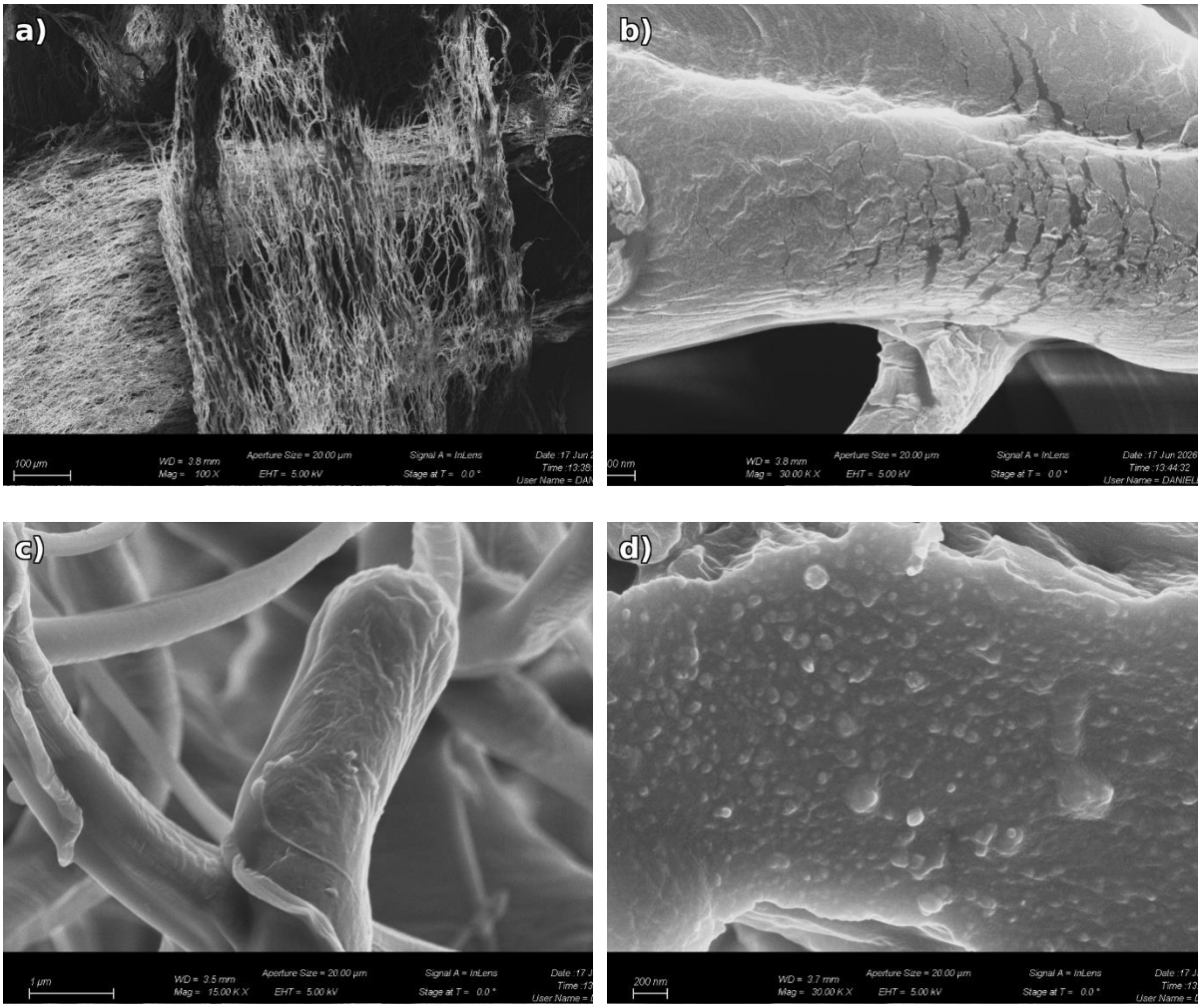
5.1.2 FESEM

Field emission scanning electron microscopy was performed on the fracture surfaces of specimens following tensile testing (*Figure 39*). For the Mix sample, imaging at 100X magnification of the region proximal to fracture (*Figure 39 a*) revealed a pronounced directional

alignment of the fibres along the tensile axis, with the bilayer structure retaining overall cohesion. At 30'000X magnification (*Figure 39 b*), transverse micro-fractures were observed on the surface of stretched fibres of the Mix sample.

For the β-Carotene sample, imaging at 15'000X magnification (*Figure 39 c*) revealed a nodular swelling within a fibre, consistent in size and morphology with an undissolved β-carotene macro-aggregate; plastic deformation of the surrounding polymer matrix was observed around this feature. At 30'000X magnification (*Figure 39 d*) of the specimen's cut edge, granular structures and nano-aggregates were observed on the surface. At 100X magnification (*Figure 39 e*), the final fracture edge of the β-Carotene sample showed extensive fraying of the fibrous mesh.

For the Curcumin sample, imaging at 5'000X magnification (*Figure 39 f*) revealed a single thickened nodal structure, around which adjacent fibres showed pronounced elongation and thinning.



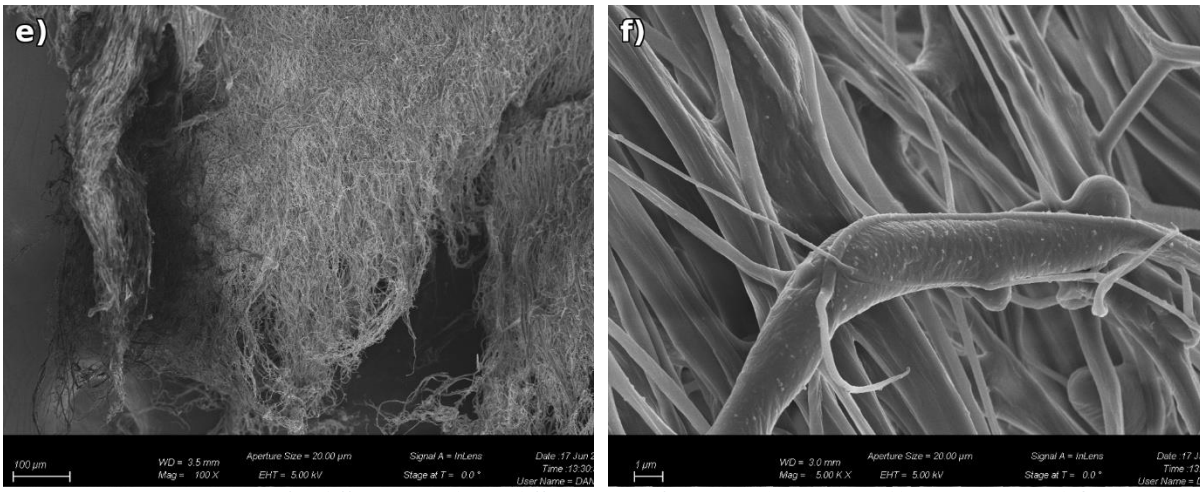


Figure 39 – FESEM images for different samples at different magnification – a) Mix 100X, b) Mix 30'000X, c) β-Carotene 15'000X, d) β-Carotene and nano-aggregates 15'000X, e) β-Carotene 100X, f) Curcumin 5'000X

5.1.3 Fluorescence Confocal Laser Scanning Microscopy

Confocal fluorescence microscopy was performed on all sample groups using three acquisition channels (DAPI, Rhodamine, Green), exploiting the intrinsic autofluorescence of curcumin and β-carotene (*Figure 40-43*). The control sample (*Figure 40*) showed no detectable signal in the Rhodamine channel.

The β-Carotene (*Figure 41*) sample showed a fluorescent signal tracing the fibre network in all three channels, with isolated high-intensity bright spots superimposed on the fibre structure and an inhomogeneous signal distribution in the Rhodamine channel.

The Curcumin (*Figure 42*) sample showed a diffuse and homogeneous fluorescent signal in the DAPI channel, without isolated high-intensity spots. In the Rhodamine channel, the nanofiber network was distinctly traced by the fluorescent signal, without luminescent clumps. In the Green channel, the signal intensity was uniform and regular across the acquired area.

For the Mix sample (*Figure 43*), the DAPI channel was not acquired due to a technical acquisition issue. The Rhodamine channel showed a high overall signal intensity, with discrete bright spots superimposed on a diffuse background. The Green channel showed a high-intensity signal across the acquired area, within which the underlying fibrous structure remained distinguishable.

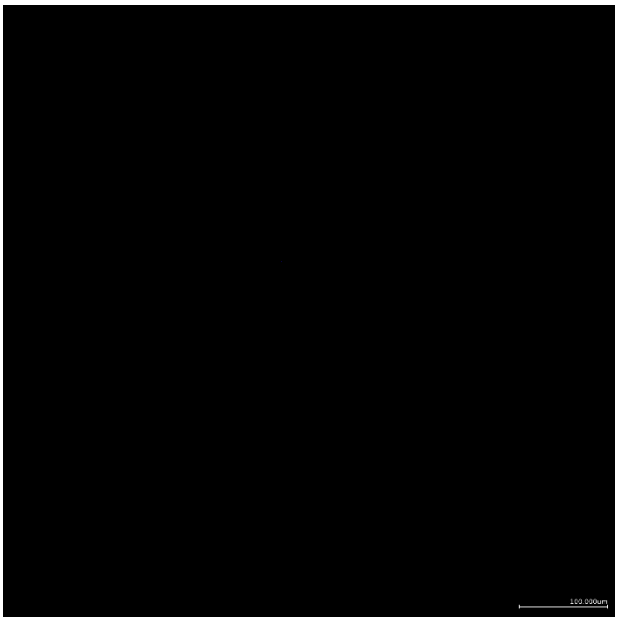
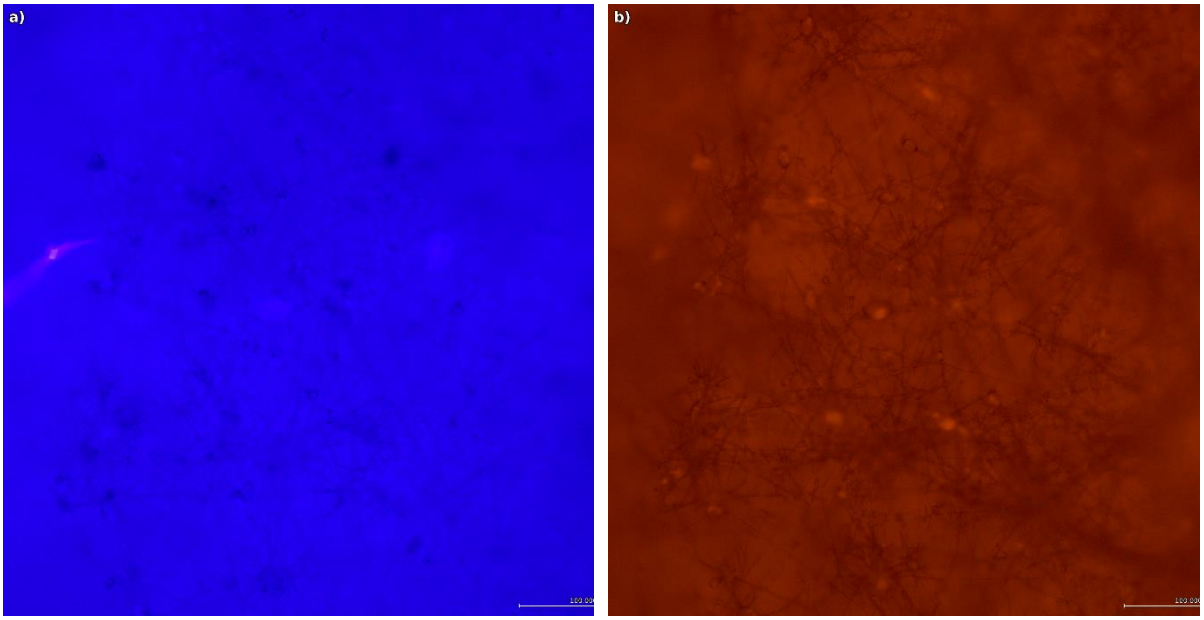


Figure 40 – PCL control



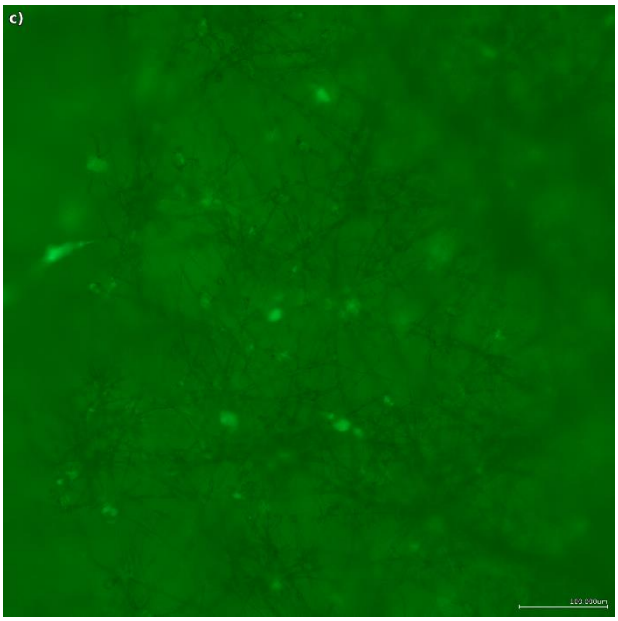
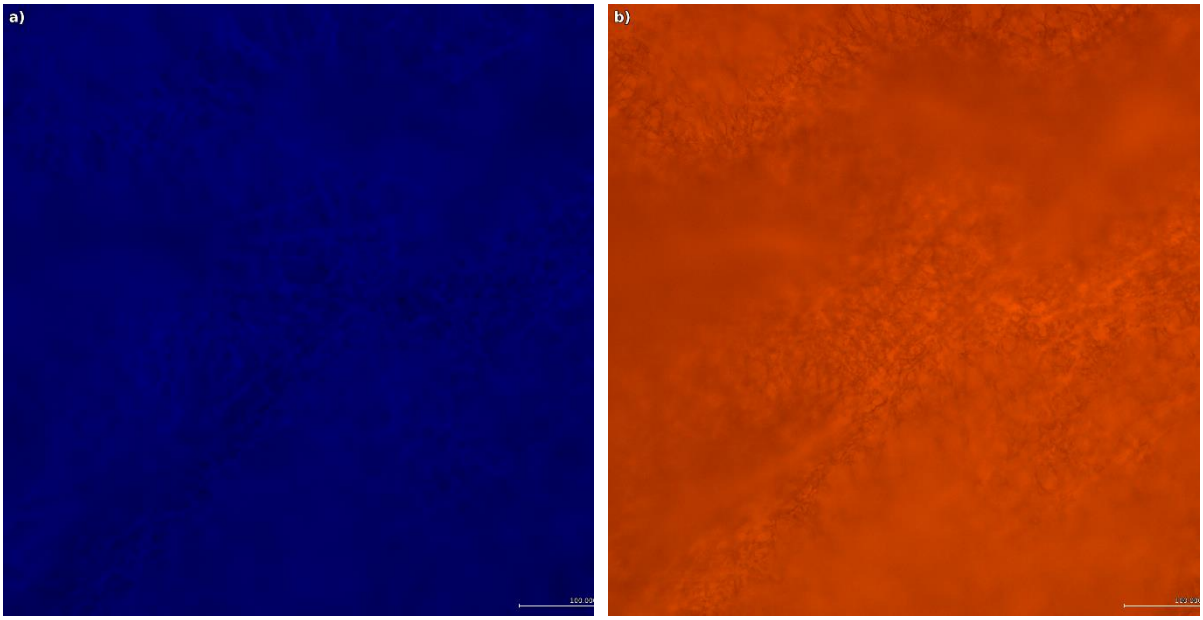


Figure 41 – β-Carotene sample images – a) DAPI, b) Rhodamine, c) Green



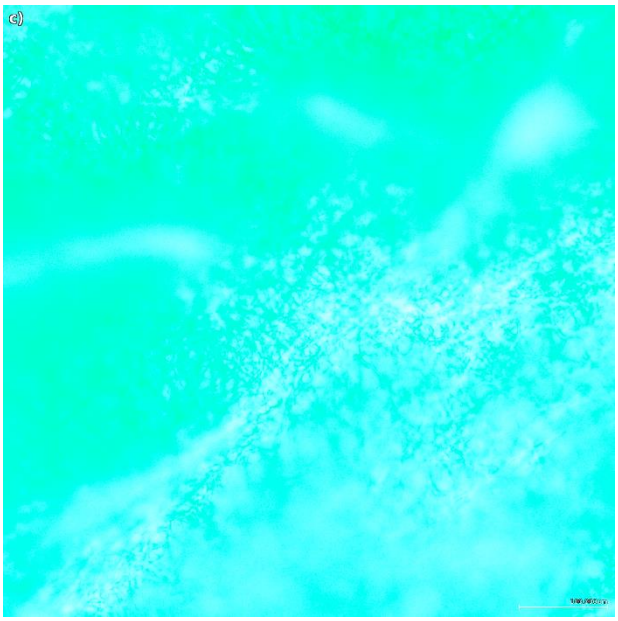


Figure 42 – Curcumin sample images – a) DAPI, b) Rhodamine, c) Green

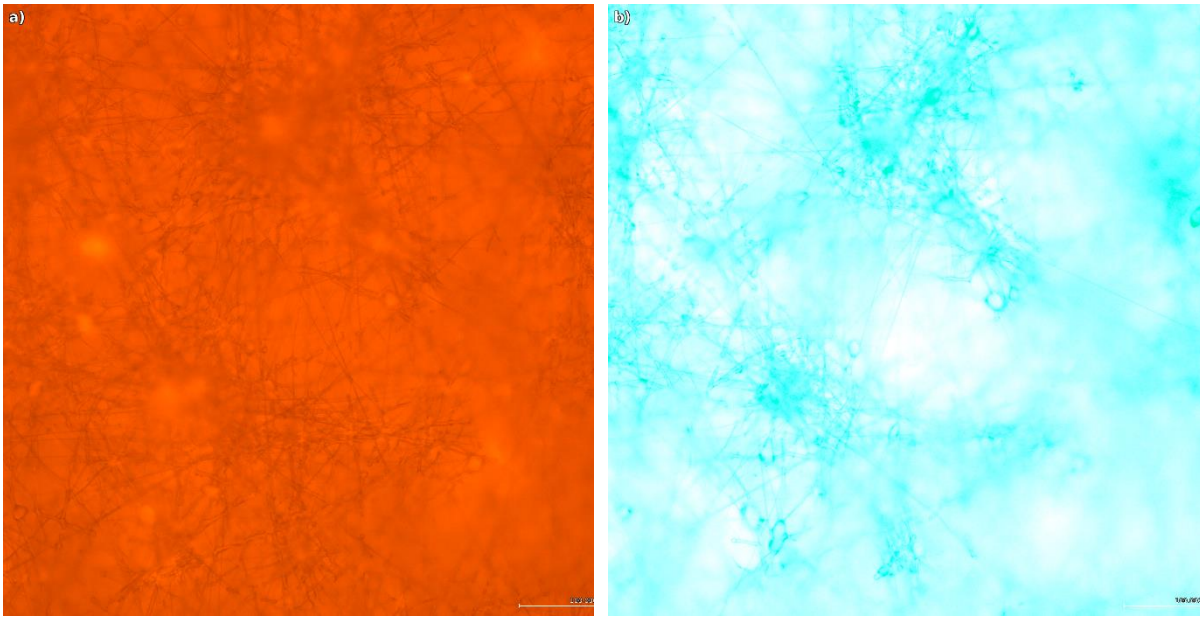


Figure 43 – Mix sample images – a) Rhodamine, b) Green

5.2 Chemical and Structural Characterization

5.2.1 FTIR

FTIR-ATR spectra were acquired for all four experimental groups (Control, β-Carotene, Curcumin and Mix) to verify the chemical fingerprint of the electrospun scaffolds and assess whether the incorporation of the bioactive agents induced detectable chemical alterations to the PCL matrix (*Figure 44*).

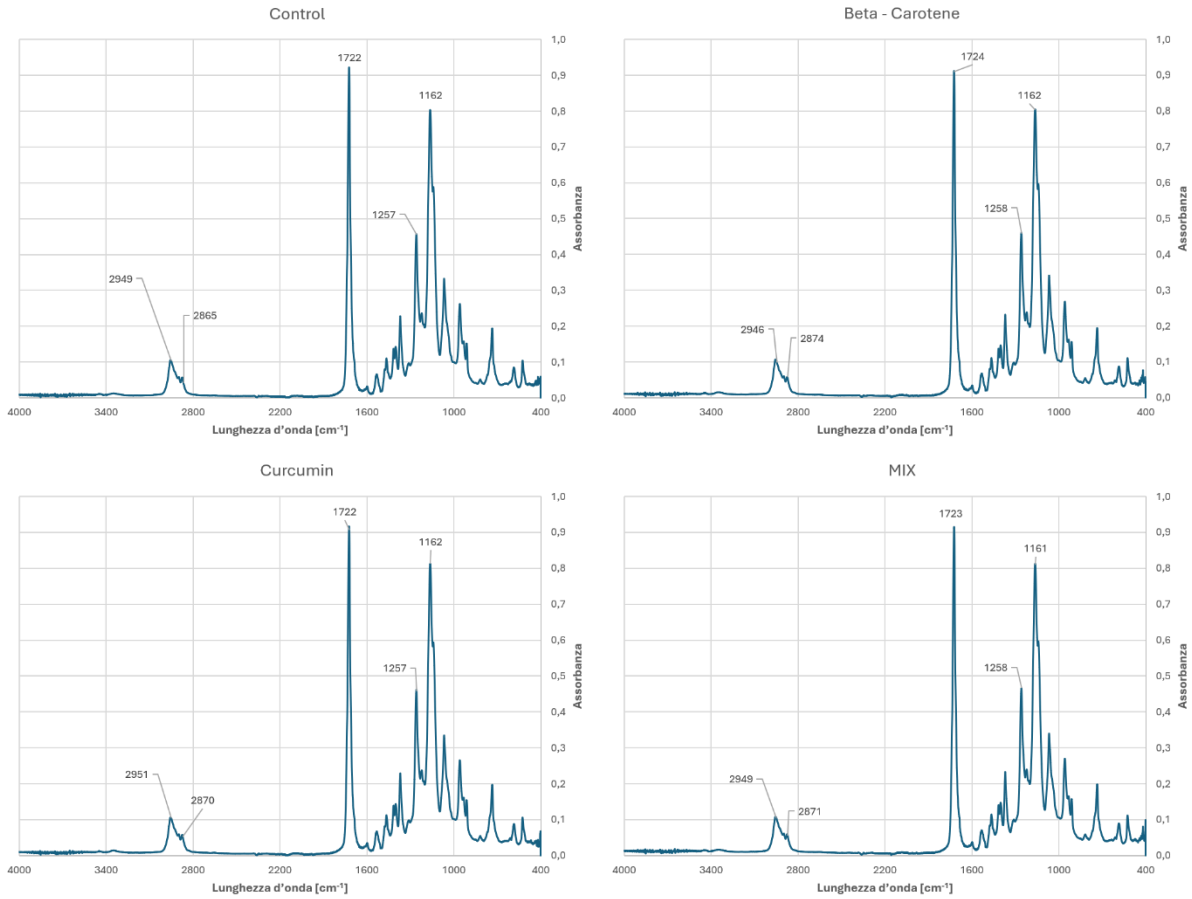


Figure 44 – FTIR-ATR spectra of the Control, β-Carotene, Curcumin, and Mix bilayer scaffolds, showing the characteristic PCL absorption bands (C=O stretching ~ 1722 cm^{-1}, C-H stretching 2949/2865 cm^{-1}, C-O-C stretching 1160-1250 cm^{-1})

The Control spectrum (*Figure 44 - Control*) reproduced the characteristic absorption bands of PCL, with the dominant carbonyl (C=O) stretching peak at 1722 cm^{-1}, the asymmetric and symmetric aliphatic C-H stretching peaks at 2949 cm^{-1} and 2865 cm^{-1}, and the C-O-C stretching region between 1160 and 1250 cm^{-1}.

The β-Carotene spectrum (*Figure 44 – β-Carotene*) showed the same characteristics PCL peaks, at essentially unchanged wavenumbers (1724 cm^{-1} and 2946 cm^{-1} for the carbonyl and C-H bands, respectively). No signals attributable to β-carotene were distinguishable in the spectrum.

The Curcumin spectrum (*Figure 44 – Curcumin*) likewise reproduced the carbonyl peak at 1722 cm^{-1} and the remaining characteristic bands without detectable shifts. No curcumin-specific bands were resolved in the spectrum.

The Mix spectrum (*Figure 44 - Mix*) reproduced the same set of PCL bands (1723, 2949 and 1161 cm^{-1}), consistent with the spectra of the individual formulations.

Across all functionalized groups, no new absorption bands or peak shifts relative to the Control spectrum were observed.

5.2.2 Raman Spectroscopy

Raman spectra were acquired for the four experimental groups (Control, grey; β-Carotene, orange; Curcumin, yellow; Mix, purple) (*Figure 45*).

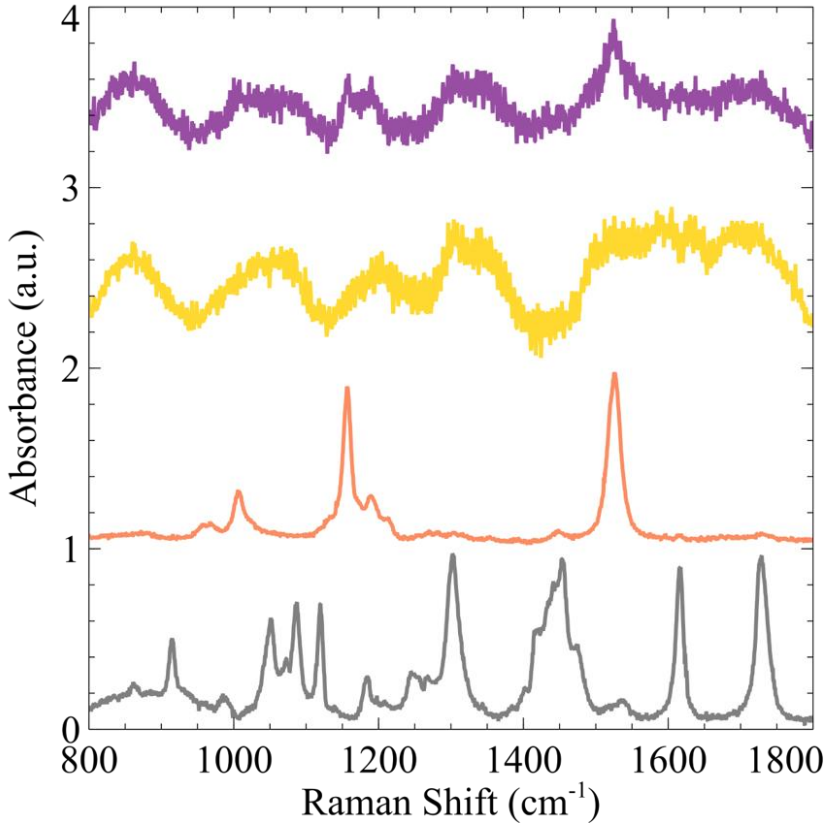


Figure 45 – Raman spectra of the Control (grey), β-Carotene (orange), Curcumin (yellow) and Mix (purple bilayer scaffolds, acquired under 488 nm laser excitation

The control spectrum showed a series of sharp, well-resolved bands, summarised in *Table 5.5* together with their tentative assignment based on literature data for PCL. [62]

Observed Band [cm^{-1}]	**Tentative assignment**
~915	ν(C-COO)
~1050-1120 (unresolved multiplet)	ν(C-COO) / skeletal C-C stretching
~1300	ω(CH_2) twisting
~1440-1460	δ(CH_2) bending
~1610	(*not univocally assigned*)
~1721	ν(C=O)

Table 5.5 – Raman bands identified in the Control (PCL) spectrum and their tentative assignment. [62]

The β-Carotene spectrum was dominated by three sharp, high-intensity bands centred at approximately 1005 cm^{-1}, 1155 cm^{-1} and 1519 cm^{-1}, consistent in position with the ν_3, ν_2 and ν_1 modes of the conjugated polyene backbone described in *Chapter 3*. No bands attributable to the underlying PCL matrix were distinguishable in this spectrum.

The curcumin spectrum showed a broad, high-intensity fluorescence background across the entire acquisition range, with no sharp bands attributable to either curcumin or PCL resolvable above this background.

The Mix spectrum showed the same broad fluorescence background observed for the Curcumin group; superimposed on this background, a single sharp band was resolved at approximately

1517 cm^{-1}, matching the position of the dominant ν_1 band of β-carotene. No other bands were distinguishable above the fluorescence background.

5.3 Thermal Analysis (DSC)

DSC analysis was performed on all four experimental groups following the three-stage thermal protocol described in *Chapter 4.8.1* (first heating to 120°C, cooling to -80°C, second heating to 120°C). Melting enthalpies and crystallization enthalpies were obtained by integrating the area under the respective DSC peaks using the trapezoidal rule, and the corresponding fractional crystallinity values were calculated according to *Equation (4)* (*Chapter 4.8.1*), using a reference melting enthalpy of 139 J/g for 100% crystalline PCL [13]. All values are reported in *Table 5.6*.

Parameter	Control	β -Carotene	Curcumin	Mix
Melting enthalpy, 1st heating [J/g]	34.64	28.27	66.01	72.55
Melting enthalpy, 2nd heating [J/g]	48.08	27.72	44.99	47.96
Crystallization enthalpy [J/g]	53.85	13.86	54.18	55.77
Crystallinity, 1st heating [%]	24.83	20.26	47.32	52.01
Crystallinity, 2nd heating [%]	34.47	19.87	32.25	34.38
Crystallinity, cooling [%]	38.60	9.94	38.84	39.98

Table 5.6 – Melting enthalpy (1st and 2nd heating), crystallization enthalpy and fractional crystallinity (1st heating, 2nd heating and cooling) for the Control, β-Carotene, Curcumin and Mix bilayer scaffolds.

For the Control group (*Figure 46 - Control*) the first-heating crystallinity (24.83%) was lower than the second-heating value (34.47%). For the β-Carotene group (*Figure 46 – β-Carotene*), crystallinity values were markedly lower than those of the other groups across all three thermal steps, with comparable values recorded for the first and second heating (20.26% and 19.87%, respectively) and a further decrease observed during cooling (9.94%). For the Curcumin group (*Figure 46 - Curcumin*), the first-heating crystallinity (47.32%) was higher than the second-heating value (32.25%). The Mix group (*Figure 46 - Mix*) showed the highest first-heating crystallinity of all four groups (52.01%), with the second-heating value (34.38%) comparable to that of the Control and Curcumin groups.

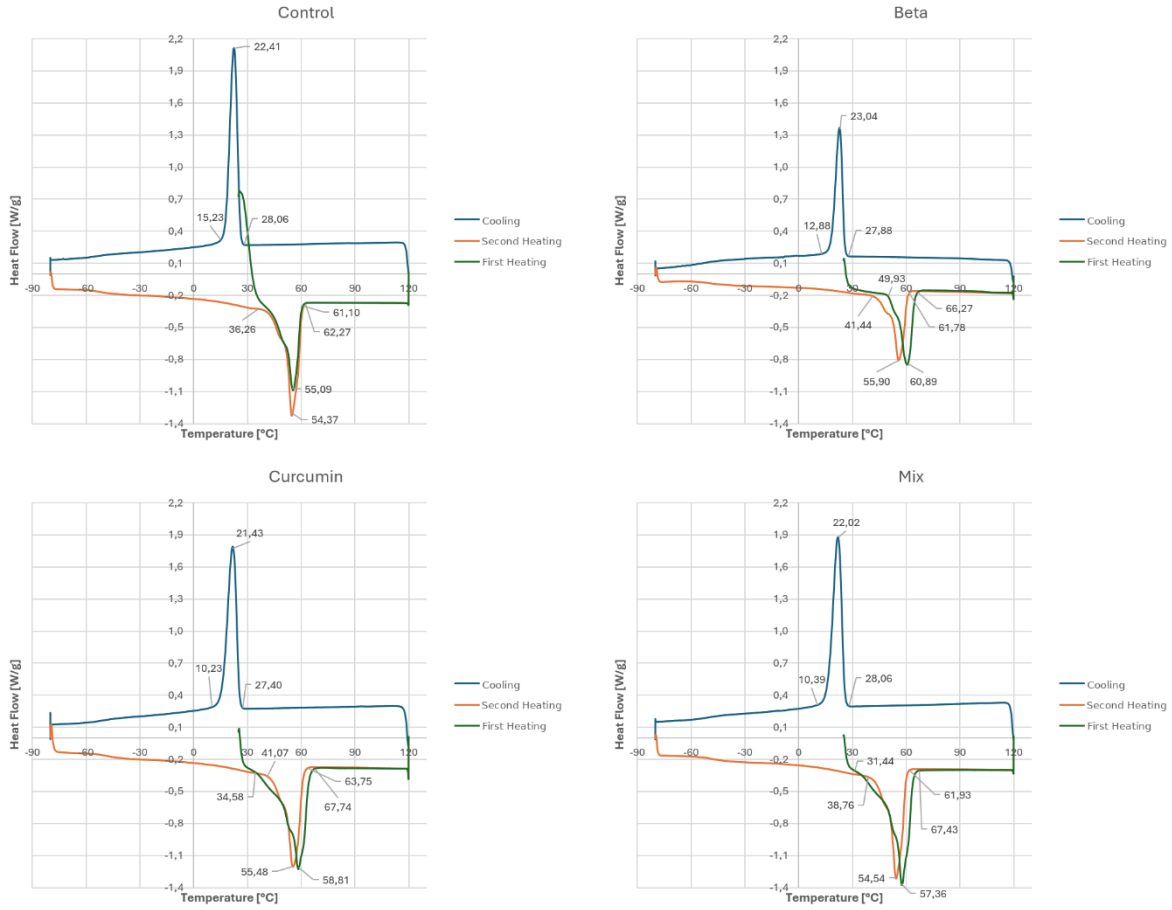


Figure 46 – DSC thermograms (first heating, cooling and second heating) of the Control, β-Carotene, Curcumin and Mix bilayer scaffolds

5.4 Colloidal and Surface Characterization

This section presents the results of the colloidal and surface electrokinetic characterization of the bilayer scaffolds, comprising three complementary measurements: the surface zeta potential of the intact solid patches, the zeta potential of the species released into the ethanol eluate (ELS), and the hydrodynamic diameter of these released species (DLS).

5.4.1 Zeta Potential of Released Species (ELS)

The zeta potential of the species released into the ethanol-based eluate was measured by ELS as a function of pH, for the same eight target pH values (approximately pH 2.8 to 9.6) used for the DLS analysis (*Chapter 4.9.1*), for all four experimental groups (*Figure 47*).

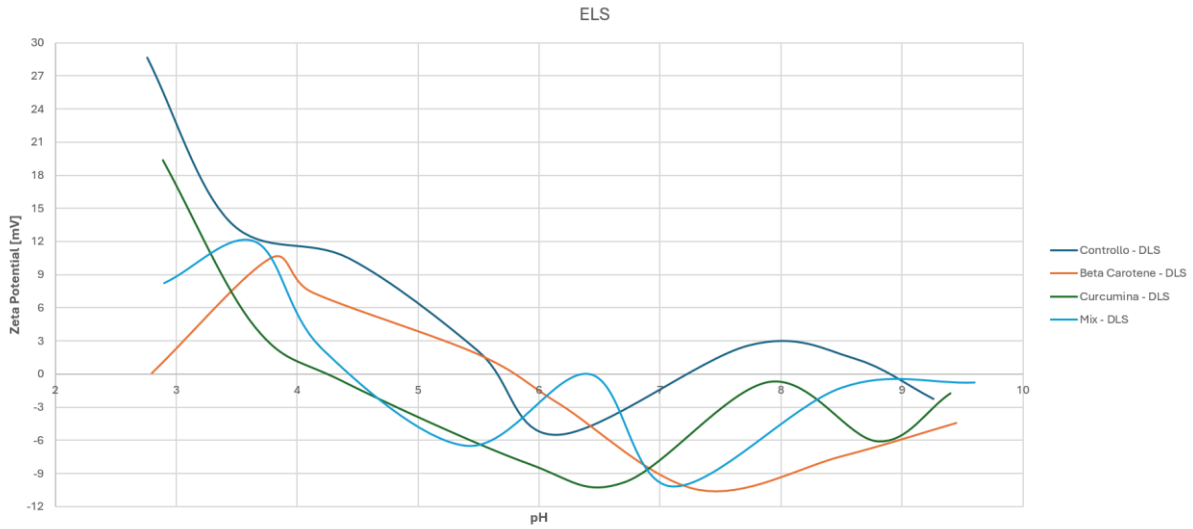


Figure 47 – Zeta potential of the species released in the ethanol eluate as a function of pH, for the Control, β-Carotene, Curcumin and Mix groups, measured by ELS

Across the entire pH range investigated, all four groups, including the Control, showed values remaining close to zero, oscillating approximately between +20 mV and -10 mV, without clearly defined isoelectric point or a consistent monotonic trend with pH. This behaviour contrasts with that recorded for the intact solid surface (*Chapter 5.4.1*), where substantially more negative values (down to approximately -80 mV) were measured across the same pH range. Considering the chemistry of curcumin and β-carotene without reactive functional groups, as previously described, the absence of an IEP is consistent with expectations.

5.4.2 Surface Zeta Potential

PCL is a hydrophobic polymer without functional groups with acidic-basic reaction and an IsoElectric Point (IEP) close to 4 – 4.5 is expected. If residual carboxylic groups are present in the polymer, a shift of the IEP toward more acidic pH values should be measured [63], but this is not the case confirming the effectiveness of the PCL synthesis. The absence of a plateau at very low/high pH values is also consistent with the absence of completely protonated/deprotonated reactive functional groups. A strong variation of zeta potential by changing the pH of the electrolyte is expected because of the adsorption of hydroxonium or hydroxyl groups from the solution on the PCL surface instead of water molecules which are weakly adsorbed on a hydrophilic surface, this hydrophobic behaviour was also experimentally confirmed with zeta potential as low as -80 mV which is close to the maximum absolute values of zeta potential detected on surfaces. The zeta potential values of hydrophobic surfaces are strongly dependent from the electrolyte composition (ionic force) and are not an intrinsic chemical surface property of PCL. The low standard deviation of zeta potential measured at any pH was a prove of its chemical stability in the measurement conditions (under a flux of an aqueous medium with variations in pH).

Curcumin is a hydrophobic molecule with three distinct pKa values (approximately 8.31, 9.88, and 10.51) due to basic (or very low acidic) reactivity of enolic and phenolic OH groups which are deprotonated only at very high pH values. Usually, these functional groups do not give a

positive charge to the molecule, even at pH 2-3, but the shift toward higher pH values of the IEP of the sample functionalized with curcumin and the plateau measured in the acidic range (pH 2-3) on this sample should be connected to the protonation of functional groups. A hypothesis is that the protonation usually occurred in curcumin only at pH lower than 1 [64] was shifted to higher values because of its interaction with PCL. This different chemical reactivity of curcumin coupled to PCL should be further investigated. Curcumin is less stable in the basic pH than in the acidic one and the higher standard deviation values registered in the basic range in the sample functionalized with curcumin should be related to partial reactivity of the molecule. The sample had strong change of zeta potential by changing the pH of the electrolyte because of its hydrophobicity, as already explained for PCL, but the presence of reactive OH groups reduced this effect in the basic range, confirming the previous hypothesis.

Conversely, β-carotene is a hydrophobic molecule without any reactive acidic/basic functional group and the titration curve of the sample functionalized with this molecule is very similar to PCL with even higher absolute values of zeta potential due to higher hydrophobicity.

As reasonable, the sample functionalized with a mixture of curcumin and β-carotene had an intermediate behaviour.

Within the pH window corresponding to intact skin (pH 4.5-5.5), the Control, β-Carotene and Mix groups showed a moderately negative surface charge, in the range of approximately -10 to -30 mV, with overlapping trends among the three groups across this interval.

Across the broader pH range investigated, the surface zeta potential of all four groups reached markedly more negative values than those recorded within the skin-relevant window, down to approximately -80 mV at the extremes of the titration range. As already explained, these values are mainly due to the adsorption of ions from the electrolyte and not to deprotonated functional groups of the materials.

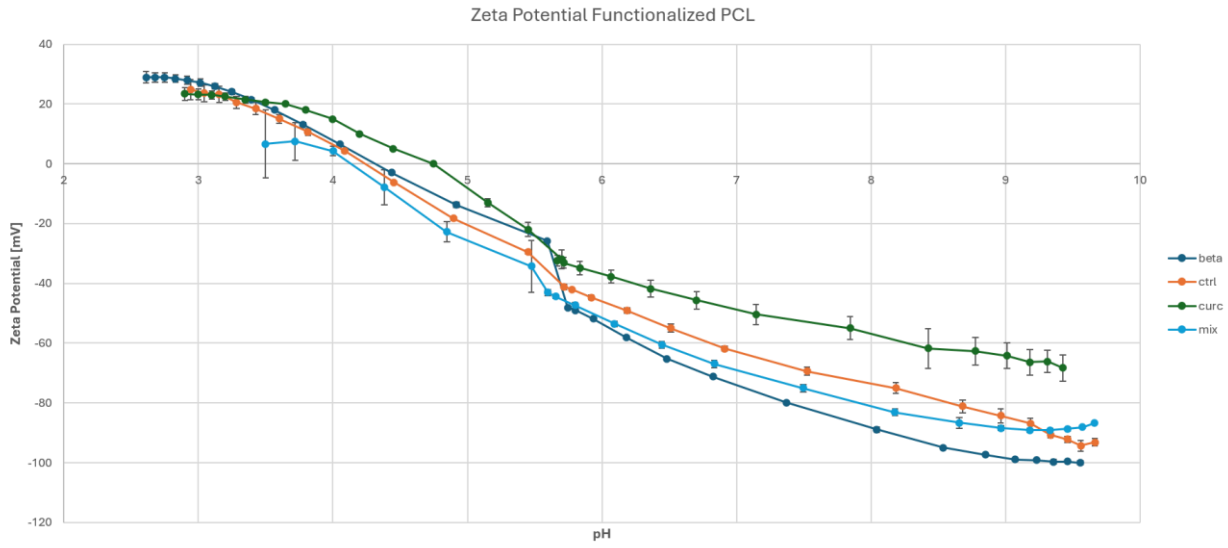


Figure 48 – Surface zeta potential as a function of pH for the Control, β-Carotene, Curcumin and Mix bilayer scaffolds, measured by streaming potential

5.4.3 DLS Particle Size

The hydrodynamic diameter and polydispersity of the species released in the ethanol eluate were measured by DLS, in triplicate, for the Control, β-Carotene and Mix groups (*Table 5.7*). No distinct, measurable particle population was resolved for the Curcumin group.

Group	Hydrodynamic diameter [nm]	Polydispersity [%]
Control	978.89 ± 275.27	21.95 ± 6.61
β-Carotene	158.03 ± 1.04	15.83 ± 5.49
Mix	176.75 ± 1.61	11.86 ± 1.78

Table 5.7 – Hydrodynamic diameter and polydispersity of the species released in the ethanol eluate, measured by DLS

The Control group showed the largest mean hydrodynamic diameter among the three groups (978.89 ± 275.27 nm), together with the highest polydispersity value (21.95 ± 6.61%), indicative of a comparatively broad size distribution (*Figure 49*). The β-Carotene group showed a substantially smaller mean diameter (158.03 ± 1.04 nm) and a low polydispersity (15.83 ± 5.49%), consistent with a narrow, apparently unimodal size distribution (*Figure 50*). The Mix group showed a mean diameter (176.75 ± 1.61 nm) close to that of the β-Carotene group, with the lowest polydispersity value among the three groups (11.86 ± 1.78%); for this group, the full size-distribution profile could not be retrieved due to a data-export issue at the time of acquisition.

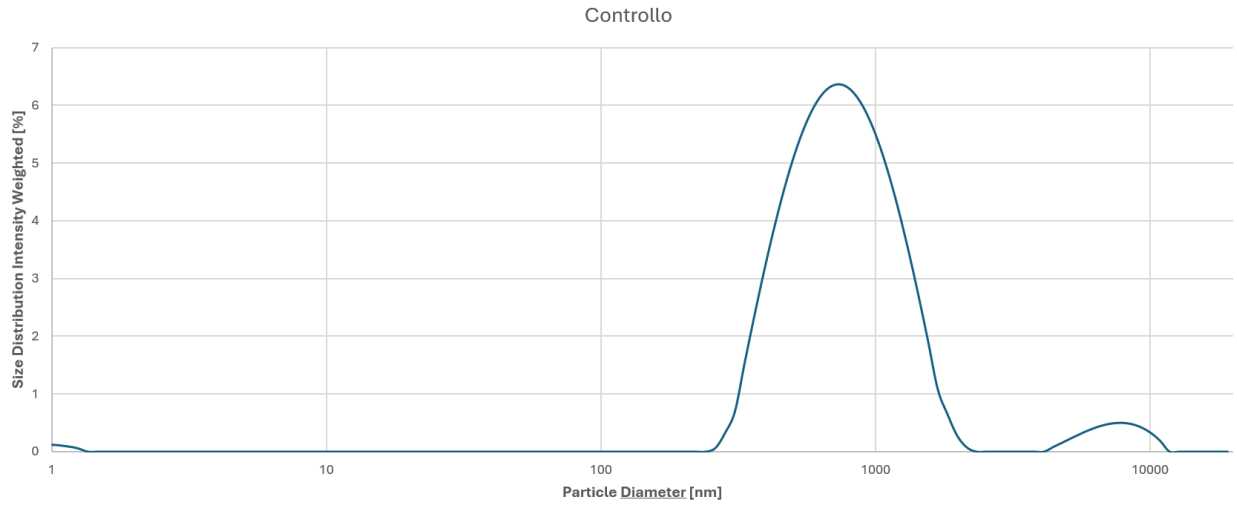


Figure 49 – Hydrodynamic distribution of the species released in the ethanol eluate for the Control group, measured by DLS

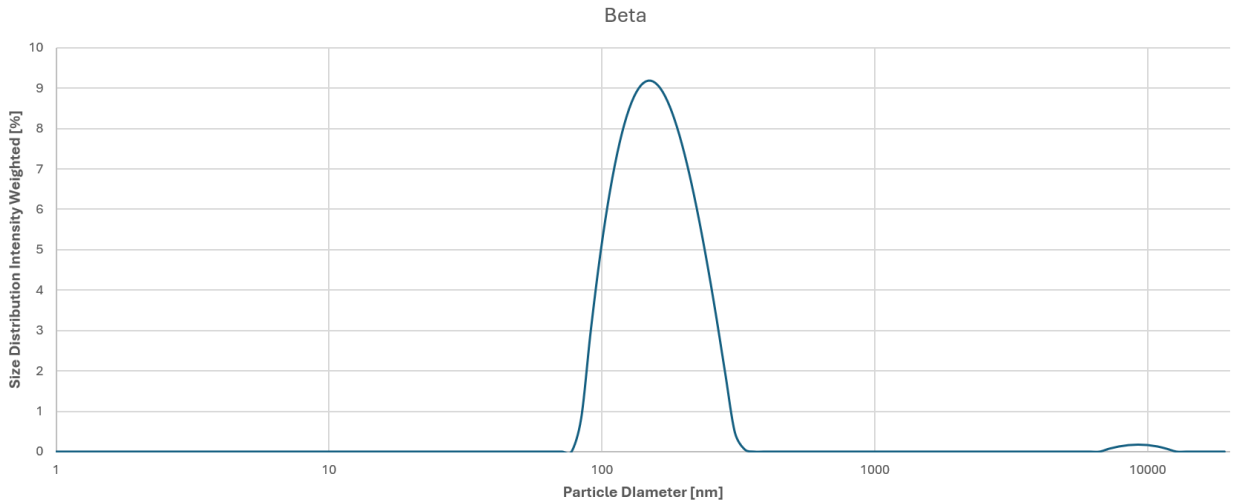


Figure 50 – Hydrodynamic distribution of the species released in the ethanol eluate for the β-Carotene group, measured by DLS

5.4.4 Water Contact Angle (WCA)

All four groups showed a contact angle above 90° (*Table 5.8*), consistent with a hydrophobic surface. The Curcumin group showed the lowest contact angle among the four groups, while the β-Carotene group showed the highest (*Figure 51*).

Group	**Contact angle [°]**
Control	117.0 ± 7.0
β-Carotene	135.9 ± 3.0
Curcumin	97.9 ± 5.0
Mix	124.9 ± 4.0

Table 5.8 – Water contact angle (°) of the functionalized layer of the Control, β-Carotene, Curcumin and Mix bilayer scaffolds (mean ± standard deviation, n = 5)

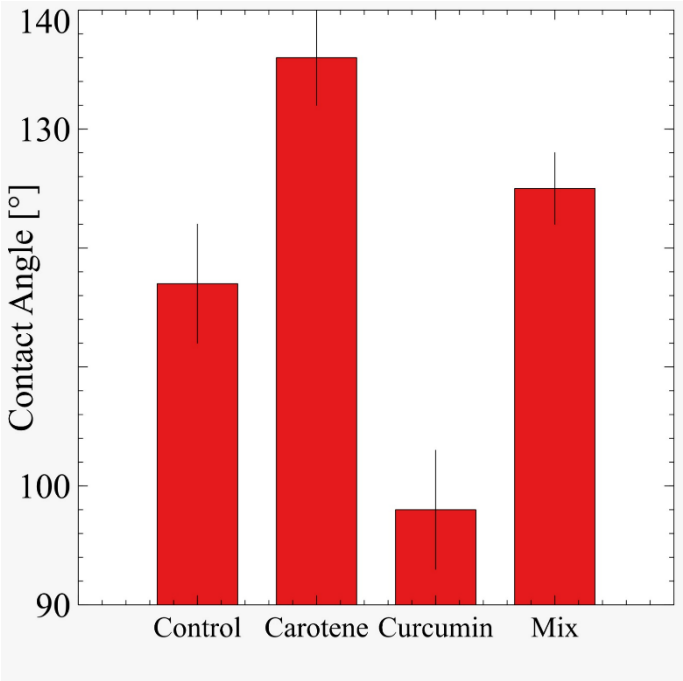


Figure 51 – Water contact angle (°) of the Control, β-Carotene, Curcumin and Mix bilayer scaffolds (mean ± standard deviation)

5.5 Mechanical Characterization (Tensile Test)

Uniaxial tensile tests were performed on rectangular specimens (20 x 5 mm) of the Control, Curcumin, β-Carotene and Mix bilayer scaffolds, following the protocol described in *Chapter 4.10*. For the Control group, one specimen (Sample 1) was excluded from the dataset due to a preparation-related issue that produced out-of-scale values; the reported Control values are therefore based on n = 5, while all other groups are based on n = 6.

Representative stress-strain curves for the four groups are shown in *Figure 52 to 55*. The Control group (*Figure 52*) showed a moderate variability in the plastic elongation region prior to failure. The β-Carotene group (*Figure 53*) showed curves terminating at markedly lower strain values and lower stress levels than the other three groups. The Curcumin group (*Figure 54*) reached comparatively higher stress values before failure while retaining substantial elongation. The Mix group (*Figure 55*) showed curves falling between those of the Curcumin and β-Carotene groups.

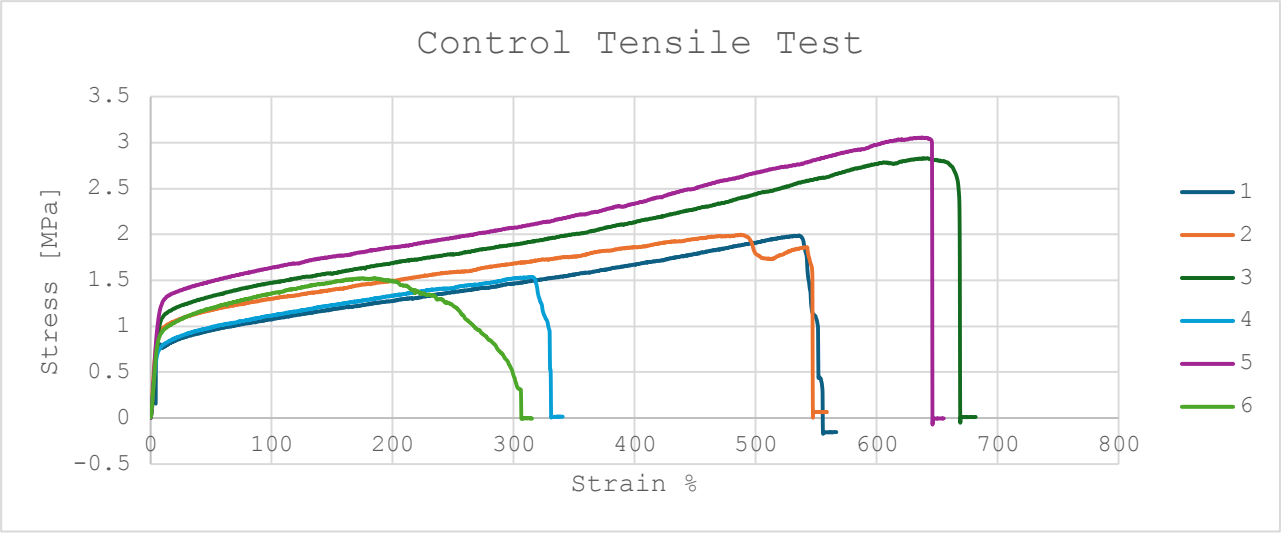


Figure 52 – Representative stress-strain curves of the Control bilayer scaffold obtained by uniaxial tensile testing

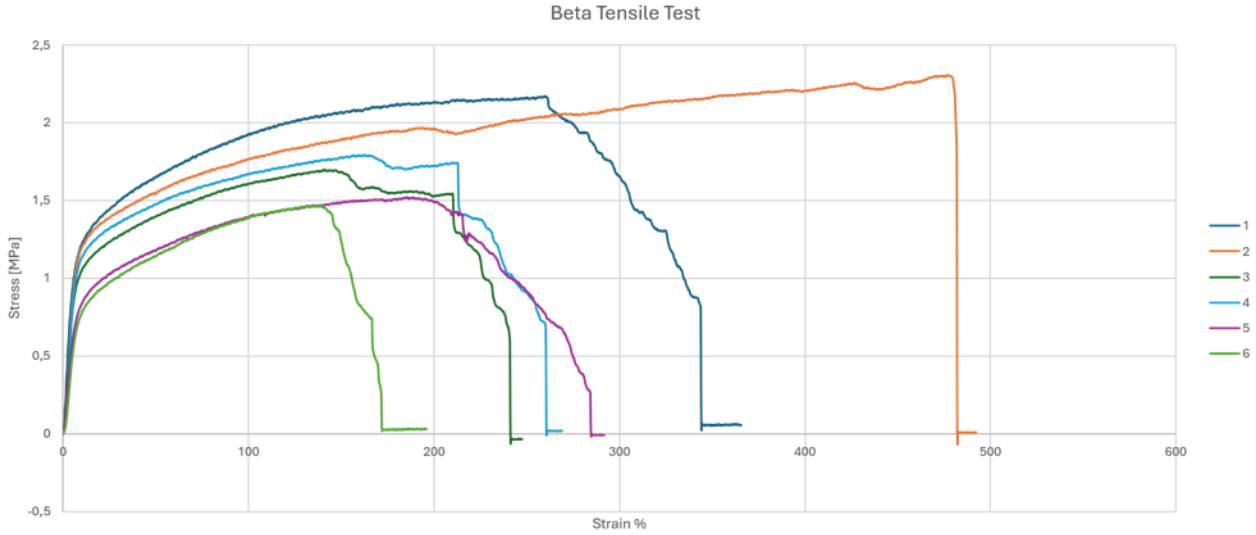


Figure 53 – Representative stress-strain curves of the β-Carotene bilayer scaffold obtained by uniaxial tensile testing

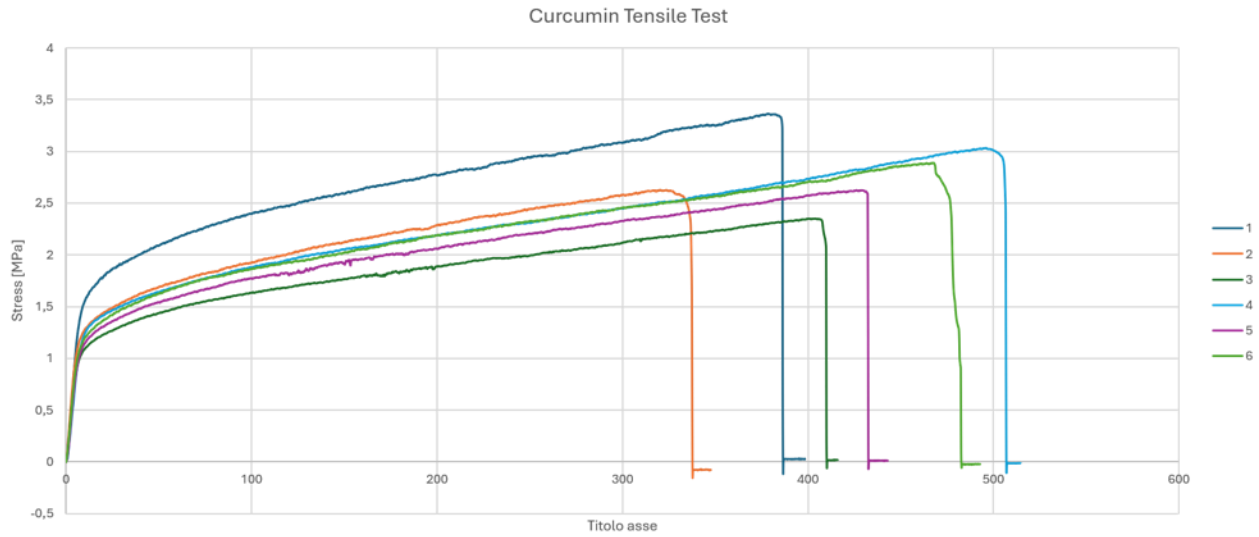


Figure 54 – Representative stress-strain curves of the Curcumin bilayer scaffold obtained by uniaxial tensile testing

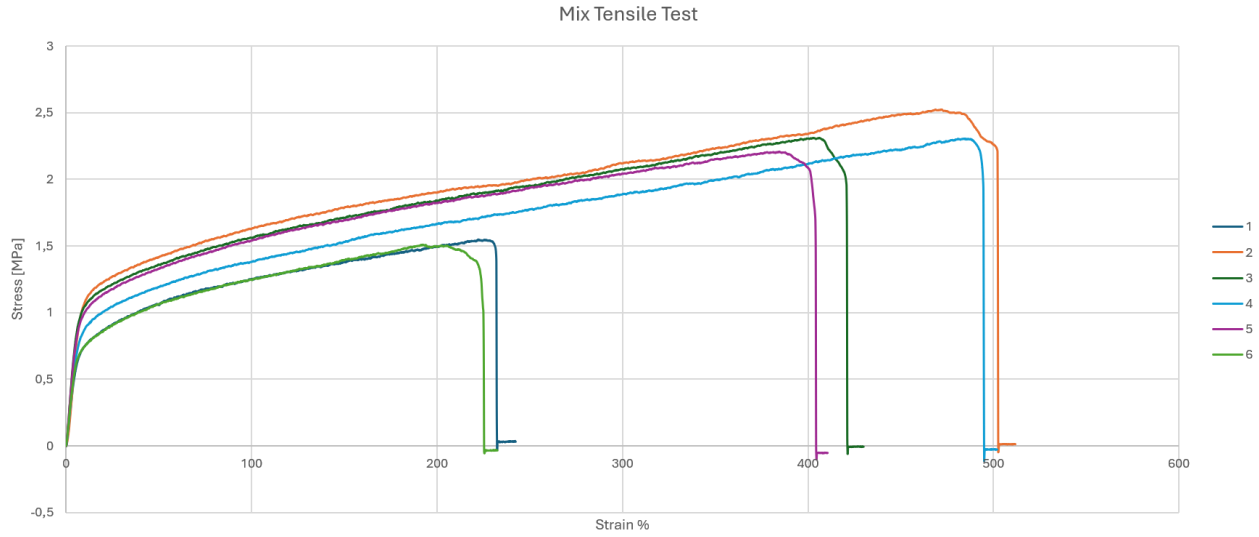


Figure 55 – Representative stress-strain curves of the Mix bilayer scaffold obtained by uniaxial tensile testing

5.5.1 Young's Modulus

The mean Young's modulus (*Table 5.9*) was highest for the Curcumin group (20.75 ± 2.90 MPa), followed by the Control (18.95 ± 2.59 MPa) and β-Carotene (18.53 ± 4.18 MPa) groups, which showed comparable mean values. The Mix group showed the lowest mean Young's modulus among the four groups (15.82 ± 2.02 MPa) (*Figure 56*).

Group	1	2	3	4	5	6	Mean	Std Dev
Control	-	25.55	19.12	15.05	21.85	18.16	18.95	2.59
Curcumin	25.40	22.85	19.24	17.36	19.27	20.37	20.75	2.90
β-Carotene	23.73	20.90	18.95	20.55	13.83	13.21	18.53	4.18
Mix	13.50	17.15	18.62	14.49	16.91	14.26	15.82	2.02

Table 5.9 – Young's modulus (MPa) of individual specimens and group mean ± standard deviation, for the Control (n = 5), Curcumin, β-Carotene and Mix (n = 6) groups

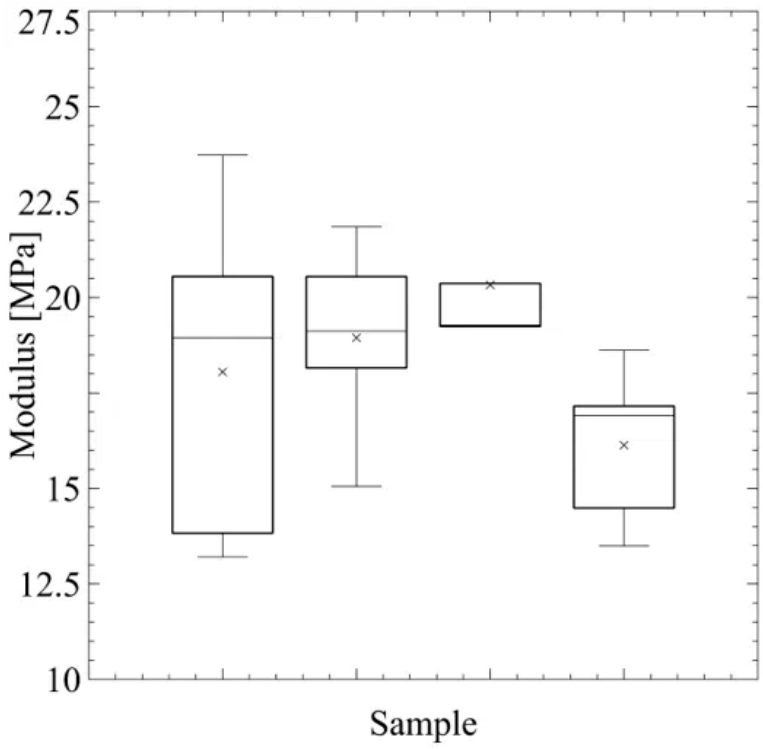


Figure 56 – Young's modulus of the bilayer scaffolds (mean ± standard deviation), shown left to right for β-Carotene, Control, Curcumin and Mix

5.5.2 Elongation at Break

The Control and Curcumin groups showed the highest mean elongation at break (*Table 5.10*) (451.2 ± 203.9 % and 416.0 ± 62.2 % respectively). The β-Carotene group showed the lowest mean elongation at break (227.3 ± 130.3 %), approximately half that of the Control and Curcumin groups. The Mix group showed an intermediate mean value (360.3 ± 124.7 %) (*Figure 57*).

Group	1	2	3	4	5	6	Mean	Std Dev
Control	-	487.8	639.2	315.8	638.4	175.0	451.2	203.9
Curcumin	378.8	323.8	400.8	496.0	429.0	467.6	416.0	62.2
β-Carotene	260.0	477.2	140.8	161.8	185.4	138.8	227.3	130.3
Mix	222.2	472.0	406.2	484.2	384.6	192.4	360.3	124.7

Table 5.10 – Elongation at break (%) of individual specimens and group mean ± standard deviation, for the Control (n = 5), Curcumin, β-Carotene and Mix (n = 6) groups

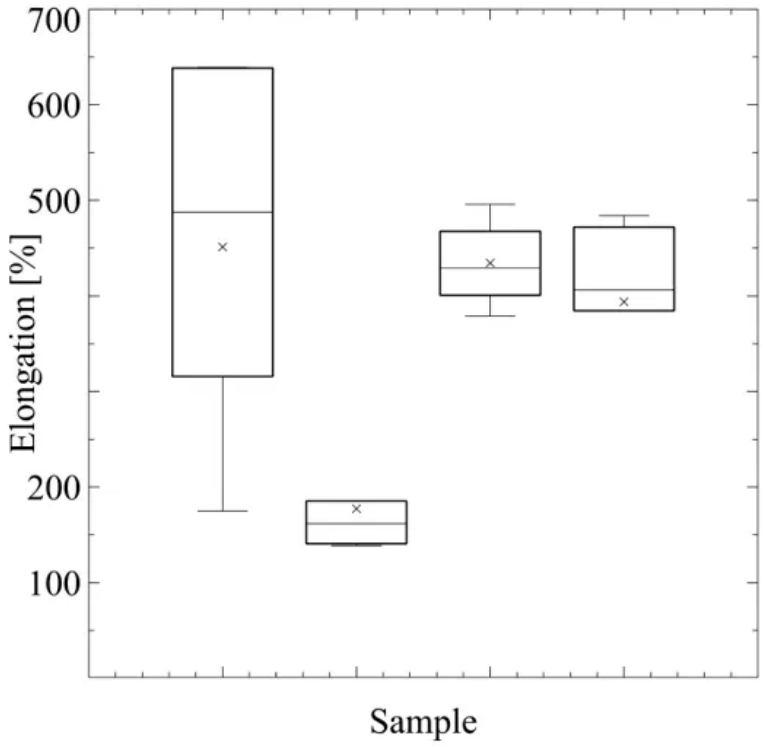


Figure 57 – Elongation at break of the bilayer scaffolds (mean ± standard deviation), shown left to right for Control, β-Carotene, Curcumin and Mix

5.5.3 Maximum Stress (Ultimate Tensile Strength)

The Curcumin group (*Table 5.11*) showed the highest mean maximum stress (2.81 ± 0.36 MPa), above the Control group value (2.19 ± 0.72 MPa). The β-Carotene group showed the lowest mean maximum stress (1.83 ± 0.34 MPa). The Mix group showed an intermediate mean value (2.07 ± 0.43 MPa) (*Figure 58).*

Group	1	2	3	4	5	6	Mean	Std Dev
Control	-	2.00	2.83	1.54	3.06	1.52	2.19	0.72
Curcumin	3.36	2.63	2.35	3.03	2.62	2.89	2.81	0.36
β-Carotene	2.17	2.31	1.70	1.79	1.52	1.47	1.83	0.34
Mix	1.55	2.52	2.31	2.30	2.21	1.51	2.07	0.43

Table 5.11 – Maximum stress (MPa) of individual specimens and group mean ± standard deviation, for the Control (n = 5), Curcumin, β-Carotene and Mix (n = 6) groups

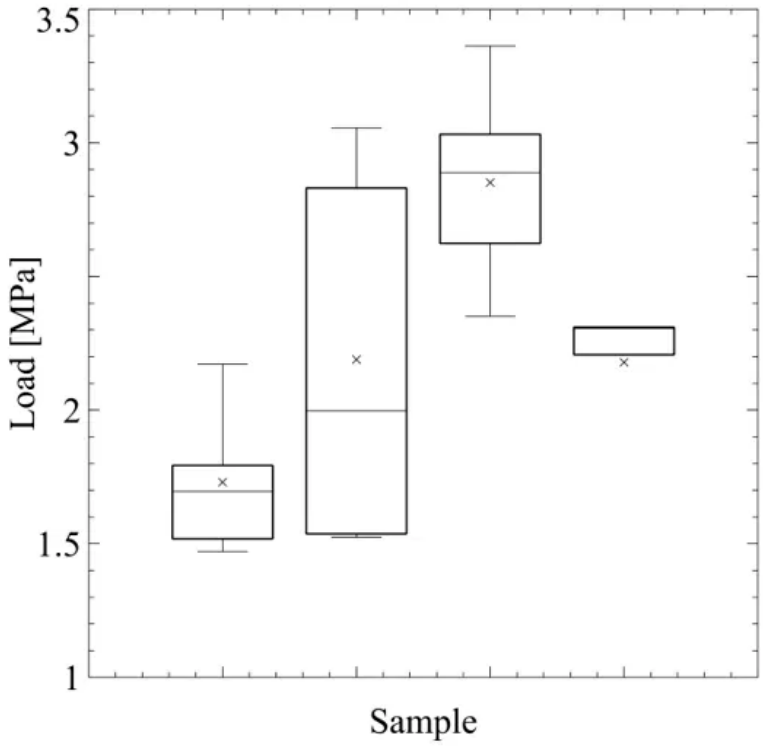


Figure 58 – Maximum stress of the bilayer scaffolds (mean ± standard deviation), shown left to right for β-Carotene, Control, Curcumin and Mix

5.6 In Vitro Biological Assay

Human dermal fibroblast viability and proliferation were evaluated after 24 hours of exposure to scaffold-conditioned eluates collected at 24 hours, 72 hours and 7 days, following the indirect cytotoxicity protocol described in *Chapter 4.11*. For each condition and time point, three wells were prepared, with three fluorescence images acquired per well; reported values represent the mean of the three well-level means. For the Control group at 7 days, one well was excluded from the analysis due to accidental contamination (*Chapter 4.11.8*), and reported value is based on the remaining two wells (n = 2).

Fluorescence microscopy imaging of Hoechst 33342-stained nuclei showed a dense and evenly distributed cell population across the imaged area for all experimental conditions (*Figure 59*).

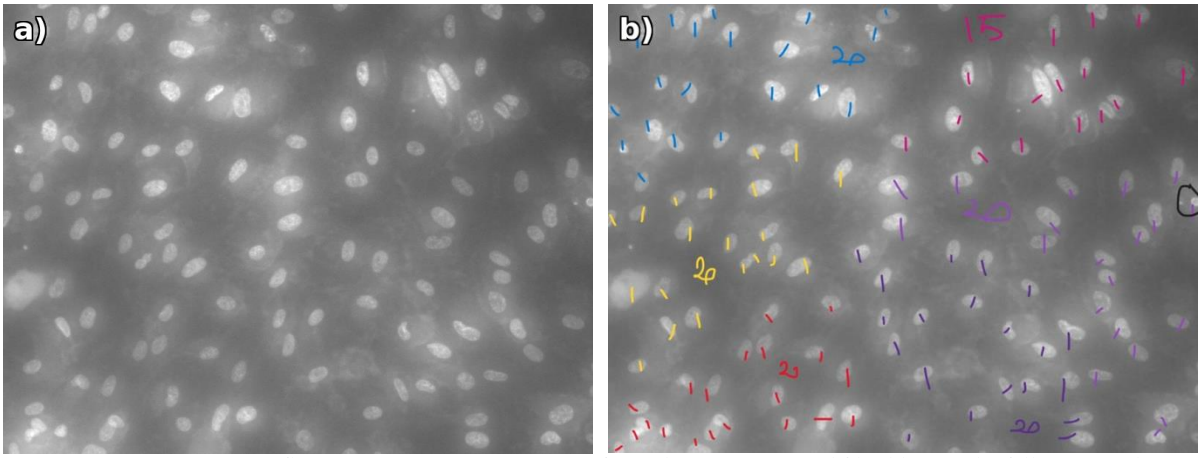


Figure 59 – Representative fluorescence microscopy image of Hoechst 33342-stained fibroblast nuclei following 24-hour exposure to a scaffold-conditioned eluate (a), and corresponding manual cell-counting methodology (b, viable cells in colour groups of 20; non-viable cell circled in black)

5.6.1 Cell Viability

Cell viability, expressed as the percentage of viable cells relative to the total cell count, was determined for the Control, β-Carotene, Curcumin and Mix groups at each of the three eluate collection time points (*Table 5.12, Figures 60-61*).

Group	1 day	3 days	7 days
Control	97.84	97.09	95.69[a]
β-Carotene	96.98	96.75	98.07
Curcumin	98.09	98.99	97.93
Mix	97.93	97.75	96.94

Table 5.12 – Cell viability (%) of human dermal fibroblasts exposed to scaffold-conditioned eluates for 24 hours, at each eluate time point

[a] *n=2 wells (one well excluded due to accidental contamination, Chapter 4.11.8)*

Across all groups and time points, cell viability ranged from 95.69% to 98.99%. Statistical comparison between all pairs of groups at each individual time point showed no significant differences (ns) in cell viability (*Figure 61*).

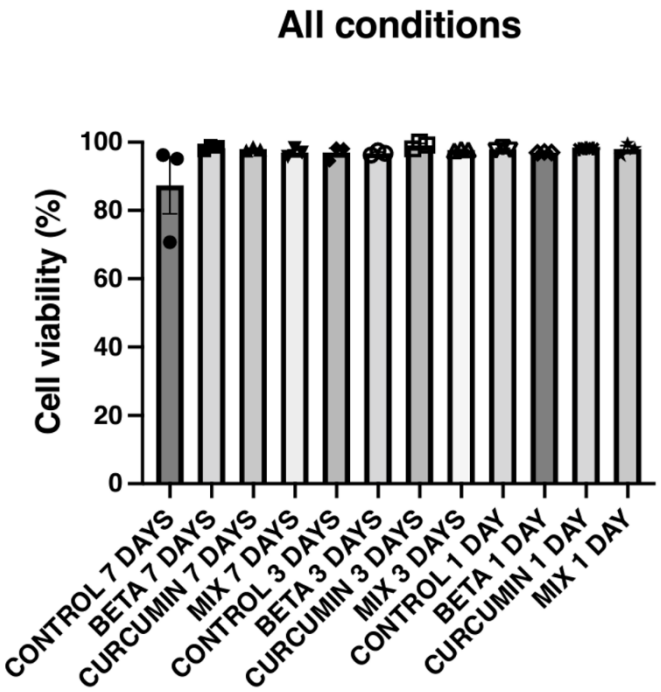
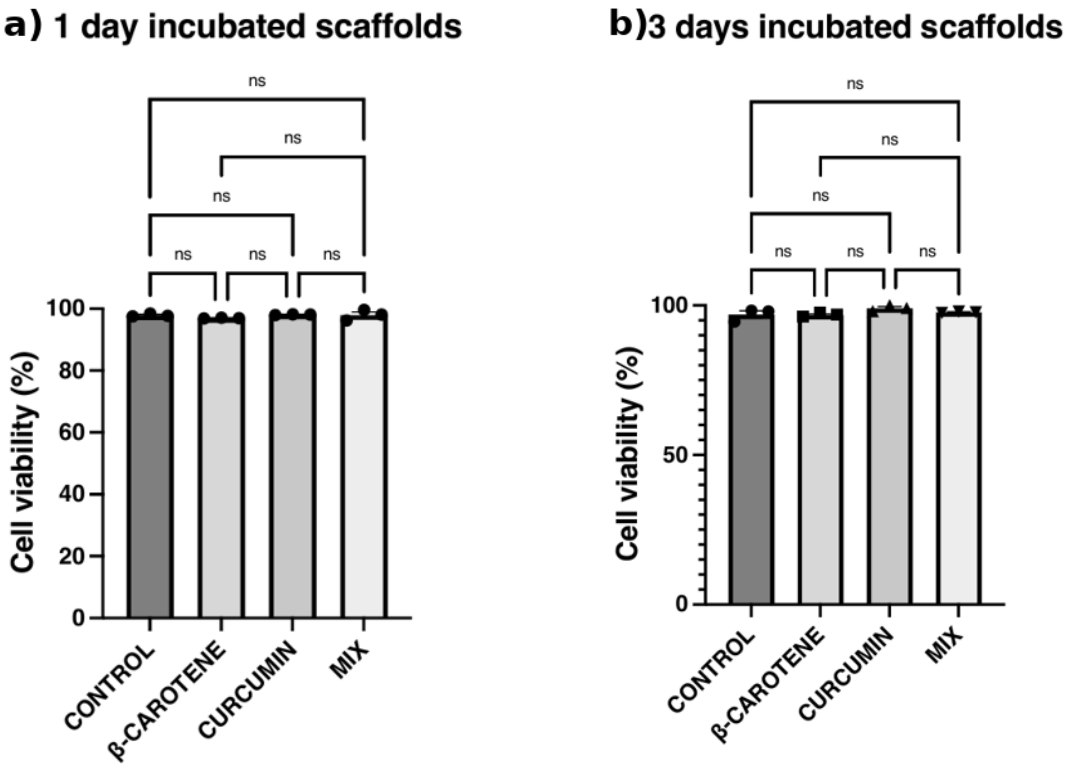


Figure 60 – Cell viability (%) of human dermal fibroblasts across all experimental conditions and eluate collection time points (1, 3 and 7 days)



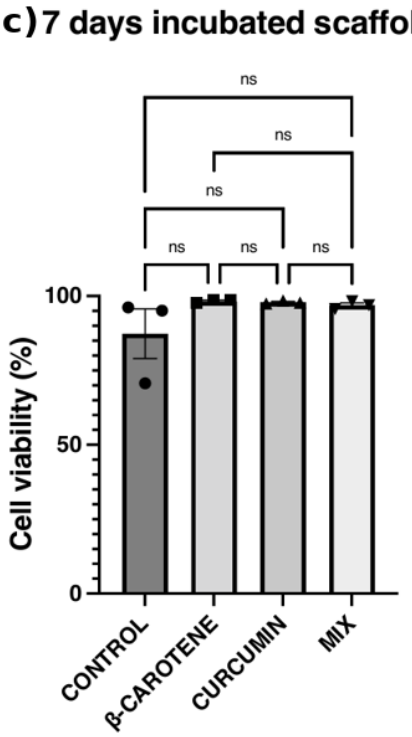


Figure 61 – Cell viability (%) of human dermal fibroblasts exposed to Control, β-Carotene, Curcumin and Mix eluates, shown separately for 1 (a), 3 (b) and 7 (c) days of eluate collection (ns = not significant)

5.6.2 Cell Proliferation (Total Cell Count)

The total number of cells per field (normalized to an area of 1.4 x 10^5 μm^2) was determined for the same four groups and time points (*Table 5.13, Figure 62-63*).

Group	1 day	3 days	7 days
Control	82.33	87.67	60.83[a]
β-Carotene	84.67	78.56	86.56
Curcumin	87.22	77.33	91.22
Mix	96.56	83.89	83.44

Table 5.13 – Total cell count (mean number of cells per image, area 1.4 x 10^5 μm^2) of human dermal fibroblasts exposed to scaffold-conditioned eluates for 24 hours, at each eluate collection point

[a] *n = 2 wells (one well excluded due to accidental contamination, Chapter 4.11.8)*

At 7 days, the Control group showed the lowest total cell count among all conditions (60.83), while the β-Carotene, Curcumin and Mix groups showed comparatively higher counts (83.44 – 91.22). Statistical comparison between all pairs of groups at each individual time point showed no significant differences (ns) in total cell count (*Figure 63*).

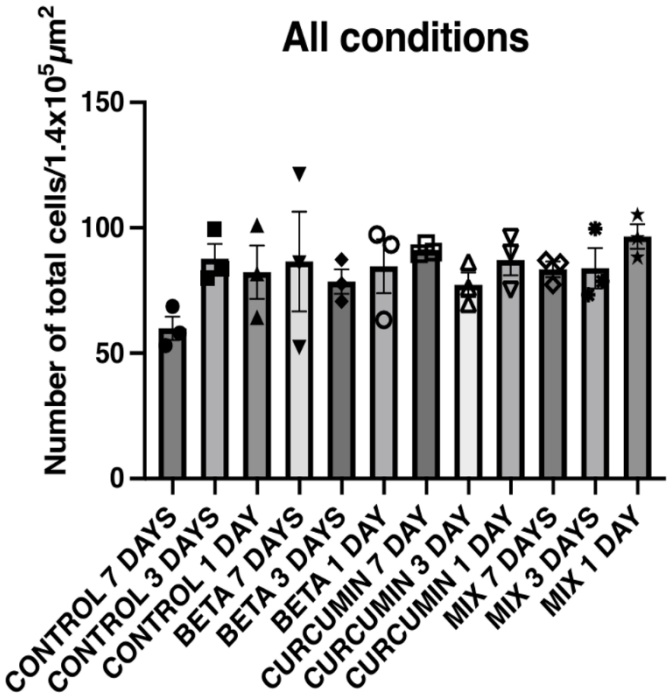
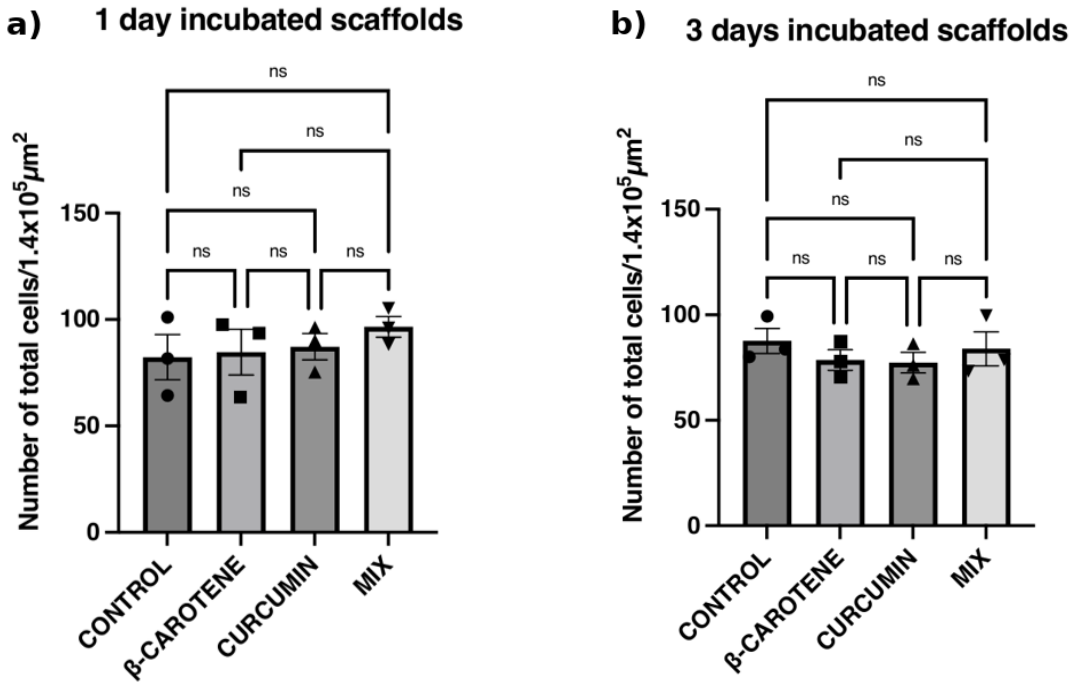


Figure 62 – Total cell count (cells per 1.4 × 10⁵ µm²) across all experimental conditions and eluate collections time points (1, 3 and 7 days)



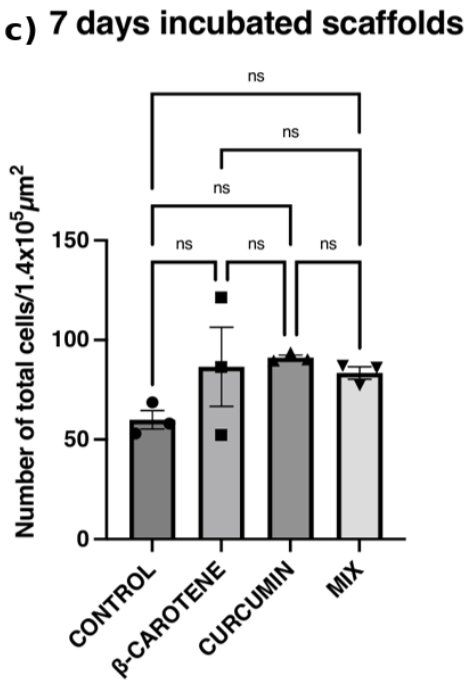


Figure 63 – Total cell count (cells per 1.4 × 10⁵ µm²) of human dermal fibroblasts exposed to Control, β-Carotene, Curcumin and Mix eluates, shown separately for 1 (a), 3 (b) and 7 (c) days of eluate collection (ns = not significant)

5.7 Drug Release Kinetics (UV-Vis)

Cumulative release of curcumin and β-carotene into the PBS + 0.1% SDS medium was monitored by UV-Vis spectrophotometry at the characteristic absorption wavelength of 420 nm, following the protocol described in *Chapter 4.12*, at three pH values (5.5, 7.4 and 9.0) and three time points (24 hours, 72 hours and 7 days). The unloaded PCL control was used as the background reference at pH 5.5, as described in *Chapter 4.12.4*; consequently, no separate release data are reported for the Control group at this pH.

5.7.1 β-Carotene Release

Across all three pH conditions, the absorbance signal of the β-Carotene group increased progressively from 24 hours to 7 days (*Table 5.14, Figure 64*).

pH	24 h	72 h	7 days
5.5	0.028	0.043	0.066
7.4	0.047	0.060	0.066
9.0	0.026	0.059	0.085

Table 5.14 – Absorbance at 420 nm of the release medium for the β-Carotene group, at each pH and time point

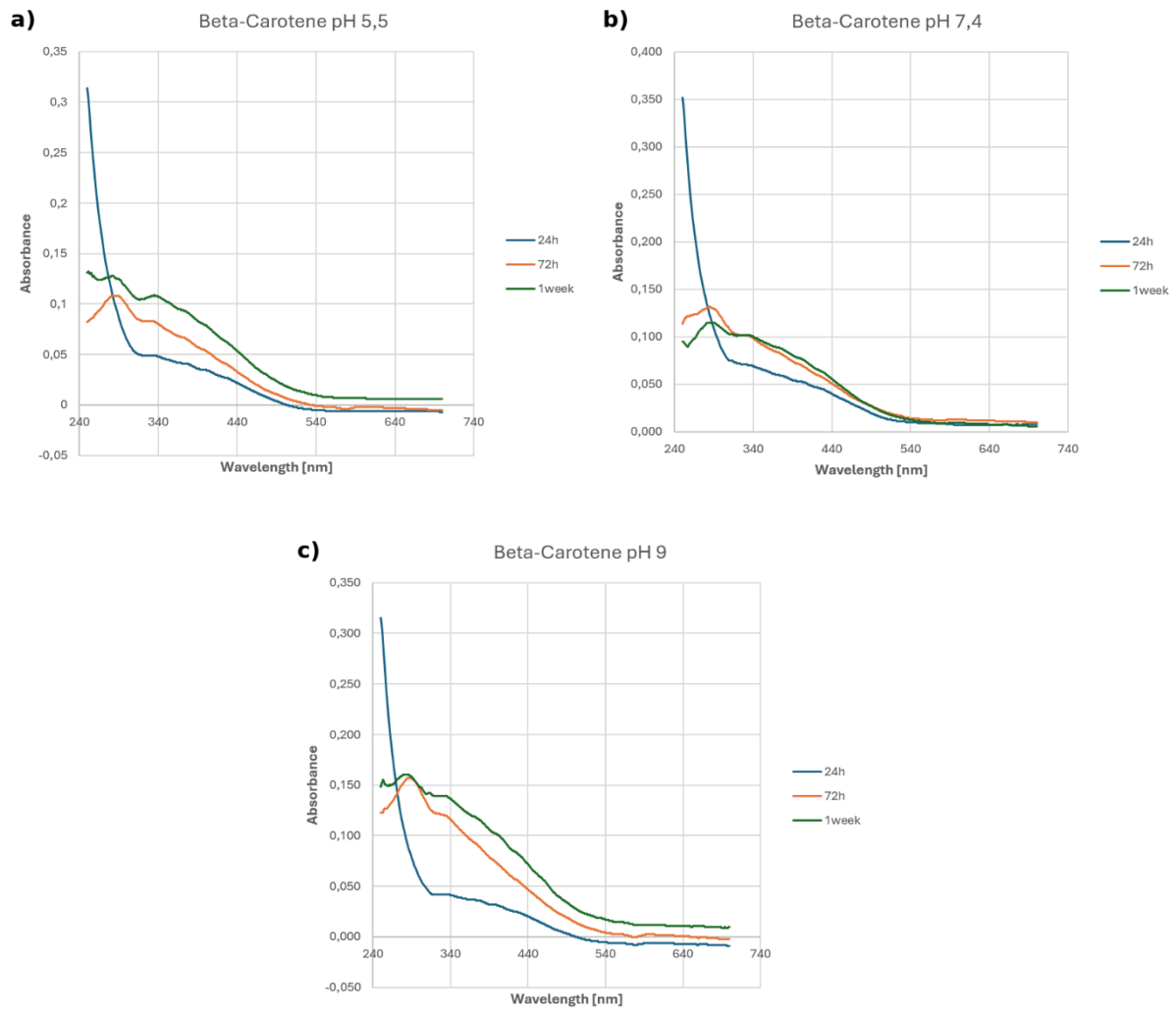


Figure 64 – UV-Vis absorbance spectra (250 – 700 nm) of the release medium for the β-Carotene group at pH 5.5, 7.4 and 9.0, after 24 hours, 72 hours and 7 days.

5.7.2 Curcumin Release

The absorbance values recorded for the Curcumin group were markedly higher, by approximately one order of magnitude, than those of the β-Carotene group across all pH conditions and time points. At pH 5.5, absorbance increased from 24 hours to 7 days. At pH 7.4, absorbance peaked at 72 hours (1.130) before decreasing at 7 days (0.839). at pH 9.0 absorbance was highest at 72 hours (0.403) and lowest at 7 days (0.182), with overall values markedly lower than those recorded at pH 5.5 and 7.4 (*Table 5.15, Figure 65*).

pH	24 h	72 h	7 days
5.5	0.849	0.758	1.054
7.4	0.875	1.130	0.839
9.0	0.295	0.403	0.182

Table 5.15 – Absorbance at 420 nm of the release medium for the Curcumin group, at each pH and time point

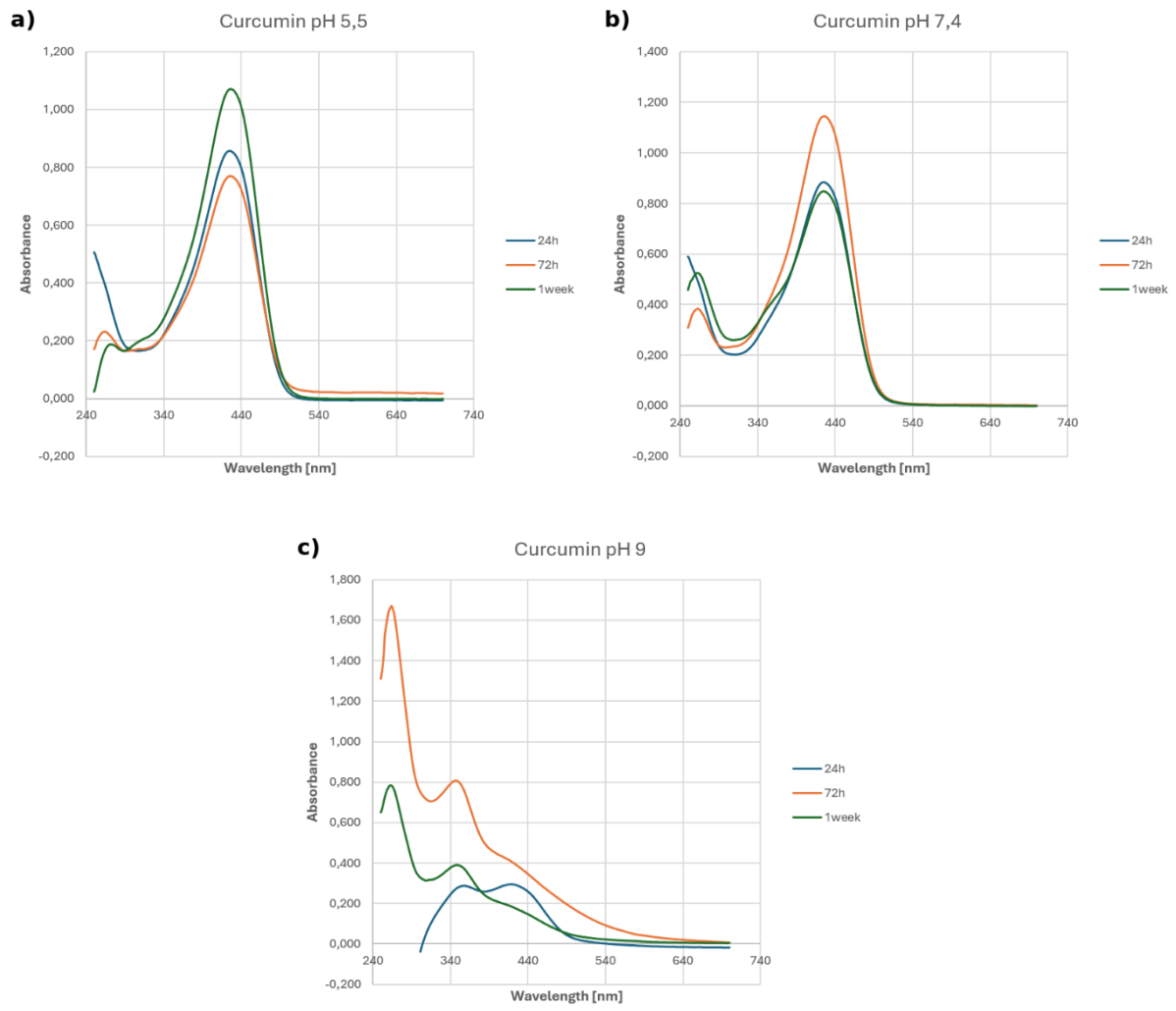


Figure 65 – UV-Vis absorbance spectra (250 – 700 nm) of the release medium for the Curcumin group at pH 5.5, 7.4 and 9.0, after 24 hours, 72 hours and 7 days

5.7.3 Mix Release

For the Mix group, absorbance values at pH 5.5 were higher than those recorded at pH 7.4 and 9.0 across all time points. At pH 5.5, absorbance peaked at 72 hours (0.666). At pH 9.0, the lowest overall absorbance values among the three pH conditions were recorded, with a peak at 72 hours (0.246) followed by a decrease at 7 days (0.082) (*Table 5.16, Figure 66*).

pH	24 h	72 h	7 days
5.5	0.584	0.666	0.420
7.4	0.382	0.244	0.294
9.0	0.162	0.246	0.082

Table 5.16 – Absorbance at 420 nm of the release medium for the Mix group, at each pH and time point

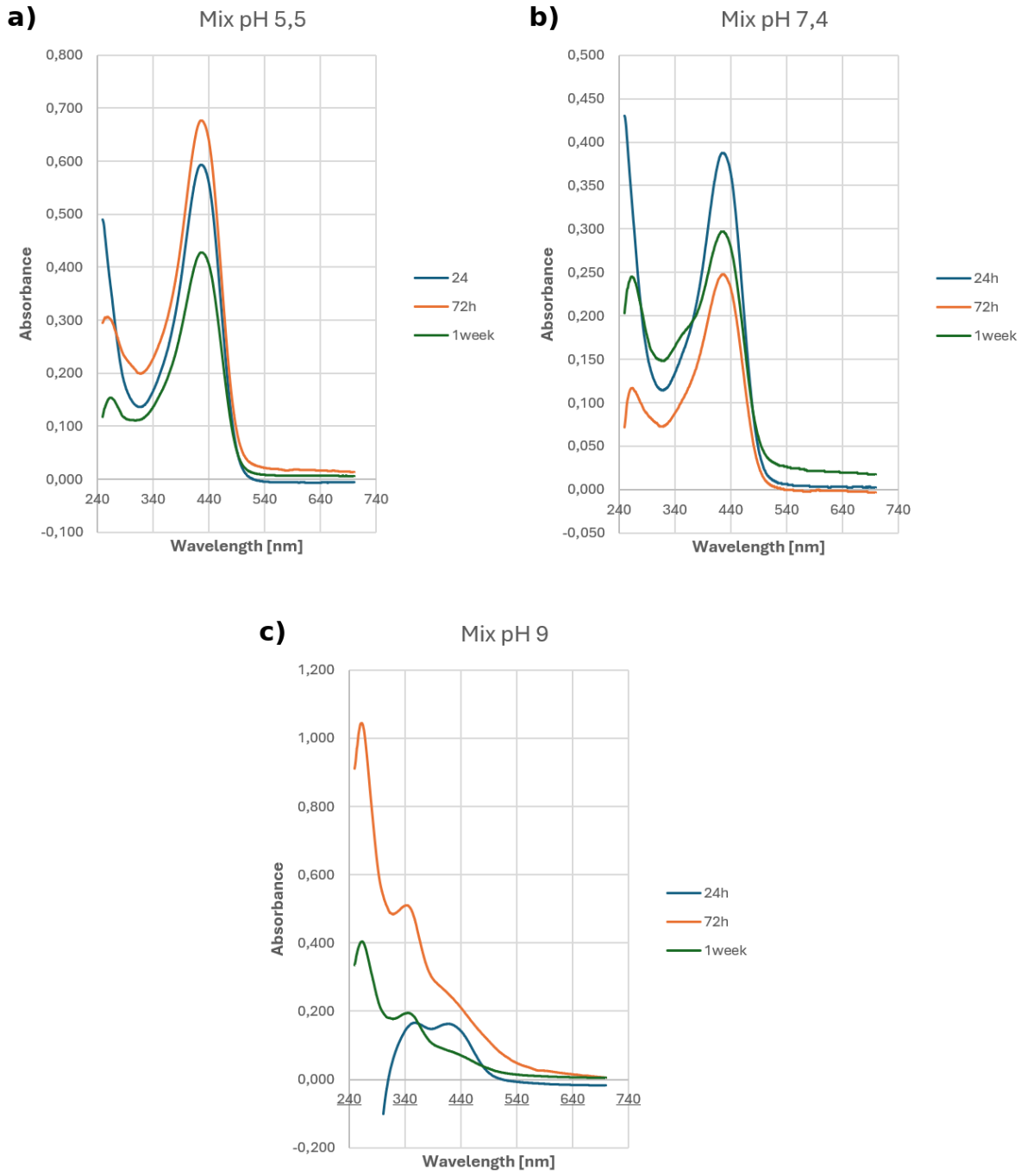


Figure 66 – UV-Vis absorbance spectra (250 – 700 nm) of the release medium for the Mix group at pH 5.5, 7.4 and 9.0, after 24 hours, 72 hours and 7 days

5.7.4 PCL Control Background

Absorbance values for the Control group remained below 0.03 across both pH conditions and all time points, approximately one to two orders of magnitude lower than those recorded for the functionalized groups (*Table 5.17, Figure 67*).

pH	24 h	72 h	7 days
7.4	0.004	0.023	0.010
9.0	0.000	0.007	0.019

Table 5.17 – Absorbance at 420 nm of the release medium for the unloaded PCL Control group, at pH 7.4 and 9.0

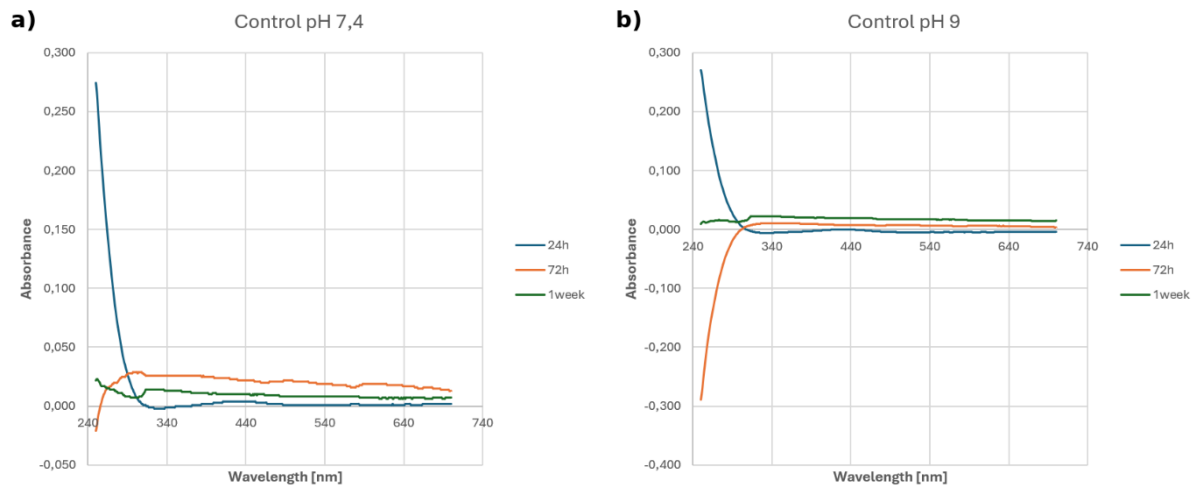


Figure 67 – UV-Vis absorbance spectra (250–700 nm) of the release medium for the unloaded PCL Control group at pH 7.4 and 9.0, after 24 hours, 72 hours and 7 days.

5.7.5 Estimated Released Concentration and Calibration-Related Limitations

To convert the absorbance values reported in *Chapters 5.7.1 – 5.7.3* into an estimate of released concentration, calibration curves were constructed for curcumin and β-carotene at each pH value, using the absorbance at 420 nm of three known concentrations spanning the expected release range (*Chapter 4.12.4*). A linear regression was fitted to each calibration set; the resulting curves showed good linearity for β-carotene at all three pH values (R^2 = 0.96 – 0.99) and for curcumin at pH 5.5 and 7.4 (R^2 = 0.99 and 0.99, respectively), but markedly poorer linearity for curcumin at pH 9.0 (R^2 = 0.83). The corresponding calibration spectra and fitted regression lines are shown in *Figure 68* (β-carotene) and *Figure 69* (curcumin).

Table 5.18, Table 5.19 and *Table 5.20* report the estimated released concentration for the β-Carotene, Curcumin and Mix groups, respectively, obtained by interpolating the absorbance values in *Chapter 5.7.1 – 5.7.3* against the corresponding calibration curve. For the Curcumin and Mix groups at pH 9.0, this interpolation produced negative or otherwise physically inconsistent concentration values and is therefore not reported; only the raw absorbance values given in *Table 5.15* and *5.16* apply to this condition.

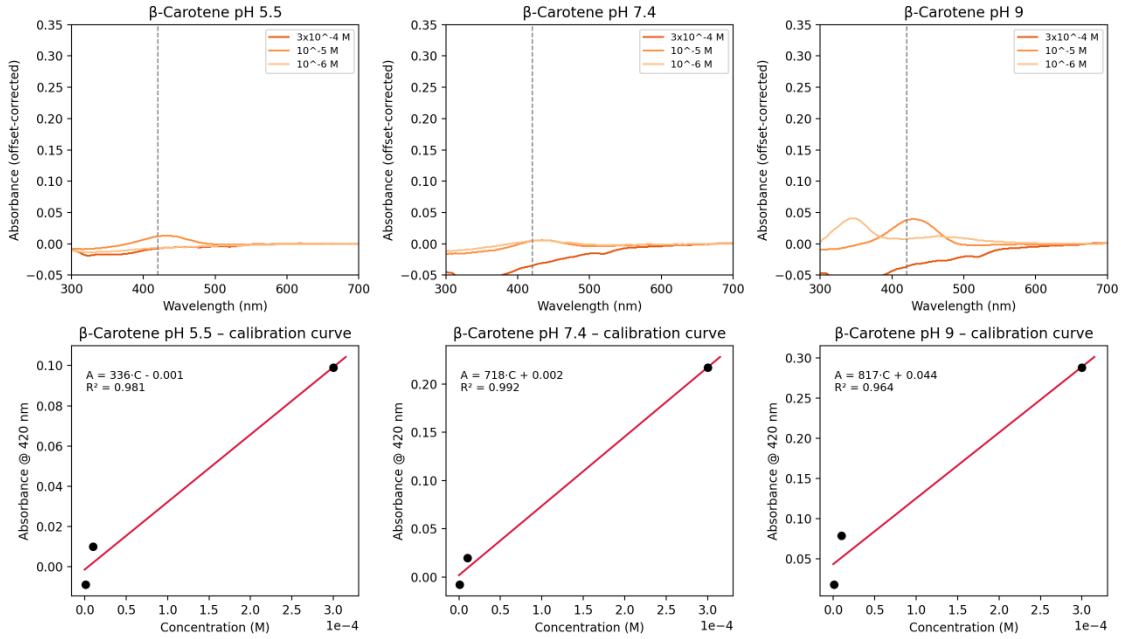


Figure 68 – Calibration spectra (top row) and resulting linear calibration curves (bottom row) for β-carotene at pH 5.5, 7.4 and 9.0. Spectra were offset-corrected by subtracting the mean absorbance in the 650-700 nm region for display purposes; reported absorbance values at 420 nm (Chapter 5.7) and the calibration fits are based on the original, uncorrected data

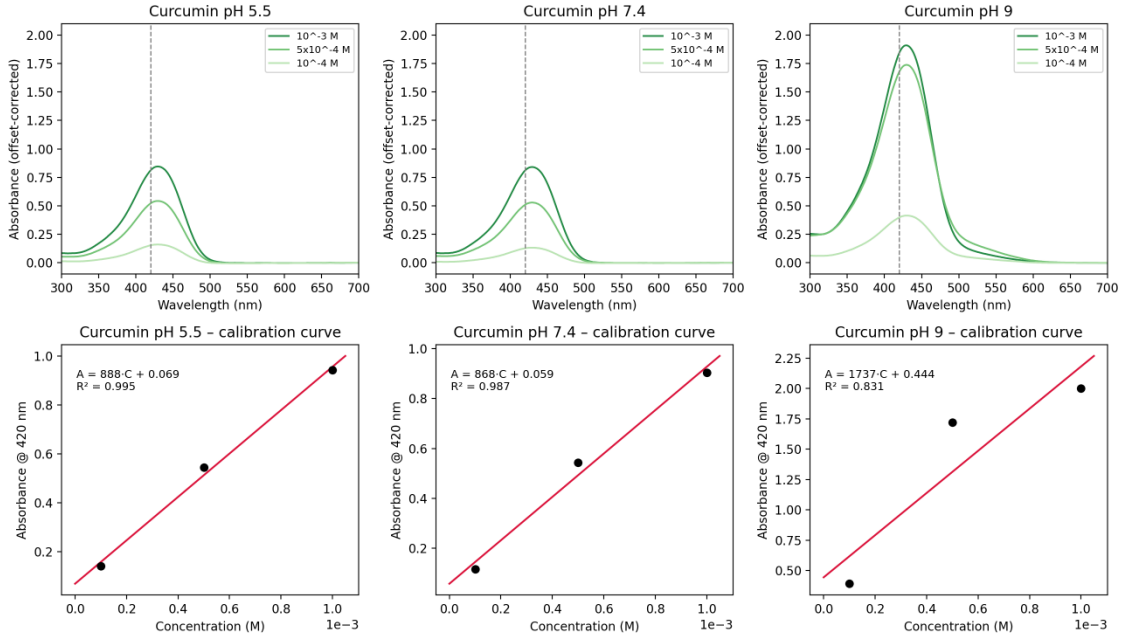


Figure 69 – Calibration spectra (top row) and resulting linear calibration curves (bottom row) for curcumin at pH 5.5, 7.4 and 9.0. Spectra were offset-corrected by subtracting the mean absorbance in the 650-700 nm region for display purposes; reported absorbance values at 420 nm (Chapter 5.7) and the calibration fits are based on the original, uncorrected data

pH	24 h	72 h	7 days
5.5	87.8	132.0	200.7
7.4	62.8	80.9	89.3
9.0	~0[a]	18.8	50.7

Table 5.18 – Estimated β-carotene released concentration (μM) at each pH and time point, obtained from the corresponding calibration curve

pH	24 h	72 h	7 days
5.5	879	776	1108
7.4	940	1228	899

Table 5.19 – Estimated curcumin released concentration (μM) at pH 5.5 and 7.4, obtained from the corresponding calibration curve. No value is reported at pH 9.0

pH	24 h	72 h	7 days
5.5	580	673	396
7.4	372	213	271

Table 5.20 - Estimated mix released concentration (μM, curcumin channel) at pH 5.5 and 7.4, obtained from the corresponding calibration curve. No value is reported at pH 9.0

[a] *Value obtained by interpolation fell marginally below zero and is reported as approximately zero, within the noise level of the calibration*

The reduced reliability of the curcumin calibration at pH 9.0 is attributed primarily to the chemical instability of curcumin itself in alkaline medium. Curcumin is reported in the literature to undergo rapid degradation under alkaline conditions (*Chapter 3.1*), a process associated with a change in its absorption spectrum [24]. Consistent with this, a visible colour change was observed even during the brief preparation time of the pH 9.0 calibration standards, indicating that degradation begins essentially as soon as curcumin is dissolved at this pH rather than only becoming relevant over longer timescales. Since the extent of this rapid, pre-measurement degradation may not be strictly proportional across the three standard concentrations, the assumption of a fixed, linear absorbance-to-concentration relationship is likely violated, which plausibly explains the reduced linearity of the calibration curve at pH 9.0 ($R^2 = 0.83$).

A secondary, more limited artefact also affected the 24-hour release measurement specifically: different cuvettes were used for the Curcumin and Mix samples at this single time point compared to all other conditions, a known source of measurement artefact that may affect the absolute comparability of the 24-hour value alone. Consistent cuvettes were used for the 72-hour and 7-day measurements.

For these reasons, the absorbance values at pH 9.0 for the Curcumin and Mix groups (*Table 5.15* and *5.16*) are reported without conversion to concentration, and any comparison of these two conditions with pH 5.5 and 7.4 should be treated with caution, particularly at the 24-hour time point.

It should additionally be noted that difficulties were encountered during the preparation of the β-carotene calibration standards themselves, owing to the compound's extremely poor solubility even in the chosen solvent system. While the resulting calibration curves showed acceptable linearity (R^2 = 0.96–0.99, *Figure 68*), the possibility that the calibration standards did not

consist of fully dissolved, homogeneous solutions cannot be excluded; any residual undissolved fraction or light scattering from incompletely solubilized material would affect the assumed proportionality between absorbance and concentration underlying the Beer-Lambert-based calibration, independently of the curve-fitting statistics. This caveat should be borne in mind when interpreting the estimated β-carotene release concentrations reported in Table 5.18, which — despite the statistically acceptable calibration fits — may carry a systematic uncertainty not captured by the reported R^2 values alone.

.

6 Discussion

6.1 Process Robustness and Fibre Morphology

The morphological characterization of the electrospun bilayer scaffolds provides fundamental insights into how the physical state of the incorporated bioactive agents dictates the stability of the electrospinning process. As outlined in the methodological validation, the successful fabrication of homogeneous nanofibers relies heavily on the physicochemical properties of the polymeric solution.

The macroscopic and microscopic evaluations revealed a stark contrast between the formulations, primarily driven by the solubility of the functionalizing agents in the chosen CF/EtOH (7:3) solvent system. Curcumin demonstrated complete dissolution at the 5% wt. loading, evidenced by the absence of the Tyndall effect during solution preparation. This optimal solvation translated into a highly stable electrospinning process, yielding a visually uniform yellowish mesh. This was corroborated at the fluorescence level: the DAPI channel showed a diffuse, homogeneous signal free of isolated bright spots, while the rhodamine and green channels confirmed a regular signal distribution along the fibre network without luminescent clumps. Although laser-optical microscopy detected a wider range of mean fibre diameters (0.69 to 1.78 μm) compared to the pristine PCL control (mean ~ 0.96 μm), the overall nanofibrous architecture was preserved. FESEM analysis corroborated this structural integrity, showing only isolated thickened nodes around which adjacent fibres elongated smoothly. This morphological consistency suggests that curcumin, likely facilitated by its ability to transition into a reactive keto-enol form, integrates proficiently within the PCL matrix without drastically perturbing the electrohydrodynamic drawing forces. [8]

Conversely, the incorporation of β-carotene introduced significant process instabilities. Lacking highly polar functional groups and possessing extreme hydrophobicity, β-carotene failed to dissolve fully, forming a suspension characterized by distinct light diffraction (Tyndall effect). The consequences of spinning a suspended phase were immediately apparent at the macroscopic level, where the scaffolds exhibited distinct reddish spots and aggregates. Confocal microscopy further highlighted this phase separation, revealing high-intensity bright spots superimposed on the fibre network, indicating localized accumulations of the carotenoid. Morphologically, this led to severe deposition anomalies: laser-optical analysis recorded extreme outliers in fibre diameter, with one specific deposition (Beta 1) reaching a mean

diameter of 4.213 ± 0.953 μm, drastically higher than the baseline. High-resolution FESEM imaging provided the structural explanation for these defects, revealing nodular swellings within the fibres that matched the morphology of undissolved β-carotene macro-aggregates, alongside localized plastic deformation of the surrounding polymer matrix and extensive fraying at the fracture edges.

From an electrohydrodynamic perspective, it is plausible that these solid macro-aggregates act as physical disruptors during the chaotic whipping phase of the polymer jet. During electrospinning, the jet undergoes a rapid, non-axisymmetric bending instability — the whipping motion responsible for the extreme elongation and thinning that ultimately yields nanoscale fibres [65]. Studies on the electrospinning of nanoparticle-loaded polymer solutions — including PCL among the polymers investigated — have shown that the interaction between dispersed solid particles and the polymer matrix directly affects fibre morphology, with particle-laden systems typically showing greater morphological variability than their neat-polymer counterparts [66]. This is consistent with reports that a fraction of drug remaining undissolved at high loading, rather than fully incorporated in the polymer solution, is associated with reduced encapsulation efficiency and a more pronounced burst-release behaviour in electrospun drug-loaded fibres [67], an outcome compatible with the localized, poorly integrated β-carotene aggregates observed here. As the jet undergoes this rapid elongation and solvent evaporation, the solid, non-deformable β-carotene particles likely create localized points of mechanical stress and charge accumulation, disrupting the smooth propagation of the whipping instability described above. This perturbation interrupts the uniform transmission of viscoelastic forces along the jet, causing the surrounding fluid to wrap around the inclusion, ultimately generating the radial entanglement and structural defects observed under the laser-optical magnification. [65], [66], [67]

The Mix scaffolds predictably exhibited a hybrid morphological behaviour. The simultaneous presence of fully dissolved curcumin and suspended β-carotene generated a dual-phase spinning dope. Macroscopically and under confocal observation, the mesh displayed a uniform yellowish background and diffuse fluorescence typical of curcumin, interspersed with the distinct macroscopic red aggregates and high-intensity confocal bright spots characteristic of β-carotene. Consequently, the Mix group also suffered from process instability, highlighted by a notable diameter outlier (Mix 1 at 3.543 ± 0.518 μm). FESEM cross-sections of the stretched Mix specimens revealed transverse micro-fractures on the fibre surfaces, suggesting that the inclusion of particulate matter with a highly loaded, plasticized matrix creates microstructural stress concentrators that compromise the integrity of the individual fibres under tension.

Overall, while the bilayer strategy successfully provided a robust pure-PCL foundation capable of physically supporting the functionalized top layer, the inherent morphological quality of the active layer remains strictly dependent on the initial phase state (solution vs suspension) of the loaded biomolecules.

6.2 Molecular-Level Integration of the Bioactive Agents

To fully understand the structural and mechanical impact of the bioactive agents on the PCL matrix, it is imperative to investigate their molecular-level integration. The combination of

FTIR and Raman spectroscopy provided a comprehensive, complementary picture of these chemical interactions.

As discussed in the literature review (*Chapter 3*), integration of curcumin into PCL is typically expected to induce non-covalent interactions. Specifically, the electrospinning process often facilitates a structural transition of curcumin into a reactive keto-enol form, enabling its central hydrogen to act as a donor and form hydrogen bonds with the carbonyl (C=O) groups of the PCL matrix. However, the FTIR-ATR analysis performed on the highly loaded (5% wt.) functionalized layers yielded spectra essentially identical to pristine PCL, completely dominated by the characteristic matrix bands, including the primary carbonyl stretching peak at 1722 cm^{-1}. This apparent absence of new spectral features can be explained by two non-exclusive factors. First, the resulting hydrogen-bond-induced shift of the carbonyl band — typically only a few wavenumbers — may be diluted within, and masked by, the intrinsically broad envelope of the dominant, unperturbed C=O peak, especially since only a fraction of the curcumin population is expected to engage in this interaction. Second, the extremely rapid evaporation rate of the CF/EtOH solvent system during the electrospinning flight may freeze the polymer chains in place so quickly that widespread, systemic keto-enol hydrogen bonding is kinetically restricted, leaving the interactions highly localized and below the detection threshold of the ATR crystal.

Where FTIR reached its limitations – particularly in detecting non-polar inclusions – Raman spectroscopy proved exceptionally effective. The Raman selection rules rely on changes in electron cloud polarizability rather than dipole moments, making the technique extremely sensitive to the heavily conjugated carbon backbone of β-carotene. The Raman spectrum of the β-Carotene scaffold irrefutably confirmed the structural integrity of the biomolecule within the mesh. The appearance of massive, sharp bands at 1005 cm^{-1} (ν_3, methyl rocking), 1155 cm^{-1} (ν_2, C-C stretching) and 1519 cm^{-1} (ν_1, C=C stretching) completely overshadowed the underlying PCL signals. This confirmation provides strong evidence that the delicate conjugated polyene chain of β-carotene successfully survived the harsh 15 kV electrical field and the rapid phase transition without degrading. Furthermore, the lack of chemical shifts in the PCL FTIR spectrum combined with these intense Raman peaks reinforces the conclusion that β-carotene acts purely as a physical, particulate inclusion rather than a chemically bonded crosslinker.

For the Curcumin and Mix groups, Raman spectroscopy yielded a massive, broad fluorescence background that masked sharp vibrational modes. While this obscures specific bond stretching, this intense autofluorescence is a direct analytical confirmation of the highly conjugated, active state of the polyphenolic molecule distributed homogeneously throughout the mesh. The Mix scaffold perfectly demonstrated its hybrid nature under Raman excitation: it exhibited both the broad fluorescence background typical of curcumin and a distinct, sharp peak at 1517 cm^{-1} perfectly matching the dominant ν_1 mode of β-carotene.

Together, these spectroscopic techniques confirm that the 5% bioactive loading was successfully integrated into the top layer of the bilayer constructs. The active agents maintained their structural and chemical viability, acting as non-covalent, physical plasticizers that interact with the PCL matrix without permanently altering its covalent backbone.

A further analytical detail of interest emerges from the Raman spectrum of the pure PCL control. The analysis revealed a minor, not univocally assigned band at approximately 1610 cm^{-1}. Since the aliphatic structure of pristine polycaprolactone lacks aromatic rings or conjugated double bonds that typically resonate in this specific region, this signal may originate from trace industrial additives (e.g., phenolic antioxidants or thermal stabilizers commonly used in commercial PCL pellets), though this attribution remains unconfirmed and would require targeted reference spectra (e.g., FTIR/Raman of the neat additive) for verification.

6.3 Thermal Behaviour and Crystallinity

The DSC analysis elucidated how the physical presence of the bioactive agents, confirmed by the spectroscopic and morphological data, influences the macroscopic chain packing and thermal phase transitions of the PCL matrix.

For the pristine PCL Control group, the fractional crystallinity calculated during the first heating scan (24.83%) was notably lower than the value recorded in the second heating scan (34.47%). This discrepancy perfectly illustrates the kinetic constraints imposed by the electrospinning process. The exceptionally rapid evaporation rate of the CF/EtOH solvent system restricts the time available for the polymer chains to organize into a highly ordered crystalline lattice prior to complete fibre solidification. Once this processing thermal history is erased by melting, the subsequent slow, controlled cooling inside the DSC crucible allows the PCL to reorganize reaching higher, intrinsic structural order.

The inclusion of β-carotene introduced a profound and persistent plasticizing effect on the polymeric structure. The fractional crystallinity of the β-Carotene group remained depressed around 20% during both heating scans and plummeted drastically to 9.94% during the second cooling phase. This thermal behaviour strongly corroborates the FESEM and Raman findings. Because β-carotene remains suspended as non-bonding, highly hydrophobic solid macro-aggregates, it acts as a severe steric hindrance. These bulky inclusions physically block the PCL chains from folding and packing closely into the ordered lamellae, forcing the matrix into a highly amorphous plasticized state.

Conversely, the Curcumin and Mix groups exhibited a markedly different, almost counterintuitive thermal profile. In the first heating scan, both groups showed an anomalously high initial crystallinity (47.32% and 52.01%, respectively), drastically exceeding the pristine Control. However, in the second heating scan – after the electrospinning-induced thermal history had been completely erased – their crystallinities dropped to 32.25% and 34.38%. These second-heating values align almost perfectly with the intrinsic crystallinity of pure PCL (34.47%), confirming that the polymer's covalent backbone was not permanently altered or chemically crosslinked by the additives.

The massive spike in the as-spun (first heating) crystallinity for the Curcumin and Mix groups points to a phenomenon directly driven by the electrohydrodynamic process. Because curcumin achieves complete molecular dissolution and interacts with PCL via keto-enol hydrogen bonding, its presence likely alters the viscosity, surface tension, or electrical conductivity of the spinning dope. Such solution-property changes are known to modulate jet stretching dynamics

during electrospinning [68]; more specifically, faster jet rigidification has been shown to promote molecular orientation and a fraction of strain-induced crystallinity in electrospun fibres [69], a mechanism that may analogously apply here if curcumin's presence accelerates the effective solidification of the jet. This elevated drawing force forces strong macromolecular alignment along the longitudinal axis of the fibre, generating extensive, stress-induced crystalline regions during flight. The Mix sample, which exhibited the highest overall first-heating crystallinity (52.01%), likely experienced a synergistic effect: the extreme stretching facilitated by the dissolved curcumin, combined with the physical stress-concentrators provided by the suspended β-carotene particles, maximized the mechanical alignment of the polymer chains before solvent evaporation was complete.

6.4 Surface Properties and their Biological Relevance

The transition from the bulk structural properties to the scaffold's surface characterizes its most critical function: the interface with the biological environment. Initial protein adsorption, exudate absorption and subsequent cell adhesion are heavily dictated by the wettability and surface charge of the functionalized layer.

Water contact angle (WCA) measurements confirmed the intrinsic hydrophobicity of pristine PCL (117.0°). The addition of β-carotene significantly exacerbated this hydrophobicity, raising the contact angle to 135.9°. This aligns perfectly with the morphological and spectroscopic evidence: β-carotene acts as a highly non-polar, particulate inclusion that increases surface roughness without providing hydrophilic binding sites, creating a highly repellent interface. Conversely, the incorporation of curcumin notably improved surface wettability, dropping the WCA to 97.9°, placing it nearest to the hydrophilic threshold. This increased affinity for aqueous media is a direct consequence of the abundant phenolic hydroxyl groups and the polar keto-enol structure of curcumin exposed on the fibre surface. Predictably, the Mix scaffold demonstrated an intermediate behaviour (124.9°), balancing the hydrophilic pull of curcumin with the hydrophobic shielding of β-carotene.

The surface zeta potential of the solid scaffolds provided further insight into this fluid-interface dynamic. Within the physiological pH window of healthy intact skin (pH 4.5 – 5.5), the Control, β-Carotene and Mix groups maintained a moderately negative surface charge (between -10 and -30 mV).

The Curcumin scaffold, however, displayed a unique surface charge profile, characterized by an isoelectric point precisely at 5 pH. This exact neutrality in the physiological skin window is likely driven by the protonation of its exposed phenolic and hydroxyl groups. From a biological perspective, a near-neutral or slightly negative surface in this specific pH range is highly advantageous. It prevents extreme electrostatic repulsion of circulating proteins, potentially facilitating a more rapid and stable formation of the initial protein corona, which is essential for subsequent integrin-mediated cell adhesion. [70] At highly alkaline pH values (up to 9.0), simulating chronic wound environments, all scaffold surfaces shifted to highly negative values (down to approximately -80 mV), suggesting that in non-healing wounds, strong electrostatic repulsion might alter protein dynamics. As already explained, the zeta potential value of these hydrophobic materials without acidic/basic functional groups is strongly dependent on the

chemistry of the liquid environment and must be verified in relevant media. Evidence of a chemical modification of the reactivity of curcumin's functional groups after embedding in PCL is worth further investigation.

It should be noted that the ELS measurements discussed below were performed on the pH- and ionic-strength-adjusted ethanol-based eluate obtained after a 2-hour extraction (*Chapter 4.9.1*), used here for colloidal characterisation purposes, and not on the release profile obtained under simulated physiological wound conditions (PBS + 0.1% SDS, *Chapter 5.7*). Furthermore, the comparison that follows involves two different techniques and media: aqueous streaming potential on the intact solid surface versus electrophoretic mobility in a predominantly ethanolic extract. The substantially lower dielectric constant of ethanol relative to water (~24 vs ~80) is expected to strongly affect the electrical double layer and the resulting zeta potential values, independently of any genuine change in the released species themselves. With this methodological caveat in mind, electrophoretic light scattering of the eluates revealed that the released species showed near-neutral values, hovering between -10 and +20 mV across the entire pH range, markedly different from the substantially more negative surface zeta potential of the intact solid scaffold (down to approximately -80 mV). Rather than indicating a genuine loss of surface charge upon release into the wound environment, this near-neutrality should primarily be interpreted in light of the change in technique and solvent system, and only tentatively, if at all, as evidence of an intrinsic electrical transformation of the released species. Dynamic light scattering clarified the colloidal nature of these eluates. For the Curcumin group, the instrument failed to resolve a distinct particulate population. This is an excellent outcome, confirming that curcumin fully dissolves into single molecules or unresolvably small molecular clusters upon release, maximizing its immediate bioavailability. On the contrary, β-carotene (unable to fully dissolve) was released as remarkably stable, narrowly distributed nano-suspensions (mean diameter ~158 nm, low polydispersity of 15.8%). The Mix eluate showed a virtually identical stable nanoparticulate profile (~177 nm). In contrast, the pure PCL control released much larger, highly polydisperse fragments (~979 nm), likely representing minor polymeric degradation products or debris.

Ultimately, these surfaces analyses demonstrate that while curcumin improves macroscopic wettability and provides a biologically favourable, near-neutral surface charge for initial skin contact, β-carotene relies on the release of highly stable, uniform nanoscale suspension to deliver its therapeutic effect into the wound bed.

6.5 Mechanical Performance and the Bilayer Strategy

The central engineering challenge addressed by this thesis was overcoming the severe mechanical degradation typically associated with incorporating high concentrations of natural biomolecules into polymeric electrospun meshes. As discussed in *Chapter 3*, single-layer PCL scaffolds functionalized with 5% wt. active agents often suffer a catastrophic loss of load-bearing capacity, driven by profound plasticization and disrupted polymer chain entanglement. The tensile testing results demonstrate unequivocally that the proposed bilayer architecture successfully circumvented this fundamental limitation.

By decoupling the therapeutic function (the highly loaded top layer) from the structural function (the pristine PCL base layer), the composite scaffolds retained robust mechanical profiles. The pristine PCL Control exhibited a Young's modulus of 18.95 ± 2.59 MPa and an ultimate tensile strength (UTS) of 2.19 ± 0.72 MPa, with an extreme elongation at break of 451.2%. Across all functionalized groups, the Young's modulus remained between approximately 15 and 21 MPa, and the UTS fluctuated tightly between 1.8 and 2.8 MPa. Crucially, when benchmarked against the physiological mechanical properties of human skin – which typically exhibits an elastic modulus ranging from 60 to 850 kPa (0.06 to 0.85 MPa) [20] – all fabricated bilayer patches provided more than sufficient stiffness, strength and conformability to safely endure clinical handling, application and physiological stress over a wound bed.

While the base layer anchored the overall stability, the distinct physicochemical nature of the active agents in the top layer subtly dictated the specific failure mechanisms, mirroring the morphological and thermal findings.

The Curcumin scaffold exhibited the highest overall mechanical performance, achieving a peak UTS of 2.81 ± 0.36 MPa and a Young's modulus of 20.75 ± 2.90 MPa, while retaining an excellent elongation of 416.0%. This slight reinforcement effect compared to the Control aligns with the DSC data, which revealed massive stress-induced crystallization during the electrospinning of curcumin-loaded fibres.

It is highly likely that the complete molecular dissolution of curcumin and its keto-enol hydrogen bonding not only enhanced the electrostatic stretching of the fibres but also improved the interfacial adhesion between the pristine PCL base and the functionalized top layer. This is consistent with previous reports on curcumin-loaded bilayer electrospun constructs, where hydrogen bonding between the phenolic hydroxyl groups of curcumin and the carbonyl groups of an adjacent polyester later was shown to promote strong interfacial adhesion between two otherwise distinct solid layers, complementing any hydrophobic-hydrophobic interactions already present between the base polymers themselves [71]. Notably, PCL was itself one of the three polyesters constituting the adjacent layer in that study, meaning the reported hydrogen-bonding interaction directly involved PCL carbonyl groups; an analogous mechanism may therefore reasonably extend to the present bilayer system, where curcumin's phenolic hydroxyl groups are equally positioned to hydrogen-bond with the carbonyl groups of the pristine PCL exposed at the base layer surface. As seen in the FESEM images, adjacent fibres around nodes thinned and elongated significantly before failure, demonstrating excellent stress transfer and ductility.

Conversely, the β-Carotene scaffold suffered a drastic reduction in elongation at break (227.3 ± 130.3%) and exhibited the lowest maximum stress (1.83 ± 0.34 MPa). The FESEM analysis provides the direct structural explanation for this premature failure: the undissolved β-carotene macro-aggregates act as critical stress concentrators. When longitudinal tension is applied, the polymer matrix plastically deforms and pulls away from these stiff, non-bonded solid inclusions, initiating localized void formation and rapid tear propagation, leading to the extensive fraying observed at the macroscopic fracture edge. However, because the pristine PCL base layer

absorbed most of the tensile load, the scaffold still failed at a highly respectable 1.83 MPa, preventing the total structural collapse that would have occurred in a single-layer equivalent.

The Mix scaffold reflected a mechanical compromise (modulus: 15.82 ± 2.02 MPa; UTS: 2.07 ± 0.43 MPa; Elongation: 360.3 ± 124.7%); it benefited from the ductility and structural integration provided by curcumin, allowing it to stretch further than the pure β-carotene mesh, but ultimately succumbed to the same premature failure induced by the particulate inclusions. FESEM images of the stretched Mix fibres captured the exact moment of failure, revealing distinct transverse micro-fractures propagating across the fibres, highlighting the contrast between the ductilising effect of curcumin and the embrittling effect of the solid β-carotene defects.

6.6 Biocompatibility

The ultimate prerequisite for any advanced wound dressing is its ability to safely interface with the native host tissues without eliciting cytotoxic responses. Given the high concentration of bioactive agents loaded into the top layer and the potential retention of organic solvents, an indirect *in vitro* compatibility assay was critical to validate the clinical safety of the bilayer scaffolds.

The results of the indirect assay on human dermal fibroblasts demonstrated outstanding biocompatibility across all experimental formulations. Cell viability remained remarkably high, ranging from 95.69% to 98.99% across the 24-hours, 72-hours and 7-day eluate collection points, with no statistically significant differences observed between the pristine PCL control and the functionalized groups. This universally high survival rate provides two key confirmations. First, it verifies that the optimized CF/EtOH binary solvent system evaporates entirely during the electrospinning flight, leaving no toxic halogenated residues within the mesh. Second, it indicates that the high localized dosage of curcumin, β-carotene and their mixture released into the medium does not exceed the toxicity threshold for human fibroblasts.

While viability remained universally high, the evaluation of cell proliferation (total cell count) highlighted subtle, biological trends over the long-term incubation period. Fluorescence imaging revealed dense, evenly distributed cell populations for all conditions. However, at the 7-day time point, the pristine PCL Control group recorded the lowest total cell count among all conditions (60.83 cells/field), while the eluates from the β-Carotene, Curcumin and Mix scaffolds maintained comparatively higher cell counts (ranging from 83.44 to 91.22 cells/field). It should be noted that the Control value at this time point is based on n = 2 wells, following the exclusion of one well due to accidental contamination (*Chapter 4.11.8*); this reduced sample size, together with the lack of statistical significance between groups, warrants some caution in interpreting the apparent difference as a genuine biological effect rather than, at least partly, a consequence of the smaller Control sample at this specific time point.

With the above caveat in mind, the biological trend is nonetheless worth discussing, as it is mechanistically plausible and potentially clinically relevant. In a static *in vitro* culture, prolonged incubation (such as the 7-day eluate) often leads to natural nutrient depletion or the accumulation of metabolic oxidative stress, as cells progressively consume the available

substrates and generate reactive oxygen species (ROS) as by-products of sustained metabolic activity. Both curcumin and β-carotene are renowned for their potent antioxidant and ROS-scavenging properties. It is plausible that the sustained release of these natural molecules into the conditioning medium creates a chemically protective microenvironment: curcumin has been shown to protect human dermal fibroblasts specifically against H_2O_2-induced oxidative damage *in vitro*, with protective effects reported even at low micromolar concentrations [72], and carotenoids more broadly have been shown to protect dermal fibroblasts from oxidative-stress-induced damage through a reduction in intracellular ROS levels, partly via activation of the ARE/Nrf2 antioxidant response pathway [73] (though this latter study tested a lycopene-rich tomato extract rather than β-carotene specifically, so its extension to β-carotene here remains an analogy based on shared carotenoid class rather than a directly confirmed effect). By quenching metabolic reactive oxygen species, the functionalized eluates may subtly buffer the cells against standard culture stress, potentially supporting the maintenance and slight proliferation of the fibroblast population over extended periods compared to the inert PCL control.

This mechanism, if confirmed, would carry particular relevance beyond the standard cell culture setting used here. Chronic, non-healing wounds are characterised by a persistently pro-oxidant local environment, driven by prolonged inflammation and elevated ROS production, which is itself a recognised contributor to impaired healing. If the sustained, low-level release of curcumin and β-carotene observed in this study (*Chapter 5.7*) similarly buffers oxidative stress once the scaffold is applied *in vivo*, the bilayer dressing may offer a secondary therapeutic benefit beyond simple biocompatibility — actively counteracting one of the pathophysiological features of the chronic wound environment discussed elsewhere in this work (*Chapter 6.4*), rather than merely failing to harm the surrounding tissue. This remains a hypothesis to be tested in future work, ideally under an induced oxidative stress challenge (e.g., H_2O_2 exposure) rather than the standard, unchallenged culture conditions used in the present cytotoxicity assay, which are not designed to detect an antioxidant benefit directly.

Ultimately, these biological findings confirm that the bilayer architecture not only provides a mechanically robust matrix but also serves as a safe and potentially supportive delivery vehicle for tissue regeneration.

6.7 Release Kinetic and Clinical Implications

The ultimate efficacy of a functionalized wound dressing depends on its ability to deliver bioactive agents at a controlled rate, tailored to the physiological state of the target tissue. The release kinetics, evaluated across three distinct pH levels simulating healthy / re-epithelializing skin (pH 5.5), acute systemic wounds (pH 7.4) and chronic infected lesions (pH 9.0), perfectly encapsulated the stark physicochemical differences between curcumin and β-carotene.

The β-Carotene scaffolds exhibited a steady, progressive and sustained release profile across all three pH conditions, with absorbance values gradually increasing from 24 hours up to 7 days. This steady kinetic behaviour perfectly aligns with the morphological and colloidal data. Because β-carotene remains locked within the PCL matrix as highly hydrophobic, solid macro-aggregates, it does not burst-release via simple diffusion. Instead, its release is governed by the

slow, progressive detachment of stable nanoparticulate suspensions (as proven by DLS) into the surrounding medium. It is worth noting that the β-carotene calibration standards themselves were difficult to prepare as fully homogeneous solutions given the compound's extreme hydrophobicity (*Chapter 5.7.5*); the estimated concentration values discussed elsewhere in this chapter should therefore be interpreted as indicative rather than exact. This caveat, however, does not affect the qualitative release trend discussed here, which is based on the raw, unconverted absorbance signal (*Table 5.14*) rather than on the estimated concentration. Clinically, this makes β-carotene an exceptional candidate for long-term wound protection: it guarantees a sustained, localized delivery of antioxidant and osteoinductive nanoparticles directly at the tissue interface over extended periods of time, without being exhausted in the first few days of application.

Conversely, the Curcumin scaffolds demonstrated a drastically different release dynamic. Because curcumin achieved complete molecular dissolution during electrospinning, its bioavailability was immensely higher, generating absorbance values approximately an order of magnitude greater than those of β-carotene across all conditions. However, the release profile was heavily dictated by the pH of the environment, unveiling a crucial clinical challenge. At pH 5.5, the release was robust and progressive up to 7 days. But at pH 7.4 and predominantly at pH 9.0, the recorded absorbance peaked at 72 hours and subsequently dropped at 7 days.

This drop in absorbance does not indicate that the drug is re-entering the scaffold; rather, it is consistent with the well-documented chemical instability of curcumin in alkaline media. As previously noted (*Chapter 3*), curcumin undergoes rapid auto-oxidation and hydrolytic degradation under alkaline conditions, and a visible colour change was indeed observed even during the short preparation time of the pH 9.0 calibration standards themselves. This suggests that curcumin degradation begins essentially as soon as it is dissolved at pH 9.0, rather than only becoming relevant over the multi-day timescale of the release experiment; partial, and possibly concentration-dependent, degradation of the calibration standards during preparation likely explains the poor linearity ($R^2 = 0.83$) of the curcumin calibration curve at this pH, since the assumption of a fixed absorbance-to-concentration relationship no longer holds once a variable fraction of the compound has already degraded before measurement. This effect is expected to be substantially more pronounced for the actual release samples, which remained in the pH 9.0 medium for up to 7 days rather than being measured immediately after dissolution; for this reason, absorbance values at pH 9.0 were not converted into estimated concentrations (*Chapter 5.7.4*) and should be interpreted qualitatively rather than quantitatively. A secondary, more limited confound also affected the 24-hour release measurement specifically: different cuvettes were used for the Curcumin and Mix samples at this single time point compared to all other conditions (*Chapter 5.7.4*), which may affect the absolute comparability of the 24-hour value alone. Notably, the 72-hour and 7-day measurements were acquired with consistent cuvettes, so the drop in absorbance observed between these two later time points is not attributable to this artefact and can be more confidently attributed to progressive curcumin degradation. Consequently, in the highly alkaline environment of a chronic, non-healing wound (pH 9.0), the released curcumin is likely to undergo substantial, and progressively worsening, chemical inactivation over time.

The Mix scaffold reflected this dual reality, successfully proving the feasibility of co-delivering a dissolved drug and a suspended particulate from a single polymeric matrix. It showed its maximum release efficacy at pH 5.5, where both active agents remain chemically stable.

The comprehensive evaluation of these release profiles provides clear guidelines for the clinical translation of this bilayer architecture. The patch performs optimally in slightly acidic to neutral environments (pH 5.5 – 7.4). In acute wounds or during the active re-epithelialization phase, the rapid, high-concentration diffusion of curcumin can immediately quench the initial inflammation and bacterial colonization, while the slow, sustained particulate release of β-carotene provides long-term cellular stimulation. However, if applied to severely alkaline, chronically infected wounds (pH 9.0), curcumin's therapeutic contribution becomes temporally limited due to its rapid degradation. In such extreme clinical scenarios, β-carotene appears comparatively more resilient: unlike curcumin, its release profile showed no equivalent decline at pH 9.0 over the 7-day observation window (*Table 5.14*), consistent with reports that carotenoids can be less susceptible to pH-driven degradation than curcumin, which is markedly more stable under acidic than alkaline conditions [74]. While this comparison was established in a different delivery system (oil-in-water nanoemulsions rather than solid nanoparticulate suspensions), it supports the plausibility of β-carotene remaining a comparatively more resilient therapeutic payload under these extreme conditions, warranting direct confirmation via dedicated stability assays in future work.

7 Conclusions

The aim of this thesis was to develop and characterise a PCL-based bilayer electrospun patch, functionalized with high concentration of curcumin, β-carotene or their combination, and to evaluate how the bilayer architecture affects the mechanical performance and pH-dependent release kinetics of the incorporated biomolecules. The results obtained across morphological, chemical, thermal, surface, mechanical, biological and release-kinetic characterizations collectively demonstrate that the proposed decoupled-layer strategy successfully addresses the mechanical fragility that typically limits highly loaded (5% wt.) single-layer electrospun scaffolds, while preserving the distinct therapeutic profiles of both bioactive agents.

The morphological investigation revealed that the physical state of the loaded biomolecules in the CF/EtOH (7:3) spinning dope was the primary determinant of process stability. Curcumin, fully dissolved at the 5% wt. loading, yielded a homogeneous nanofibrous mesh comparable to the pristine PCL control, whereas the intrinsic hydrophobicity of β-carotene forced it into a suspended phase, generating macro-aggregates that acted as physical disruptors of the electrospinning jet and produced localized morphological defects, nodular swelling and diameter outliers. The Mix scaffold displayed a predictable hybrid behaviour, combining the homogeneous background of curcumin with the aggregate-driven defects of β-carotene. FTIR and Raman spectroscopy confirmed that both agents were successfully and stably incorporated into the top layer: curcumin’s interactions with the PCL carbonyl groups remained below the ATR detection threshold but were consistent with expected hydrogen bonding, while the sharp, intense Raman bands of β-carotene’s conjugated backbone confirmed that it survived electrospinning intact as a physically dispersed, non-covalently bonded inclusion. DSC analysis

corroborated this picture, showing that β-carotene imposed a persistent plasticizing effect that suppressed crystallinity, while curcumin's molecular dissolution promoted transient stress-induced crystallization during fibre drawing without permanently altering the PCL backbone.

At the biointerface level, curcumin markedly improved surface wettability and produced a favourable, near-neutral surface charge within the physiological pH range of skin, while β-carotene increased both hydrophobicity and surface roughness; the Mix scaffold occupied an intermediate position. Colloidal analysis of the eluates showed that curcumin is released essentially as free, fully dissolved molecules, whereas β-carotene and the Mix formulation release stable, narrowly distributed nanoparticulate suspensions, indicating two fundamentally different but equally viable delivery mechanisms.

Mechanically, the bilayer strategy fulfilled its central engineering objective. By confining the highly loaded, therapeutically active formulation to a top layer while relying on a pristine PCL base for load-bearing, all functionalized scaffolds maintained a Young's modulus of approximately 15 – 21 MPa and an ultimate tensile strength between 1.8 and 2.8 MPa, comfortably exceeding the physiological mechanical requirements of human skin. Curcumin-loaded fibres benefited from improved interfacial adhesion and stress-induced crystallinity, achieving the highest overall mechanical performance, while β-carotene's solid aggregates acted as stress concentrators that reduced elongation at break and lowered maximum stress; nonetheless, the pristine base layer prevented the catastrophic mechanical failure typically reported for equivalent single-layer systems.

The indirect in vitro biocompatibility assay confirmed that all formulations are safe for use on human dermal fibroblasts, with cell viability consistently above 95% and no cytotoxic effect attributable to residual solvent or to the high bioactive loading. A subtle, though not statistically significant, trend toward higher long-term cell proliferation in the functionalized groups compared to the pristine control was also observed, plausibly linked to the antioxidant, ROS-scavenging properties of curcumin and β-carotene, suggesting a potential secondary therapeutic benefit that merits dedicated investigation under oxidative-stress-challenged conditions.

Finally, the release kinetics evaluated at pH 5.5, 7.4 and 9.0 encapsulated the complementary clinical roles of the two agents. β-carotene provided a slow, sustained, pH independent release governed by nanoparticulate detachment, making it well suited for long-term wound protection, whereas curcumin achieved a much higher and faster bioavailability but underwent progressive chemical degradation in alkaline media, limiting its effective therapeutic window in chronically infected, high-pH wounds. Taken together, these findings indicate that the bilayer patch performs optimally across the slightly acidic to neutral range typical of healthy and acute wound environments (pH 5.5 – 7.4), where the rapid action of curcumin and the sustained delivery of β-carotene can act synergistically, while β-carotene's comparative resilience may retain therapeutic value even in more extreme, alkaline chronic-wound conditions.

In conclusion, this thesis demonstrates that a bilayer electrospinning architecture is an effective strategy for combining high, clinically relevant bioactive loadings with retained mechanical integrity, biocompatibility and pH-tuneable release behaviour in a single wound dressing construct.

Several limitations, however, remain open for future investigation: the curcumin calibration at pH 9.0 was affected by compound degradation during standard preparation, limiting the quantitative interpretation of high-pH release data; β-carotene's extreme hydrophobicity similarly constrained the accuracy of its calibration curves; and several assays, including cell proliferation counts, would benefit from larger sample sizes to confirm the biological trends observed.

Future work should therefore prioritize the direct experimental confirmation of the hypothesized antioxidant protective effect under an induced oxidative-stress challenge, dedicated pH-stability assays for both bioactive agents, and ultimately in vivo validation of the bilayer patch's performance in a physiologically representative wound model, as a necessary step toward its clinical translation.

8 References

[1] L. A. Schneider, A. Korber, S. Grabbe, e J. Dissemond, «Influence of pH on wound-healing: a new perspective for wound-therapy?», *Arch. Dermatol. Res.*, vol. 298, fasc. 9, pp. 413–420, gen. 2007, doi: 10.1007/s00403-006-0713-x.

[2] X. Wang, H. Zhao, L.-S. Turng, e Q. Li, «Crystalline Morphology of Electrospun Poly(ε-caprolactone) (PCL) Nanofibers», *Ind. Eng. Chem. Res.*, vol. 52, fasc. 13, pp. 4939–4949, apr. 2013, doi: 10.1021/ie302185e.

[3] A. Haider, S. Haider, e I.-K. Kang, «A comprehensive review summarizing the effect of electrospinning parameters and potential applications of nanofibers in biomedical and biotechnology», *Arab. J. Chem.*, vol. 11, fasc. 8, pp. 1165–1188, dic. 2018, doi: 10.1016/j.arabjc.2015.11.015.

[4] D. Cicėnas e A. Šešok, «Influence of Different Solvents on the Mechanical Properties of Electrospun Scaffolds», *Materials*, vol. 18, fasc. 2, p. 355, gen. 2025, doi: 10.3390/ma18020355.

[5] C. J. Angammana e S. H. Jayaram, «Fundamentals of electrospinning and processing technologies», *Part. Sci. Technol.*, vol. 34, fasc. 1, pp. 72–82, gen. 2016, doi: 10.1080/02726351.2015.1043678.

[6] A. Keirouz *et al.*, «The History of Electrospinning: Past, Present, and Future Developments», *Adv. Mater. Technol.*, vol. 8, fasc. 11, p. 2201723, giu. 2023, doi: 10.1002/admt.202201723.

[7] O. Yoshikawa *et al.*, «Simple Electrospinning Method for Biocompatible Polycaprolactone β-Carotene Scaffolds: Advantages and Limitations», *Polymers*, vol. 16, fasc. 10, p. 1371, mag. 2024, doi: 10.3390/polym16101371.

[8] O. Yoshikawa *et al.*, «Electrospun Polycaprolactone-Curcumin Scaffolds: Optimization of fiber production for enhanced Nanotopography and improved biological cell adhesion», *Eur. Polym. J.*, vol. 222, p. 113616, gen. 2025, doi: 10.1016/j.eurpolymj.2024.113616.

[9] J. Elangovan, G. E. Paulraj, S. N. T. S. Nellaiappan, e R. Kulanthaivelu, «Fabrication of Electrospun Polycaprolactone Nanofibers for Drug Delivery Application and Development of an Electrospinnability Map», *J. Appl. Polym. Sci.*, vol. 142, fasc. 33, p. e57334, set. 2025, doi: 10.1002/app.57334.

[10] S. Mitra, T. Mateti, S. Ramakrishna, e A. Laha, «A Review on Curcumin-Loaded Electrospun Nanofibers and their Application in Modern Medicine», *JOM*, vol. 74, fasc. 9, pp. 3392–3407, set. 2022, doi: 10.1007/s11837-022-05180-9.

[11] W. Zeng *et al.*, «Electrospun polycaprolactone nanofibrous membranes loaded with baicalin for antibacterial wound dressing», *Sci. Rep.*, vol. 12, fasc. 1, p. 10900, giu. 2022, doi: 10.1038/s41598-022-13141-0.
[12] A. Cipitria, A. Skelton, T. R. Dargaville, P. D. Dalton, e D. W. Hutmacher, «Design, fabrication and characterization of PCL electrospun scaffolds—a review», *J. Mater. Chem.*, vol. 21, fasc. 26, pp. 9419–9453, giu. 2011, doi: 10.1039/c0jm04502k.
[13] M. A. Woodruff e D. W. Hutmacher, «The return of a forgotten polymer—Polycaprolactone in the 21st century», *Prog. Polym. Sci.*, vol. 35, fasc. 10, pp. 1217–1256, ott. 2010, doi: 10.1016/j.progpolymsci.2010.04.002.
[14] E. Malikmammadov, T. E. Tanir, A. Kiziltay, V. Hasirci, e N. Hasirci, «PCL and PCL-based materials in biomedical applications», *J. Biomater. Sci. Polym. Ed.*, vol. 29, fasc. 7–9, pp. 863–893, giu. 2018, doi: 10.1080/09205063.2017.1394711.
[15] M. Rajeev e C. C. Helms, «A Study of the Relationship between Polymer Solution Entanglement and Electrospun PCL Fiber Mechanics», *Polymers*, vol. 15, fasc. 23, p. 4555, nov. 2023, doi: 10.3390/polym15234555.
[16] A. A. Conte, K. Sun, X. Hu, e V. Z. Beachley, «Effects of Fiber Density and Strain Rate on the Mechanical Properties of Electrospun Polycaprolactone Nanofiber Mats», *Front. Chem.*, vol. 8, p. 610, lug. 2020, doi: 10.3389/fchem.2020.00610.
[17] H. H. Kim, M. J. Kim, S. J. Ryu, C. S. Ki, e Y. H. Park, «Effect of fiber diameter on surface morphology, mechanical property, and cell behavior of electrospun poly(ε-caprolactone) mat», *Fibers Polym.*, vol. 17, fasc. 7, pp. 1033–1042, lug. 2016, doi: 10.1007/s12221-016-6350-x.
[18] A. Dabouian, H. Bakhshi, S. Irani, e M. Pezeshki-Modaress, «β-Carotene: a natural osteogen to fabricate osteoinductive electrospun scaffolds», *RSC Adv.*, vol. 8, fasc. 18, pp. 9941–9945, 2018, doi: 10.1039/C7RA13237A.
[19] E. Altun, J. Ahmed, M. Onur Aydogdu, A. Harker, e M. Edirisinghe, «The effect of solvent and pressure on polycaprolactone solutions for particle and fibre formation», *Eur. Polym. J.*, vol. 173, p. 111300, giu. 2022, doi: 10.1016/j.eurpolymj.2022.111300.
[20] C. F. Guimarães, L. Gasperini, A. P. Marques, e R. L. Reis, «The stiffness of living tissues and its implications for tissue engineering», *Nat. Rev. Mater.*, vol. 5, fasc. 5, pp. 351–370, feb. 2020, doi: 10.1038/s41578-019-0169-1.
[21] E. Polonio-Alcalá, E. Casanova-Batlle, T. Puig, e J. Ciurana, «The solvent chosen for the manufacturing of electrospun polycaprolactone scaffolds influences cell behavior of lung cancer cells», *Sci. Rep.*, vol. 12, fasc. 1, p. 19440, nov. 2022, doi: 10.1038/s41598-022-23655-2.
[22] H. Lian e Z. Meng, «Melt electrospinning vs. solution electrospinning: A comparative study of drug-loaded poly (ε-caprolactone) fibres», *Mater. Sci. Eng. C*, vol. 74, pp. 117–123, mag. 2017, doi: 10.1016/j.msec.2017.02.024.
[23] P. Costa e J. M. Sousa Lobo, «Modeling and comparison of dissolution profiles», *Eur. J. Pharm. Sci.*, vol. 13, fasc. 2, pp. 123–133, mag. 2001, doi: 10.1016/S0928-0987(01)00095-1.
[24] A. E. Hamilton e R. J. Gilbert, «Curcumin Release from Biomaterials for Enhanced Tissue Regeneration Following Injury or Disease», *Bioengineering*, vol. 10, fasc. 2, p. 262, feb. 2023, doi: 10.3390/bioengineering10020262.
[25] «CAPA 6800 | Adhesive Applications & Rapid Prototype Applications | Thermoplastic». Consultato: 22 luglio 2026. [Online]. Disponibile su: https://www.tri-iso.com/perstorp/capa-6800.html
[26] «Product Information | Chloroform 08426-71 1L NACALAI TESQUE, INC. | e-Nacalai Search Version». Consultato: 22 luglio 2026. [Online]. Disponibile su:

https://www.e-nacalai.jp/ec2/EC-srchdetl.cfm?jump=EC-srchdetl&syohin=0842671&syubetsu=3&l=EN&lc=1
[27] «Product Information | Ethanol(99.5) 14712-05 500ML NACALAI TESQUE, INC. | e-Nacalai Search Version». Consultato: 22 luglio 2026. [Online]. Disponibile su: https://www.e-nacalai.jp/ec2/EC-srchdetl.cfm?jump=EC-srchdetl&syohin=1471205&syubetsu=3&l=EN&lc=1
[28] «Product Information | Curcumin 09822-54 5G NACALAI TESQUE, INC. | e-Nacalai Search Version». Consultato: 22 luglio 2026. [Online]. Disponibile su: https://www.e-nacalai.jp/ec2/EC-srchdetl.cfm?jump=EC-srchdetl&syohin=0982254&syubetsu=3&l=EN&lc=1
[29] «Product Information | β-Carotene 07312-81 1G NACALAI TESQUE, INC. | e-Nacalai Search Version». Consultato: 22 luglio 2026. [Online]. Disponibile su: https://www.e-nacalai.jp/ec2/EC-srchdetl.cfm?jump=EC-srchdetl&syohin=0731281&syubetsu=3&l=EN&lc=1
[30] «Human Dermal Fibroblasts: HDF», Cell Applications. Consultato: 27 luglio 2026. [Online]. Disponibile su: https://cellapplications.com/product/human-dermal-fibroblasts-hdf/
[31] «Product Information | DMEM(4.5g/l Glucose) with L-Gln and Sodium Pyruvate, liquid 08458-45 500ML NACALAI TESQUE, INC. | e-Nacalai Search Version». Consultato: 27 luglio 2026. [Online]. Disponibile su: https://www.e-nacalai.jp/ec2/EC-srchdetl.cfm?jump=EC-srchdetl&syohin=0845845&syubetsu=3&l=EN&lc=1
[32] «35-079-CV | Corning® Fetal Bovine Serum, 500 mL, Regular, South American Origin | Corning». Consultato: 27 luglio 2026. [Online]. Disponibile su: https://ecatalog.corning.com/life-sciences/b2b/BY/en/Media%2C-Sera%2C-and-Reagents/Animal-Sera/Animal-Sera/Corning%C2%AE-Fetal-Bovine-Serum/p/35-079-CV
[33] «(H1399) Hoechst 33342, Trihydrochloride, Trihydrate, 100 mg - Thermo Scientific - CiteAb». Consultato: 27 luglio 2026. [Online]. Disponibile su: https://www.citeab.com/biochemicals/13227507-h1399-hoechst-33342-trihydrochloride-trihydrate
[34] «Product Information | Paraformaldehyde, granular 02890-45 500G NACALAI TESQUE, INC. | e-Nacalai Search Version». Consultato: 27 luglio 2026. [Online]. Disponibile su: https://www.e-nacalai.jp/ec2/EC-srchdetl.cfm?jump=EC-srchdetl&syohin=0289045&syubetsu=3&l=EN&lc=1
[35] «Product Information | Tris(hydroxymethyl)aminomethane 35406-75 500G NACALAI TESQUE, INC. | e-Nacalai Search Version». Consultato: 27 luglio 2026. [Online]. Disponibile su: https://www.e-nacalai.jp/ec2/EC-srchdetl.cfm?jump=EC-srchdetl&syohin=3540675&syubetsu=3
[36] «Product Information | Sodium Chloride 31320-05 500G NACALAI TESQUE, INC. | e-Nacalai Search Version». Consultato: 27 luglio 2026. [Online]. Disponibile su: https://www.e-nacalai.jp/ec2/EC-srchdetl.cfm?jump=EC-srchdetl&syohin=3132005&syubetsu=3&l=EN&lc=1
[37] «Product Information | Polyoxyethylene Sorbitan Monolaurate 35624-15 500G NACALAI TESQUE, INC. | e-Nacalai Search Version». Consultato: 27 luglio 2026. [Online]. Disponibile su: https://www.e-nacalai.jp/ec2/EC-srchdetl.cfm?Dum=1&syohin=3562415&syubetsu=3
[38] «Product Information | di-Sodium Hydrogenphosphate 12-Water 31722-45 500G NACALAI TESQUE, INC. | e-Nacalai Search Version». Consultato: 27 luglio 2026. [Online]. Disponibile su: https://www.e-nacalai.jp/ec2/EC-srchdetl.cfm?Dum=1&syohin=3172245&syubetsu=3

[39] «Product Information | Potassium Dihydrogenphosphate 28720-65 500G NACALAI TESQUE, INC. | e-Nacalai Search Version». Consultato: 27 luglio 2026. [Online]. Disponibile su: https://www.e-nacalai.jp/ec2/EC-srchdetl.cfm?Dum=1&syohin=2872065&syubetsu=3
[40] «Product Information | Potassium Chloride 28513-85 500G NACALAI TESQUE, INC. | e-Nacalai Search Version». Consultato: 27 luglio 2026. [Online]. Disponibile su: https://www.e-nacalai.jp/ec2/EC-srchdetl.cfm?Dum=1&syohin=2851385&syubetsu=3
[41] «Sodio dodecil solfato ACS reagent, ≥99.0% | Sigma-Aldrich». Consultato: 6 agosto 2026. [Online]. Disponibile su: https://www.sigmaaldrich.com/IT/it/product/sial/436143?srsltid=AfmBOor8ogjmv5JaaZeU6QrKoT8AUO6I8KI0H-zw9X-HA8KTYVPNHchB
[42] «Product Information | 1mol/l-Hydrochloric Acid 37314-15 500ML NACALAI TESQUE, INC. | e-Nacalai Search Version». Consultato: 27 luglio 2026. [Online]. Disponibile su: https://www.e-nacalai.jp/ec2/EC-srchdetl.cfm?jump=EC-srchdetl&syohin=3731415&syubetsu=3&l=EN&lc=1
[43] «Product Information | Sodium Hydroxide 31511-05 500G NACALAI TESQUE, INC. | e-Nacalai Search Version». Consultato: 27 luglio 2026. [Online]. Disponibile su: https://www.e-nacalai.jp/ec2/EC-srchdetl.cfm?jump=EC-srchdetl&syohin=3151105&syubetsu=3&l=EN&lc=1
[44] V. Staven, M. Waaseth, S. Wang, I. Grønlie, e I. Tho, «Utilization of the Tyndall Effect for Enhanced Visual Detection of Particles in Compatibility Testing of Intravenous Fluids: Validity and Reliability», *PDA J. Pharm. Sci. Technol.*, vol. 69, fasc. 2, pp. 270–283, mar. 2015, doi: 10.5731/pdajpst.2015.01020.
[45] A. Wennerberg, R. Ohlsson, B.-G. Rosén, e B. Andersson, «Characterizing three-dimensional topography of engineering and biomaterial surfaces by confocal laser scanning and stylus techniques», *Med. Eng. Phys.*, vol. 18, fasc. 7, pp. 548–556, ott. 1996, doi: 10.1016/1350-4533(95)00005-4.
[46] J. I. Goldstein, D. E. Newbury, J. R. Michael, N. W. M. Ritchie, J. H. J. Scott, e D. C. Joy, *Scanning Electron Microscopy and X-Ray Microanalysis*. New York, NY: Springer, 2018. doi: 10.1007/978-1-4939-6676-9.
[47] J. B. Pawley, A c. di, *Handbook Of Biological Confocal Microscopy*. Boston, MA: Springer US, 2006. doi: 10.1007/978-0-387-45524-2.
[48] B. H. Stuart, *Infrared Spectroscopy: Fundamentals and Applications*, 1ª ed. in Analytical Techniques in the Sciences. Wiley, 2004. doi: 10.1002/0470011149.
[49] T. M. Kolev, E. A. Velcheva, B. A. Stamboliyska, e M. Spiteller, «DFT and experimental studies of the structure and vibrational spectra of curcumin», *Int. J. Quantum Chem.*, vol. 102, fasc. 6, pp. 1069–1079, gen. 2005, doi: 10.1002/qua.20469.
[50] M. Ranjbar-Mohammadi, S. H. Bahrami, e M. T. Joghataei, «Fabrication of novel nanofiber scaffolds from gum tragacanth/poly(vinyl alcohol) for wound dressing application: In vitro evaluation and antibacterial properties», *Mater. Sci. Eng. C*, vol. 33, fasc. 8, pp. 4935–4943, dic. 2013, doi: 10.1016/j.msec.2013.08.016.
[51] R. R. Jones, D. C. Hooper, L. Zhang, D. Wolverson, e V. K. Valev, «Raman Techniques: Fundamentals and Frontiers», *Nanoscale Res. Lett.*, vol. 14, fasc. 1, p. 231, lug. 2019, doi: 10.1186/s11671-019-3039-2.
[52] E. Smith e G. Dent, *Modern Raman Spectroscopy – A Practical Approach*, 1ª ed. Wiley, 2004. doi: 10.1002/0470011831.
[53] H. Schulz, M. Baranska, e R. Baranski, «Potential of NIR-FT-Raman spectroscopy in natural carotenoid analysis», *Biopolymers*, vol. 77, fasc. 4, pp. 212–221, mar. 2005, doi: 10.1002/bip.20215.

[54] G. W. H. Höhne, W. F. Hemminger, e H.-J. Flammersheim, *Differential Scanning Calorimetry*. Berlin, Heidelberg: Springer Berlin Heidelberg, 2003. doi: 10.1007/978-3-662-06710-9.
[55] P. A. Hassan, S. Rana, e G. Verma, «Making Sense of Brownian Motion: Colloid Characterization by Dynamic Light Scattering», *Langmuir*, vol. 31, fasc. 1, pp. 3–12, gen. 2015, doi: 10.1021/la501789z.
[56] S. Bhattacharjee, «DLS and zeta potential – What they are and what they are not?», *J. Controlled Release*, vol. 235, pp. 337–351, ago. 2016, doi: 10.1016/j.jconrel.2016.06.017.
[57] S. Rudaz, T. Le Saux, J. Prat, P. Gareil, e J. Veuthey, «Ultrashort partial-filling technique in capillary electrophoresis for infinite resolution of tramadol enantiomers and its metabolites with highly sulfated cyclodextrins», *ELECTROPHORESIS*, vol. 25, fasc. 16, pp. 2761–2771, ago. 2004, doi: 10.1002/elps.200406052.
[58] G. Agrawal, Y. S. Negi, S. Pradhan, M. Dash, e S. K. Samal, «Wettability and contact angle of polymeric biomaterials», in *Characterization of Polymeric Biomaterials*, Elsevier, 2017, pp. 57–81. doi: 10.1016/B978-0-08-100737-2.00003-0.
[59] «ISO 10993-5:2009 - Biological evaluation of medical devices — Part 5: Tests for in vitro cytotoxicity». Consultato: 1 agosto 2026. [Online]. Disponibile su: https://www.iso.org/standard/36406.html?
[60] R. Gupta, Y. Chen, M. Sarkar, e H. Xie, «Surfactant Mediated Accelerated and Discriminatory In Vitro Drug Release Method for PLGA Nanoparticles of Poorly Water-Soluble Drug», *Pharmaceuticals*, vol. 15, fasc. 12, p. 1489, nov. 2022, doi: 10.3390/ph15121489.
[61] J. Huang, C. Fan, Y. Ma, e G. Huang, «Exploring Thermal Dynamics in Wound Healing: The Impact of Temperature and Microenvironment», *Clin. Cosmet. Investig. Dermatol.*, vol. Volume 17, pp. 1251–1258, mag. 2024, doi: 10.2147/CCID.S468396.
[62] A. Wesełucha-Birczyńska *et al.*, «Early Recognition of the PCL/Fibrous Carbon Nanocomposites Interaction with Osteoblast-like Cells by Raman Spectroscopy», *Nanomaterials*, vol. 11, fasc. 11, p. 2890, ott. 2021, doi: 10.3390/nano11112890.
[63] M. Manso, A. Valsesia, G. Ceccone, e F. Rossi, «Activation of PCL Surface by Ion Beam Treatment to Enhance Protein Adsorption», *J. Bioact. Compat. Polym.*, vol. 19, fasc. 4, pp. 287–300, lug. 2004, doi: 10.1177/0883911504045174.
[64] W.-H. Lee, C.-Y. Loo, M. Bebawy, F. Luk, R. Mason, e R. Rohanizadeh, «Curcumin and its Derivatives: Their Application in Neuropharmacology and Neuroscience in the 21st Century», *Curr. Neuropharmacol.*, vol. 11, fasc. 4, pp. 338–378, giu. 2013, doi: 10.2174/1570159X11311040002.
[65] Y. M. Shin, M. M. Hohman, M. P. Brenner, e G. C. Rutledge, «Experimental characterization of electrospinning: the electrically forced jet and instabilities», *Polymer*, vol. 42, fasc. 25, pp. 09955–09967, dic. 2001, doi: 10.1016/S0032-3861(01)00540-7.
[66] B. Yalcinkaya e M. Buzgo, «A Guide for Industrial Needleless Electrospinning of Synthetic and Hybrid Nanofibers», *Polymers*, vol. 17, fasc. 22, p. 3019, nov. 2025, doi: 10.3390/polym17223019.
[67] R. CeCe, L. Jining, M. Islam, J. G. Korvink, e B. Sharma, «An Overview of the Electrospinning of Polymeric Nanofibers for Biomedical Applications Related to Drug Delivery», *Adv. Eng. Mater.*, vol. 26, fasc. 1, p. 2301297, gen. 2024, doi: 10.1002/adem.202301297.
[68] N. Bhardwaj e S. C. Kundu, «Electrospinning: A fascinating fiber fabrication technique», *Biotechnol. Adv.*, vol. 28, fasc. 3, pp. 325–347, mag. 2010, doi: 10.1016/j.biotechadv.2010.01.004.

[69] A. W. Laramée e C. Pellerin, «Raman Analysis of Orientation and Crystallinity in High T_g , Low Crystallinity Electrospun Fibers», *Appl. Spectrosc.*, vol. 77, fasc. 11, pp. 1289–1299, nov. 2023, doi: 10.1177/00037028231202791.
[70] S. Metwally e U. Stachewicz, «Surface potential and charges impact on cell responses on biomaterials interfaces for medical applications», *Mater. Sci. Eng. C*, vol. 104, p. 109883, nov. 2019, doi: 10.1016/j.msec.2019.109883.
[71] A. Tuanchai *et al.*, «Bilayer Scaffolds of PLLA/PCL/CAB Ternary Blend Films and Curcumin-Incorporated PLGA Electrospun Nanofibers: The Effects of Polymer Compositions and Solvents on Morphology and Molecular Interactions», *Polymers*, vol. 16, fasc. 12, p. 1679, giu. 2024, doi: 10.3390/polym16121679.
[72] T.-T. Phan, P. See, S.-T. Lee, e S.-Y. Chan, «Protective Effects of Curcumin against Oxidative Damage on Skin Cells In Vitro: Its Implication for Wound Healing»:, *J. Trauma Inj. Infect. Crit. Care*, vol. 51, fasc. 5, pp. 927–931, nov. 2001, doi: 10.1097/00005373-200111000-00017.
[73] A. Darawsha, A. Trachtenberg, J. Levy, e Y. Sharoni, «The Protective Effect of Carotenoids, Polyphenols, and Estradiol on Dermal Fibroblasts under Oxidative Stress», *Antioxidants*, vol. 10, fasc. 12, p. 2023, dic. 2021, doi: 10.3390/antiox10122023.
[74] C. Qian, E. A. Decker, H. Xiao, e D. J. McClements, «Physical and chemical stability of β-carotene-enriched nanoemulsions: Influence of pH, ionic strength, temperature, and emulsifier type», *Food Chem.*, vol. 132, fasc. 3, pp. 1221–1229, giu. 2012, doi: 10.1016/j.foodchem.2011.11.091.

9 Appendix

Unless otherwise specified, for figures composed of two juxtaposed micrographs, panel (a) refers to the image on the left and panel (b) to the image on the right.

9.1 Morphological Characterisation

9.1.1 Laser-Optical Microscopy

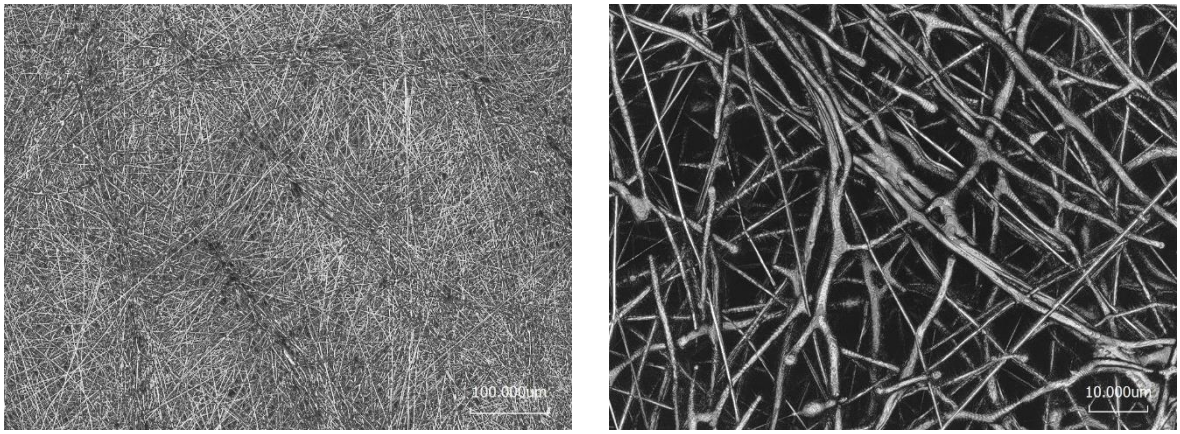


Figure A 1 – Laser-optical microscopy of the PCL-PCL (7:3) control bilayer scaffold, deposition 1 – a) 20X overview showing homogeneous, randomly oriented fibre deposition; b) 150X detail of the interconnected fibrous network, consistent with the morphology reported in the main text.

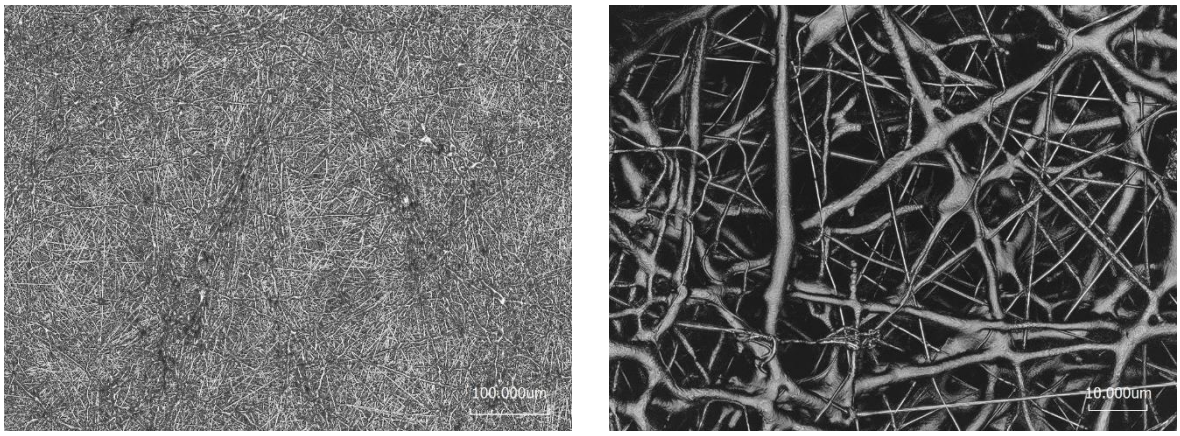


Figure A 2 – Laser-optical microscopy of the PCL-PCL (7:3) control bilayer scaffold, deposition 2 – a) 20X overview; b) 150X detail, confirming the reproducibility of the fibrous morphology across depositions (same field of view as Figure 37a).

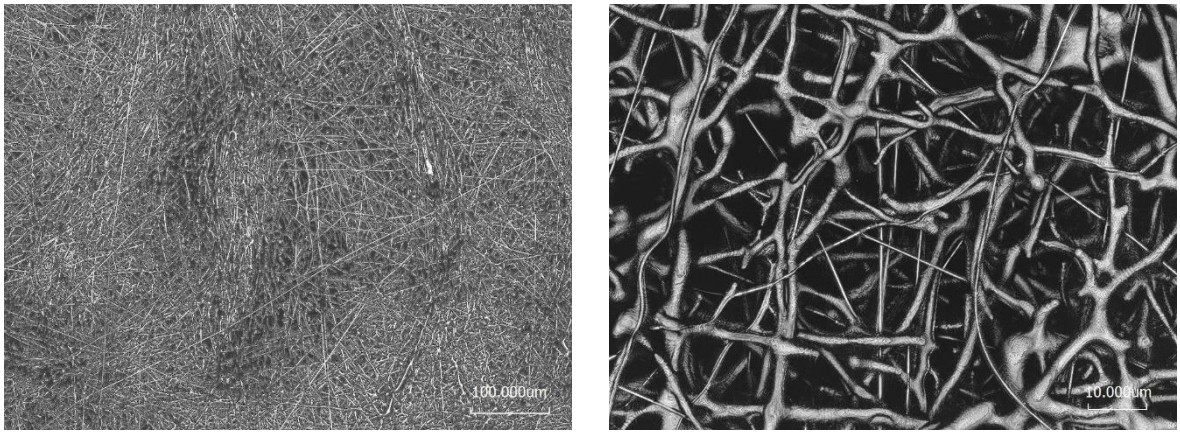


Figure A 3 – Laser-optical microscopy of the PCL-PCL (7:3) control bilayer scaffold, deposition 3 – a) 20X overview; b) 150X detail, showing a homogeneous mesh comparable to the previous depositions.

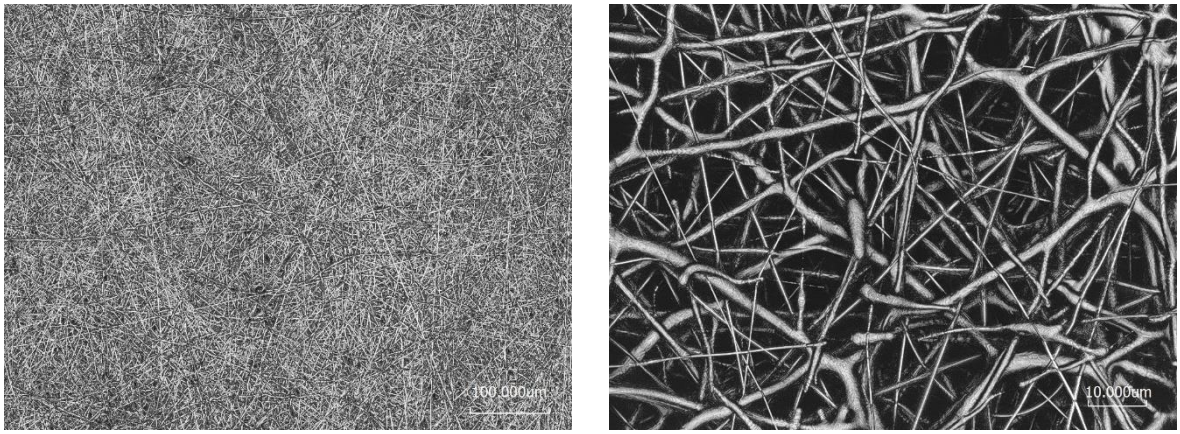


Figure A 4 – Laser-optical microscopy of the PCL-PCL (7:3) control bilayer scaffold, deposition 4 – a) 20X overview; b) 150X detail, further confirming batch-to-batch morphological consistency.

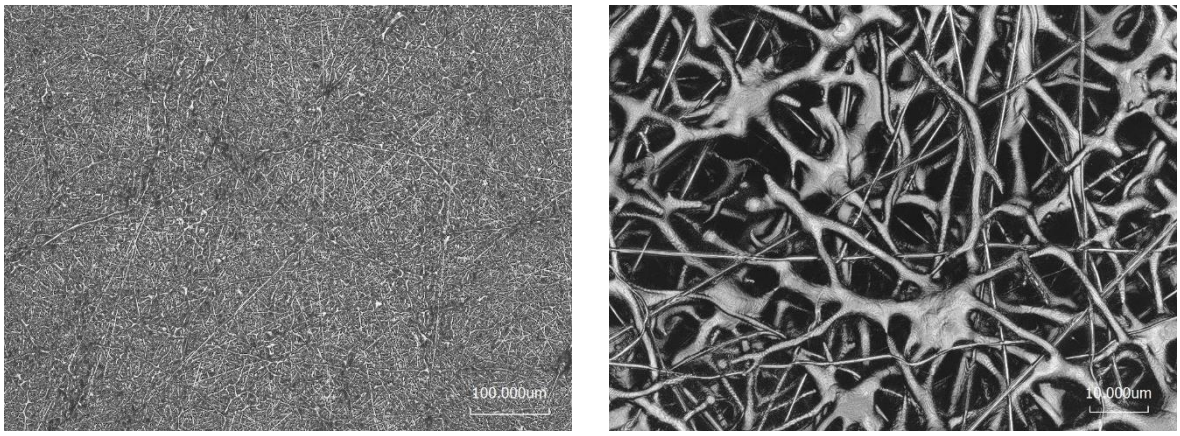


Figure A 5 – Laser-optical microscopy of the PCL-PCL (7:3) control bilayer scaffold, deposition 5 – a) 20X overview; b) 150X detail, showing a slightly more open pore structure with thicker fibre bundles, still within the expected morphological variability.

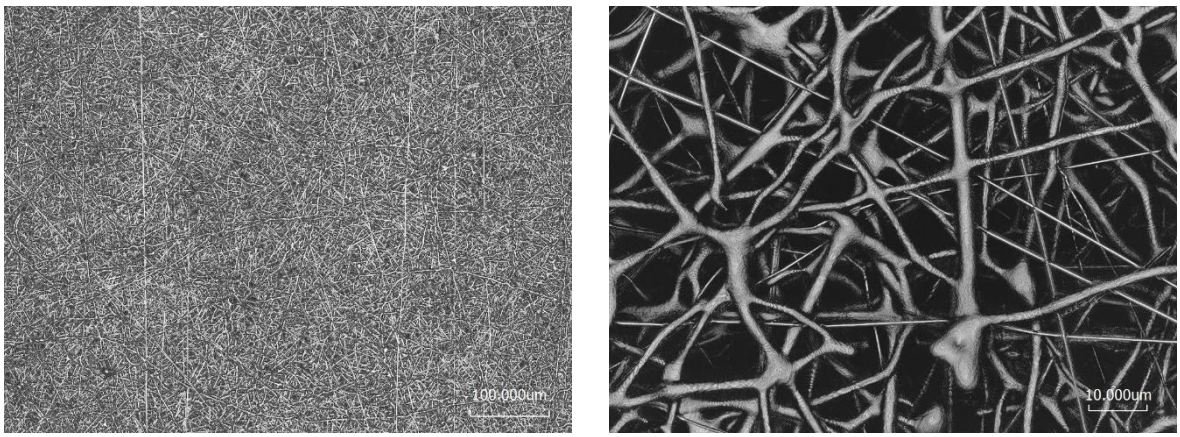


Figure A 6 – Laser-optical microscopy of the PCL-PCL (7:3) control bilayer scaffold, deposition 6 – a) 20X overview; b) 150X detail, showing a homogeneous fibrous network consistent with the other depositions.

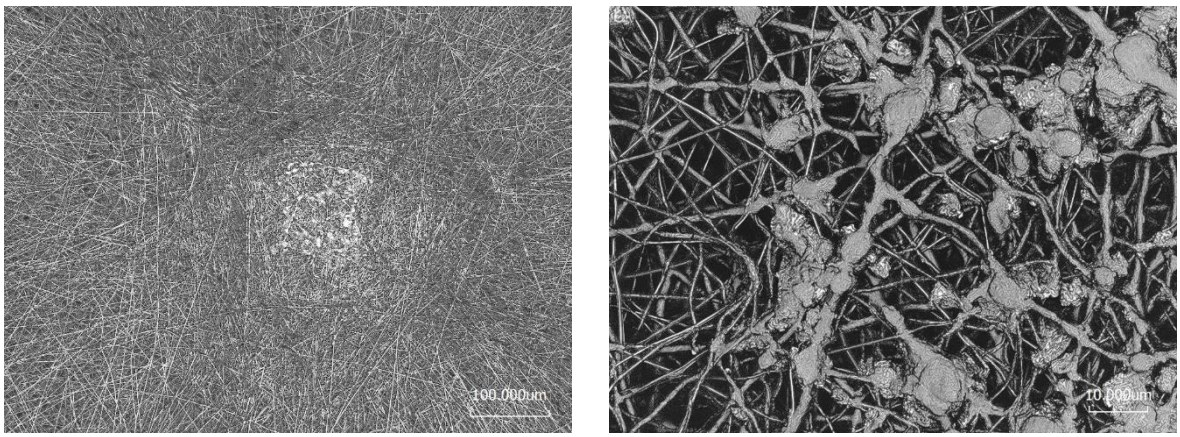


Figure A 7 – Laser-optical microscopy of the PCL-PCL (7:3) control bilayer scaffold, deposition 7 – a) 20X overview showing a localised deposition defect (bright, square-shaped patch) within an otherwise homogeneous fibrous mat; b) 150X detail resolving the defect as a cluster of granular/particulate agglomerates deposited on the fibre network.

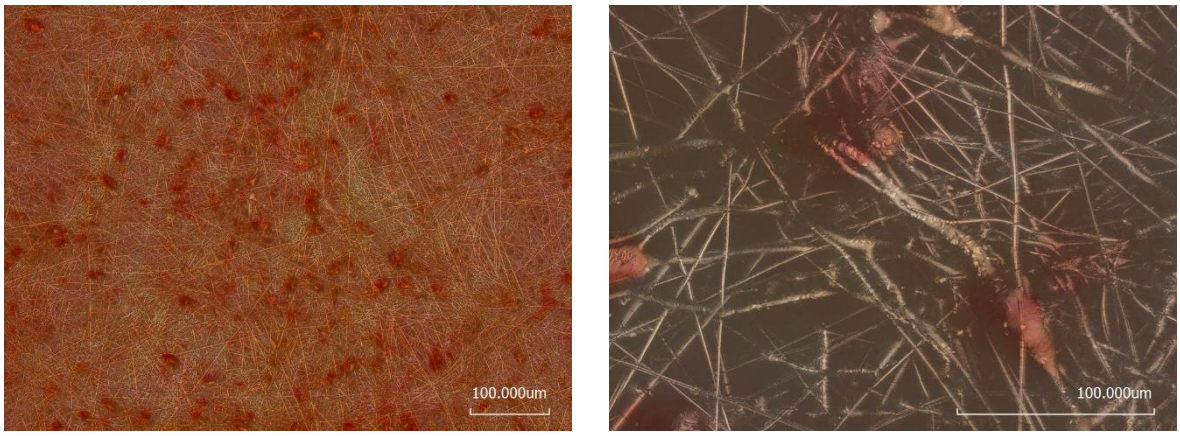


Figure A 8 – Laser-optical microscopy of the β-Carotene-functionalized bilayer scaffold, deposition 1 – a) 100X overview (same field of view as Figure 36b); b) 100X detail, showing β-carotene aggregates distributed across the fibrous network.

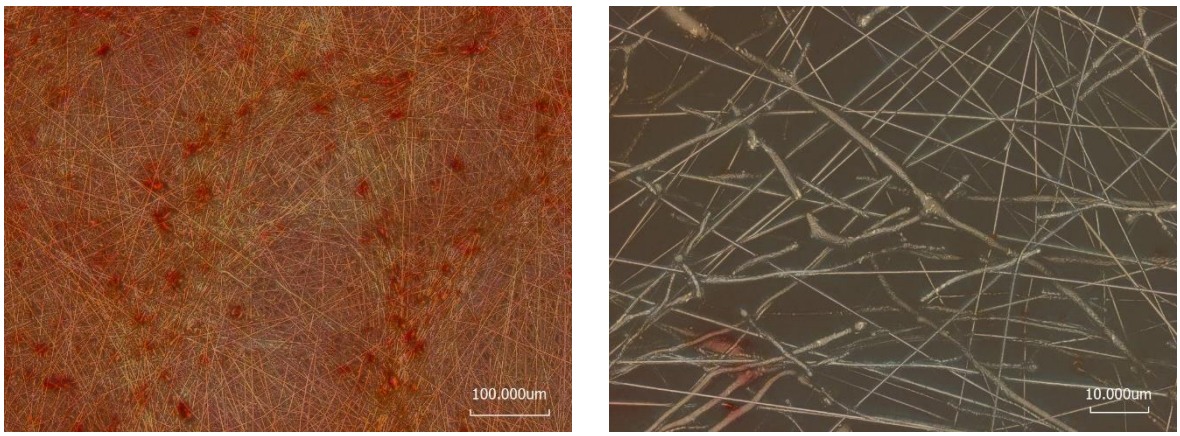


Figure A 9 – Laser-optical microscopy of the β-Carotene-functionalized bilayer scaffold, deposition 2 – a) 100X overview; b) 150X detail, confirming the presence of carotenoid aggregates consistent with deposition 1.

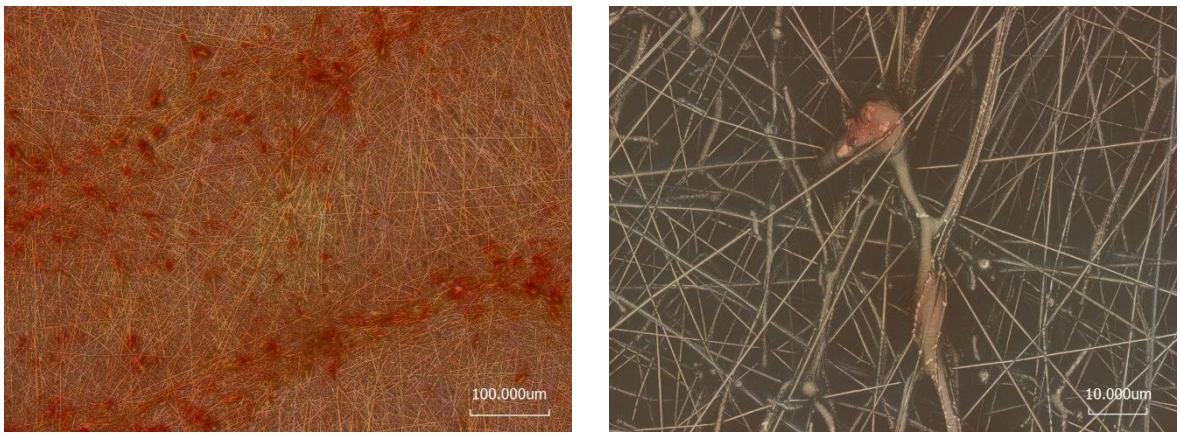


Figure A 10 – Laser-optical microscopy of the β-Carotene-functionalized bilayer scaffold, deposition 3 – a) 100X overview; b) 150X detail, showing an aggregate embedded within the fibrous mesh (same field of view as Figure 37b).

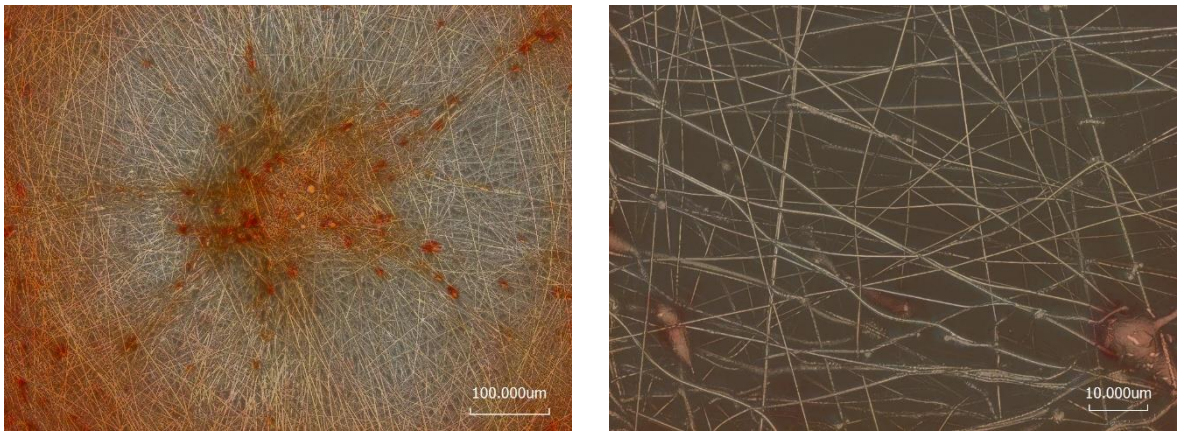


Figure A 11 – Laser-optical microscopy of the β-Carotene-functionalized bilayer scaffold, deposition 4 – a) 100X overview showing a localised deposition defect, with fibres converging radially around a central aggregate (same field of view as Figure 38b); b) 150X detail of the same region.

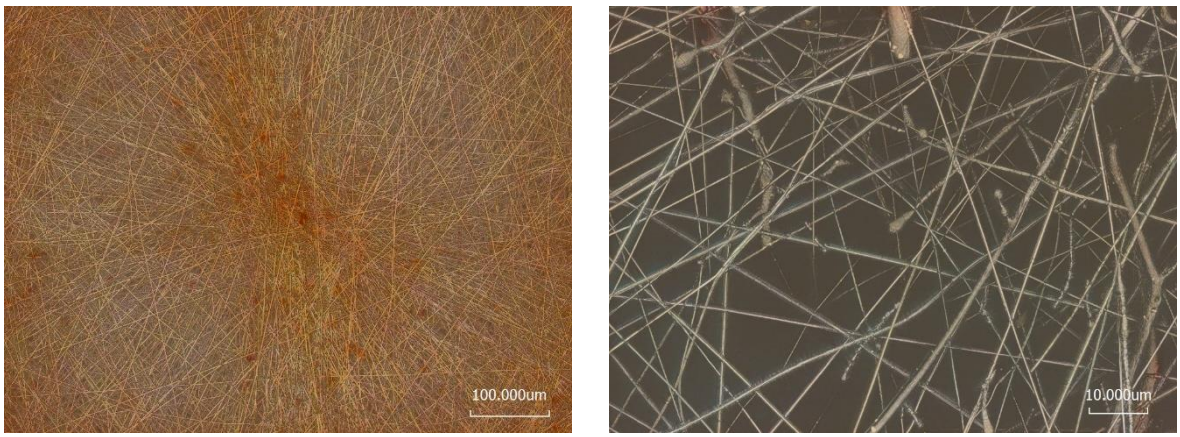


Figure A 12 – Laser-optical microscopy of the β-Carotene-functionalized bilayer scaffold, deposition 5 – a) 100X overview showing a similar localised deposition defect, with radial fibre convergence around a central aggregate; b) 150X detail.

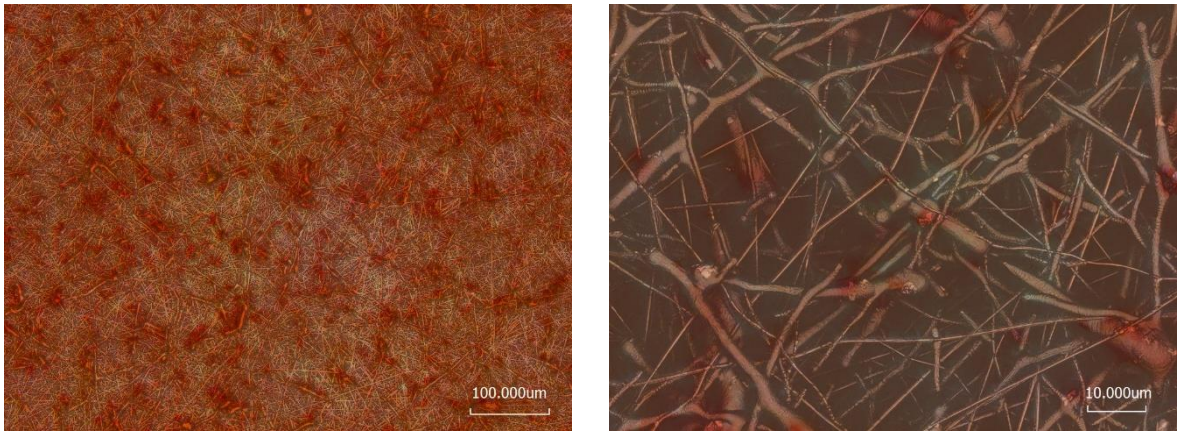


Figure A 13 – Laser-optical microscopy of the β-Carotene-functionalized bilayer scaffold, deposition 6 – a) 100X overview; b) 150X detail, showing a fibrous network with distributed carotenoid aggregates comparable to the previous depositions.

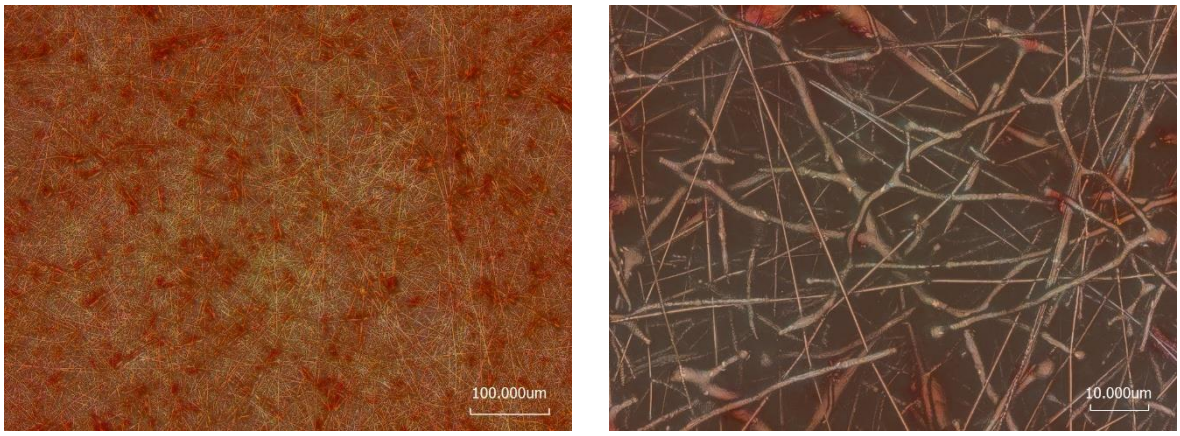


Figure A 14 – Laser-optical microscopy of the β-Carotene-functionalized bilayer scaffold, deposition 7 – a) 100X overview; b) 150X detail, confirming the reproducibility of the fibrous morphology and aggregate distribution across depositions.

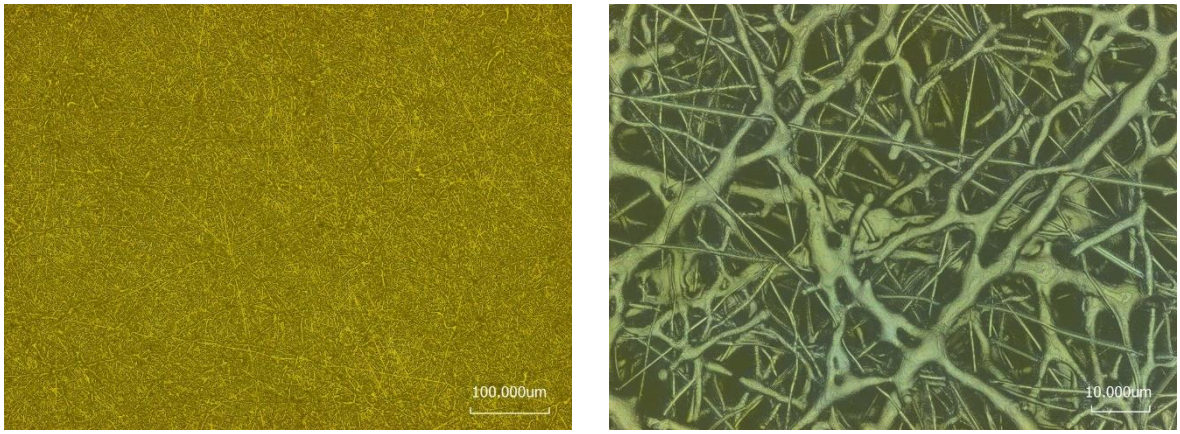


Figure A 15 – Laser-optical microscopy of the Curcumin-functionalized bilayer scaffold, deposition 1 – a) 100X overview showing a homogeneous fibrous network; b) 150X detail of the interconnected fibres.

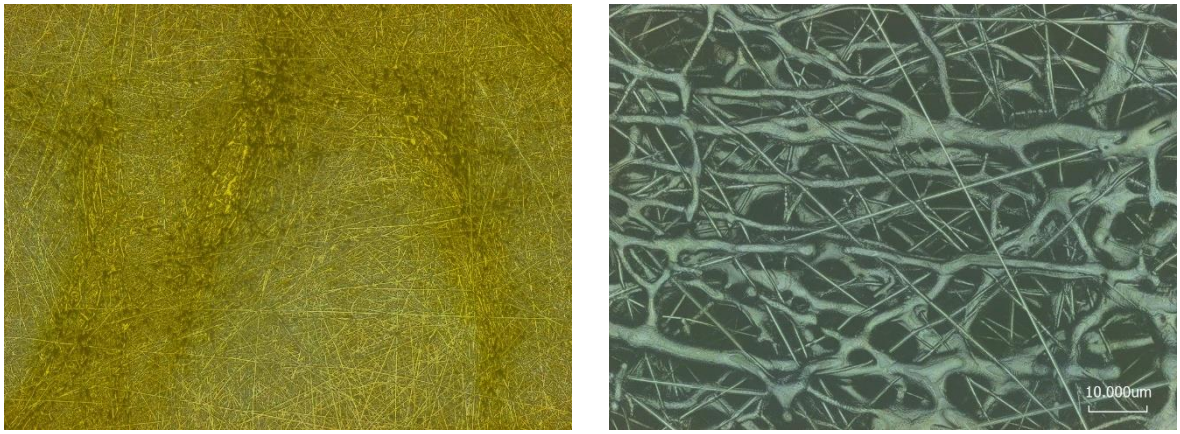


Figure A 16 – Laser-optical microscopy of the Curcumin-functionalized bilayer scaffold, deposition 2 – a) 100X overview; b) 150X detail, confirming the reproducibility of the fibrous morphology.

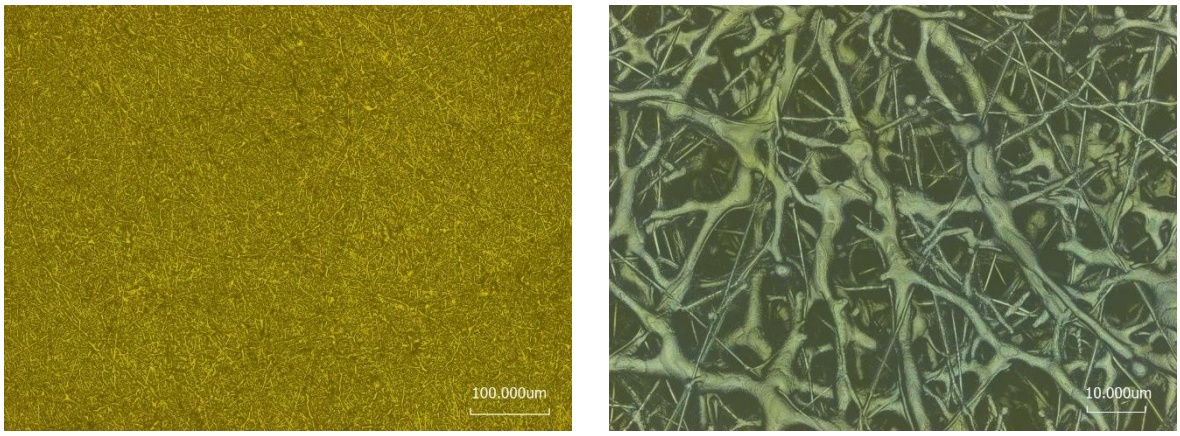


Figure A 17 – Laser-optical microscopy of the Curcumin-functionalized bilayer scaffold, deposition 3 – a) 100X overview (same field of view as Figure 36c); b) 150X detail, showing a homogeneous mesh comparable to the previous depositions.

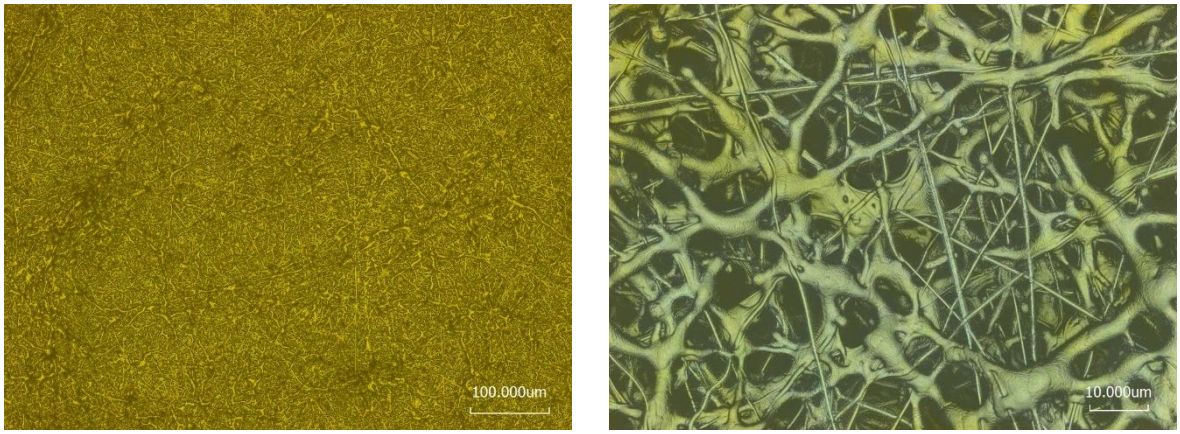


Figure A 18 – Laser-optical microscopy of the Curcumin-functionalized bilayer scaffold, deposition 4 – a) 100X overview; b) 150X detail, further confirming batch-to-batch morphological consistency.

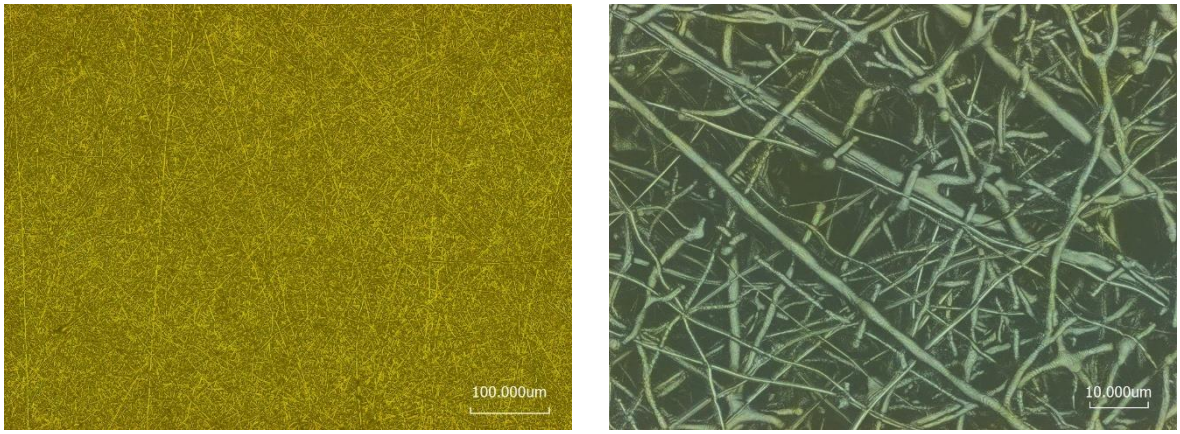


Figure A 19 – Laser-optical microscopy of the Curcumin-functionalized bilayer scaffold, deposition 5 – a) 100X overview; b) 150X detail, confirming the reproducibility of the fibrous morphology across depositions (same field of view as Figure 37c).

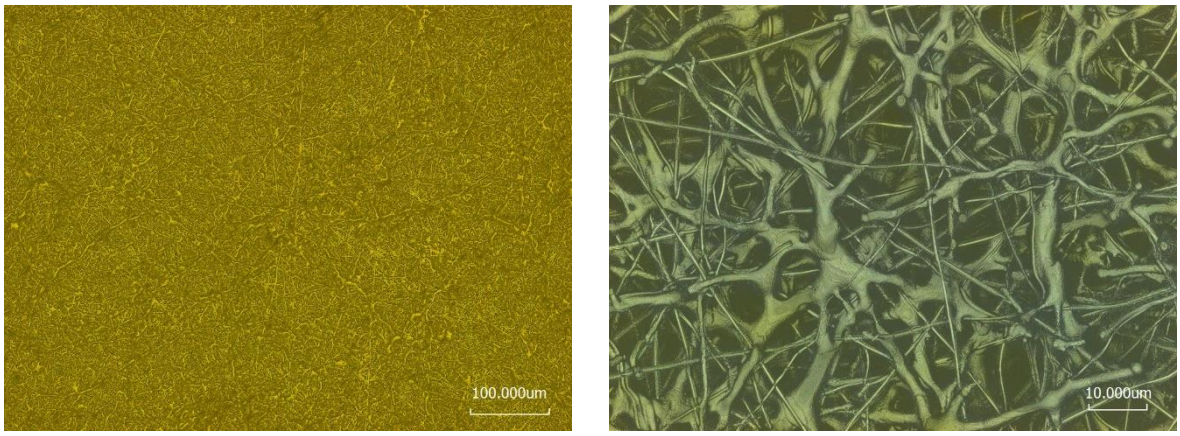


Figure A 20 – Laser-optical microscopy of the Curcumin-functionalized bilayer scaffold, deposition 6 – a) 100X overview; b) 150X detail, comparable to the previous depositions.

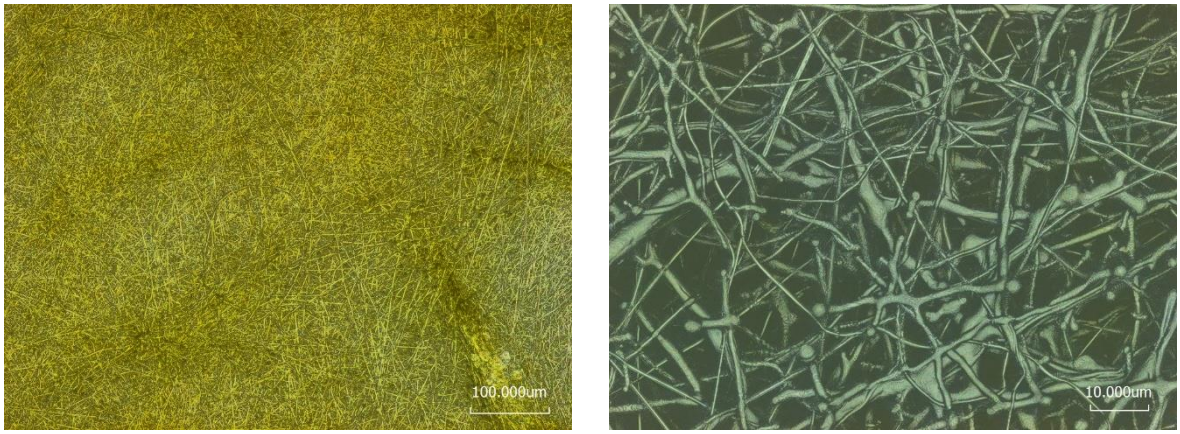


Figure A 21 – Laser-optical microscopy of the Curcumin-functionalized bilayer scaffold, deposition 7 – a) 100X overview; b) 150X detail, confirming the reproducibility of the fibrous morphology across the batch.

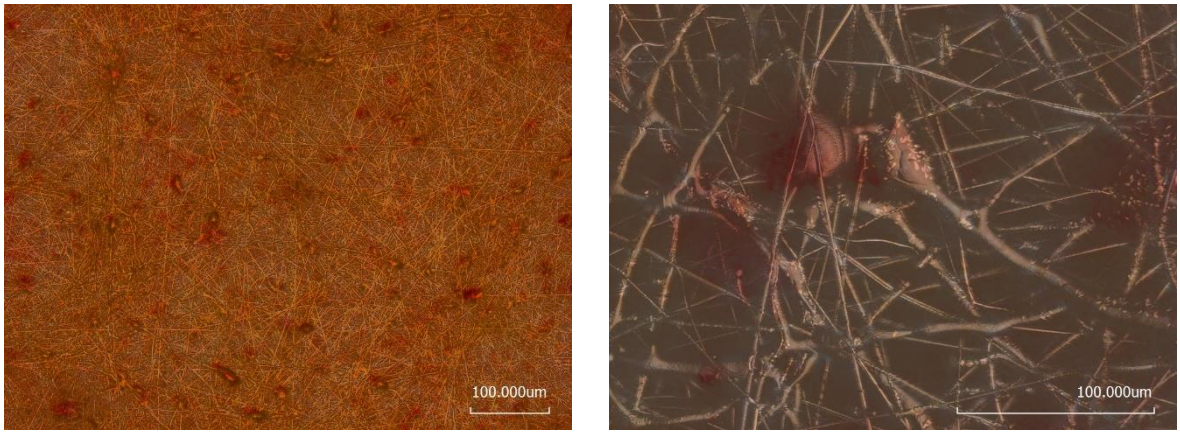


Figure A 22 – – Laser-optical microscopy of the Mix-functionalized bilayer scaffold, deposition 1 – a) 100X overview; b) 100X detail, showing aggregates of the combined bioactive agents distributed across the fibrous network.

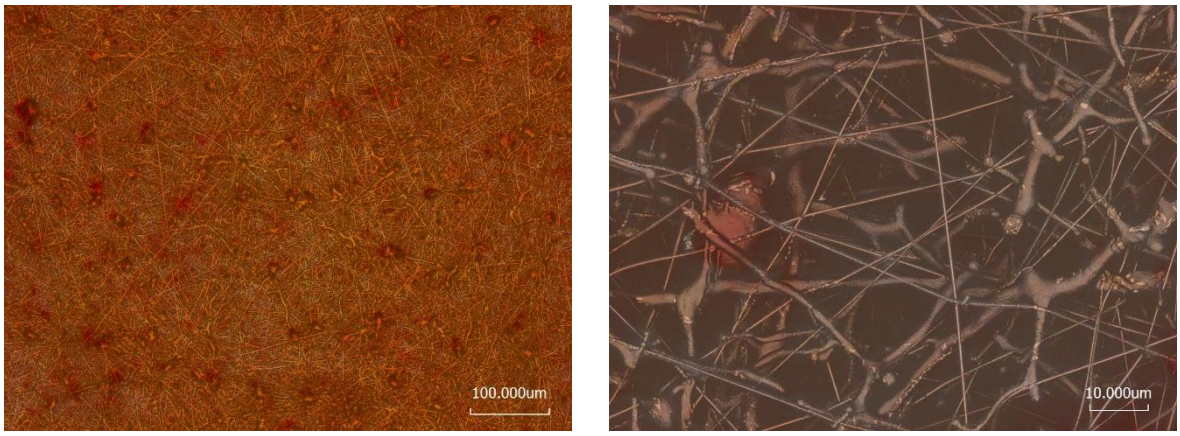


Figure A 23 – Laser-optical microscopy of the Mix-functionalized bilayer scaffold, deposition 2 – a) 100X overview (same field of view as Figure 36d); b) 150X detail (same field of view as Figure 37d).

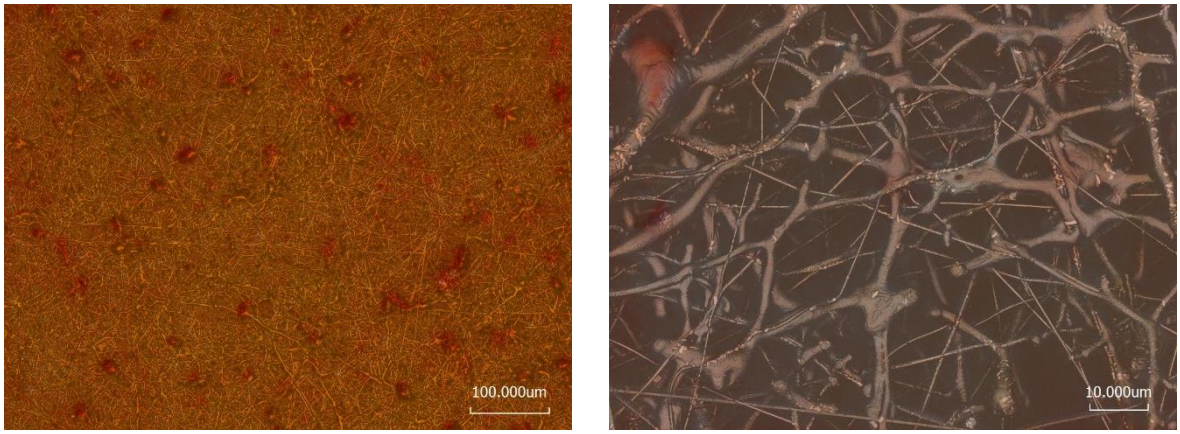


Figure A 24 – Laser-optical microscopy of the Mix-functionalized bilayer scaffold, deposition 3 – a) 100X overview; b) 150X detail, showing a fibrous network with distributed aggregates comparable to the previous depositions.

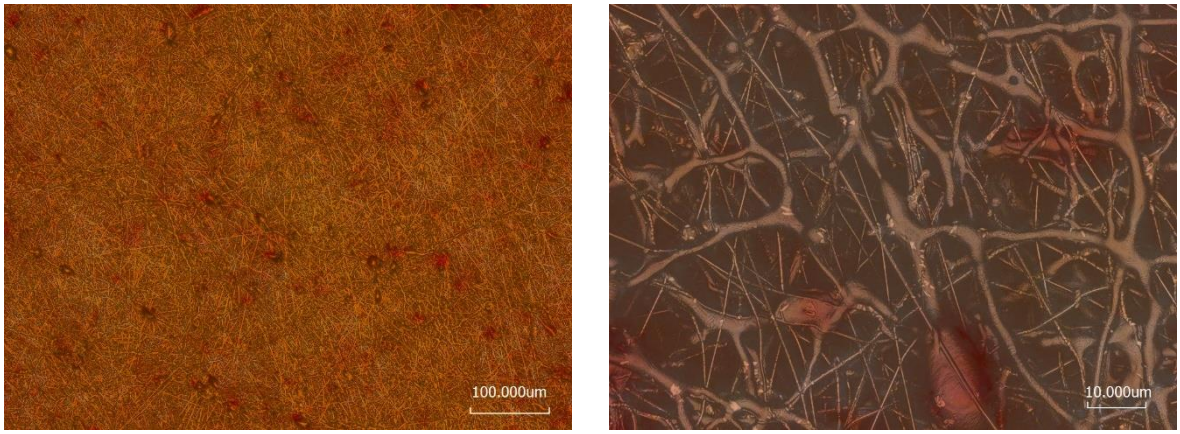


Figure A 25 – Laser-optical microscopy of the Mix-functionalized bilayer scaffold, deposition 4 – a) 100X overview; b) 150X detail, confirming the reproducibility of the fibrous morphology and aggregate distribution across depositions.

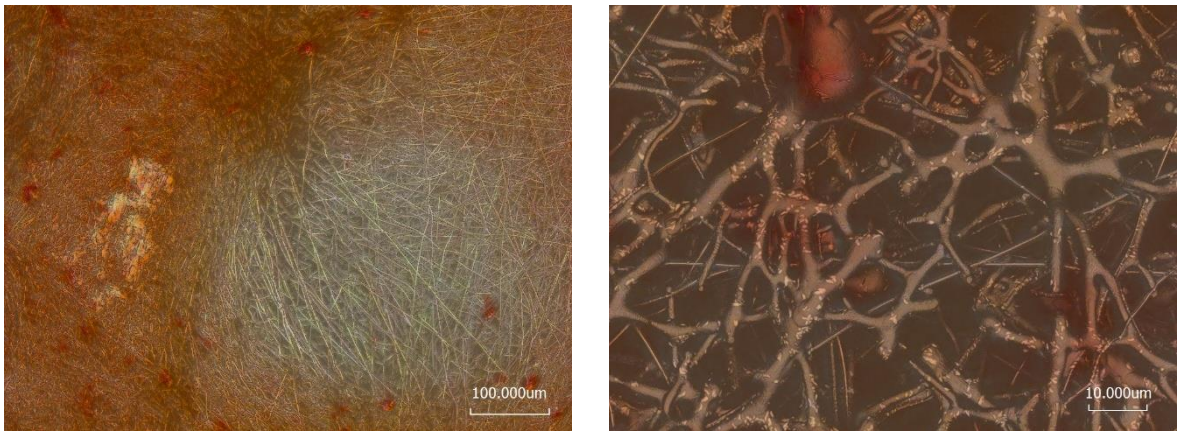


Figure A 26 – Laser-optical microscopy of the Mix-functionalized bilayer scaffold, deposition 5 – a) 100X overview showing a localised deposition defect at the boundary between a denser aggregate region and an area of altered fibre alignment; b) 150X detail of the same region.

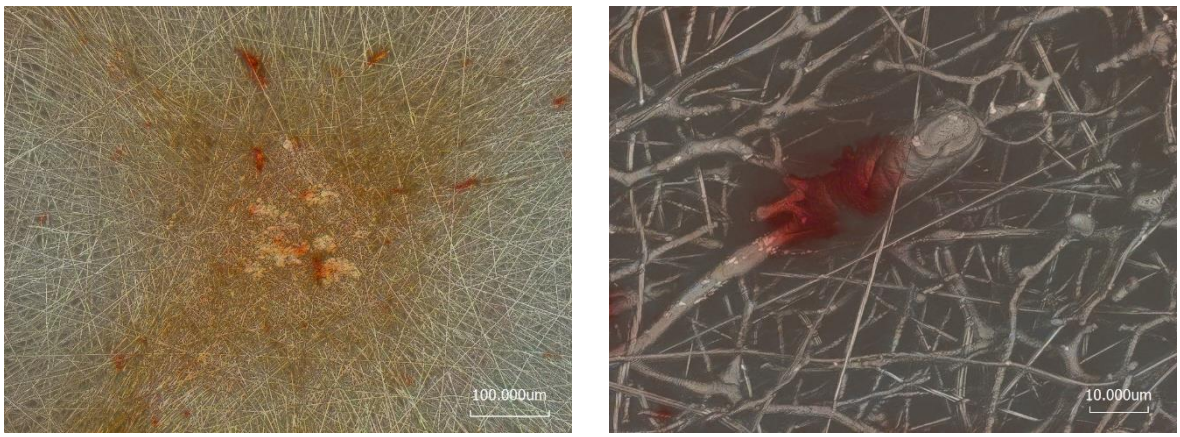


Figure A 27 – Laser-optical microscopy of the Mix-functionalized bilayer scaffold, deposition 6 – a) 100X overview showing a localised deposition defect, with fibres converging radially around a central aggregate, consistent with the defect observed in the β-Carotene scaffold (see Figure A 11); b) 150X detail of the same region.

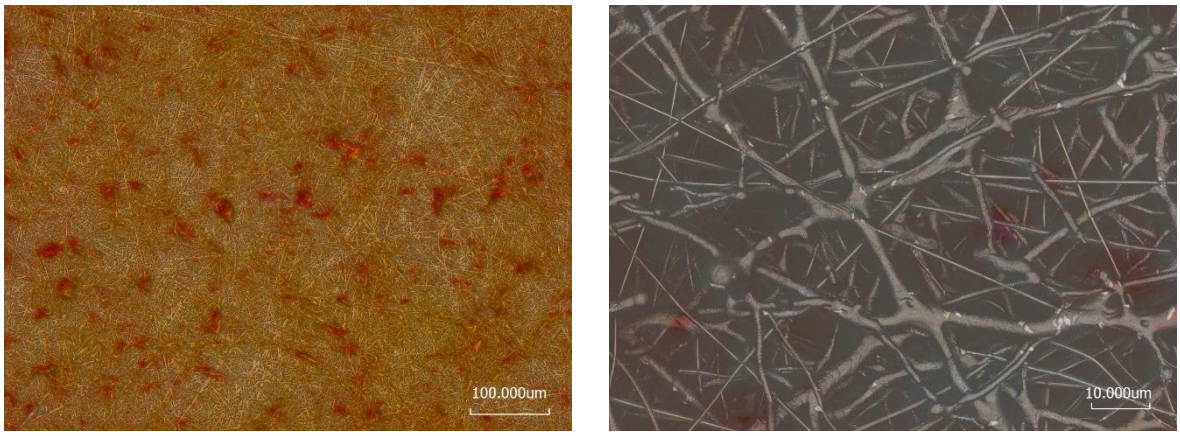


Figure A 28 – Laser-optical microscopy of the Mix-functionalized bilayer scaffold, deposition 7 – a) 100X overview; b) 150X detail, showing a fibrous network with distributed aggregates comparable to the other depositions.

9.1.2 FESEM

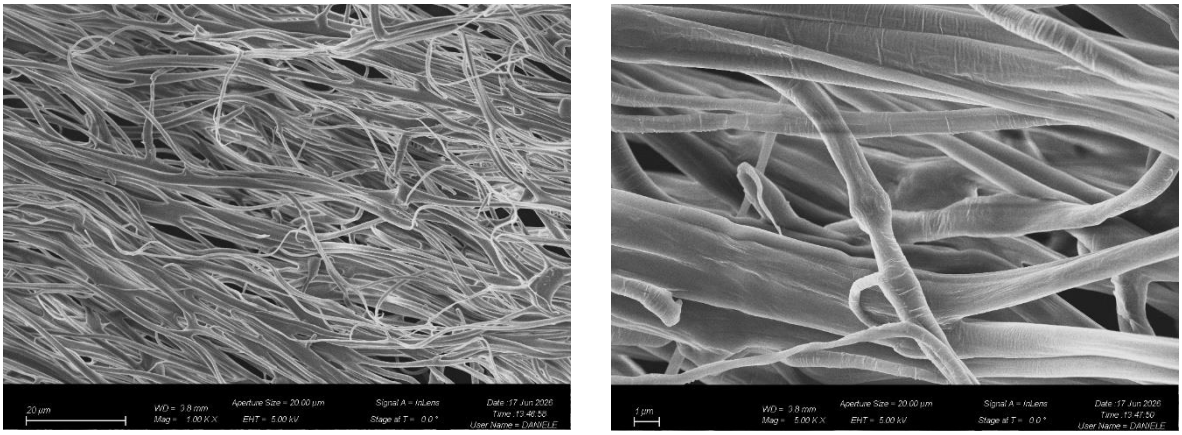


Figure A 29 – FESEM images of the PCL-PCL (7:3) control bilayer scaffold – a) 1.00KX overview showing smooth, ribbon-like fibres; b) 5.00KX detail of the fibre surface, showing no visible aggregates or defects.

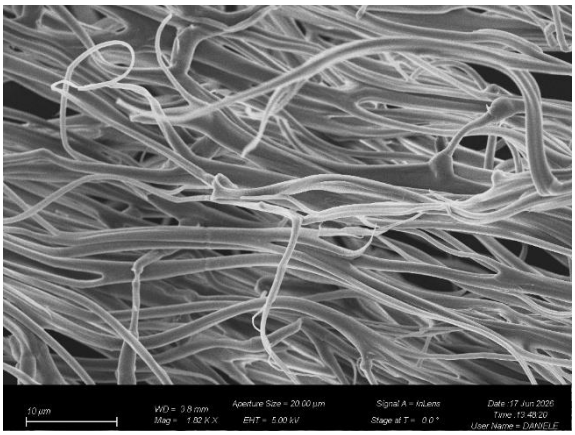


Figure A 30 – FESEM image of the PCL-PCL (7:3) control bilayer scaffold, additional field of view at 1.02KX, confirming the smooth fibre morphology observed in Figure A 29.

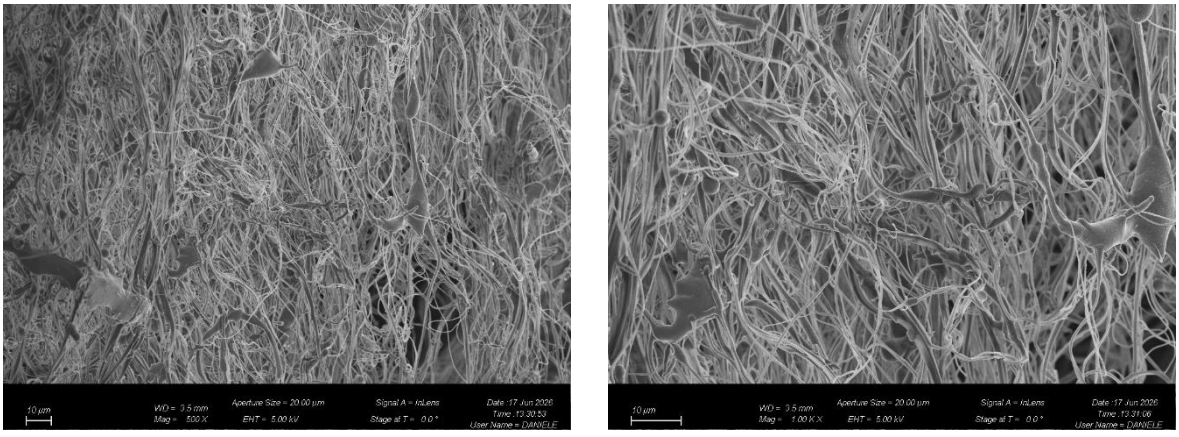


Figure A 31 – FESEM images of the β-Carotene-functionalized bilayer scaffold – a) 500X overview; b) 1.00KX detail, showing irregular aggregate deposits distributed across the fibrous network.

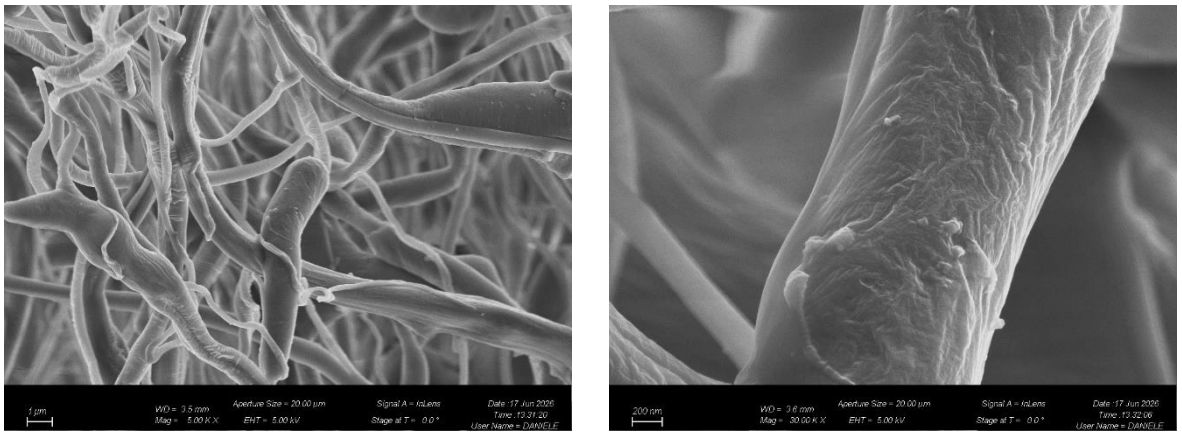


Figure A 32 – FESEM images of the β-Carotene-functionalized bilayer scaffold – a) 5.00KX detail of a fibre bundle; b) 30.00KX detail showing nano-aggregates on the fibre surface.

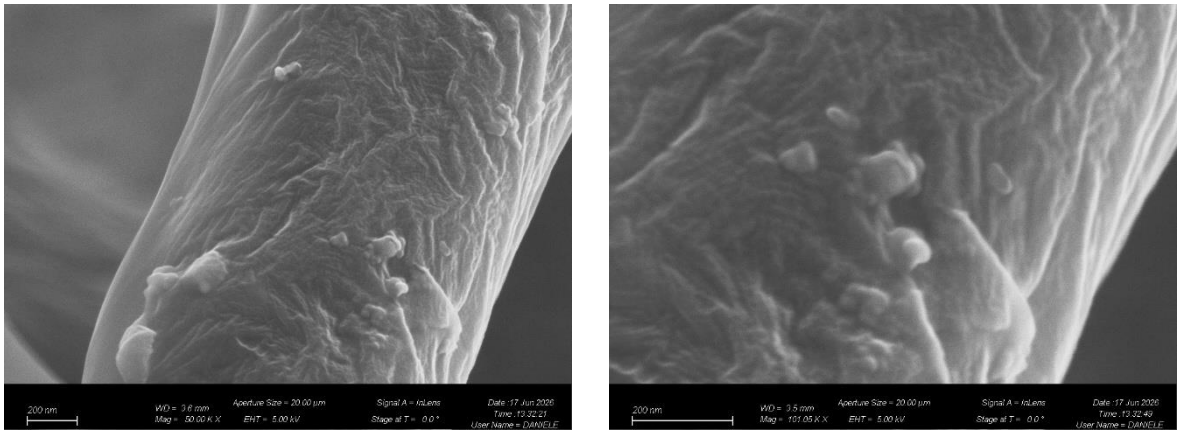


Figure A 33 – FESEM images of the β-Carotene-functionalized bilayer scaffold – a) 50.00KX and b) 101.05KX close-up detail of surface nano-aggregates on a single fibre.

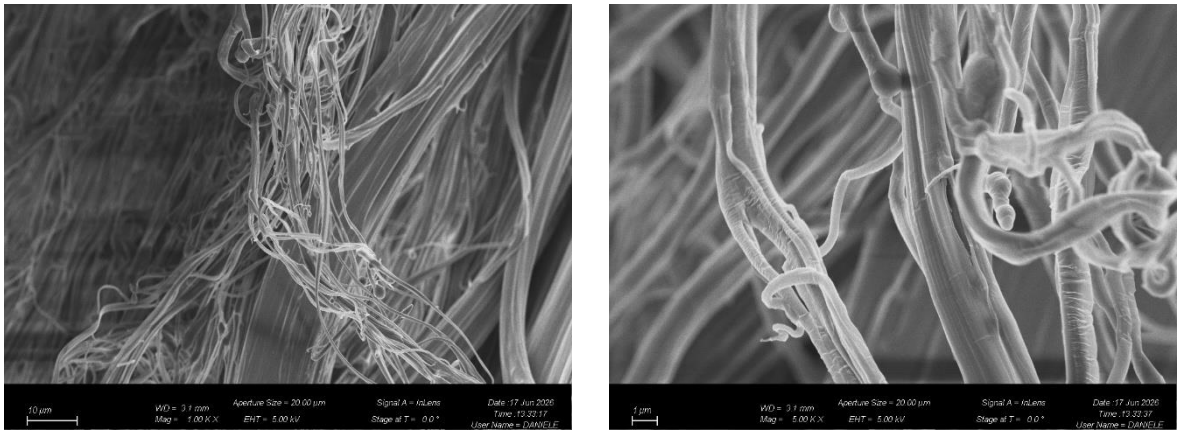


Figure A 34 – FESEM images of the β-Carotene-functionalized bilayer scaffold – a) 1.00KX and b) 5.00KX detail of a fibre bundle region without visible aggregates.

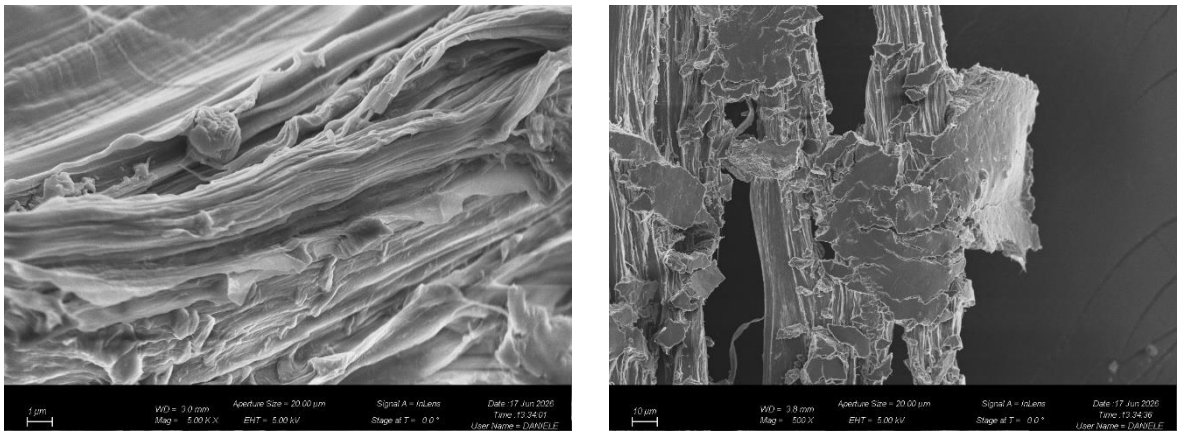


Figure A 35 – FESEM images of the β-Carotene-functionalized bilayer scaffold – a) 5.00KX detail showing a nano-aggregate on the fibre surface; b) 500X fractured fibre cross-section (from laser cutting).

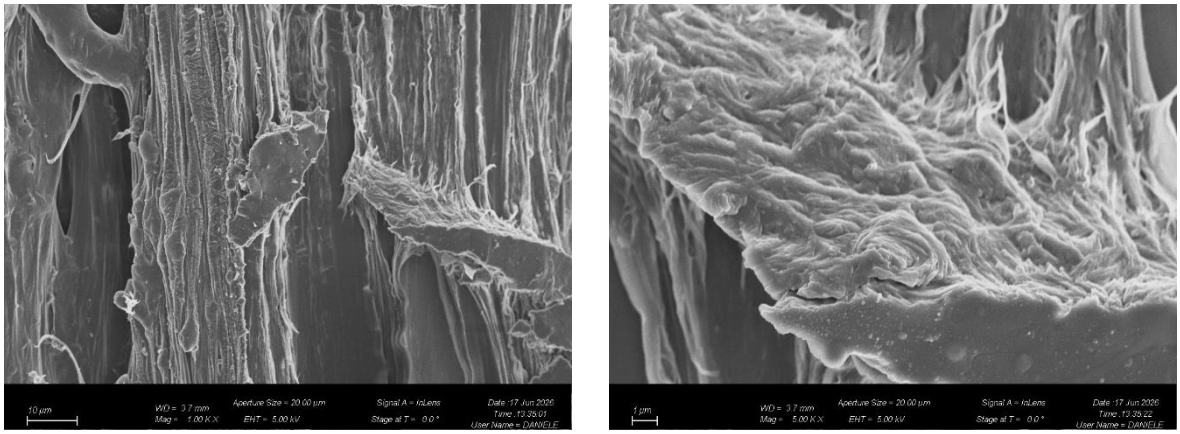


Figure A 36 – FESEM images of the β-Carotene-functionalized bilayer scaffold – a) 1.00KX and b) 5.00KX detail of a fracture surface.

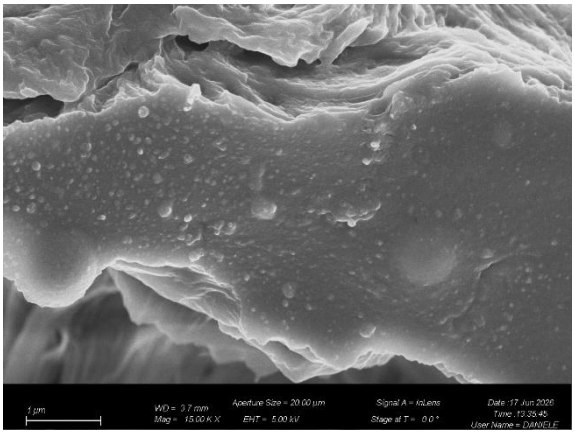


Figure A 37 – FESEM image of the β-Carotene-functionalized bilayer scaffold, 15.00KX detail showing nano-aggregates coating the fibre surface.

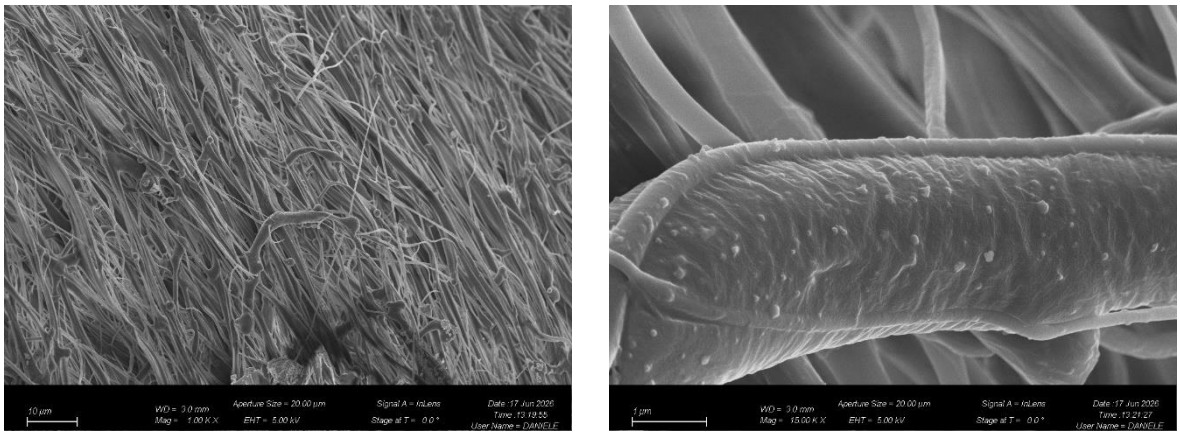


Figure A 38 – FESEM images of the Curcumin-functionalized bilayer scaffold – a) 1.00KX overview; b) 15.00KX detail, showing fine nanoparticles distributed on the fibre surface.

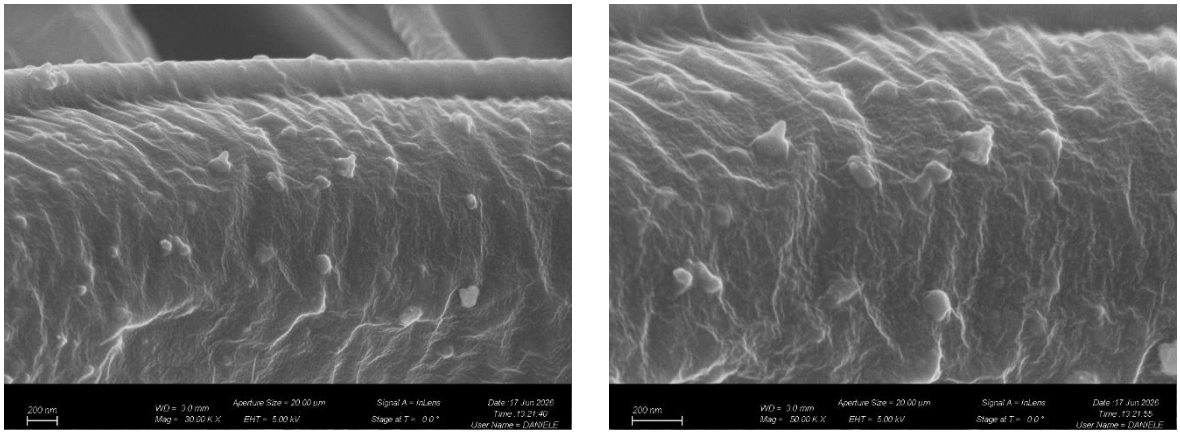


Figure A 39 – FESEM images of the Curcumin-functionalized bilayer scaffold – a) 30.00KX and b) 50.00KX detail of the surface nanoparticles.

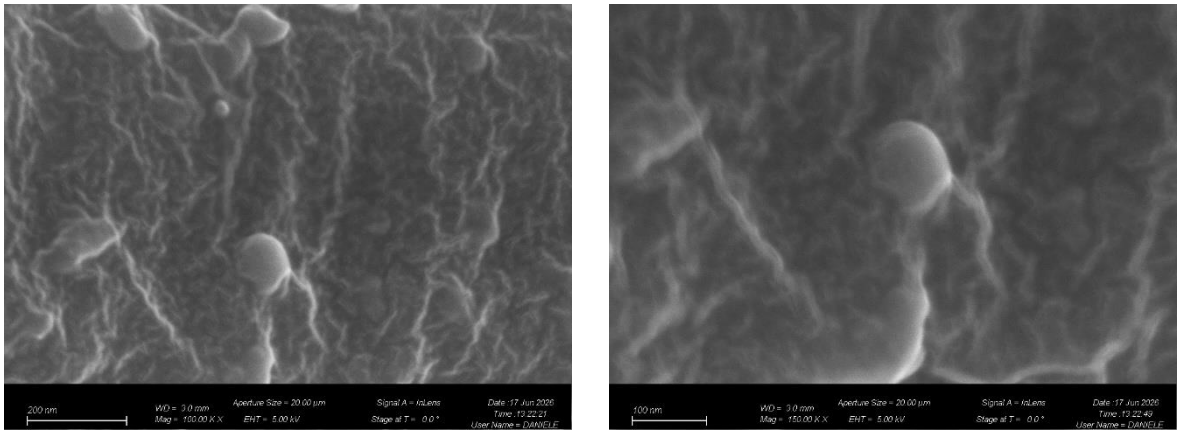


Figure A 40 – FESEM images of the Curcumin-functionalized bilayer scaffold – a) 100.00KX and b) 150.00KX high-magnification detail of individual nanoparticles.

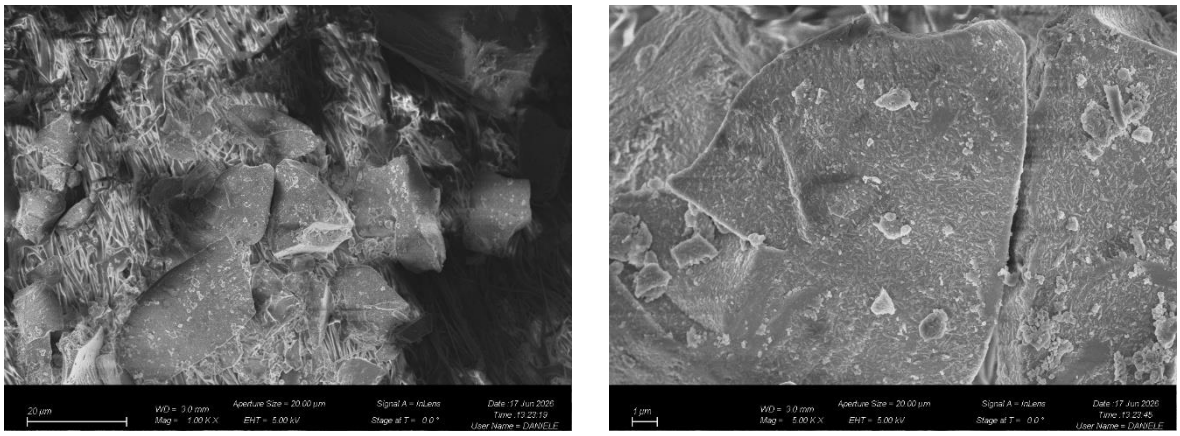


Figure A 41 – FESEM images of the Curcumin-functionalized bilayer scaffold – a) 1.00KX and b) 5.00KX detail of a fracture surface with embedded crystalline particles (due to laser cutting).

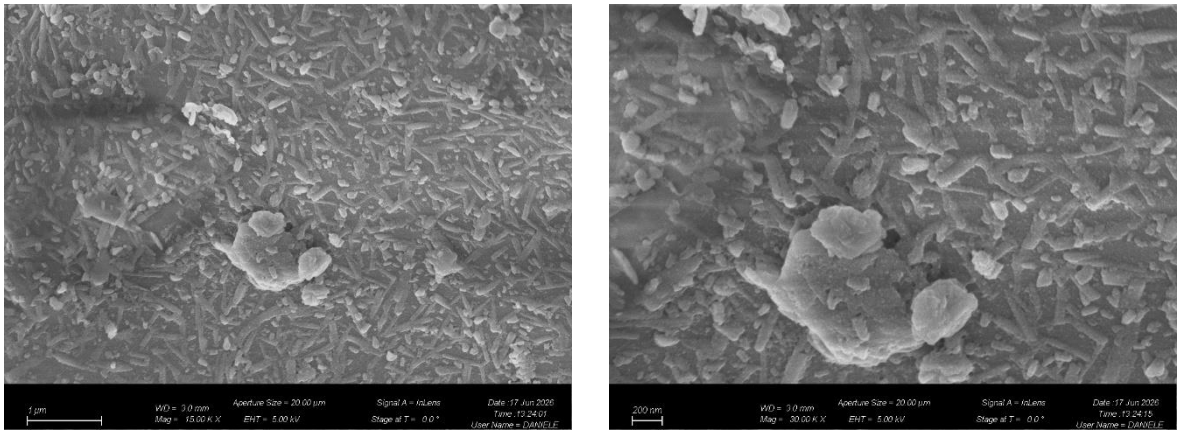


Figure A 42 – FESEM images of the Curcumin-functionalized bilayer scaffold – a) 15.00KX and b) 30.00KX detail showing needle-shaped curcumin nanocrystals on the fracture surface.

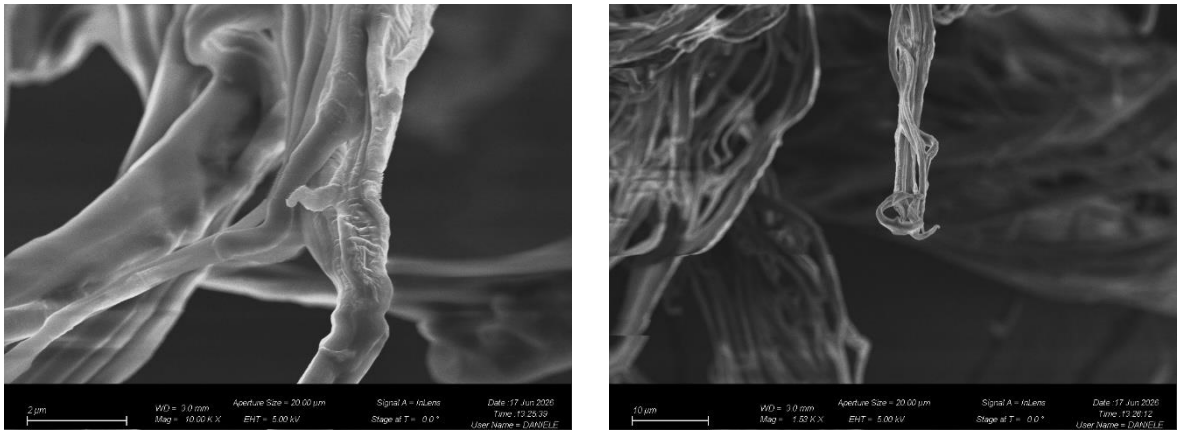


Figure A 43 – FESEM images of the Curcumin-functionalized bilayer scaffold – a) 10.00KX and b) 1.50KX detail of folded fibre morphology.

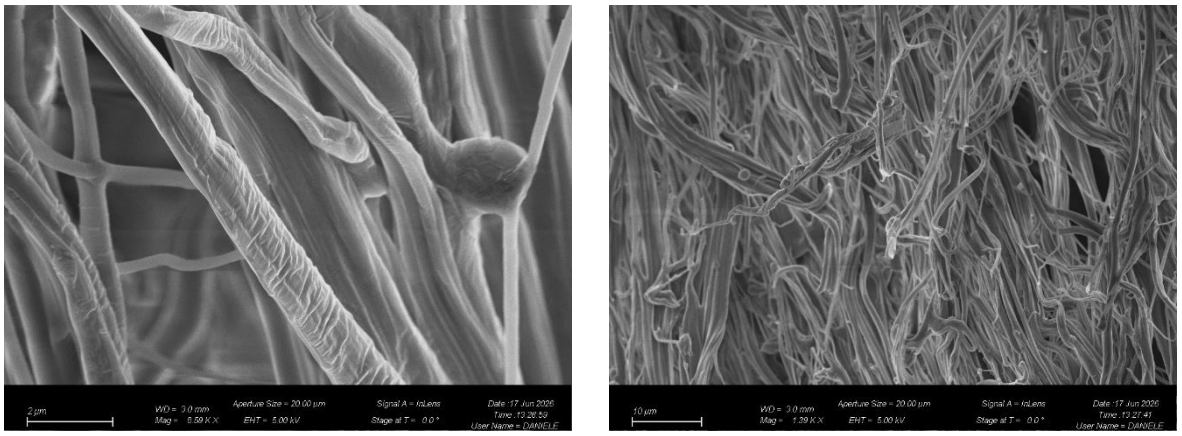


Figure A 44 – FESEM images of the Curcumin-functionalized bilayer scaffold – a) 8.59KX detail showing a bead-on-string defect at a fibre junction; b) 1.39KX overview of the surrounding fibrous network.

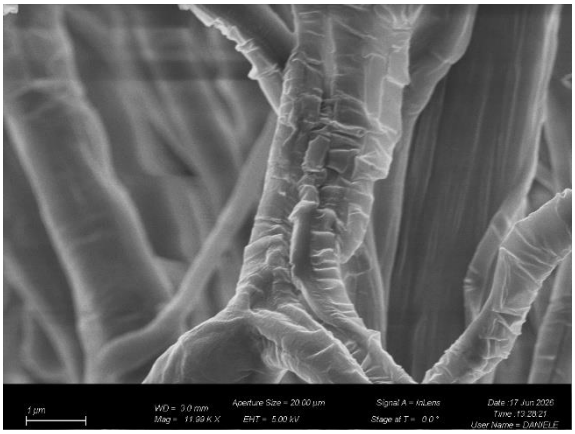


Figure A 45 – FESEM image of the Curcumin-functionalized bilayer scaffold, 11.93KX detail of a fibre junction.

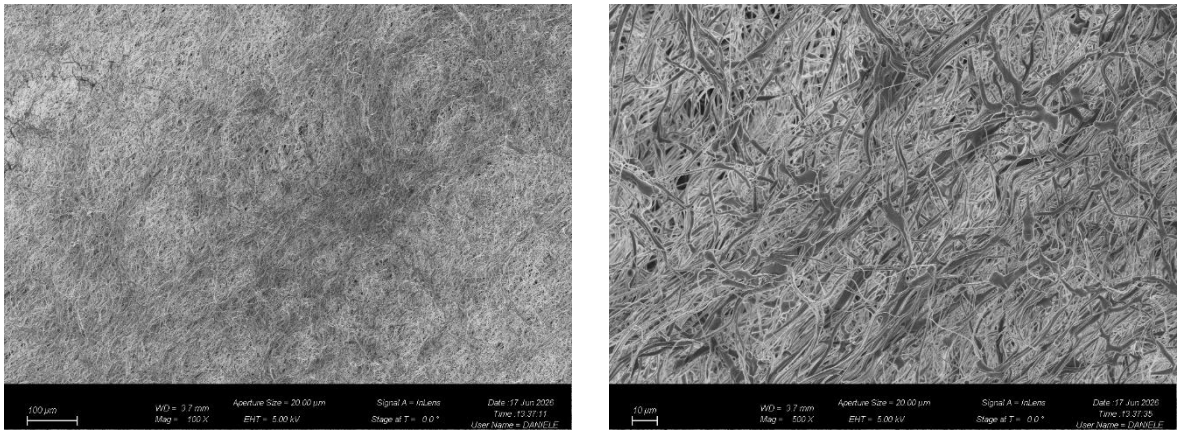


Figure A 46 – FESEM images of the Mix-functionalized bilayer scaffold – a) 100X overview; b) 500X detail, showing beading and aggregate deposits from the combined bioactive agents.

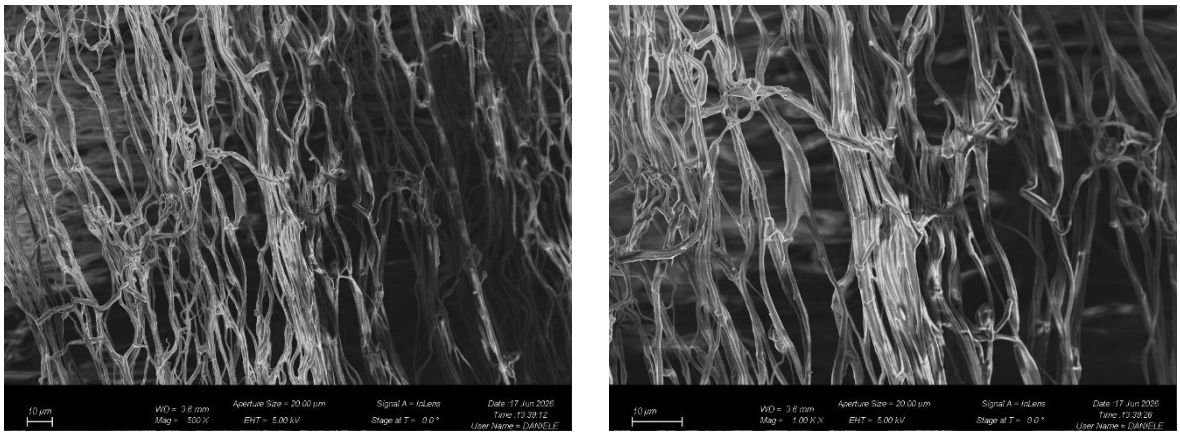


Figure A 47 – FESEM images of the Mix-functionalized bilayer scaffold – a) 500X and b) 1.00KX detail of a fibre bundle.

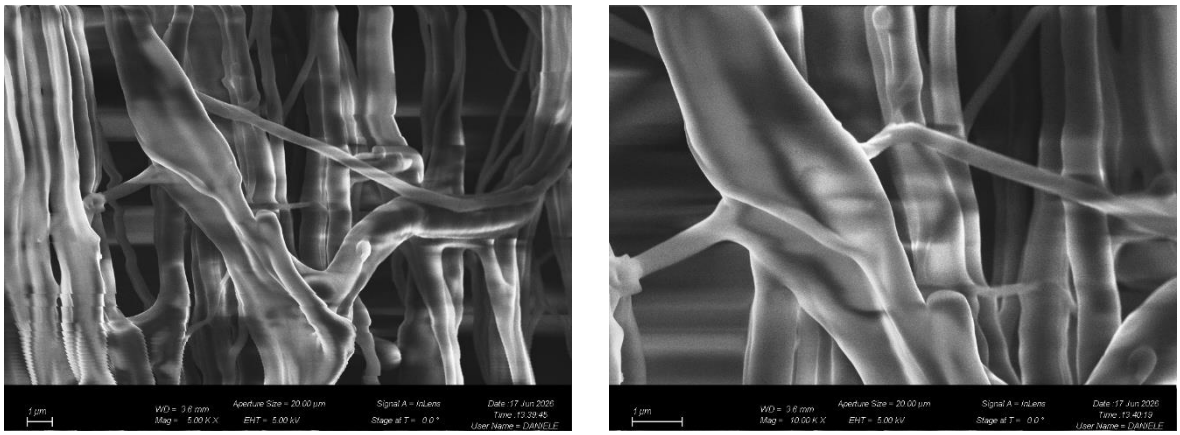


Figure A 48 – FESEM images of the Mix-functionalized bilayer scaffold – a) 5.00KX and b) 10.00KX detail of a fibre junction.

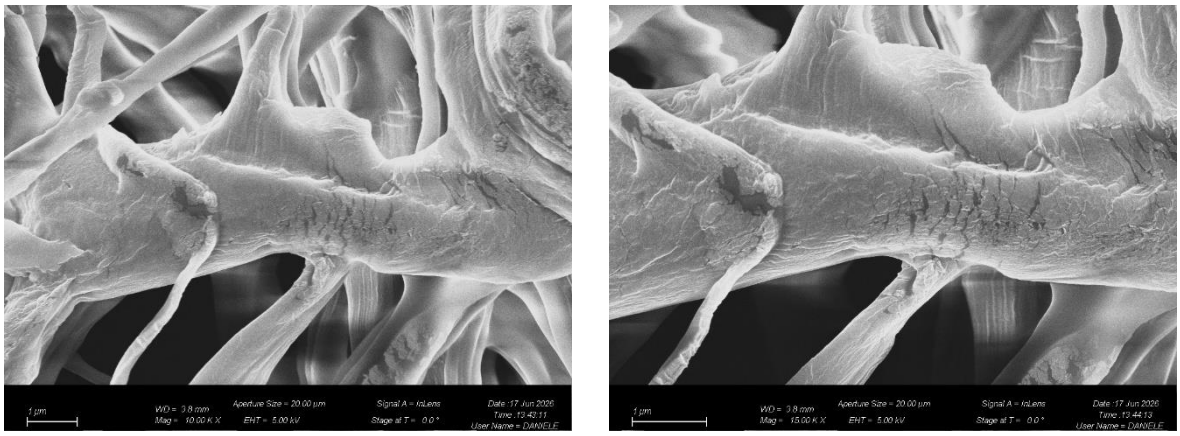


Figure A 49 – FESEM images of the Mix-functionalized bilayer scaffold – a) 10.00KX and b) 15.00KX detail of a surface deposit on a fibre.

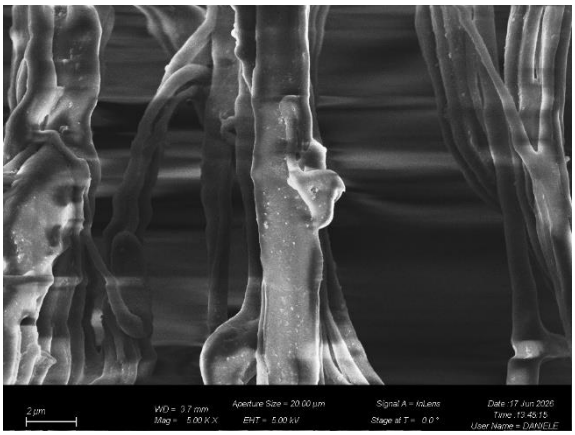


Figure A 50 – FESEM image of the Mix-functionalized bilayer scaffold, 5.00KX detail of a fibre bundle with a small surface deposit.

9.2 Chemical and Structural Characterisation

9.2.1 Raman Spectroscopy

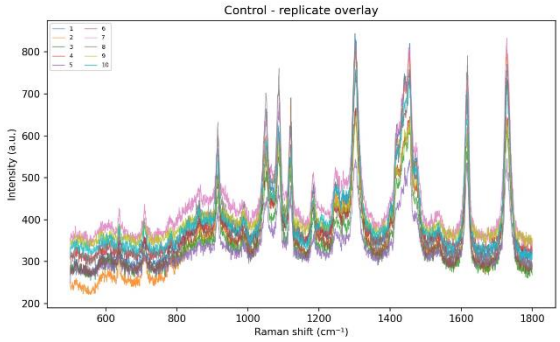


Figure A 51 – Raman spectra (overlay of 10 replicates) of the PCL-PCL (7:3) control bilayer scaffold, front layer.

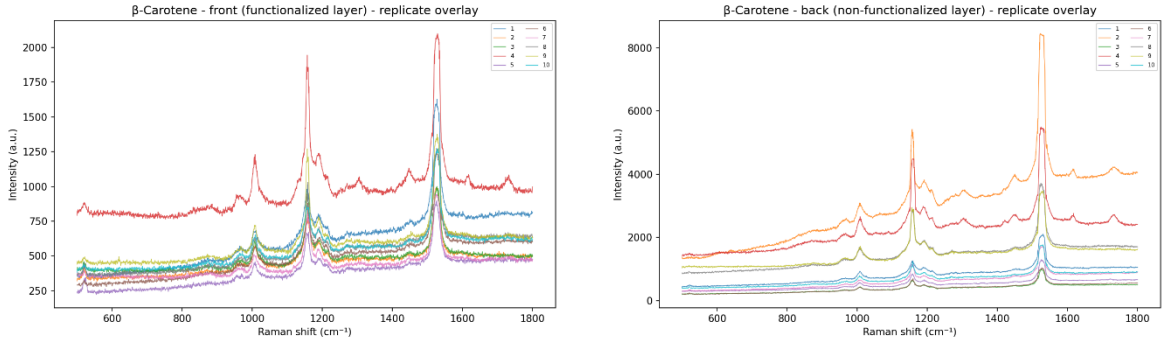


Figure A 52 – Raman spectra of the β-Carotene-functionalized bilayer scaffold – a) front (functionalized layer), overlay of 10 replicates; b) back (non-functionalized layer), overlay of 10 replicates.

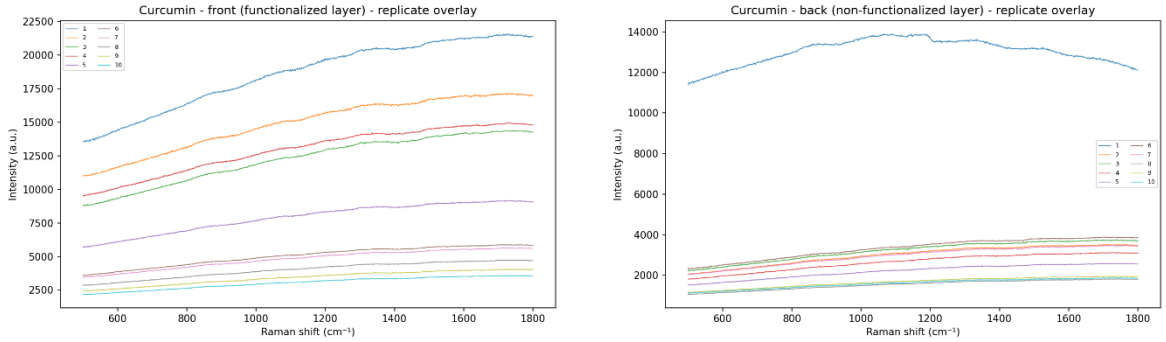


Figure A 53 – Raman spectra of the Curcumin-functionalized bilayer scaffold – a) front (functionalized layer), overlay of 10 replicates; b) back (non-functionalized layer), overlay of 10 replicates.

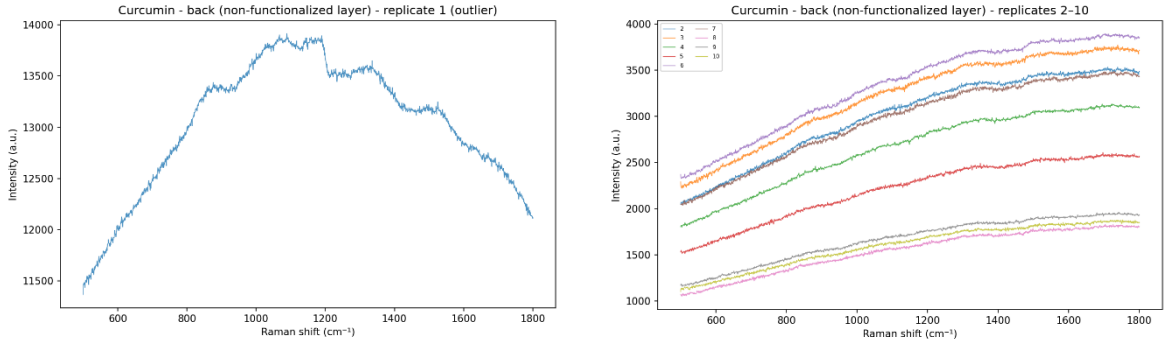


Figure A 54 – Raman spectra of the back (non-functionalized layer) of the Curcumin-functionalized bilayer scaffold, replicate overlay split for clarity due to a large intensity outlier – a) replicate 1 (outlier); b) replicates 2–10.

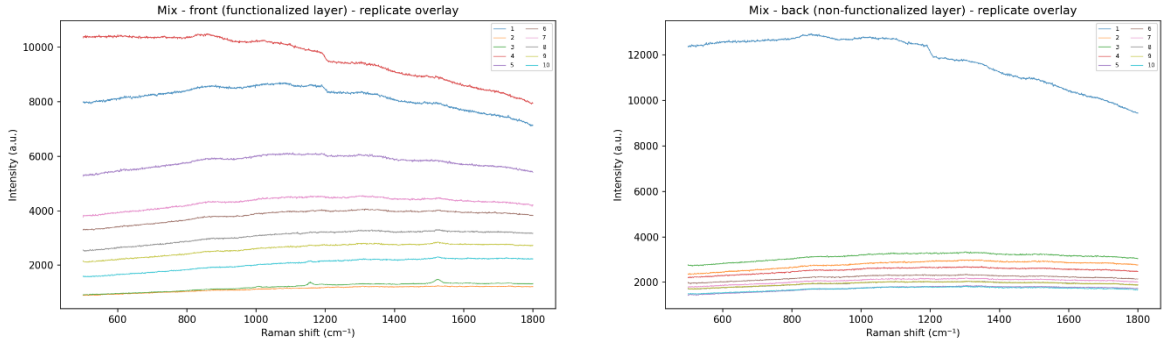


Figure A 55 – Raman spectra of the Mix-functionalized bilayer scaffold – a) front (functionalized layer), overlay of 10 replicates; b) back (non-functionalized layer), overlay of 10 replicates.

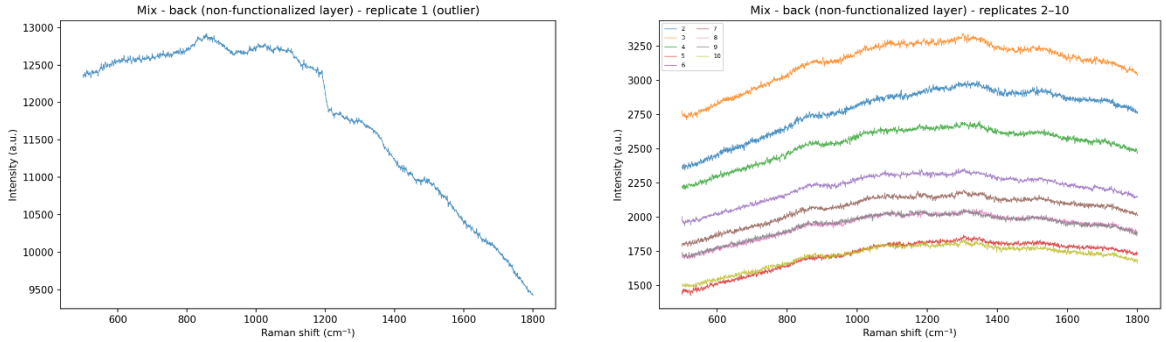


Figure A 56 – Raman spectra of the back (non-functionalized layer) of the Mix-functionalized bilayer scaffold, replicate overlay split for clarity due to a large intensity outlier – a) replicate 1 (outlier); b) replicates 2–10.

9.3 In Vitro Biological Assay

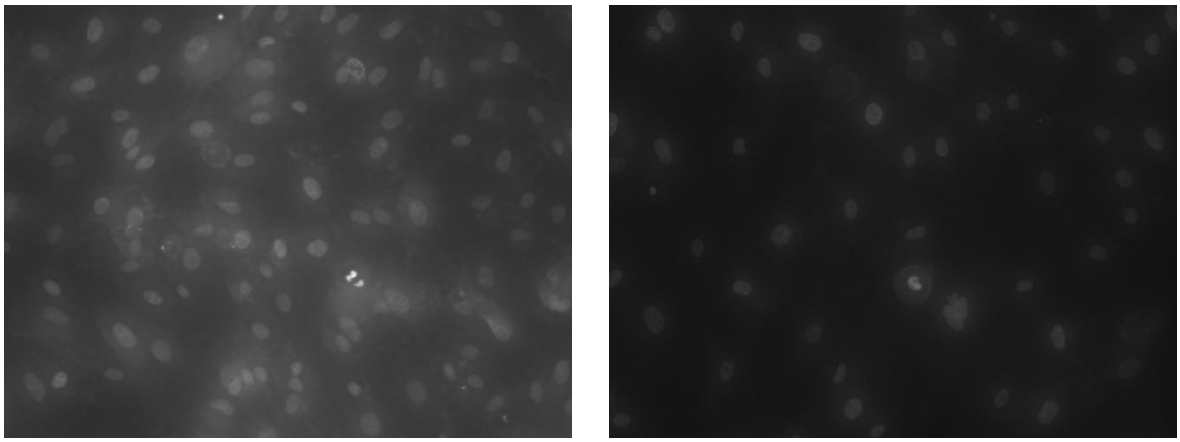


Figure A 57 – Fluorescence microscopy of human dermal fibroblasts exposed to the PCL control scaffold eluate, 1-day time point – a) replicate 1; b) replicate 2.

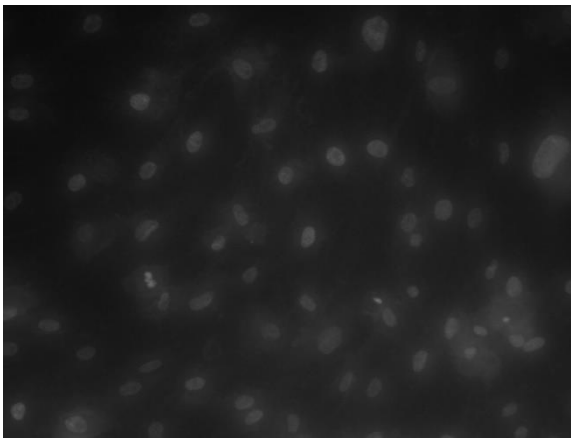


Figure A 58 – Fluorescence microscopy of human dermal fibroblasts exposed to the PCL control scaffold eluate, 1-day time point, replicate 3.

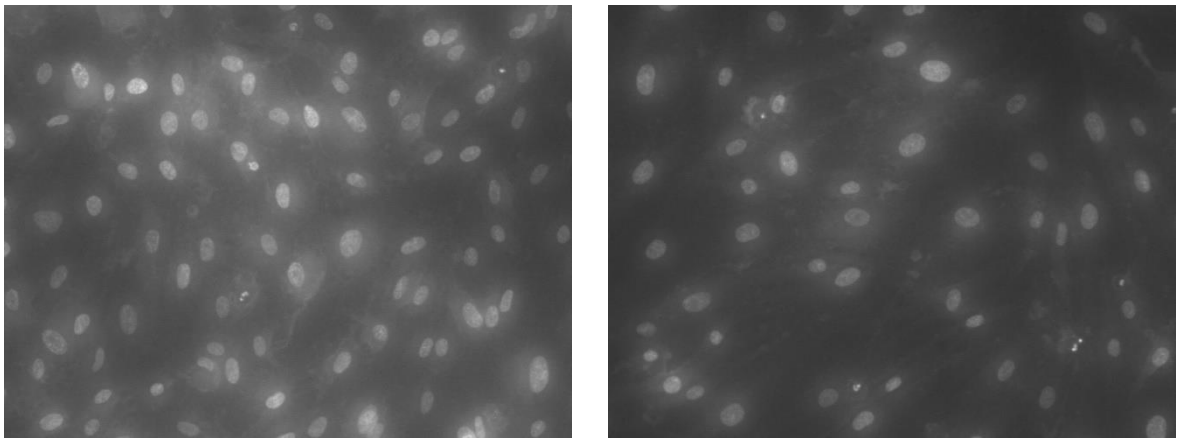


Figure A 59 – Fluorescence microscopy of human dermal fibroblasts exposed to the PCL control scaffold eluate, 3-day time point – a) replicate 1; b) replicate 2

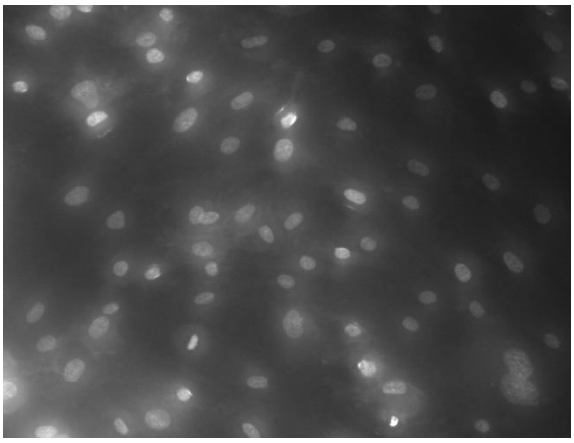


Figure A 60 – Fluorescence microscopy of human dermal fibroblasts exposed to the PCL control scaffold eluate, 3-day time point, replicate 3.

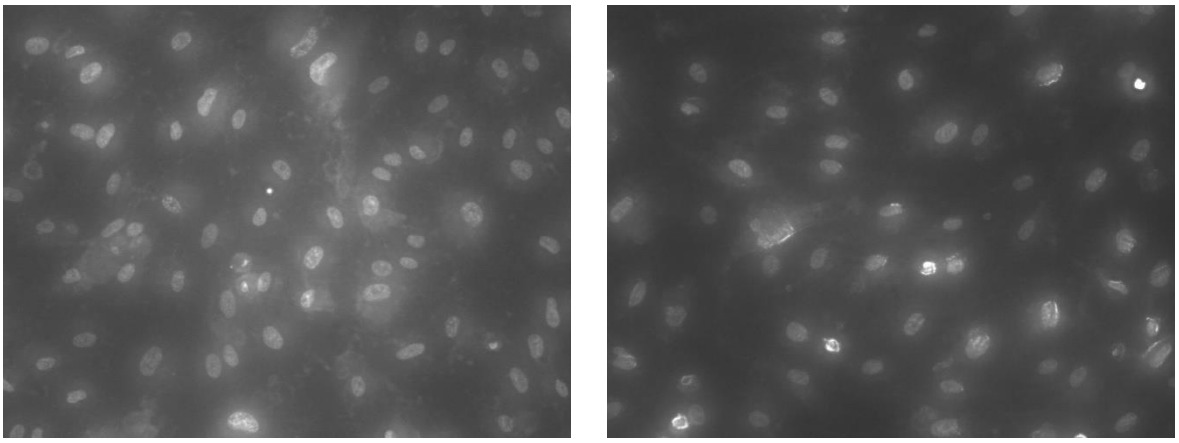


Figure A 61 – Fluorescence microscopy of human dermal fibroblasts exposed to the PCL control scaffold eluate, 7-day time point – a) replicate 1; b) replicate 2.

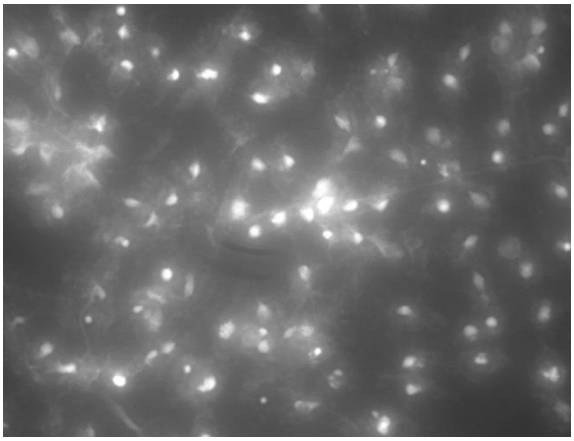


Figure A 62 – Fluorescence microscopy of human dermal fibroblasts exposed to the PCL control scaffold eluate, 7-day time point, replicate 3.

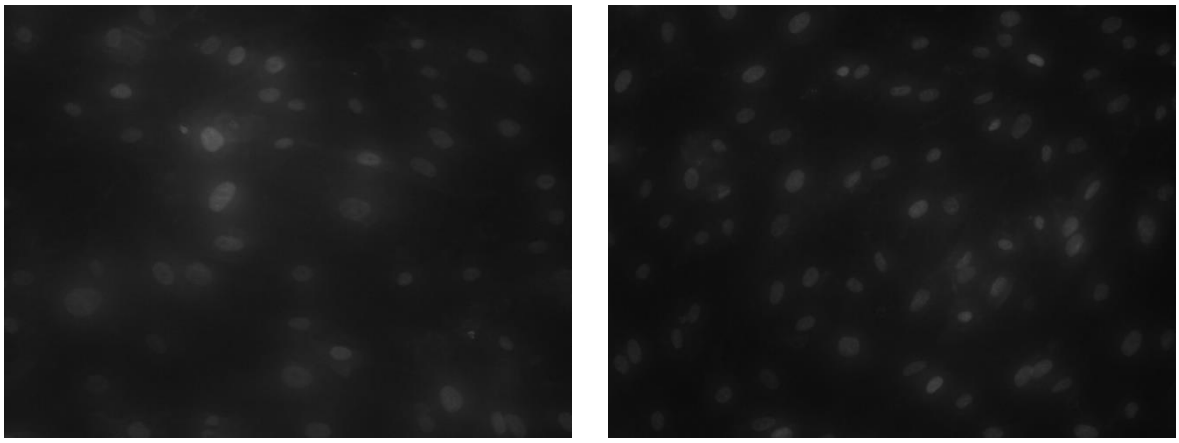


Figure A 63 – Fluorescence microscopy of human dermal fibroblasts exposed to the β-Carotene-functionalized scaffold eluate, 1-day time point – a) replicate 1; b) replicate 2.

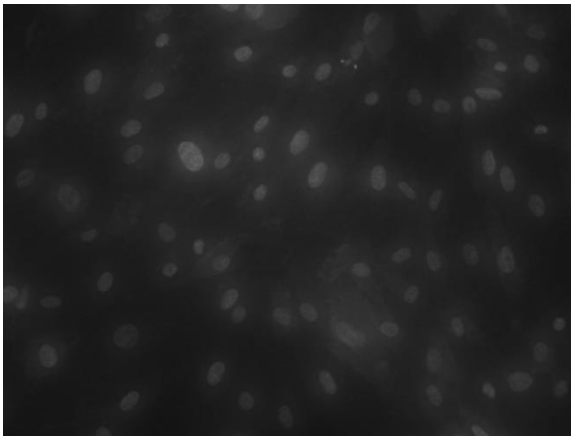


Figure A 64 – Fluorescence microscopy of human dermal fibroblasts exposed to the β-Carotene-functionalized scaffold eluate, 1-day time point, replicate 3.

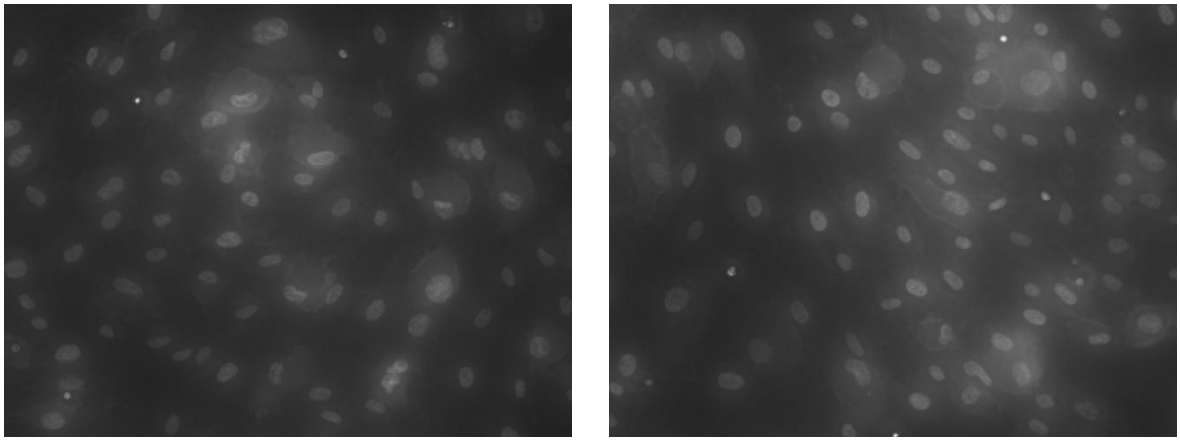


Figure A 65 – Fluorescence microscopy of human dermal fibroblasts exposed to the β-Carotene-functionalized scaffold eluate, 3-day time point – a) replicate 1; b) replicate 2

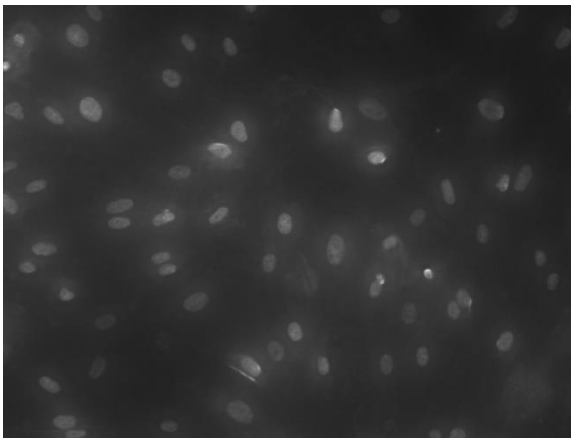


Figure A 66 – Fluorescence microscopy of human dermal fibroblasts exposed to the β-Carotene-functionalized scaffold eluate, 3-day time point, replicate 3.

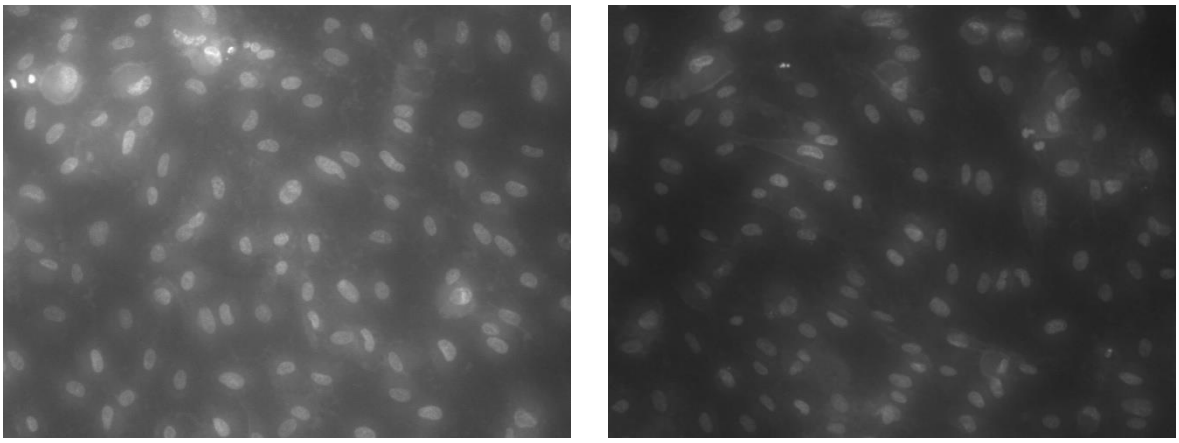


Figure A 67 – Fluorescence microscopy of human dermal fibroblasts exposed to the β-Carotene-functionalized scaffold eluate, 7-day time point – a) replicate 1; b) replicate 2.

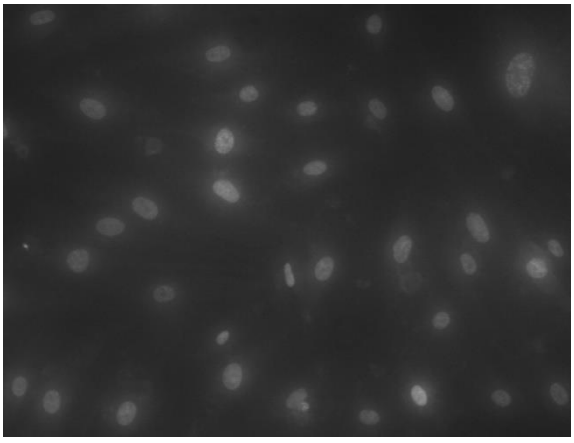


Figure A 68 – Fluorescence microscopy of human dermal fibroblasts exposed to the β-Carotene-functionalized scaffold eluate, 7-day time point, replicate 3.

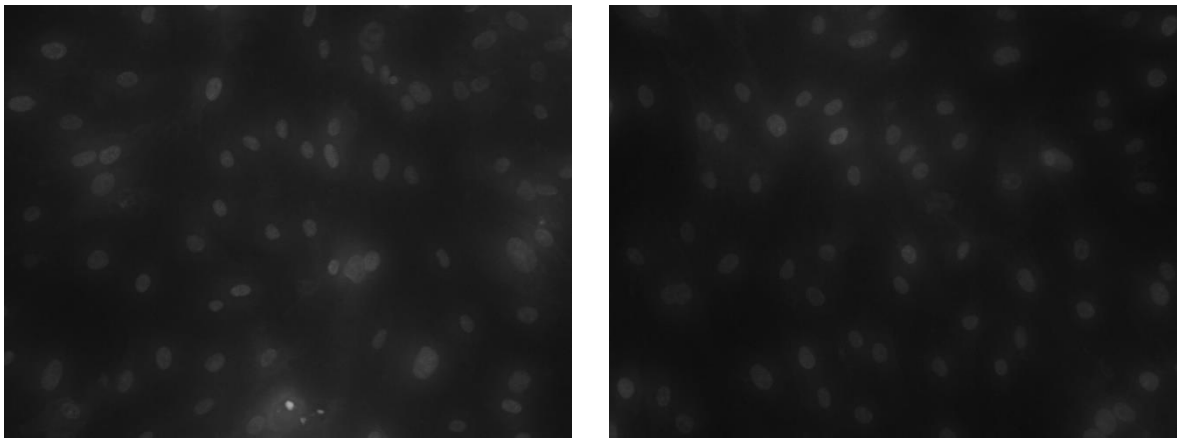


Figure A 69 – Fluorescence microscopy of human dermal fibroblasts exposed to the Curcumin-functionalized scaffold eluate, 1-day time point – a) replicate 1; b) replicate 2

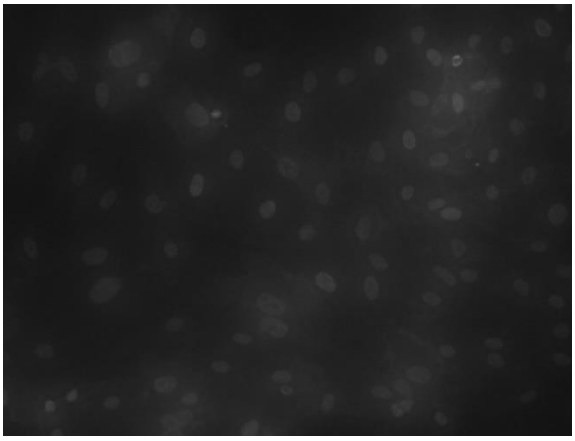


Figure A 70 – Fluorescence microscopy of human dermal fibroblasts exposed to the Curcumin-functionalized scaffold eluate, 1-day time point, replicate 3.

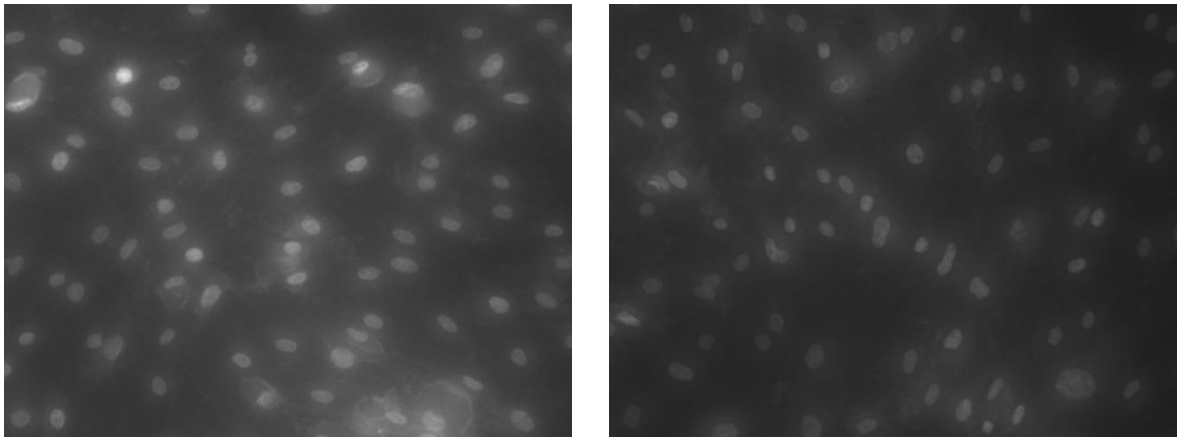


Figure A 71 – Fluorescence microscopy of human dermal fibroblasts exposed to the Curcumin-functionalized scaffold eluate, 3-day time point – a) replicate 1; b) replicate 2.

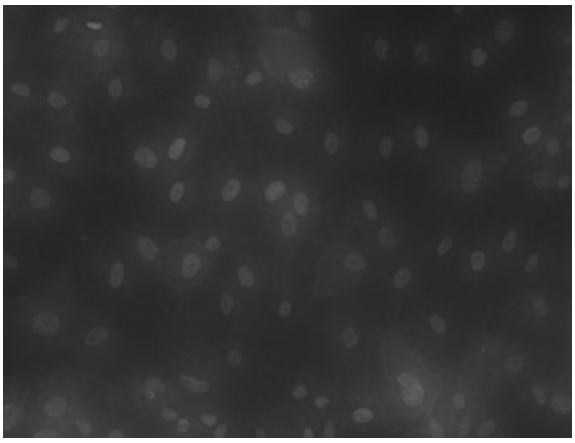


Figure A 72 – Fluorescence microscopy of human dermal fibroblasts exposed to the Curcumin-functionalized scaffold eluate, 3-day time point, replicate 3.

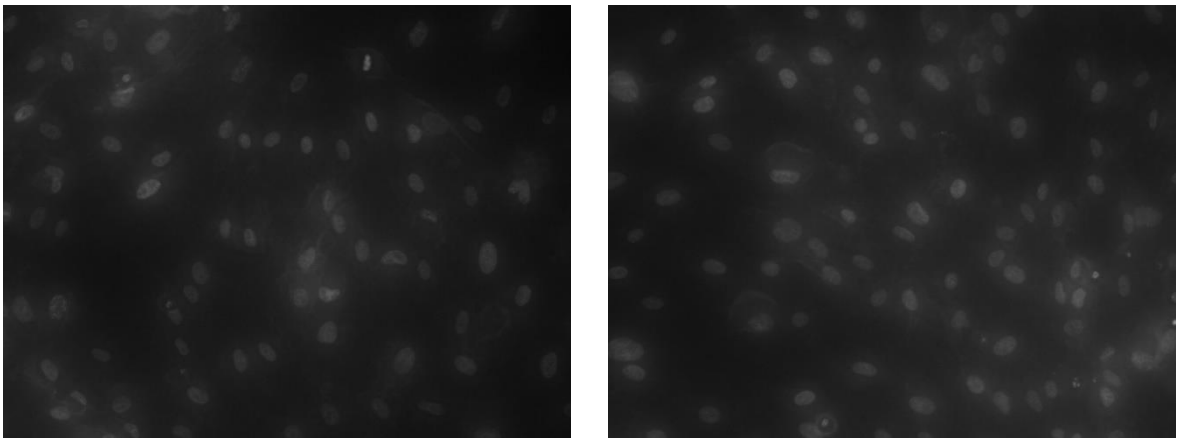


Figure A 73 – Fluorescence microscopy of human dermal fibroblasts exposed to the Curcumin-functionalized scaffold eluate, 7-day time point – a) replicate 1; b) replicate 2.

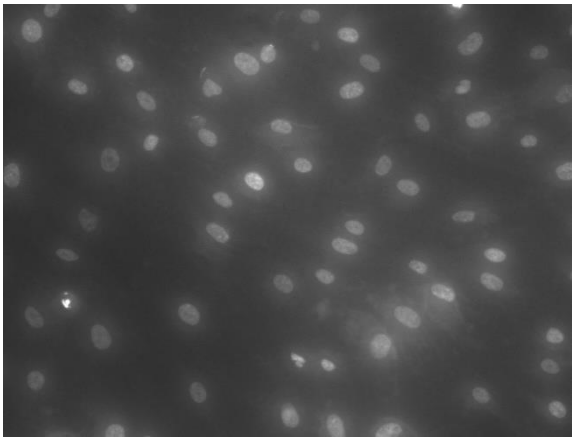


Figure A 74 – Fluorescence microscopy of human dermal fibroblasts exposed to the Curcumin-functionalized scaffold eluate, 7-day time point, replicate 3.

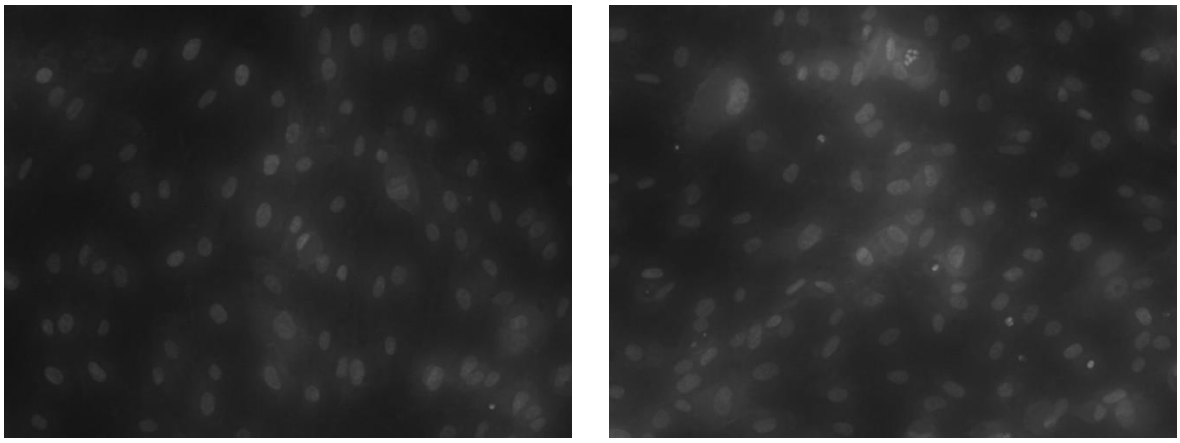


Figure A 75 – Fluorescence microscopy of human dermal fibroblasts exposed to the Mix-functionalized scaffold eluate, 1-day time point – a) replicate 1; b) replicate 2.

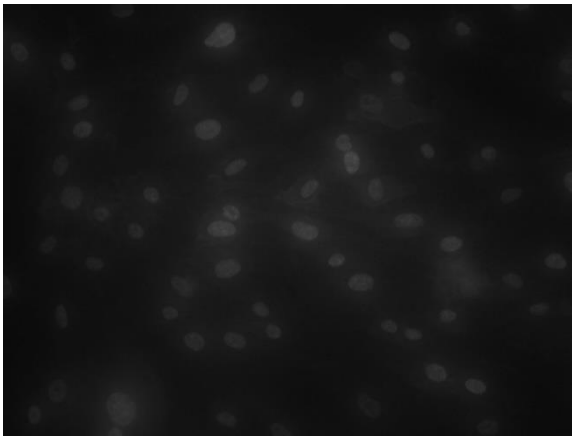


Figure A 76 – Fluorescence microscopy of human dermal fibroblasts exposed to the Mix-functionalized scaffold eluate, 1-day time point, replicate 3.

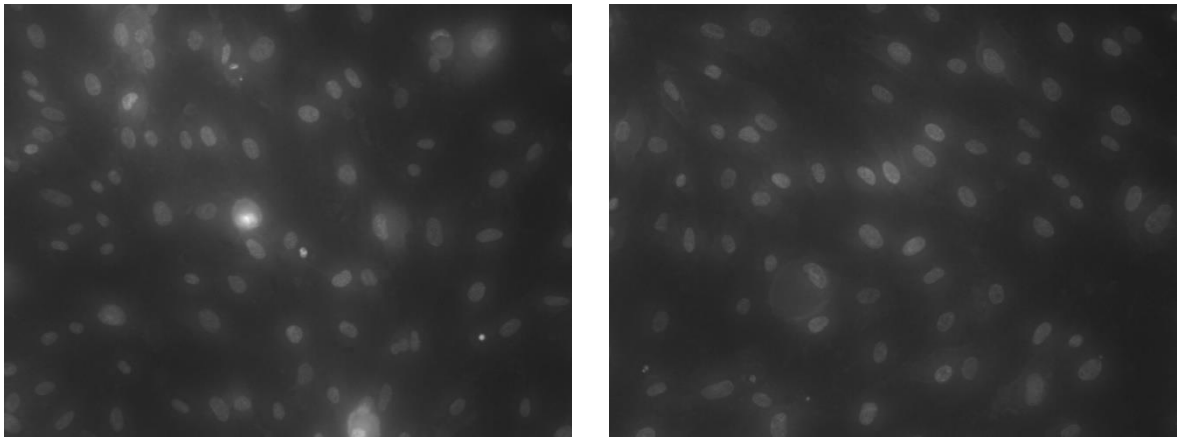


Figure A 77 – Fluorescence microscopy of human dermal fibroblasts exposed to the Mix-functionalized scaffold eluate, 3-day time point – a) replicate 1; b) replicate 2.

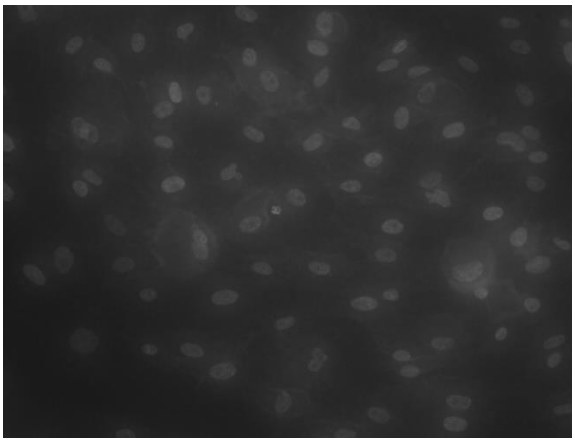


Figure A 78 – Fluorescence microscopy of human dermal fibroblasts exposed to the Mix-functionalized scaffold eluate, 3-day time point, replicate 3.

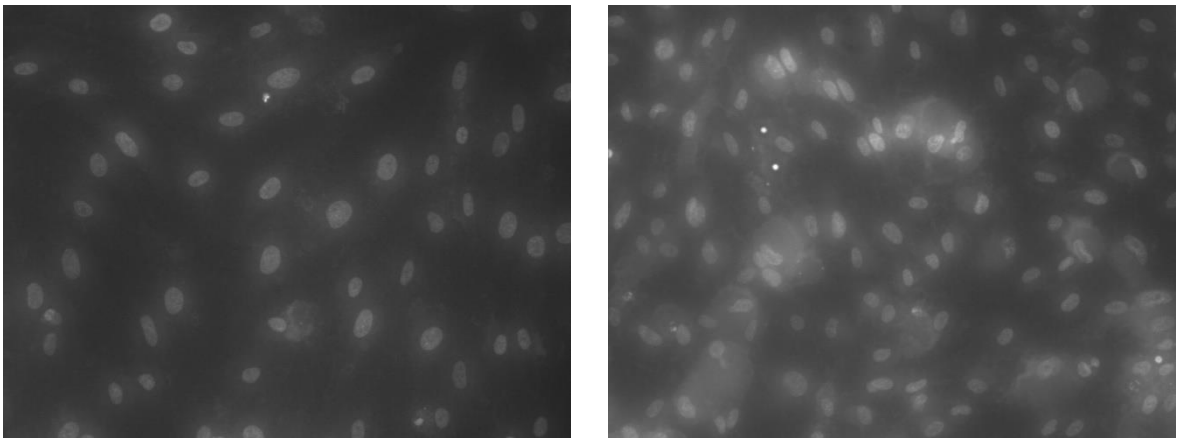


Figure A 79 – Fluorescence microscopy of human dermal fibroblasts exposed to the Mix-functionalized scaffold eluate, 7-day time point – a) replicate 1; b) replicate 2.

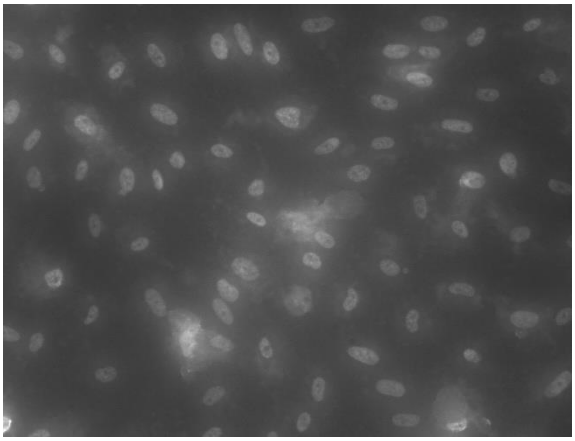


Figure A 80 – Fluorescence microscopy of human dermal fibroblasts exposed to the Mix-functionalized scaffold eluate, 7-day time point, replicate 3.

10 Acknowledgements

It is difficult, in just a few lines, to fully express how much this journey has given me. From the professors at Politecnico di Torino, who supported me throughout these years, to those at Kyoto Institute of Technology, who welcomed me as if I were one of their own from the very beginning.

In particular, I would like to express my gratitude to Professor Sangermano, who has essentially been following me since my second year and who made it possible for me to achieve my dream of going to Japan to study. To Professor Spriano, who guided me before, during, and after my thesis work, and to the members of the Glance group, especially Anna, who accompanied me during the final stages of my work. To Professor Marin, who made me feel at home in Kyoto, as well as to the people at the office, with whom I shared so much despite the short time we had together.

Behind this journey, however, there are people who have supported me long before I even started university and whom I will never be able to thank enough.

To my parents, who have never failed to support me in everything I have done, giving me peace of mind and showing me that, no matter how things might turn out, I would always have them by my side.

To my grandparents, who, despite their aches and occasional lapses in memory, have always encouraged me to do more and supported me every step of the way.

To my uncles and aunts, who have always been an important presence in my life and have never failed to give me their love and support.

To Giulia, Gabri, and little Lapo, who made me a "progino" and who, despite the distance, have always remained close to me.

To my brother, who, even though he will never show it, I know is a little proud of me deep down.

To Nives and Yue, who have been great study companions, and to Kira, who left us two years ago, but who is still always with me.

And, last but certainly not least, I want to thank Giorgia, the best person I could have ever had by my side. Throughout these years, she has not simply accompanied me on my journey, but has lived it alongside me, standing by me through every moment and supporting every choice I have made. She gave me the strength to keep going through the most difficult moments, believed in me even when perhaps I was the first not to believe in myself, and never failed to give me her support.

If I have reached this milestone today, part of the credit is yours as well. Thank you for being my strength when I needed it the most and for sharing with me not only this journey, but

everything that came with it. I cannot wait to discover what the future has in store for us and to continue living it together with you.